
*Investigation of Cementitious Materials and
Fibre Reinforced Mortar in 3D Printing*

Pshtiwan Nasruldeen Shakor

A thesis in fulfilment of the requirement for the award of the degree

DOCTOR OF PHILOSOPHY

School of Civil and Environmental Engineering

Faculty of Engineering and Information Technology

May 2019

Certificate of Original Authorship

I, **Pshtiwan Shakor**, declare that this thesis, submitted in fulfilment of the requirements for the award of Doctor of Philosophy, in the School of Civil and Environmental Engineering, Faculty of Engineering and Information Technology at the University of Technology Sydney.

This thesis is wholly my own work unless otherwise referenced or acknowledged. In addition, I certify that all information sources and literature used are indicated in the thesis. This document has not been submitted for qualifications at any other academic institution. This research is supported by the Australian Government Research Training Program.

Production Note:

Signature: Signature removed prior to publication.

Date: 25 Oct 2019

To my family

Acknowledgement

I would like to thank Centre for Built Infrastructure Research (CBIR), School of Civil and Environmental Engineering, Faculty of Engineering and Information Technology (FEIT) at the University of Technology Sydney (UTS).

I wish to express sincere gratitude to my principal supervisor A/Prof Shami Nejadi for his patience, outstanding guidance, motivation and caring support provided throughout my thesis. I would also like to gratitude my co-supervisor Dr Gavin Paul for their invaluable guidance, positive attitude and support over the course of this research.

I also acknowledge the assistance of the technical staff from the Civil Engineering Laboratories and Mechanical Engineering Laboratories. I also gratefully acknowledge the ProtoSpace Laboratory for their support. Working in the lab would never have been easy without the assistance provided by all these people.

My special thanks go to my colleagues and capstone students from the Mechanical and Civil Engineering departments at the UTS for fostering an enjoyable working environment. Many thanks to HCED program for their support during my PhD research.

Finally, I greatly thank my parents and my siblings for their unconditional love and support.

List of Research Papers

Published Research Papers:

- Shakor, P., Sanjayan, J., Nazari, A. & Nejadi, S. 2017, 'Modified 3D printed powder to cement-based material and mechanical properties of cement scaffold used in 3D printing', *Construction and Building Materials*, vol. 138, pp. 398-409.
- Shakor, P., Nejadi, S., Paul, G. & Malek, S. 2019, 'Review of emerging additive manufacturing technologies in 3D printing of cementitious materials in the construction industry', *Frontiers in Built Environment*, vol. 4, pp. 85.
- Shakor, P., Nejadi, S., Paul, G., Sanjayan, J. & Nazari, A. 2019, 'Mechanical Properties of Cement-Based Materials and Effect of Elevated Temperature on Three-Dimensional (3-D) Printed Mortar Specimens in Inkjet 3-D Printing', *ACI Materials Journal*, vol. 116, pp. 55-67.
- Shakor, P., Nejadi, S. & Paul, G. 2019, 'A study into the effect of different nozzles shapes and fibre-reinforcement in 3D printed mortar', *Materials*, vol. 12, pp. 1708.
- Shakor, P., Nejadi S., Paul, G., Sanjayan, J. & Aslani, F. 2019 'Heat Curing as a Means of Post-processing Influence on 3D Printed Mortar Specimens in Powder-based 3D Printing', vol. 93, pp. 65-74.

Submitted Research Papers:

- Shakor, P., Nejadi, S., Paul, G. 'Effects of Different Orientation Angle on the Mechanical Behaviours of the Cementitious Powder and Gypsum Powder in Inkjet 3DP ', *Cement and Concrete Composites Journal*.

- Shakor, P., Nejadi, S., Paul, G. 'Investigation into the effect of delays between printed layers on the mechanical strength of inkjet 3DP mortar ', *Manufacturing Letters*. (Accepted)
- Shakor, P., Nejadi, S., Paul, G.& Sanjayan J., 'Dimensional accuracy, wettability, flowability and porosity in the inkjet 3DP for the gypsum and cement mortar materials', *Automation in Construction*. (Accepted)

Conference Papers:

- Shakor, P., Renneberg, J., Nejadi, S. & Paul, G. 2017, 'Optimisation of Different Concrete Mix Designs for 3D Printing by Utilising 6DOF Industrial Robot', ISARC. 34th Proceedings of the International Symposium on Automation and Robotics in Construction, Taipei, Taiwan.
- Shakor, P. & Nejadi, S. 2017, '3D Printed Concrete Evaluations by Using Different Concrete Mix Designs', 7th Recent Trends in Engineering and Technology, Bangkok, Thailand.
- Shakor, P., Nejadi, S., Paul, G. & Sanjayan, J. 2018, 'A Novel Methodology of Powder-based Cementitious Materials in 3D Inkjet Printing for Construction Applications ', 6th International Conference on the Durability of Concrete Structures, Leeds, UK.
- Shakor, P., Nejadi, S. & Paul, G. 2018, 'An investigation into the behaviour of cementitious mortar in the construction of 3D printed members by the means of extrusion printing', 3DcP. 1st international conference on 3D Construction Printing, Melbourne, Australia.

- Shakor, P., Nejadi, S. & Paul, G. 2018, 'Wettability, flowability and porosity in the inkjet 3DP for the gypsum and cement mortar materials.', 6th conference of the combined Australian Materials Societies; incorporating materials Australia and the Australian Ceramic Society, Wollongong, Australia.
- Shakor, P., Nejadi, S., and Paul, G. 2019, 'An Investigation into the Effects of Deposition Orientation of Material on the Mechanical Behaviours of the Cementitious Powder and Gypsum Powder in Inkjet 3D Printing' 36th International Symposium on Automation and Robotics in Construction Alberta, Canada.
- Shakor, P., Nejadi, S., and Paul, G. 2019, 'Effect of Elevated Temperatures as a means of Curing in Inkjet 3D Printed Mortar Specimens', 29th Biennial National Conference, Concrete Institute of Australia, Sydney, Australia.

The author has received an award for excellence in concrete 2017 at the Concrete Institute of Australia-VIC for an innovative study for construction applications.

Contents

Acknowledgement	iii
List of Research Papers	iv
Contents	v
List of Figures	vi
List of Tables	vii
Abstract	viii
CHAPTER ONE	1
1. INTRODUCTION	1
1.1 ADDITIVE MANUFACTURING OF CONCRETE	1
1.2 CONCRETE FORMWORK	1
1.3 STATE OF THE PROBLEM	2
1.4 SCOPE AND OBJECTIVES OF THE RESEARCH	3
1.5 THESIS OUTLINE	5
CHAPTER TWO	6
2. LITERATURE REVIEW	6
2.1 INTRODUCTION	6
2.2 OVERVIEW OF RAPID PROTOTYPE TECHNOLOGIES	8
2.2.1 POWDER-BASED (INKJET PRINTING)	10
2.2.2 SELECTIVE LASER SINTERING (SLS)	13
2.2.3 EXTRUSION PRINTING (EXTRUSION BASED PROCESS)	15
2.2.4 STEREOLITHOGRAPHY APPARATUS (SLA)	20
2.2.5 LAMINATED-OBJECT MANUFACTURING (LOM)	21
2.2.6 FUSED-DEPOSITION MODELLING (FDM)	21
2.2.7 LASER-ENGINEERED NET SHAPING (LENS)	23
2.2.8 ROBOCASTING	24
2.3 SUMMARY	25
CHAPTER THREE	27
3. MATERIAL PROPERTIES	27
3.1 INTRODUCTION	27

3.2 MATERIAL PROPERTIES FOR 3DP	27
3.3 BENCHMARK EXPERIMENTAL RESULTS	34
3.3.1 POWDER-BASED (INKJET PRINTING (BINDER JETTING))	34
3.3.1.1 FORMULATION OF THE POWDER FOR INKJET 3DP	34
3.3.1.2 SPECIMEN PREPARATION AND DETERMINATION OF THE WATER/CEMENT RATIO	36
3.3.1.3 RESOLUTION AND SURFACE ROUGHNESS OF THE POWDER-BED	38
3.3.2 SELECTIVE LASER SINTERING	39
3.3.3 EXTRUSION PRINTING	41
3.3.3.1 MIX DESIGN FOR CEMENTITIOUS MATERIALS	41
3.3.3.2 EXTRUDER ADAPTATION AND DELIVERY SYSTEM	43
3.4 SUMMARY AND DISCUSSION	45
CHAPTER FOUR	52
4. TECHNIQUES AND METHODOLOGY	52
4.1 POWDER-BASED (INKJET) PRINTING TECHNIQUE	52
4.1.1 DELIVERY SYSTEM	52
4.1.2 PRINTING APPLICATIONS	55
4.2 EXTRUSION PRINTING TECHNIQUE	56
4.2.1 DELIVERY SYSTEMS	57
4.2.1.1 ADAPTED AUGER EXTRUDER	60
4.2.1.2 PERISTALTIC PUMPS	62
4.2.1.3 PROGRESSIVE CAVITY PUMPS	63
4.2.2 PRINTING APPLICATIONS	65
CHAPTER FIVE	67
5. EXPERIMENTAL PROGRAM	67
5.1 EXPERIMENTAL PROGRAM	67
5.1.1 POWDER-BASED 3D PRINTING TECHNIQUE	67
5.1.2 EXTRUSION PRINTING TECHNIQUE	71
5.2 EXPERIMENTAL PROGRAM FOR THE POWDER-BASED 3D PRINTING	73
5.2.1 EXPERIMENTAL PROGRAM AND CURING CONDITIONS	78
5.2.1.1 COMPRESSIVE STRENGTH TEST	80

5.2.1.2 FLEXURAL STRENGTH TEST.....	90
5.2.1.3 TENSILE STRENGTH TEST	94
5.2.1.4 SHEAR STRENGTH TEST	94
5.2.1.5 POROSITY TEST.....	95
5.2.1.6 FLOWABILITY TEST	98
5.2.1.7 WETTABILITY TEST.....	98
5.2.1.8 DIMENSIONAL ACCURACY TEST	101
5.2.1.9 DELAY PRINTING TIME	102
5.2.1.10 UTILISING THREE-DIMENSIONAL SCANNING AND SCANNING ELECTRON MICROSCOPE..	104
5.2.1.11 MECHANICAL CHARACTERIZATION OF GLASS FIBRE REINFORCEMENT IN INKJET 3DP SPECIMENS.....	104
5.3 ANALYTICAL RELATIONSHIPS FOR THE MECHANICAL AND MATERIAL PROPERTIES (POWDER- BASED 3DP).....	106
5.3.1 COMPRESSIVE STRESS-STRAIN RELATIONSHIP.....	106
5.3.2 POROSITY-SATURATION LEVEL RELATIONSHIP	107
5.3.3 COMPRESSIVE STRENGTH-SATURATION LEVEL RELATIONSHIP.....	110
5.4 EXPERIMENTAL PROGRAM FOR EXTRUSION PRINTING.....	111
5.4.1 EXPERIMENTAL PROGRAM AND CURING CONDITIONS.....	112
5.4.1.1 PROGRAMMING OF THE ROBOT AND CONTROL METHODOLOGY	116
5.4.1.2 COMPRESSIVE STRENGTH TEST	121
5.4.1.3 FLEXURAL STRENGTH TEST.....	123
5.4.1.4 SQUEEZE-FLOW TEST	124
5.4.1.5 SLUMP AND SPREAD-FLOW TEST	124
5.4.1.6 SETTING TIME TEST	125
5.5 ANALYTICAL DETERMINATION OF THE MECHANICAL PROPERTIES.....	126
5.5.1 END-EFFECTOR SPEED-SLURRY DISCHARGE/LINE WIDTH RELATIONSHIP.....	136
5.5.2 REGRESSION RELATIONSHIP FOR VELOCITY AND SLURRY DISCHARGE.....	140
CHAPTER SIX.....	142
6. EXPERIMENTAL RESULTS AND DISCUSSIONS	142
6.1 RESULTS AND DISCUSSIONS - 3DP PARTS.....	142

6.1.1 POWDER-BASED (INKJET) 3D PRINTING MATERIALS.....	142
6.1.2 EXTRUSION PRINTING MATERIALS.....	217
6.2 NUMERICAL ANALYSIS USING ABAQUS	243
6.3 STRESS-STRAIN DIAGRAM FOR INKJET 3DP MORTAR.....	246
CHAPTER SEVEN	252
7. SUMMARY AND CONCLUSION.....	252
7.1 SUMMARY.....	252
7.2 CONCLUSION.....	253
7.2.1 INKJET 3D PRINTING	253
7.2.2 EXTRUSION 3D PRINTING.....	256
7.3 RECOMMENDATIONS FOR FUTURE RESEARCH.....	257
REFERENCES:.....	260
APPENDIX A	295
INTRODUCTION	295
SPECIFICATIONS	295
IMPORTANT TERMS	296
ZPRINTER 150 AND PROJET 360 COMPONENTS.....	299
SYSTEM EXTERIOR PARTS DESCRIPTION.....	300
APPENDIX B	302
GENERAL INTRODUCTION TO OPERATION MODES AND ADDITIONAL FUNCTIONS	302
OPERATING PROCEDURE	303
FROM THE TEACH PENDANT.....	303
COORDINATES.....	305
POSITION DATA.....	306
APPENDIX C	309
APPENDIX D	319
OVERVIEW	319
DEFINING LINEAR ELASTIC MATERIAL BEHAVIOUR.....	319
DEFINING LINEAR ELASTIC RESPONSE FOR VISCOELASTIC MATERIALS.....	319
DIRECTIONAL DEPENDENCE OF LINEAR ELASTICITY	320

STABILITY OF A LINEAR ELASTIC MATERIAL.....	320
DEFINING ISOTROPIC ELASTICITY	321
DEFINING ORTHOTROPIC ELASTICITY BY SPECIFYING THE ENGINEERING CONSTANTS	322
DEFINING TRANSVERSELY ISOTROPIC ELASTICITY.....	323
DEFINING ORTHOTROPIC ELASTICITY IN PLANE STRESS	324
DEFINING ORTHOTROPIC ELASTICITY BY SPECIFYING THE TERMS IN THE ELASTIC STIFFNESS MATRIX.....	325
DEFINING FULLY ANISOTROPIC ELASTICITY	326
DEFINING ORTHOTROPIC ELASTICITY FOR WARPING ELEMENTS.....	327

List of Figures

FIGURE 2. 1: OVERVIEW OF RAPID PROTOTYPING TECHNOLOGIES AND THE TECHNIQUES DISCUSSED IN THIS CHAPTER. THE BOX HIGHLIGHTS THE TECHNIQUES EMPLOYED IN THIS THESIS.	8
FIGURE 2. 2: SUBTRACTIVE MANUFACTURING PROCESS (A), ADDITIVE MANUFACTURING PROCESS FOR EXTRUSION PRINTING AND INKJET PRINTING (B).	9
FIGURE 2. 3: SCHEMATIC ILLUSTRATION OF THE INKJET 3D PRINTING PROCESS.	11
FIGURE 2. 4: SELECTIVE SINTERING DIAGRAM.	14
FIGURE 2. 5: EXTRUSION PRINTING PROCESS FOR THE CONCRETE	16
FIGURE 2. 6: GRAPHICAL EXPLANATION OF EXTRUSION PRINTING USING 6 DOF ROBOT WITH A PROGRESSIVE CAVITY PUMP.	17
FIGURE 2. 7: SLA DIAGRAM PROCESS (REPRODUCED AFTER (CAÑETE VELA 2014)).....	20
FIGURE 2. 8: LOM DIAGRAM PROCESS (REPRODUCED AFTER (3DPRINTINGFROMSCRATCH 2019)).....	21
FIGURE 2. 9: FDM DIAGRAM PROCESS (REPRODUCED AFTER (ZEIN ET AL. 2002))	22
FIGURE 2. 10: FDM DIAGRAM PROCESS (REPRODUCED AFTER (ARD09-8 2009))	24
FIGURE 2. 11: ROBOCASTING APPARATUS (REPRODUCED AFTER (MORISSETTE ET AL. 2000))	25
FIGURE 3. 1: PRINTED CONCRETE THROUGH A CUSTOM-MADE DELIVERY SYSTEM (NOTE: A MAX. PARTICLE SIZE OF COARSE AGGREGATE OF APPROXIMATELY 5MM).....	28
FIGURE 3. 2: (A) PARTICLE SIZE DISTRIBUTION OF CEMENT MORTAR AND ZPOWDER (ZP 151) FOR THE INKJET PRINTING, (B) PARTICLE SIZE ANALYSIS OF MORTAR VERSUS PERCENTAGE PASSING FOR THE EXTRUSION PRINTING.....	36
FIGURE 3. 3: PRINTED CEMENTITIOUS CUBE VIA INKJET 3D PRINTER: (A) COMPRESSED UNDER A UNIAXIAL LOAD, (B) CRACKING AND DETACHING OF THE SHELL AND CORE PARTS.	37
FIGURE 3. 4: USING LASER SINTERING (SLS) FOR CEMENT PASTE USING DIFFERENT POWERS (WATTS).....	40
FIGURE 3. 5: (A) PRINTED MORTAR VIA EXTRUSION PRINTING, (B) PRINTED MORTAR USING ROBOT EXTRUSION DRIED IN AMBIENT TEMPERATURE FOR ONE DAY.	42
FIGURE 3. 6: EXTRUDER MOUNTED TO THE END-EFFECTOR OF THE ROBOT.	43
FIGURE 4. 1: SCHEMATIC ILLUSTRATION OF POWDER-BASED 3D PRINTER WITH RELATIONSHIP BETWEEN FLOWABILITY, WETTABILITY, POWDER-BED POROSITY AND POROSITY IN THE SPECIMEN.	53
FIGURE 4. 2: INSIDE THE FEEDER CONTAINER SHOWING THE NUMBER OF HOLES IN THE BIN.	54
FIGURE 4. 3: 3DP CONCRETE PROCEDURES FOR CONSTRUCTION APPLICATIONS (REPRODUCED AFTER (PAUL ET AL. 2018))..	59

FIGURE 4. 4: (A) SIMULATED ROBOT WITH A PRINT NOZZLE ASSEMBLY ATTACHED, TO DEMONSTRATE AND CHECK MOTION PLANS AND PATHS. (B) REAL WORLD ROBOT AND AUGER NOZZLE ASSEMBLY.....	60
FIGURE 4. 5: (A) EXTRUDER JOINED TO THE DENSO ROBOT. (B) NOZZLE TYPES MADE WITH ALUMINIUM AND PLA.	61
FIGURE 4. 6: RESULTANT PRINT OF SUCCESSFUL PRINT YIELDING A STABLE MORTAR AND DECENT SLUMP SLURRY. ISSUES WITH THE AUGER DELIVERY STRUGGLING TO CONSISTENTLY PUSH OUT MATERIALS.....	61
FIGURE 4. 7: PERISTALTIC PUMP WITH AN EXPLANATION OF THE PUMPING PROCESS.....	62
FIGURE 4. 8: PRINTED CEMENT MORTAR USING A PERISTALTIC PUMP WITH A 7.9MM DIAMETER.....	63
FIGURE 4. 9: SCHEMATIC ILLUSTRATION OF THE PROGRESSIVE CAVITY PUMP WITH THE DETAIL OF THE PUMPING SYSTEM.	64
FIGURE 4. 10: PRODUCT OF THE PROGRESSIVE CAVITY PUMP USING A 20 MM CIRCULAR NOZZLE.	64
FIGURE 5. 1: SCHEMATIC ILLUSTRATION OF THE SELECTIVE BINDER (CEMENT) ACTIVATION TECHNIQUE IN INKJET 3D PRINTING.	68
FIGURE 5. 2: SCHEMATIC DEPICTION OF POWDER-BED PRINTING (LAYER TECHNIQUE) IN INKJET 3D PRINTING.....	69
FIGURE 5. 3: SCHEMATIC ILLUSTRATION OF THE ROBOTIC ARM MOVEMENT TO PRINT A HOLLOW-COLUMN USING MATLAB SOFTWARE.....	72
FIGURE 5. 4: PARTICLE SIZE DISTRIBUTIONS FOR Z-PRINTER POWDER, OPC, CAC AND COMBINATION OF CAC & OPC.	74
FIGURE 5. 5: PARTICLE SIZE DISTRIBUTIONS OF ZPOWDER AND CAC&OPC POWDER. *Q3 IS THE UNIT STANDING FOR THE LOGARITHM OF THE PERCENTAGE OF TOTAL PARTICLES.....	75
FIGURE 5. 6: HISTOGRAM AND CURVE OF PARTICLE SIZE DISTRIBUTIONS OF ZP 151 AND CP POWDER. *Q3 IS THE UNIT REPRESENTING THE DENSITY DISTRIBUTION OF THE TOTAL PARTICLES.	75
FIGURE 5. 7: SCHEMATIC ILLUSTRATION OF THE PROCESS FOR PREPARING CEMENTITIOUS POWDER.....	76
FIGURE 5. 8: DIRECTIONAL DEPICTION OF THE 3D PRINTING PROCESS.....	79
FIGURE 5. 9: SCHEMATIC DIAGRAM OF THE 3D PRINTING PROCESS AND CURING PROCESS.....	80
FIGURE 5. 10: INTERIOR (CORE) AND EXTERIOR (SHELL) FOR SAME SATURATION LEVELS IN 3DP SAMPLE.....	82
FIGURE 5. 11: MORPHOLOGY SURFACE OF CUBIC SPECIMENS (LEFT) (OLYMPUS BX61 MICROSCOPE-10x) AND SAMPLES OF CAC, OPC WITH Li2CO3 PREPARED BY 3D PRINTING (RIGHT).	83
FIGURE 5. 12 LAYER EXPLANATION AND POWDER/BINDER INTERACTION BETWEEN LAYERS.....	85
FIGURE 5. 13: (A) REAL-WORLD 3DP CUBES IN (0°,30°,37.7°,45°,90°) ORIENTATION (B) CAD FILE OF 3DP CUBES IN (0°,30°,37.7°,45°,90°).....	89

FIGURE 5. 14: (A) CUBIC SPECIMENS (20×20×20MM), (B) PRISM SPECIMENS (60×5×5MM).	90
FIGURE 5. 15: DIFFERENT PLANES IN THE 3DP SOFTWARE FOR EACH AXIS (X, Y, Z), THE PRISM(70×10×4MM) PRESENTED IN THE PLANE OF YZ 0° AND YZ 90°.....	91
FIGURE 5. 16: (A)-PRISM SPECIMEN (70×10×4MM) (YZ90) DEGREES, (B)-PRISM SPECIMEN (70×10×4MM) (YZ0) DEGREES.	91
FIGURE 5. 17: (A) GREEN PART OF 3DP CEMENT MORTAR PRISM, (B) GREEN PART OF 3DP CEMENT MORTAR CUBE.	94
FIGURE 5. 18: A) LOADING LAYOUT IN X-AXIS (0° ORIENTATION) ON THE CP SAMPLE; B) EXPERIMENTAL PRINCIPLE FOR SETTING UP THE SPECIMENS AND APPLYING THE LOAD.	95
FIGURE 5. 19: STEPS OF THE PENETRATION OF ZB63 LIQUID INTO ZPOWDER, (A) IMPACT TIME OF DROPLET ON THE SURFACE OF THE POWDER, (B) PENETRATION PROCESS OF LIQUID ON THE POWDER AFTER 16 SECONDS, (C) ABSORBING MOST OF THE LIQUID INTO THE POWDER.....	99
FIGURE 5. 20: ILLUSTRATION OF THE DROP PENETRATION TEST SETUP.....	100
FIGURE 5. 21: MAXIMUM COMPRESSIVE STRESS-STRAIN DIAGRAM FOR THE PRINTED CUBIC (50×50×50)MM.....	106
FIGURE 5. 22: 3DP SPECIMENS ARE CURED USING DIFFERENT AGENTS.....	109
FIGURE 5. 23: POROSITY VERSUS SATURATION LEVELS FOR CP SPECIMENS WITHOUT LITHIUM CARBONATE.	109
FIGURE 5. 24: COMPRESSIVE STRENGTH VERSUS SATURATION LEVELS FOR CP SPECIMENS WITHOUT LITHIUM CARBONATE.	110
FIGURE 5. 25: TOP-DOWN VIEW OF THE 6-DOF ROBOTIC ARM AND PUMP SETUP.	111
FIGURE 5. 26: (A) FINE SAND AND ORDINARY PORTLAND CEMENT PARTICLE SIZE DISTRIBUTION, (B) COARSE AGGREGATE PARTICLE SIZE DISTRIBUTION.....	113
FIGURE 5. 27: EXPLODED VIEW OF THE EXTRUDER ASSEMBLY THAT IS CONNECTED TO THE PROGRESSIVE CAVITY PUMP AND IS ATTACHED TO THE END OF THE ROBOT.	113
FIGURE 5. 28: THE FINAL SYSTEM WITH THE PROGRESS CAVITY PUMP CONNECTED TO THE ROBOT.	114
FIGURE 5. 29: TRIPLE LAYERS OF THE MORTAR AFTER SQUEEZING UNDER A UNIAXIAL COMPRESSION LOAD.....	124
FIGURE 5. 30: SCHEMATIC ILLUSTRATION OF THE PREDICTION OF THE PRINTED MORTAR PASSED THROUGH THE CIRCULAR NOZZLE.	128
FIGURE 5. 31: CROSS-SECTION OF THE DETAILS OF THE PRINTED LAYERS AFTER CRUSHING UNDER A UNIAXIAL COMPRESSION LOAD, USING A CAVITY PUMP AS A DELIVERY SYSTEM (NOZZLE Ø50MM).	129

FIGURE 5. 32: (A) REAL PRINTED CIRCULAR AND RECTANGULAR SHAPE; (B) LUBRICATION SQUEEZE FLOW BETWEEN TWO SPHERICAL PARTICLES (LEFT) AND TWO CUBIC PARTICLES (RIGHT) WITH AN IDENTICAL CHARACTERISTIC HALF-WIDTH, R (REPRODUCED BY (C WALINA, HARRISON & WAGNER 2016)).	132
FIGURE 5. 33: (A) THREE LAYERS OF THE PRINTED OBJECT; (B) ONE LAYER OF THE PRINTED OBJECT.	132
FIGURE 5. 34: THE MOVEMENT OF THE ROBOT ARM HAS A MAJOR EFFECT ON THE PRINTING PROCESS, PARTICULARLY WHEN THE HEIGHT OF THE OBJECT INCREASED TO MORE THAN 7 LAYERS.	133
FIGURE 5. 35: SCHEMATIC ILLUSTRATION OF FLOW PROBLEMS ENCOUNTERED IN HOPPERS, NAMELY, ARCHING AND RAT-HOLING, DURING (A) MASS-FLOW AND (B) CORE-FLOW, RESPECTIVELY, WHERE D = OUTLET DIAMETER, $D_{ARCHING}$ = MINIMUM ARCHING DIAMETER, D_{RH} = MINIMUM RAT-HOLE DIAMETER AND ϕ = HOPPER HALF ANGLE (CROWLEY ET AL. 2014), (C) PICTORIAL ILLUSTRATION SHOWED THE RAT-HOLING FLOW IN THE BUCKET ABOVE THE PUMP DURING PUMPING.	133
FIGURE 5. 36: THE HOPPER WITH AN ANGLE OF $\phi 45^\circ$ AND THE CORE-FLOW CONCEPT.	134
FIGURE 5. 37: (A) THE PRINTED PART IMMEDIATELY AFTER PRINTING; (B) THE PRINTED PART AFTER ONE-DAY DRYING.	136
FIGURE 5. 38: HORIZONTAL PRINTED PATH CROSS-SECTION "FOUR LINES PRINTED SPECIMEN".	138
FIGURE 5. 39: A SERIES OF PHOTOGRAPHS SHOWING THE RESULTS OF THE VARIOUS SPEED OF END-EFFECTOR, RESULTED IN VARIOUS SHAPE IN THE PRINTING LINE OUTCOMES.	139
FIGURE 5. 40: POWER REGRESSION RELATIONSHIP BETWEEN VELOCITY AND SLURRY OUTPUT MASS OF THE MORTAR FOR THE PRINTED LINE.	141
FIGURE 6. 1: COMPRESSIVE STRENGTH OF 3DP CUBIC SAMPLES WITH LITHIUM CARBONATE.	143
FIGURE 6. 2: COMPRESSIVE STRENGTH OF HAND MIXED CUBIC SAMPLES.	144
FIGURE 6. 3: (50 x 50) MM DIAGONAL CRACK INSIDE THE Z-POWDER SPECIMEN.	145
FIGURE 6. 4: COMPRESSIVE STRENGTH TEST OF 3DP CUBIC SPECIMENS WITHOUT LITHIUM CARBONATE (Li_2CO_3).	146
FIGURE 6. 5: POROSITY OF 3D PRINTED SAMPLES.	147
FIGURE 6. 6: SEM IMAGE OF 3D PRINTED SAMPLES (LEFT (1 μm) RIGHT (20 μm)).	148
FIGURE 6. 7: 3D PROFILING FOR 3D PRINTED SAMPLES.	149
FIGURE 6. 8: 3D PROFILING FOR 3D PRINTED SAMPLES AFTER 7DAYS CURING.	150
FIGURE 6. 9: FLEXURAL STRENGTH OF MANUAL MIXTURE CEMENTITIOUS PRISM SPECIMENS.	153

FIGURE 6. 10: FLEXURAL STRENGTH OF CEMENTITIOUS PRINTED PRISM TESTED IN DIFFERENT DIRECTIONS (X, Y, AND Z) AND SATURATION LEVELS.	154
FIGURE 6. 11: FLEXURAL STRENGTH OF CEMENTITIOUS PRISM SAMPLES WHEN IT TESTED IN (YZ0°).....	155
FIGURE 6. 12: FLEXURAL STRENGTH OF CEMENTITIOUS PRISM SAMPLES WHEN IT TESTED IN (YZ90°).....	155
FIGURE 6. 13: CEMENTITIOUS CUBE (A) SAMPLE UNDER UNIAXIAL COMPRESSIVE STRENGTH TEST, (B) AFTER REMOVAL FROM THE UNIAXIAL COMPRESSIVE STRENGTH TEST.	156
FIGURE 6. 14: COMPRESSIVE STRENGTH OF CEMENTITIOUS CUBE AT DIFFERENT CURING CONDITIONS AND SATURATION LEVEL S170C340.	157
FIGURE 6. 15: COMPRESSIVE STRENGTH OF CEMENTITIOUS CUBE AT DIFFERENT SATURATION LEVEL AND CURING IN NORMAL TEMPERATURE WATER.	158
FIGURE 6. 16: COMPARISON OF THE COMPRESSIVE STRENGTH OF 3DP CEMENT MORTAR CUBE AT DIFFERENT SIZES.....	161
FIGURE 6. 17: LINEAR REGRESSION RELATIONSHIP BETWEEN POROSITY VERSUS W/C RATIO IN THE 3DP SCAFFOLD.	163
FIGURE 6. 18: COMPRESSIVE STRENGTH FOR THE ZP 151 CUBES AND CP CUBES (AVERAGE ±STANDARD DEVIATION) AT SATURATION LEVEL S170C340 IN DIFFERENT ANGLES.	164
FIGURE 6. 19: THE DIFFERENCE BETWEEN: (LEFT) CURING IN AN OVEN FOR 3 HOURS THEN SUBMERGED IN WATER; AND (RIGHT) NOT CURED IN THE OVEN BUT INSTEAD SUBMERGED DIRECTLY IN WATER. THE AIR BUBBLES (VOIDS) ARE MORE PRONOUNCED ON THE (RIGHT) THAN THE (LEFT).	166
FIGURE 6. 20: COMPRESSIVE STRENGTH RESULTS IN THE DIFFERENT CURING PROCESS, ALL RESULTS FOR A PRINTED PART (20×20×20)MM AT AN ANGLE OF (0°) IN THE XZ PLANE ONLY.	166
FIGURE 6. 21: TENSILE STRENGTH RESULTS FOR THE ZP 151 SPECIMENS AND CP SPECIMENS (AVERAGE ±STANDARD DEVIATION) AT SATURATION LEVEL S170C340 IN DIFFERENT ANGLES.	168
FIGURE 6. 22: CRACKING PRESENT AT THE DOGBONE SAMPLES FOR ZP 151 AT DIFFERENT ORIENTATION ANGLES.....	168
FIGURE 6. 23: SHEAR STRENGTH FOR THE ZP 151 CUBES AND CP CUBES (AVERAGE ±STANDARD DEVIATION) AT SATURATION LEVEL S170C340 IN DIFFERENT ANGLES.	170
FIGURE 6. 24: FRACTURE IN THE PRINTED 45° SPECIMENS IN BOTH (A) COMPRESSIVE TEST FOR ZP 151 AND (B) SHEAR TEST FOR CP.....	170
FIGURE 6. 25: FLEXURAL STRENGTH RESULTS FOR THE ZP 151 SPECIMENS AND CP SPECIMENS (AVERAGE ±STANDARD DEVIATION) AT SATURATION LEVEL S170C340 IN DIFFERENT ANGLES.	172

FIGURE 6. 26: SURFACE IMAGES OF THE CUBIC SPECIMENS OF CP AT ORIENTATION ANGLES OF (0°, 30°, 37.5°, 45° AND 90°) BY THE NIKON AND OLYMPUS 3D LASER MICROSCOPES.	173
FIGURE 6. 27: (A) PENETRATION TIME PER VOLUME (μL) CONSUMES IN ZPOWDER, (B) PENETRATION TIME PER VOLUME (μL) CONSUMES IN CAC&OPC POWDER.	174
FIGURE 6. 28: IMAGES FROM A VIDEO RECORDING FOR THE PENETRATION TIME PER DROP OF BINDER IN ZPOWDER AND CAC&OPC POWDER.....	175
FIGURE 6. 29: STEPS IN THE PENETRATION ZB63 LIQUID INTO ZP 151, (A) IMPACT TIME OF DROPLET ON THE SURFACE OF THE POWDER, (B) PENETRATION PROCESSES OF LIQUID ON THE POWDER AFTER 16 SECONDS, (C) ABSORBING MOST OF THE LIQUID INTO THE POWDER.	178
FIGURE 6. 30: SCHEMATIC EXPLANATION OF THE BINDER DROP BETWEEN TWO LAYERS AND BINDING TWO LAYERS TOGETHER, THE SCHEMATIC SHOWS WHAT HAPPENS AT THE 16 SECOND MARK.	179
FIGURE 6. 31: ILLUSTRATION OF THE DEFLECTION FOR THE ZP 151 SPECIMEN (45°) IN THE BUILD CHAMBER OF THE 3DP.	183
FIGURE 6. 32: THE RELATIONSHIP BETWEEN DIMENSIONAL ACCURACY AND SATURATION LEVEL (W/C) FOR PRINTED GREEN CUBE CP SPECIMENS (CAD 20×20×20MM), PRINTED BY PROJET CJP (304 NOZZLES). (NOTE: THE BOX IS THE MEAN ±STANDARD DEVIATION, AND THE WHISKER IS ±MINIMUM AND MAXIMUM)	186
FIGURE 6. 33: CEMENTITIOUS CUBE (20×20×20MM) (CP) PRINTED BY PROJET 360 (LEFT), GYPSUM CUBE (ZP 151) (20×20×20MM) (RIGHT).....	188
FIGURE 6. 34: ANGLE OF REPOSE FOR (A) CP POWDERS AFTER FLOWING FROM THE FEEDER CONTAINER OF THE PRINTER, (B) ZP 151 POWDERS AFTER FLOWING FROM THE FEEDER CONTAINER OF THE PRINTER.....	190
FIGURE 6. 35: THE POWDER-BED ON THE BUILD CHAMBER: (A) ZP 151 (GYPSUM) THE POWDER ON THE BUILD CHAMBER AND (C) SCANNED OF THE BED BY THE 3D SCANNER (OLYMPUS OLS5000), AND (B) CP (MORTAR) THE POWDER ON THE BUILD CHAMBER AND (D) SCANNED POWDER BED BY THE 3D SCANNER.	193
FIGURE 6. 36: POROSITY VERSUS SATURATION LEVEL FOR SPECIMENS CP WITH/WITHOUT LITHIUM CARBONATE.	194
FIGURE 6. 37: COMPRESSIVE STRENGTH VERSUS SATURATION LEVELS FOR CP SPECIMENS WITHOUT LITHIUM CARBONATE.	195
FIGURE 6. 38: IMAGE OF SCANNING ELECTRON MICROSCOPE (10 μM) FOR THE 3DP (GREEN PART) CP SPECIMEN.....	196
FIGURE 6. 39: 3D SCANNED IMAGE (50×) OF THE PRINTED CP SPECIMEN BEFORE CURING (GREEN PART) AND AFTER CURING IN WATER FOR 7 DAYS.....	198
FIGURE 6. 40: COMPRESSIVE STRENGTH IN PRINTED CP WITH A DIFFERENT DELAY IN PRINTING TIME.	200

FIGURE 6. 41: COMPRESSIVE STRESS-STRAIN CURVE FOR DIFFERENT LAYER PRINTING DELAY TIMES OF CP SPECIMENS FOR THE MAXIMUM PRINTED SAMPLE AND WITH 7-DAY CURING.....	201
FIGURE 6. 42: GLASS FIBRE ORIENTATION WHILE BEDDING THE POWDER ON THE BUILD CHAMBER OF THE 3DP.	204
FIGURE 6. 43: GLASS FIBRE BEDDING ON THE POWDER IN THE BUILD CHAMBER OF THE 3DP (3D LASER SCANNING IMAGE LEXT OLS5000).	207
FIGURE 6. 44: SCHEMATIC ILLUSTRATION OF THE CHOPPED FIBRES SPREAD ON THE BUILD CHAMBER AND FEEDER CHAMBER.	208
FIGURE 6. 45: FIBRE BEDDED ORIENTATION BY 3D LASER SCANNING BY (LEXT OLS5000).....	208
FIGURE 6. 46: COMPRESSIVE STRENGTH OF MORTAR SAMPLE (50×50×50)MM WITH 1% GLASS FIBRE USING DIFFERENT CURING MEDIUM.	209
FIGURE 6. 47: COMPRESSIVE STRENGTH OF MORTAR SAMPLE (50×50×50)MM WITHOUT GLASS FIBRE USING DIFFERENT CURING MEDIUM.	210
FIGURE 6. 48: COMPRESSIVE STRENGTH OF MORTAR SAMPLE (20×20×20)MM USING DIFFERENT CURING MEDIA WITHOUT GLASS FIBRE.	211
FIGURE 6. 49: COMPARISON BETWEEN PRINTED CEMENT MORTAR SPECIMENS IN THE PRESENCE AND ABSENCE OF GLASS FIBRE.	212
FIGURE 6. 50: SURFACE ROUGHNESS PROFILE AND CAPTURE OF THE SURFACE OF PRINTED CEMENT MORTAR AT 20×, 50×, AND 100×.....	213
FIGURE 6. 51: FILAMENT DIAMETER AND LENGTH OF THE FIBRE IN THE PRINTED SPECIMENS.....	215
FIGURE 6. 52: FLEXURAL STRENGTH OF MORTAR SAMPLE (160×40×40)MM WITH AND WITHOUT GLASS FIBRE USING CURING MEDIA AT DIFFERENT TEMPERATURES.....	215
FIGURE 6. 53: FLEXURAL STRENGTH OF MORTAR SAMPLE (160×40×40)MM WITH GLASS FIBRE USING CURING MEDIA AT DIFFERENT TEMPERATURES.	217
FIGURE 6. 54: ‘HORIZONTAL TEST’ CROSS-SECTION PATH.....	218
FIGURE 6. 55: SEVERAL PRINTED SPECIMEN SHAPES WITH COMMENTS.....	219
FIGURE 6. 56: SQUEEZE-FLOW FOR THE DOUBLE LAYERS OF TRIAL 12.....	220
FIGURE 6. 57: MEASURE OF MANIPULABILITY.....	221
FIGURE 6. 58: VELOCITY COMPARISON FOR JOINTS: (A) 1, (B) 4, AND (C) 6.....	222

FIGURE 6. 59: MINI-CONE SLUMP TEST FOR TRIAL 8.	223
FIGURE 6. 60: SPREAD-FLOW TEST: (A) FOR TRIAL 5 WHICH DID NOT USE FIBRE; (B) FOR THE SAME TRIAL BY ADDING FIBRE WITH 1% POLYPROPYLENE FIBRE.	223
FIGURE 6. 61: SINGLE LAYER (SL), DOUBLE LAYER (DL), AND TRIPLE LAYERS (TL) FOR THE TRIALS (5,8,12) (CEMENT 1: FINE SAND 1).	225
FIGURE 6. 62: (A) HOBART MIXER A200; (B) THE SHEAR LAYER IN THE HOBART MIXER (WU & LIU 2015).	226
FIGURE 6. 63: COMPRESSIVE FOR MANUAL CONCRETE MIX AFTER 7-DAY AND 28-DAY CURING (THE VALUES SPECIFY THE ACTUAL STRENGTHS) WITH A CEMENT FINE SAND RATIO OF 1:0.5	228
FIGURE 6. 64: RESULTS AFTER 28 DAYS FOR THE SHORT COLUMN (7 LAYERS) WITHOUT ANY TIME LAPSE BETWEEN PRINTED LAYERS AND WITHOUT POST-CURING WITH A CEMENT FINE SAND RATIO OF 1:0.5.	228
FIGURE 6. 65: (A) PRINTED SPECIMEN AFTER DRYING AT LAB TEMPERATURE; (B) PRINTED SPECIMEN UNDER UNIAXIAL LOAD.	229
FIGURE 6. 66: 6-DEGREE OF FREEDOM ROBOT IN THE REAL-WORLD AND SIMULATED MATLAB MODEL.	230
FIGURE 6. 67: PRINTED PRISM AND CUBES VIA A ROBOTIC ARM FOR MORTAR SPECIMEN WITH/WITHOUT GLASS FIBRE REINFORCEMENTS.	230
FIGURE 6. 68: FLEXURAL STRENGTH OF MANUAL CONCRETE MIX AFTER 7-DAY AND 28-DAY CURING (THE VALUES SPECIFY THE ACTUAL STRENGTHS) WITH CEMENT TO THE FINE SAND RATIO OF 1:0.5.	231
FIGURE 6. 69: FLEXURAL STRENGTH FOR THE (1,2,3,4) LAYERS OF MORTAR MIX WITH 1% PP FIBRE AND WITHOUT FIBRE FOR A CIRCULAR NOZZLE OF 14MM AFTER 28 DAYS STORED IN CONTROLLED LABORATORIES AT THE DESIRED TEMPERATURE (CEMENT 1: FINE SAND 1).	232
FIGURE 6. 70: FLEXURAL STRENGTH FOR THE (1,2,3,4) LAYERS OF MORTAR MIX FOR A CIRCULAR NOZZLE (20)MM AND A RECTANGULAR NOZZLE (35×10)MM AT AIR TEMPERATURE AND WITH WATER CURING.	233
FIGURE 6. 71: VELOCITY (MM/S) VERSUS PRINTED LINE WIDTH (MM) AND SLURRY DISCHARGE (G).....	234
FIGURE 6. 72: FIBRE ORIENTATION IN THE PRINTED SPECIMENS AFTER CRASHING UNDER THE UNIAXIAL COMPRESSIVE STRENGTH.	235
FIGURE 6. 73: FIBRE ORIENTATION EMBEDDED IN HORIZONTAL LAYERS, AND JOINT GAP BETWEEN LAYERS WITH SURFACE ROUGHNESS TAKEN BY THE 3D LASER SCANNER.	236

FIGURE 6. 74: VOIDS AND GAPS BETWEEN LAYERS ARE DISTINGUISHED FROM THE PRINTED SURFACE USING THE COLOUR RED.	236
FIGURE 6. 75: IMAGE OF THE SURFACE OF THE PRINTED SAMPLE AFTER COLOUR THRESHOLD TO INDICATE THE FIBRE STRAND ON THE SURFACE OF THE PRINTED SAMPLE.	237
FIGURE 6. 76: COMPRESSIVE STRENGTH RESULTS OF CUBIC SPECIMENS CONTAINING 1% OF GLASS FIBRE CURED IN A TAP WATER BATH FOR 28 DAYS.	239
FIGURE 6. 77: COMPRESSIVE STRENGTH FOR THE (1, 2, 4, 6, CONVENTIONAL) LAYERS OF MORTAR MIX WITHOUT GLASS FIBRE.	240
FIGURE 6. 78: FLEXURAL STRENGTH FOR THE (1, 2, 4, 6, CONVENTIONAL) LAYERS OF MORTAR MIX WITH 1% GLASS FIBRE.	242
FIGURE 6. 79: RESULT OF 28 DAYS FOR FLEXURAL STRENGTH OF THE PRINTED CUBE SPECIMENS WITHOUT GLASS FIBRE.	242
FIGURE 6. 80: STRAIN GAUGE AND FAILURE DESCRIPTION ON A (50×50×50)MM SPECIMEN.	246
FIGURE 6. 81: MASONRY BLOCK MODEL WITH DIMENSIONS OF (390×190×190)MM.	247
FIGURE 6. 82: LOAD APPLIED ON THE THREE PLANES OF THE MASONRY BLOCK IN ABAQUS.....	248
FIGURE 6. 83: XY PLANE DISPLACEMENT FAILURE OF THE MASONRY BLOCK UNDER A COMPRESSION TEST.	249
FIGURE 6. 84: XY PLANE STRESS FAILURE OF THE MASONRY BLOCK UNDER A COMPRESSION TEST.	249
FIGURE 6. 85: XZ PLANE DISPLACEMENT FAILURE OF THE MASONRY BLOCK UNDER A COMPRESSION LOAD.	250
FIGURE 6. 86: XZ PLANE STRESS FAILURE OF THE MASONRY BLOCK UNDER A COMPRESSION LOAD.	250
FIGURE 6. 87: YZ PLANE DISPLACEMENT FAILURE OF THE MASONRY BLOCK UNDER A COMPRESSION LOAD.	250
FIGURE 6. 88: YZ PLANE STRESS FAILURE OF THE MASONRY BLOCK UNDER A COMPRESSION LOAD.	251
FIGURE 6. 89: STRESS-STRAIN DIAGRAM FOR THE FEA AND EXP. OF THE 3DP BLOCK UNDER COMPRESSION.	251
FIGURE A. 1: EXTERIOR PART OF THE POWDER-BASE 3DP.	300
FIGURE B. 1: MOVEMENTS IN X-Y MODE.....	302
FIGURE B. 2: BASE COORDINATES AND WORK COORDINATES	306
FIGURE B. 3: COMPONENTS OF POSITION DATA.....	307
FIGURE C. 1: CONTACT ANGLE GONIOMETRY TEST	309
FIGURE C. 2: 3D LASER SCANNER	310
FIGURE C. 3: SCANNING ELECTRONIC MICROSCOPE.....	310
FIGURE C. 4: POWDER FLOW TEST APPARATUS.....	311

<i>FIGURE C. 5: APPARENT POROSITY TEST MACHINE</i>	<i>311</i>
<i>FIGURE C. 6: SHEAR TEST</i>	<i>312</i>
<i>FIGURE C. 7: DIMENSIONAL ACCURACY</i>	<i>312</i>
<i>FIGURE C. 8: DELAY PRINTING TIME</i>	<i>313</i>
<i>FIGURE C. 9: COMPRESSIVE STRENGTH</i>	<i>313</i>
<i>FIGURE C. 10: FLEXURAL STRENGTH.....</i>	<i>314</i>
<i>FIGURE C. 11: TENSILE STRENGTH</i>	<i>314</i>
<i>FIGURE C. 12: SQUEEZE FLOW TEST</i>	<i>315</i>
<i>FIGURE C. 13: SLUMP TEST</i>	<i>315</i>
<i>FIGURE C. 14: SPREAD FLOW TEST.....</i>	<i>316</i>
<i>FIGURE C. 15: SPEED FLOW TEST.....</i>	<i>316</i>
<i>FIGURE C. 16: SETTING TIME TEST</i>	<i>317</i>
<i>FIGURE C. 17: COMPRESSIVE STRENGTH</i>	<i>317</i>
<i>FIGURE C. 18: FLEXURAL STRENGTH.....</i>	<i>317</i>

List of Tables

TABLE 2. 1 TYPES OF POWDER, BINDER AND POST-PROCESSING FOR THE INKJET PRINTING.....	12
TABLE 2. 2 TYPES OF POWDER, BINDER AND POST-PROCESSING FOR THE INKJET PRINTING (CONTINUED).....	13
TABLE 2. 3 COMPARISON OF ADDITIVE MANUFACTURING TECHNOLOGIES IN THE CONSTRUCTION FIELD.....	18
TABLE 2. 4 COMPARISON OF ADDITIVE MANUFACTURING TECHNOLOGIES IN THE CONSTRUCTION FIELD(CONTINUED).	19
TABLE 3. 1 MATERIALS COMPOSITIONS (KG/M3) FOR 3DP BY LE, AUSTIN, LIM, BUSWELL, GIBB, ET AL. (2012).....	29
TABLE 3. 2 MIX PROPORTION OF THE CONCRETE USED BY MALAEB ET AL. (2015).....	29
TABLE 3. 3 MIX PROPORTION (KG/M3) OF THE MIX TRIALS.....	30
TABLE 3. 4 MIX PROPORTION OF THE 3DP.....	30
TABLE 3. 5 MIX PROPORTION OF THE 3DP.....	31
TABLE 3. 6 MIX PROPORTION OF THE HIERARCHICAL MATERIALS OF THE 3DP.....	31
TABLE 3. 7 MIX PROPORTION OF THE DIFFERENT PROPORTION MATERIALS USED FOR 3DP.....	32
TABLE 3. 8 NON-CONVENTIONAL EXTRUSION MIXTURE PROPORTIONS, KG/M3.....	32
TABLE 3. 9 MIX PROPORTION OF THE DIFFERENT PROPORTION OF MATERIALS USED FOR EXTRUSION PRINTING BY 6 DEGREES- OF-FREEDOM ROBOT.	33
TABLE 3. 10 DEMONSTRATING THE SPEED, SPOT SIZE, POWER AND TEMPERATURE FOR EACH LINE IN FIGURE 3.4.....	41
TABLE 3. 11 EXPLANATION OF SETTINGS OF PRINTING AND PRINTING METHODS.	47
TABLE 3. 12 EXPLANATION OF SETTINGS OF PRINTING AND PRINTING METHODS(CONTINUED).	48
TABLE 3. 13 EXPLANATION OF THE TIME AND VELOCITY OF THE PRINTED CONCRETE OUTCOMES.....	50
TABLE 5. 1 PROPERTIES OF POWDERS FOR STARTING Z-POWDER AND CAC & OPC MATERIALS.	77
TABLE 5. 2 NUMBERS OF 3DP CUBIC SPECIMENS AT DIFFERENT SATURATION LEVELS WITH LITHIUM CARBONATE (Li2CO3)..	81
TABLE 5. 3 THE DIFFERENT LEVELS OF SATURATION CONVERTED INTO W/C RATIO.....	83
TABLE 5. 4 DETAILS OF THE 3D-PRINTED SPECIMENS FOR COMPRESSIVE STRENGTH	84
TABLE 5. 5 DESCRIPTION OF THE SATURATION LEVELS, CONSUMED BINDER AND TIME TAKEN TO BUILD A CUBIC (20×20×20)MM SAMPLE.....	86
TABLE 5. 6 CURING METHOD OF S170C340 IN WATER AND 5%OF Ca(OH)2 AFTER DRYING AT 40°C IN AN OVEN	88
TABLE 5. 7 DETAILED NUMBER AND DIMENSION OF SAMPLES.....	90
TABLE 5. 8 PHYSICAL PROPERTIES OF CHOPPED STRAND E6-GLASS FIBRE	90

TABLE 5. 9 DETAILS OF THE 3D-PRINTED & MANUAL MIX SPECIMENS (60×5×5MM) FOR FLEXURAL STRENGTH	92
TABLE 5. 10: DETAILS OF THE 3D-PRINTED SPECIMENS (70×10×4MM) FOR FLEXURAL STRENGTH	92
TABLE 5. 11 TESTS WITH RESPECT TO THE NUMBER OF SAMPLES, DIMENSIONS AND BUILDING ORIENTATIONS.	93
TABLE 5. 12 POROSITY WITH DIFFERENT SATURATION LEVELS OF CAC & OPC WITHOUT LI2CO3 ANALYSED USING IMAGE J.97	
TABLE 5. 13 PROPERTIES OF ZPOWDER (ZP 151) AND CEMENTITIOUS POWDER (CP)	101
TABLE 5. 14 MEASUREMENT OF 3D PRINTED (GREEN PART) CUBIC SPECIMENS.....	102
TABLE 5. 15 FEATURES AND DIFFERENT TIME DELAYS IN LAYER PRINTING OF SPECIMENS.	103
TABLE 5. 16 MECHANICAL PROPERTIES OF THE PP FIBRE AND G FIBRE THAT WERE USED IN THE MORTAR MIX.....	112
TABLE 5. 17 MORTAR MIX DESIGN WITH 1:1 AND 0.5:1 RATIO (CEMENT:SAND) WITH/WITHOUT PP FIBRE.	116
TABLE 5. 18 MORTAR MIX DESIGN FOR 1:1.2 (CEMENT: SAND) RATIO WITH/WITHOUT GLASS FIBRE.....	116
TABLE 5. 19 DETAILS OF THE PREPARED SAMPLES WITH/WITHOUT PRESENCE POLYPROPYLENE FIBRE	122
TABLE 5. 20 PREPARED SPECIMENS WITH GLASS FIBRE/WITHOUT FIBRE	122
TABLE 5. 21 SPEED OF THE HOBART MIXER (A200).....	126
TABLE 5. 22 END-EFFECTOR VELOCITY FOR THE ROBOTIC ARM FOR THE PRINTING MORTAR	138
TABLE 6. 1 PENETRATION TIME, DIAMETER OF THE DROPLET ON THE POWDER AND DEPTH OF THE PENETRATION OF THE DROPLET	178
TABLE 6. 2 DEFLECTION IN TENSILE SPECIMENS FOR THE DIFFERENT ORIENTATION ANGLE OF THE PRINTED SPECIMENS.	184
TABLE 6. 3 DIFFERENCE BETWEEN ZP 151 AND CP IN DDR FOR 3DP CUBIC SAMPLES SATURATION LEVEL (S170C340) (w/c 0.46 & 0.52).....	185
TABLE 6. 4 DIFFERENCE BETWEEN ZP 151 AND CP FOR THE ANGLE OF REPOSE FOR EACH OF THE POWDERS.....	188
TABLE 6. 5 DIFFERENCE BETWEEN ZP 151 AND CP FOR THE ANGLE OF REPOSE FOR EACH OF THE POWDERS.....	191
TABLE 6. 6 DENSITIES, CARR'S INDEX AND HAUSNER RATIO FOR THE ZP 151 AND CP POWDERS.....	192
TABLE 6. 7 BULK DENSITY, IN-PROCESS DENSITY AND POWDER BED POROSITY.....	194
TABLE 6. 8 SKEWNESS VALUE FOR THE CP SPECIMENS BEFORE AND AFTER 7-DAYS CURING IN TAP WATER.	198
TABLE 6. 9 CURING FOR 3 HOURS IN OVEN COMPARED WITH NON-CURING IN THE OVEN	200
TABLE 6. 10 THE RELATIVE SLUMP VALUE AND HEIGHT OF THE SLUMP FOR SELECTED TRIALS.	224
TABLE 6. 11 THE SETTING TIME RESULTS FOR THE THREE MAIN TRIALS.	225
TABLE 6. 12 CAULKING GUN EXTRUSION NOZZLE (Ø14MM).	226

<i>TABLE 6. 13 RESULTS OF THE COMPRESSIVE STRENGTH FOR THE PRINTED SAMPLES AND CONVENTIONAL SAMPLES.....</i>	<i>239</i>
<i>TABLE 6. 14 RESULTS OF THE FLEXURAL STRENGTH FOR THE PRINTED SAMPLES AND CONVENTIONAL SAMPLES.</i>	<i>241</i>
<i>TABLE 6. 15 COMPRESSIVE STRENGTH AND ELASTIC MODULUS FOR 3DP CEMENT MORTAR SPECIMENS.....</i>	<i>244</i>
<i>TABLE 6. 16 POISSON’S RATIO FOR 3DP CEMENT MORTAR PRINTED CUBE.....</i>	<i>244</i>
<i>TABLE 6. 17 ORTHOTROPIC PROPERTIES OF 3DP CUBIC CEMENT MORTAR.....</i>	<i>246</i>
<i>TABLE A. 1 ZPRINTER 150 BUILD SIZE DIMENSIONS.....</i>	<i>295</i>
<i>TABLE A. 2 PROJET 360 BUILD SIZE DIMENSIONS.....</i>	<i>295</i>
<i>TABLE A. 3 GENERAL SPECIFICATION FOR THE ZPRINTER 150.....</i>	<i>296</i>
<i>TABLE A. 4 GENERAL SPECIFICATION FOR THE PROJET 360.....</i>	<i>296</i>

Abstract

At present, Three-Dimensional Printing (3DP) is one of the most promising developments in modern technology. This technology innovation has shown its potential in a wide range of applications, varying from medical to food industry and from aerospace engineering to household applications. Obviously, the building industry has aimed to adopt this technique to apply it on a larger scale. 3D concrete printing technology results in low cost and faster construction methods, which allows for greater freedom in both architectural design and construction techniques. Despite these clear benefits shown by a few pioneering companies and institutes in the world, the building industry is still far behind in the development of practical 3D printing machines. This is mainly attributed to the lack of fundamental research on the materials and structural behaviour of the to-be-printed objects. This research examines the two types of Additive Manufacturing (AM) techniques for cementitious materials and fibre reinforced mortar. Mortar and Concrete are new materials in the field of additive manufacturing. Since these types of materials are hardened by chemical reactions, considerable attention needs to be applied to the workability in the AM process.

It should be emphasised that different manufacturing processes require suitable material processing modifications. This is highly applicable to the cementitious material, which has adaptability in handling, comprising ordinary mixing and cast-in-situ for the construction production; shotcrete spraying for stabilising soil in the mining industry; extrusion-based in precasting factories for the construction industry; and spinning procedures for concrete pipes. However, 3D printing for construction also faces the challenge of alteration of the mix design and the manufacturing procedure. This study shows the formulation of the cement mortar powder for a powder-based Three-

Dimensional Printer. It shows the new approach of powder preparation and mix proportions for printing cement mortar. This investigation presents an extrusion-based printing technique, including (i) an outline of the required adjustments to mix ingredients and the mixing method; (ii) a machine to provide suitable rheology in the fresh state; (iii) design and fabrication of the nozzle; (iv) temporal considerations ensuring a satisfactory time-gap between interlayer bonds; and (v) mechanical strength results of the hardened printed mortar.

The innovative achievements are finding the water/cement ratio in the powder-based 3DP and optimising the slurry materials for extrusion-based printing. Using these techniques would be cost-effective, easy-to-apply and environmentally-friendly since it drastically reduces the need and use of different types of formworks.

Abbreviations list

Acronym	Meaning
<i>3DCP</i>	Three Dimensional Concrete Printing
<i>3DP</i>	Three Dimensional Printing
<i>6DOF</i>	Six Degree Of Freedom
<i>AM</i>	Additive Manufacturing
<i>CAC</i>	Calcium Aluminate Cement
<i>CAD</i>	Computer-Aided Design
<i>CIJ</i>	Continues Ink-Jet
<i>CNC</i>	Computer Numerical Control
<i>CP</i>	Cement Mortar Powder
<i>C-S-H</i>	Calcium Silicate Hydrate
<i>DLS</i>	Damp Least Squares
<i>DOD</i>	Drop On Demand
<i>FDM</i>	Fused Deposition Modelling
<i>G</i>	Glass fibre
<i>LCA</i>	Life Cycle Assessment
<i>LENS</i>	Laser Engineered Net Shaping
<i>LOM</i>	Laminated-Object Manufacturing
<i>OPC</i>	Ordinary Portland Cement
<i>PLA</i>	Polylactic Acid
<i>PP</i>	Polypropylene fibre
<i>Ra</i>	Surface Roughness
<i>RMRC</i>	Resolved Motion Rate Control
<i>RP</i>	Rapid Prototyping
<i>RPM</i>	Revolutions Per Minute
<i>SEM</i>	Scanning Electronic Microscope
<i>SLA</i>	Stereolithography
<i>SLS</i>	Selective Laser Sintering
<i>SMA</i>	Shape Memory Alloy
<i>Ssk</i>	Value of Skewness
<i>w/c</i>	Water to Cement Ratio
<i>Zb63</i>	Clear binder solution
<i>ZP, ZP 150, ZP151</i>	Calcium Sulfate Hemihydrate

Notations list

Annotation	Meaning
$\Delta\theta$	Angular displacement
μ	Plastic viscosity
a	Air content by volume
A_{thix}	Rate of the flocculation
b	Width of specimen
d	Diameters as an average value of the spreading mortar
d_0	Base diameter of the mini cone
D_{CAD}	CAD dimension
DDR	Dimensional deviation ratio
D_e	Dimensional error
D_p	Actual printed dimension
f	Friction coefficient between the shear case and the shear load platform
F	Normal force
f	Force between the particles
f	Maximum force applied on sample
F_{cubes}	Force between cube particles
$F_{spheres}$	Force between sphere particles
G	Specific gravity of cement
h	Total height
h	Height of the pile
H	Hausner ratio
I	Carr's index
l	Length of specimen
L_{CAD}	CAD length value designed model
L_p	Real (printed) measured length value of the sample
m_1	Dry weight
m_2	Weight of the samples in soaked water
m_3	Weight of rolling the four side samples on the damp cloth
M_b	Mass of binder
M_p	Mass of powder
N_c	Number of chains
N_{pc}	Number of particles in a chain
\emptyset	Angle of repose
P	Axial force on the specimen

P_a	Apparent porosity
P_{bed}	Powder bed apparent porosity
Q	Normal shear force
R	Half-width of the line
r	Roughness ratio
r	Radius of the base
r_p	A relative slump
S	Shear area
T	Torque
V	Velocity on the centre line
V_b	Volume of binder
V_b	Bulk density
V_p	Volume of powder
V_t	Tapped density
w	Measure of manipulability
β	Shear angle
γ	Shear rate
δ	Indentation depth
ηf	Viscosity of the fluid as a newtonian
θ_m	Contact angle
θ_R	Solid-water declining contact angle
θ_w	Apparent receding contact angle for the porous surface
θ_Y	Young contact angle
λ	Damping constant
ρ_b	Density of binder
ρ_{bed}	In-process bed density
ρ_p	Density of powder
ρ_{true}	True density
σ	Compressive stress
τ	Shear stress
τ	Shear stress
τ_0	Yield stress
p	Total porosity for the fresh cement
α	Radius of the particle

CHAPTER ONE

1. INTRODUCTION

1.1 Additive Manufacturing of Concrete

There is a significant amount of materials and labour involved in concrete building structures. Moulds need to be created, reinforcement placed, concrete cast and, afterwards, the mould has to be disassembled. This process is expensive. Most of the elements are standardised since they can be made in large members, due to the optimised processes which, in turn, result in improved investments. However, the related costs and profits regarding structural optimisation in the construction industry are not as good. This method has consequences for repeated and over-dimensioned elements. The lack of freedom in form is another restraint. Despite these disadvantages, the rationalisation of the construction process has resulted in very efficient reinforced structural members. The core concept of construction industry 4.0 is an industrial revolution as digital data and digital construction technologies (Maskuriy et al. 2019). These technologies have many complexities and sometimes make high-risk if could not choose the proper selection in the construction market place (Nowotarski & Paslawski 2017).

1.2 Concrete Formwork

The construction industry faces numerous significant challenges regarding the costs of production. Firstly, cast-in-place concrete produces many waste materials which are disposed of later, particularly if the formwork is not reusable. Whereas reusable moulds reduce the amount of amount material disposed of, such moulds are rather costly to produce in the large quantities required to make these moulds economical (e.g. façade members).

The non-reusable moulds are not the only concern in construction applications. Over-constructed members in the production process are another limitation. Production methodology is highly related to the economics of the construction industry. Therefore, most of the construction members are standardised to reduce the cost. Limiting construction members to standardised sizes to reduce the amount of materials used would not be economical because the dead load in buildings is not as important as it is, for example, in aeroplanes. It does not significantly impact the energy use in its service-life and, sometimes, it is even preferable to have more mass in a building to temper the variations in temperature. Many freeform elements are cast in concrete in-situ, although the quality of cast-in-place concrete is difficult to control (Elhag et al. 2008). Therefore, high-performance concrete members are prepared in controlled environments. These precast members are part of a standardised building system, because of limitations in the size of the products that have to be transported later.

The evaluation of Life Cycle Assessment (LCA) for cast-in-place concrete can be negatively impacted by in-situ casting. Specifically, surplus ordering of concrete (Tam et al. 2006) and the wearing of formwork (Cole 1998) are the chief contributors to additional CO₂ emissions of concrete casting. Subsequently, hydration and hardening of concrete produce CO₂, so it is necessary to review the LCA to ensure that the developed technical production process has not only an economical but also a sustainable motive (Rossi et al. 2019).

1.3 State of the Problem

There are several limitations of 3D printing applications in the construction industry, such as limited use of building materials (Bai et al. 2019; Edwards et al. 2015). WinSun company used only cement paste without aggregate. However, the D-shape method

utilised sand to make a form of structure. Another limitation is size of the building to be printed because each 3D printer has its own specifications to fabricate structural elements (Lowke et al. 2018). There are also concerns when using Selective Laser Sintering (SLS) and other powder bed methods as 3D printed objects always need support to hold their own weight of scaffold until they gain enough strength to hold the structure (Lv et al. 2019). For this reason, the D-shape method has a structure size limited to 6.0m×6.0m (Dini 2009). Earlier studies have used different techniques and materials for digital construction technologies (Panda et al. 2019; Verma & Kaushal 2019); however, they have not been able to discover more about concrete and cement-based materials in the digital technologies for construction.

In this research, two types of additive manufacturing processes to obtain optimum strength and durability in 3D printed structures were studied.

It also investigated the possibility of using fibre in 3D printing to produce better reinforced mortar specimens.

The calibrations were conducted using Compressive Strength, Modulus of Rupture, Modulus of Elasticity and the experimental results were verified using the Finite Element based software ABAQUS.

1.4 Scope and Objectives of the Research

The scope of the research was the production of concrete elements, using 3D printing, of higher quality, better durability and economy by utilizing cement-based mortar slurry. It aimed to:

- i. Develop cement-based construction materials used in additive manufacturing. The intention was to critically examine the ways of producing construction elements through additive manufacturing machines.
- ii. Develop an additive manufacturing process that is economical and feasible to implement on a large scale.
- iii. Develop a manufacturing process that can produce structural members without formwork.
- iv. Investigate the suitability of producing elements of buildings using additive manufacturing.
- v. Modify ZPrinter powder to form cementitious powder by adding different types of fibres to produce reinforced mortar.
- vi. Using the extrusion method via a robotic machine (6-axis) to produce highly reinforced mortar members.
- vii. Investigate and improve bonds between layers using a Scanning Electron Microscope and profilometer to identify the surface roughness, depth of droplet of penetration and bond between layers.
- viii. Conduct wettability tests of powder-based materials to find the penetration time of liquid into the powder bed in the 3D printer.
- ix. Conduct flowability tests of the powders (Carr's index, Hausner ratio) and slump test of a slurry of the mortar.
- x. Conduct shear force tests for different directions of printed samples.
- xi. Optimise compressive strength tests by means of parallel and perpendicular printed directions.
- xii. Conduct Finite Element Analysis (FEA) of the test specimens using ABAQUS software to calibrate and verify the experimental works.

1.5 Thesis Outline

The thesis consists of seven chapters. Chapter One, provides general background information, information regarding concrete, and a statement of the scope and objectives of the project as an introduction. In Chapter Two, the literature review, we identify studies that have been conducted using 3D printing. The materials' properties are described in Chapter Three. The techniques and methodology adopted are discussed in Chapter Four. This is followed by an explanation of the experimental program in Chapter Five and the presentation of the results and discussion and numerical analysis in Chapter Six. Finally, the summary and conclusion are presented in Chapter Seven. Four appendices are included. In the appendices, 3D printer specifications for the developed cementitious mortar is presented. This specification was written based on insights gained from the detailed descriptions in Chapter Five of this thesis.

CHAPTER TWO

2. LITERATURE REVIEW

2.1 Introduction

Construction companies face numerous and substantial challenges regarding the costs of production. For instance, processes for concrete cast in-situ produce many waste materials that are later discarded, particularly if formwork is not used again. By contrast, recyclable scaffolds reduce waste. However, such moulds are relatively expensive to produce, and repeated use of this scaffolding is needed to make these moulds cost-effective (De Witte 2015). The life cycle of scaffolds is another issue in terms of the environmental footprint of scaffolds, particularly regarding greenhouse gas emissions. This, in turn, results in many repetitions, thus enabling better fabrication, precise production of elements and prints of any geometries, which are hard to make for conventional applications such as façade elements (Buswell et al. 2007; Lim et al. 2012).

It has been shown that rapid prototype technologies (e.g. 3D printing) could completely revolutionise a range of production methods (Lipson & Kurman 2013). The main advantage of rapid prototype technologies is directly constructing parts in one step from the CAD data (Vaezi & Chua 2011). For instance, the use of 3D printing could reduce the total cost of concrete construction by 35% to 60% simply by removing the need for formwork (Lloret et al. 2015).

There are issues with using moulds for construction, such as their recyclability and scaffold size limitations for a range of structural components. Many freeform components are cast in-situ, where their quality cannot be controlled (Elhag et al. 2008). For that reason, high-performance components (e.g. beams and columns) are made in controlled environments. Various 3D techniques are being used in Additive Manufacturing (AM)

processes, such as 3D scanning in the digital fabrication process and for file generation (Ma, Wang & Ju 2017).

Over-ordering of concrete (Tam et al. 2006) and tied up formwork (Cole 1998) are the main contributors to extra CO₂ emissions of concrete cast in-situ and a huge waste of materials. Next, the hardening of concrete produces CO₂. Thus, the development of new and innovative construction methods is motivated by the pursuit of economic, environmentally-friendly and architectural benefits. Bos et al. (2016) believed that using 3DP technology is a suitable introductory step towards replacing cement in the construction industry with less energy-intensive materials such as fly ash.

There are some issues and limitations associated with 3D printing, such as the low stiffness and strength of the printed building materials as well as the printing size (Edwards et al. 2015). Bos et al. (2016) mentioned that the WinSun company could print a large building component (approximately 36.6 × 12.2 × 6.1 m) with their 3D printer and an automated robotic arm. Weger, Lowke & Gehlen (2016) reported printing structural components with cross-sections up to 6 × 6 m using a D-shape printer by pouring liquid on the powder-based materials. Another limitation is that the intended printed size does not match the specifications of all kinds of 3D printers, as each printer has its own specifications for fabricating structural elements. There are also concerns regarding powder-based 3D printing methods, namely, the need for support to hold the weight of the printed object until the material gains enough strength. Mix design and the use of coarse aggregates is another challenge for 3D printing of concrete. For instance, the WinSun company used only fine cementitious materials without coarse aggregate in its 3D printing application.

In this chapter, an overview of the trending techniques for printing or plotting cementitious materials and their adaptation to different mix ingredients and the mixing process are presented. Developing modified powder is highlighted, such as finding w/c ratio, optimised w/c, optimised print materials inclusion glass fibre and cost-effective.

2.2 Overview of Rapid Prototype Technologies

According to Tay et al. (2016), rapid prototyping in the building and construction field was introduced as an innovative approach to constructing structures (Pegna 1997). Since then, rapid prototyping and, later, digital fabrication have gained popularity in the construction industry as well as many other industries such as automotive, aerospace, and biomedical (see (Berman 2012; Buswell et al. 2007)). Feng et al. (2015) classified rapid prototyping (RP) technologies into three main categories: additive, additive/subtractive and subtractive, as shown in *Figure 2. 1*.

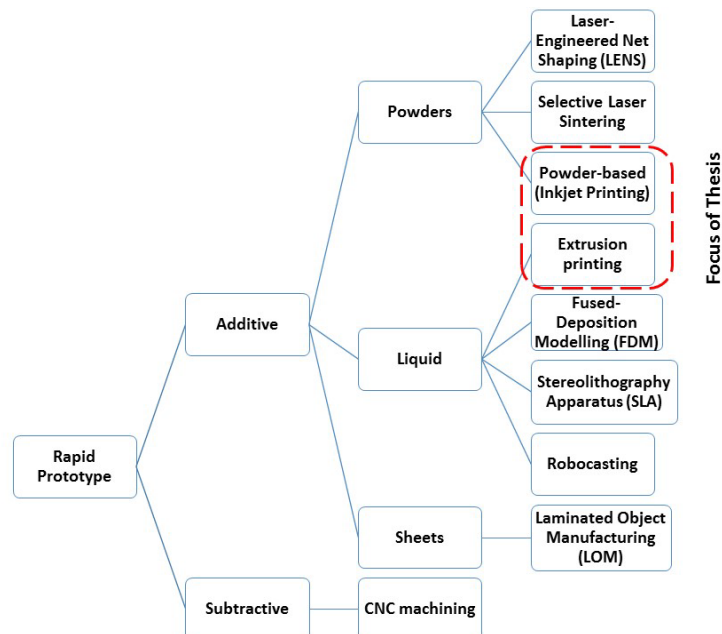


Figure 2. 1: Overview of rapid prototyping technologies and the techniques discussed in this chapter. The box highlights the techniques employed in this thesis.

In subtractive manufacturing, a 3D object is created by removing the material from a block using material-cutting machines *Figure 2. 2 (A)*. In additive manufacturing, which is the focus of this research, a feed material in the form of powder, liquid, filament, glue, or binder is added to a substrate, layer by layer, to construct a 3D object as shown in *Figure 2. 2 (B)*. The amount of leftover materials from the subtractive process is often considerably larger than that of the additive manufacturing process when creating the same 3D object (Ambrosi & Pumera 2016).

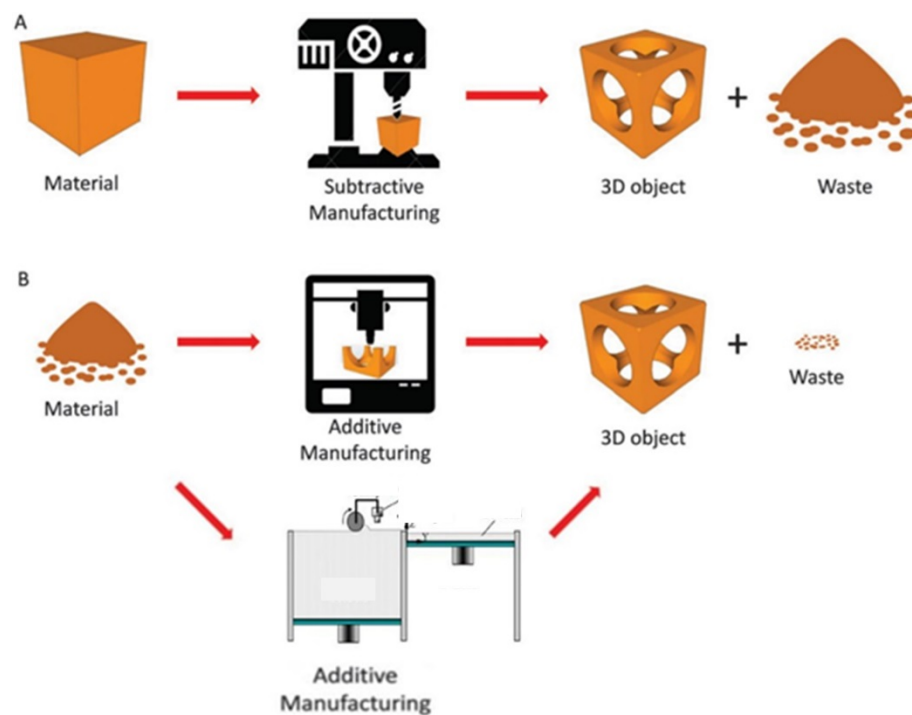


Figure 2. 2: Subtractive manufacturing process (A), Additive manufacturing process for extrusion printing and inkjet printing (B).

Li et al. (2016) reviewed additive manufacturing technologies and 3D printing with various raw materials available in the market. They found that photopolymers comprised the largest share of the 3D printing market (56% by weight), followed by thermoplastics (42%) and metals (only 1%). The market share of ceramics and concrete materials was about 1% in total.

In this chapter, we discuss the key additive manufacturing techniques with the potential to be used in the construction industry.

2.2.1 Powder-based (Inkjet Printing)

Inkjet printing, also known as binder jetting (powder-base), is one of the common printing methods used to 3D print parts in various industries. It has great potential for the construction of large structures from cementitious materials. In this method, a thin layer of the printing material, often in powder form but sometimes in chip form, is spread (e.g. with a roller) over a solid platform or tray. Next, a liquid binder is deposited over the powder bed as shown in *Figure 2. 3*. The binder glues the powder together to form a solid part. This process is repeated several times and layers are printed on top of each other to form a 3D object. It should be noted that some printing materials may require curing (Wu, Wang & Wang 2016) or kiln firing (Withell et al. 2011) in the oven as an additional post-processing step. This would make inkjet printing an energy-intensive technique for creating large structures. One of the main roles of the powder is to support the part while the binder is being deposited over the top of the layer that was printed in the previous step (Tay et al. 2017). Although complex geometries may be printed with this technique, the finished part often contains voids which reduce the quality. Inkjet printing is more suitable for printing objects and structures in which high printing speed is preferred over printing accuracy, according to Wu, Wang & Wang (2016).

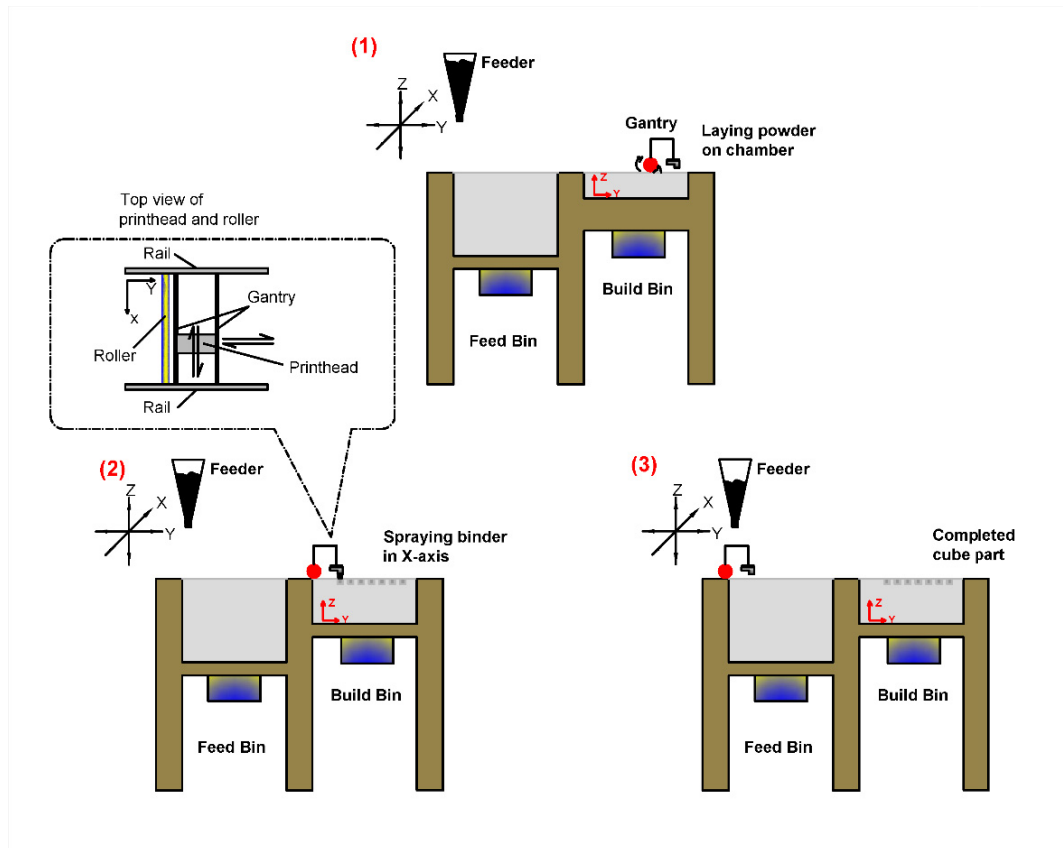


Figure 2. 3: Schematic illustration of the inkjet 3D printing process.

Researchers have reported employing various combinations of powder and binder. For instance, Feng et al. (2015) employed plaster and water as powder and binder, respectively. Withell et al. (2011) used a water-based liquid to bind clay particles while Henke & Treml (2012) tried binding wood chips (particles) with a mixture of water, cellulose and cement (binder). Gibbons et al. (2010) used rapid hardening Portland cement with polyvinyl alcohol binder to print cement-based structures. Additional procedures (listed in *Table 2. 1*) after the printing process (post-processing step) are often applied to the printed part.

Table 2. 1 Types of powder, binder and post-processing for the inkjet printing.

<i>Powder Type</i>	<i>Binder Type</i>	<i>Post-processing</i>	<i>References</i>
Rapid hardening Portland cement	Polyvinyl alcohol (Zb*)	Curing in water (room temperature) Curing in hot water (80°C)	(Gibbons et al. 2010)
TiNiHf shape memory alloy (SMA) powder	An acrylic-based aqueous binder	Cured for one hour in the oven at 170°C	(Lu & Reynolds 2008), (Wu, Wang & Wang 2016), (Utela et al. 2008), (Lu, Hiser & Wu 2009)
Amorphous calcium polyphosphate (CPP) powder	Liquid binder (Zb58)	A heat-up rate of 10°C/min from room temperature to 400°C	(Vlasea, Pilliar & Toyserkani 2015), (Vlasea, Toyserkani & Pilliar 2015)
Plaster-based powder (ZP**150)	Water-based binder solution of 2-Pyrrolidone (Zb63)	Dried in a building box for 1.5h.	(Farzadi et al. 2015), (Farzadi et al. 2014)
Calcium sulphate hemihydrate powder (ZP 102)	Water-based binder (Zb 7)	Different heat treatment protocols (150,200,250, 500, 861°C)	(Zhou et al. 2013)
Plaster-based ZP102 powder	Water-based Zb56 binder	Submerging in a liquid epoxy resin to provide strength and specific properties.	(Vaezi & Chua 2011)
Tricalcium phosphate powder (TCP)	Phosphoric acid solution, 20% by volume	Post-hardening in a binder solution for 1000 s.	(Miguel et al. 2013)
Gypsum with 5% (hydroxypropyl)methylcellulose	A liquid binder (Zb)	Infiltrated with a self-setting polyurethane resin for additional reinforcement	(Christ et al. 2015)
Hydroxyapatite granules	A liquid binder	A suitable post-processing depends on process and used materials	(Spath & Seitz 2013)
Plaster-based powder ZP150	Zb60 binder	Cured for three hours in an oven at 60 °C	(Feng, Meng & Zhang 2015),(Feng et al. 2015)

Table 2. 2 Types of powder, binder and post-processing for the inkjet printing (continued).

<i>Powder Type</i>	<i>Binder Type</i>	<i>Post- processing</i>	<i>References</i>
Composite material of plaster powder (Zp130)	Water-based binder (Zb58)	Submerging in a liquid resin (ultralow viscosity cyanoacrylate, Z-Bond 101)	(Castilho et al. 2011)
Composite material of plaster powder (Zp150)	Water-based binder (Zb60)	Super glue infiltration (Z90)	(Gharaie, Morsi & Masood 2013)
Recycled glass powder in the 40-200mm range	An appropriate binder system for glass 3DP	paraffin wax or fired	(Marchelli et al. 2011)
A calcium phosphate powder with an average particle size of 55	An aqueous solvent (Zb60)	The firing step was conducted	(Castilho et al. 2015)
Spruce chips	Synthetic resin	Activator	(Henke & Treml 2012)
Zb*: humectant and water, ZP**: Zprinter powder (plaster, vinyl polymer and carbohydrate)			

2.2.2 Selective Laser Sintering (SLS)

Selective Laser Sintering (SLS) is the process of sintering powders layer-by-layer (Kruth et al. 2005). The selected areas on the powder bed are exposed to the thermal energy of a laser beam. This technology was introduced in 1986 by Carl Deckard and Joe Beaman at the University of Texas (Lipson & Kurman 2013). Cañete Vela (2014) claimed that laser sintering can be used to make metallic and polymeric objects. The technique is similar to the one used in Stereolithography (SLA), in which a photo-solidification process is initiated by light to create a chain of interconnected molecules.

In SLS, a jet of CO₂ is used as a laser light directed at the powders. The powders could be of different materials such as alloys, ceramics, cement, nylon, glass composite, metal, steel and carbonate (Jeng, Peng & Chou 2000).

Figure 2. 4 shows schematically how the laser is employed to melt the powder or slurry. This figure also shows that the laser source directly located on the printed object. The molten materials become a liquid form and solidify completely when the temperature is reduced (Kolossoff et al. 2004). Computational modelling has been used in some studies to better understand the SLS process (Kumar 2003). Peter & Jean-Pierre (2006) examined the residual stresses in selective laser sintering (SLS) and selective laser melting (SLM), aiming to achieve a better understanding of the sintering phenomenon. The neat powder properties of various SLS powders were found to affect the fabrication process and ultimately lead to improving the mechanical properties of the resultant components (Dalgarno & Stewart 2001). Similar to inkjet printed parts, SLS parts usually need a post-processing step which could influence the structural performance of the finished part. Therefore, post-processing and knowledge of the sintering phenomena must be integrated into the design and planning process to obtain a 3D printed part with optimum quality (Ian & Dongping 1997).

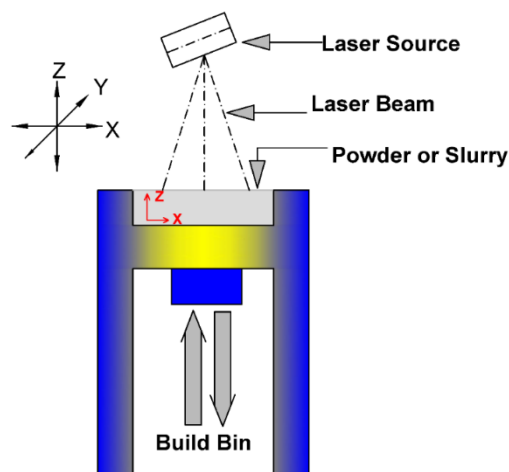


Figure 2. 4: Selective Sintering diagram.

An investigation by Dalgarno & Stewart (2001) reported the outcomes of a design study into production tools used in an industrial SLS process. The abovementioned study

evaluated the improved productivity arising from the use of conformal cooling channels and also examined tool wear.

2.2.3 Extrusion Printing (Extrusion Based Process)

The extrusion printing technique fabricates three-dimensional objects from a computer-generated model as in a typical rapid prototype process. Detailed models may be derived from computed tomography scans, magnetic resonance imaging scans or model data created from 3D object digitising systems and employed in this technique. In the Fused Deposition Modeling (FDM) technique, a thermoplastic filament material is extruded and deposited as a semi-molten polymer onto a platform in a layer-by-layer cycle. *Figure 2.5* illustrates how each layer is created: the platform base is lowered and the next layer is stacked on top of the previous layer as prescribed by the computer model (Zein et al. 2002). The 3D printing of concrete through extrusion was based on the FDM process. The initial idea of the extrusion printing for construction elements was offered in the late 1990s by (Pegna 1997). Later, this technique was utilised at the University of Southern California (USC) with some adjustments and modifications. The process was called contour crafting by (Khoshnevis & Dutton 1998) (Hwang & Khoshnevis 2004). Delgado Camacho et al. (2018) employed novel 3DP techniques (mainly extrusion) in the construction industry could reduce the labour costs, decrease material waste, and make complex geometries, which are difficult to attain using conventional construction techniques. Furthermore, Lloret et al. (2015) aimed to link all the digital design, additive manufacturing and material properties to build a complex shape from concrete structures.

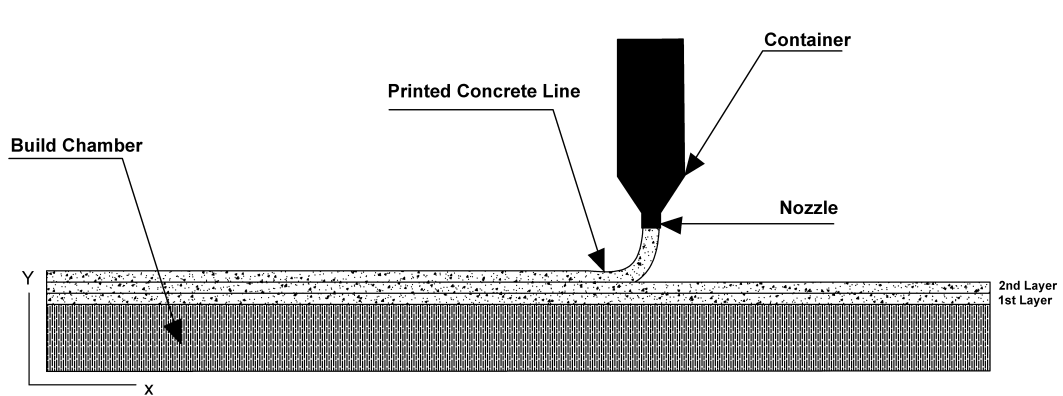


Figure 2. 5: Extrusion printing process for the concrete

Lim et al. (2012) presented the application of large-scale printed concrete via additive manufacturing processes called Concrete Printing. The extruded mortar slurry and several new criteria were discussed, such as a mix design of mortar and a delivery system that was developed for the printing process (Zhang et al. 2019). *Table 2. 3* explains the three main techniques of additive manufacturing for construction applications.

The properties of different concrete mix designs and the various ingredients have been reviewed with the appropriate rheology in wet concrete as well as the viscosity ratio for dimensional stability (Zijl et al. 2016).

Ashraf, Gibson & Rashed (2018) focused on metallic 3D printed structures and studied micro-lattice printing structures using stainless steel and titanium.

Those paths and steps are vital to building an object when the additive manufacturing process involves a controllable machine such as a robot, as shown in *Figure 2. 6*.

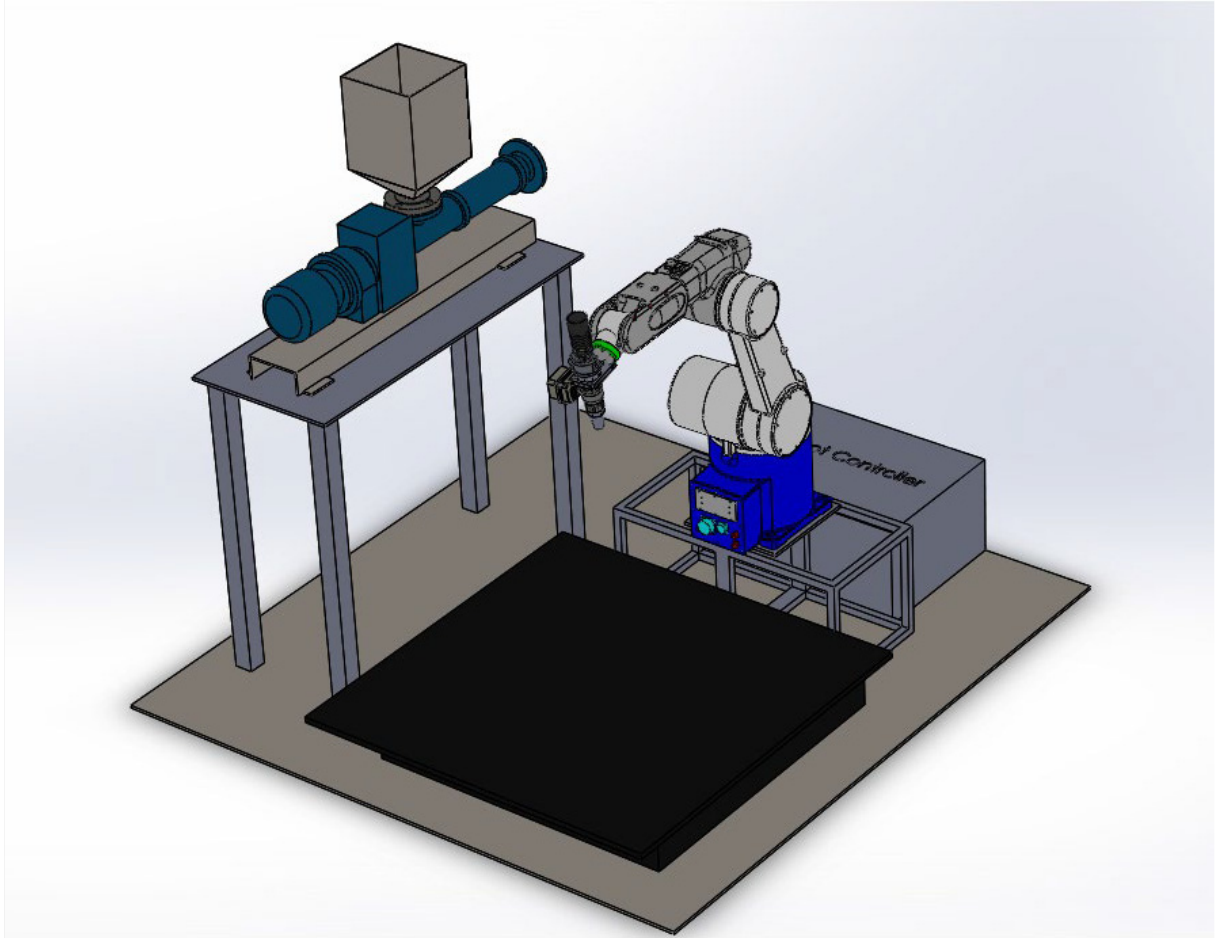


Figure 2. 6: Graphical explanation of extrusion printing using 6 DOF robot with a progressive cavity pump.

Table 2. 3 Comparison of additive manufacturing technologies in the construction field.

<i>AM Type</i>	<i>Min feature</i>	<i>Materials</i>	<i>Comments</i>	<i>References</i>
<i>Description</i>	<i>size/surface quality</i>			
Inkjet (Binder) Printing Material in powder form bonded by dropping fluid into layers to form a part	Layer Thickness: 100-150 μm Minimum thin wall width: ~ 2 mm	-Metals -Ceramics -Polymers -Cement -Gypsum	-Versatile, different materials may be printed -Low surface quality -Low density to high porosity. -Resolution depends on particle size, layer thickness and type of binder solution. -Post-processing to obtain higher strength or density.	(Gibbons et al. 2010), (Brown 2015),(Perrot, Rangeard & Pierre 2015), (Rael & San Fratello 2011), (Henke & Treml 2012),(Pegna 1997), (Dikshit et al. 2018), (Shakor, Sanjayan, et al. 2017), (Lee et al. 2007), (Le 1998)
Selective Laser Sintering (SLS) Material in powder form sintered in layers to build an object	Layer Thickness: 20–150 μm Minimum thin wall width: ~ 500 μm	-Metals -Ceramics -Thermoplastic Polymers	-High-temperature process. -Resolution is dependent on particle size and machine. -Agglomeration and oxidation occur with smaller particles. -Open porous, low density and lower strength are common issues. -Needs post-processing.	(Lipson & Kurman 2013), (Cañete Vela 2014), (Mukesh et al. 1995), (Barnett & Gosselin 2015), (Lim et al. 2016), (Ngo et al. 2018)

Table 2. 4 Comparison of additive manufacturing technologies in the construction field(continued).

<i>AM Type</i>	<i>Min feature size/surface quality</i>	<i>Materials</i>	<i>Comments</i>	<i>References</i>
Extrusion-based process and FDM	Layer thickness (FDM): 125–300 μm Minimum thin wall width (FDM): 600–1000 μm Extrusion: Layer thickness 9 ~30mm Minimum thin wall width: variable according to nozzle diameter and rheology of materials	-Thermoplastic Polymers -Metals (Bi-Sn, SnPb) composites -Multi-material composites -Cementitious materials	-Lower resolution than the other printers. -Shrinkage and layer bonding problems. -Poor surface quality. -Faster process compared to other methods. -Post-processing may be essential depending on the geometry. -Low tensile strength (significant orthotropic properties).	(Zein et al. 2002), (Shofner et al. 2003), (Jianchao et al. 2017), (Hager, Golonka & Putanowicz 2016), (Nerella et al. 2017), (Mueller et al. 2014), (Lewis et al. 2006)

2.2.4 Stereolithography Apparatus (SLA)

Additive manufacturing techniques such as Stereolithography have been employed by automotive, aerospace, and consumer producers over the last twenty years (Wohlers 2004). The application of these methods to construction and architectural modelling is growing (Kvan & Kolarevic 2002).

Zhang et al. (2014) state that stereolithography (SL) was one of the first rapid prototyping techniques. In 1988, this was commercialised by Charles W. Hull as a 3D printer. This technique is one of the most popular additive manufacturing methods because of its high-quality finish, high speed and high accuracy. According to Cañete Vela (2014), SLA uses UV light to solidify the materials based on photosensitive resin. There is a baseboard located below the surface of the resin. After the first layer has solidified, the board sinks into the liquid while another layer hardens, see *Figure 2. 7*.

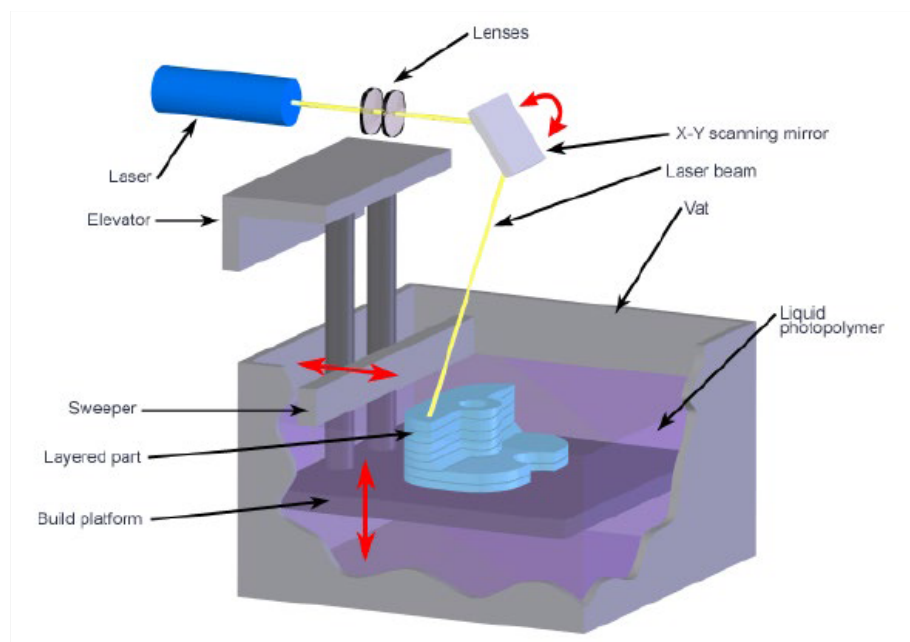


Figure 2. 7: SLA diagram process (reproduced after (Cañete Vela 2014))

2.2.5 Laminated-Object Manufacturing (LOM)

Laminated Object Manufacturing (LOM) is a technology that comes from Israel, with the patent reported in 1996. The principle of the printer is based on sticking layers on top of each other. Each layer is cut either from plastic or paper and then glued to the previous surface, *Figure 2. 8*. The film with the material is rolled from one coil to the other. Rewinding takes place over a work area where it always remains. The main advantages of this print are the high-quality surface of the model and the use of the cheapest materials. The disadvantages are a large amount of waste due to a large amount of scrap and the mechanical removal of the supporting material (Rengier et al. 2010). LOM, developed by Cubic Technology, Torrance, CA, USA, uses layers of plastic or paper film which could be glued together and make shapes using a laser cutter.

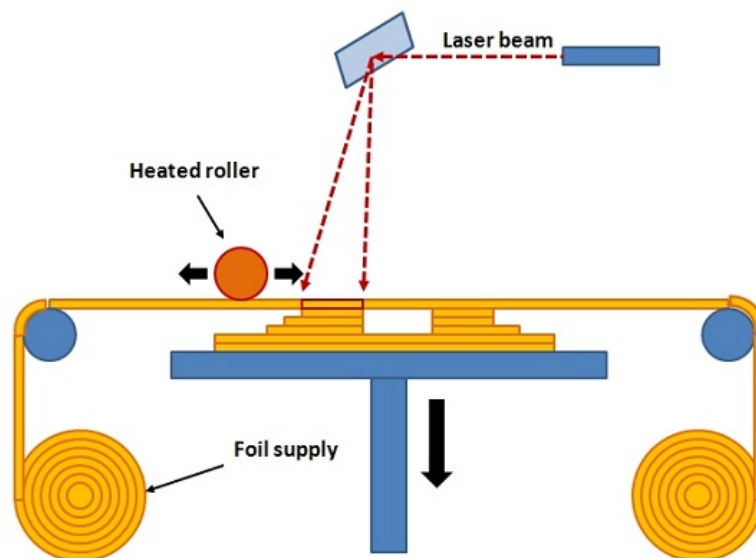


Figure 2. 8: LOM diagram process (reproduced after (3dprintingfromscratch 2019))

2.2.6 Fused-Deposition Modelling (FDM)

FDM or fused deposition modelling creates models using a print string that runs through the printhead. It melts the printing material that is applied to the construction pad. In places where it is needed, the 3D printer creates so-called support structures of water-

soluble material. The FDM technique forms three-dimensional items from computer-made solid or surface replicas as in a typical rapid prototype method. Replicas can also be obtained from computed tomography scans, model data created from 3D objects or magnetic resonance imaging scan digitising systems. FDM used a thermoplastic filament material to take out and deposit the semi-molten polymer onto a plate in a layer-on-layer procedure. When each layer is completed, the base plate is moved down and the following layer is placed, *Figure 2. 9* (Zein et al. 2002).

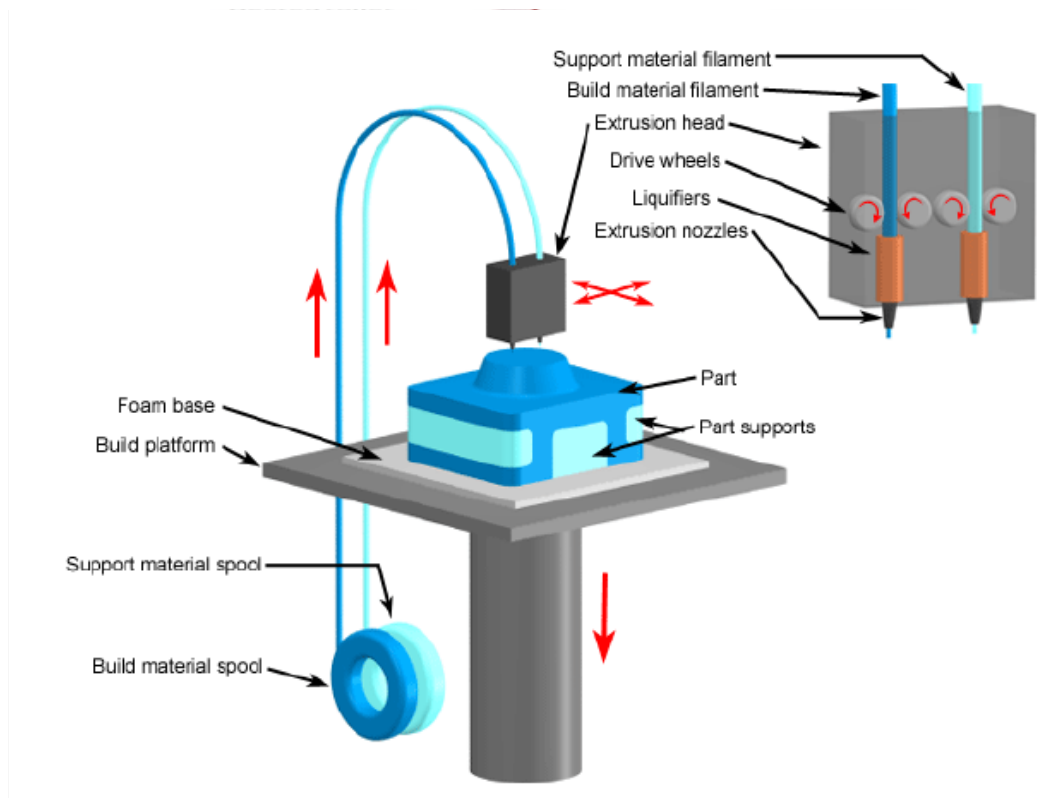


Figure 2. 9: FDM diagram process (reproduced after (Zein et al. 2002))

The advantage of FDM lies mainly in the use of durable materials, the long-term stability of mechanical properties and the quality of parts. Thermoplastic materials used by FDM technology are suitable for small-scale production or for detailed functional prototypes (Hutmacher et al. 2001). Technical specifications for FDM technology and standard production time depends on the complexity of the model. Accuracy is $\pm 0.15\%$ (with a lower limit of ± 0.2 mm). The minimum wall thickness is 1 mm, layer thickness is 0.18-

0.25 mm (Hutmacher et al. 2001). Materials suitable for FDM technology include PC (polycarbonate), ABS (acrylonitrile butadiene styrene), PC-ISO (polycarbonate ISO), PC-ABS (polycarbonate ABS), Ultem 9085 (Hutmacher et al. 2001).

2.2.7 Laser-Engineered Net Shaping (LENS)

Theoretically, the LENS or called laser powder forming method to near-net-shape element fabrication follows from the method used by additive manufacturing procedures (e.g., SL and SLS) to produce plastic patterns and forming patterns. A CAD file model of a part is sliced into tiny layers orthogonal to the Z-axis. The slice data is then converted into laser scanning pathways to construct a single layer. Each layer is made up by first generating a framework of each feature, with the cross-section later being filled by using a rastering method. This process is continued until the fragment is accomplished, *Figure 2. 10*. The significant characteristic which differentiates LENS from the other AM methods is making parts directly from scaffold materials. Hence, this is can be applied not only as an AM process for manufacturing near-net-shaped patterns but also as a manufacturing route for making quality metal objects and injection mould tooling (Atwood et al. 1998). The benefits of LENS printed parts are that they usually have dense properties and provide the required metallurgical properties. It is used not only for fabrication but also to repair parts. The disadvantage of LENS is the extreme overhangs that are a problem due to a lack of various material uses for support structures. Printed parts usually require some post-print machining.

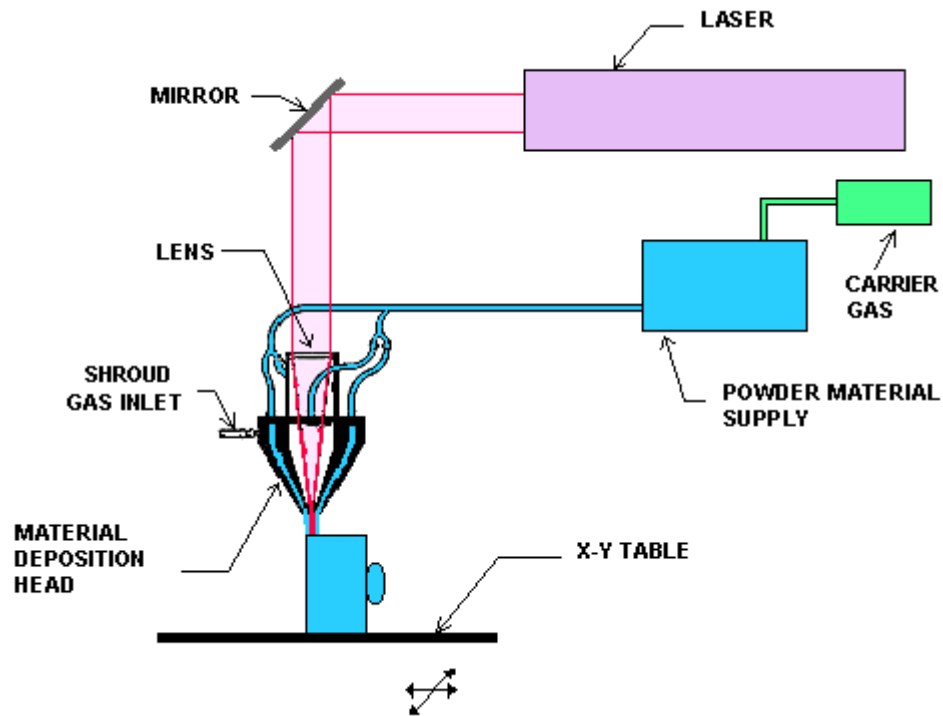


Figure 2. 10: FDM diagram process (reproduced after (ARD09-8 2009))

2.2.8 Robocasting

The Robocasting technique is a freeform manufacturing method used usually for dense ceramics and composites where slurries can be deposited as a base layer of highly loaded viscous fluid. The printed objects can be produced, dried, and totally sintered in less than 24 hours. This procedure does not need a binder and the objects can be created with less than 1% of organic materials (Cesarano 2011).

Morissette et al. (2000) claimed that the fabrication of aqueous alumina-polyvinyl alcohol via robocasting was controlled by a computer system extrusion apparatus using two-nozzles. This technique can be used with various nozzle diameters of 0.254 to 1.37 mm which are suitable and printable with all types of mixing. This technique of solid freeform is a slurry based deposition technique; it can be applied to produce a large scale of components. It is also able to use feedstock materials with low organic content

materials such as gel-casting suspensions which are used to improve the mechanical strength of the deposited materials, *Figure 2. 11*.

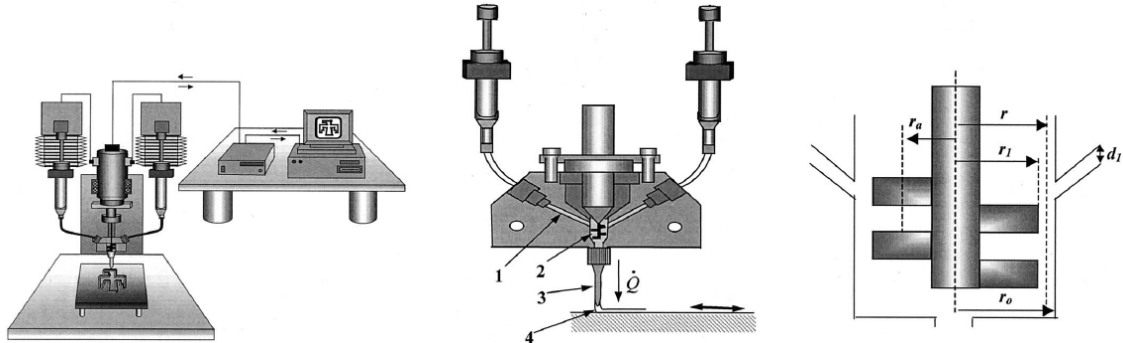


Figure 2. 11: Robocasting apparatus (reproduced after (Morissette et al. 2000))

2.3 Summary

Various additive manufacturing techniques that could be employed for plotting/printing in the construction industry have been reviewed in this chapter. The choice of the printer, mix design, and the method of printing was discussed. Three benchmark examples were selected to compare the features and limitations of various techniques for 3D printing of concrete/mortar. Results showed that extrusion printing with industrial robotic arms is a versatile technique that could be adapted for rapid and bespoke construction projects. Several parameters and printer features, including the speed, strength, accuracy and resolution of printing as well as concrete mix, were studied. It was found that by controlling various features of the extrusion printer such as speed, nozzle diameter, and the distance from the substrate, different concrete/mortar mixes could be printed. Therefore, the construction of a wide range of complex structures of different sizes is achievable in the future. However, further research is still required to improve (and predict) the mechanical properties and printability of the 3D printed structural elements. Notably, the rheology of the mix and its relationship to the orthotropic properties of the concrete/mortar need further investigation. Future work will focus on the development of

physically-based models at various scales (i.e. neat cement mortar, filled cement mortar, and finished concrete) which, in turn, would enable the printing parameters involved in the extrusion technique to be optimised.

CHAPTER THREE

3. MATERIAL PROPERTIES

3.1 Introduction

Additive manufacturing is a fabrication technology that is rapidly revolutionising the manufacturing and construction sectors. In this chapter, a review of various prototyping technologies for printing cementitious materials and selected 3D printing techniques is presented in detail. Benchmark examples are provided to compare three well-known printing techniques: inkjet printing (binder jetting), selected laser sintering (SLS) and extrusion printing (extrusion based process). A comprehensive search of the literature was conducted to identify various mix designs that could be employed when printing cementitious materials. Aspects of concrete and mortar mix design are described, and some new experiments are conducted to analyse the printability of new mixes. Future research in the area of the rheology of cementitious materials and their relationship to the structural performance of finished concretes are highlighted.

3.2 Material Properties for 3DP

The concrete/mortar mix design plays a major role in both the 3D printing process of cementitious concrete and the structural performance of the printed concrete elements. When 3D printing cementitious materials, the fresh concrete or mortar is built one layer atop another, while the lower layers hold the layers above them. Although rapid prototype technologies and 3D printing techniques have been reviewed in the literature quite extensively, only a few studies have investigated the role of concrete/mortar mix designs in the 3D printing of cementitious materials. Some recent studies focused on different proportions of chemical admixtures and water/cement ratios, while earlier ones (Jeon et al. 2013) attempted to use less coarse aggregate. It is extremely difficult to pass coarse

aggregates through the pump and the nozzle. Furthermore, layers with coarse aggregates do not hold the original shape of printed layers, *Figure 3. 1*.



Figure 3. 1: Printed concrete through a custom-made delivery system (note: a max. particle size of coarse aggregate of approximately 5mm)

Le, Austin, Lim, Buswell, Gibb, et al. (2012) prepared concrete mixes to print 3D fibre-reinforced concrete with fine aggregates. The aim of the experimental studies was to investigate the extrudability and buildability of the mixes. To enable a high printed resolution, the diameter of the nozzle delivery systems was 9 mm. *Table 3. 1* summarises the mix proportions of the concrete. In their study, Le, Austin, Lim, Buswell, Gibb, et al. (2012) addressed the shear strength for the workability of concrete and the compressive strength for the printed specimens. The optimum compressive strength that was achieved when curing for 28 days was 110 MPa.

Table 3. 1 Materials compositions (kg/m^3) for 3DP by Le, Austin, Lim, Buswell, Gibb, et al. (2012)

Mix design	Sand	Cement	Fly ash	Silica Fume	Water	w/c ratio
1	1612	376	107	54	150	0.398
2	1485	446	127	64	178	0.399
3	1362	513	147	73	205	0.399
4	1241	579	165	83	232	0.400
5	1123	643	184	92	257	0.399

Malaeb et al. (2015) tried different mix proportions of concrete to print straight lines, as shown in Table 3. 2. In their study, they chose mix proportion number 3 in Table 3. 2, which has water to cement (w/c) ratio of approximately 0.4. The lower w/c ratio increases the strength of the concrete and the suitable water ratio in the concrete assists in maintaining the greatest buildability of the printed concrete. The approximate compressive strength of such mix designs is 42 MPa.

Table 3. 2 Mix proportion of the concrete used by Malaeb et al. (2015)

Mix Number	Cement (g)	Sand (g)	Fine Aggregate (g)	w/c ratio	Superplasticizer (ml)	Flowability Rate(cm/s)	Retarder (ml)	Accelerator (ml)
1 (control)	125	80	160	0.48	0	-	1	0.5
2	125	80	160	0.42	0.5	1.1	1	0.5
3	125	80	160	0.39	1	1.13	1	0.5
4	125	80	160	0.38	1.1	1.2	1	0.5
5	125	80	160	0.36	1.3	1.4	1	0.5

Tay et al. (2016) conducted the 3DP concrete mixture design as described in Table 3. 3. They found that this mixture to be an excellent concrete mix design for 3DP (see Table 3. 3). In the current study, the low-cost mix design was produced with 1.05% of water-weight superplasticizer added to the mix design. The extrudability and buildability of the printer were changed according to the mix design variations.

Table 3. 3 Mix proportion (kg/m³) of the mix trials

Mix design	Sand	Cement	Fly Ash	Silica Fume	Water	w/c ratio
6	810	253	192	61	152	0.6

Gosselin et al. (2016) investigated the 3DP mix proportions of concrete (see Table 3. 4). The materials consisted of an ultra-high performance mortar paste, with an added polymer resin to improve the quality interfaces between layers and accelerating agents in order to attain the adequate rheology. The mechanical behaviour of the prismatic samples (40×40×160 mm) was tested for 90 days at ambient temperature. The flexural strength of the 4-point bending test was also tested. In our study, the 6 degrees-of-freedom robotic arm was used instead of a moveable crane. Structural printing of the complex geometry was presented.

Table 3. 4 Mix proportion of the 3DP

Portland cement CEM I 52.5N	Crystalline Silica	Silica Fume	Limestone filler	Water/(cement+sand)	Accelerating	Polymer-based resin
(30–40%w)	(40–50%w)	(10%w)	(10%w)	0.1	NA	NA

Hambach & Volkmer (2017) investigated 3DP mix designs and demonstrated the optimum mix proportion for their study (Table 3. 5, Table 3. 6). In their paper, they prepared and printed samples using the WASP ((World’s Advanced Saving Project) company) Clay Extruder Kit machine with a nozzle diameter of 2 mm. The tests investigated the density, porosity and strength of the 3D printed samples with short fibres (carbon, glass and basalt fibres). The fibres were used in different directions and the maximum obtained flexural strength was 30 MPa for a content of 1% volume of carbon fibre for the printed path. The optimum compressive strength reached 80 MPa for 1% volume short carbon fibres parallel to the printed part.

Table 3. 5 Mix proportion of the 3DP

Portland cement	Silica Fume	Water	Water reducer (Glenium)	w/c ratio
61.5%	21%	15%	2.5%	0.3

In the same study, the authors prepared mix proportions for the hierarchical materials. All the different types of fibre reinforcement were used in a dry mix. The water reducer agent was mixed with the water by the particular mixer to make a homogenous mix. Finally, they continued to add the fibres to the mixture until the fibres dispersed completely. The maximum flexural strength in hierarchical materials for the 3DP was 17.5 ± 0.5 MPa. The optimum three-point bending strength was in the filled mortar diagonal sections of the specimens.

Table 3. 6 Mix proportion of the hierarchical materials of the 3DP

Portland Cement	Sand	w/c
40%	60%	0.4

Kazemian et al. (2017) developed different mix designs for concrete in 3DP. Table 3. 7 shows the different mixtures such as PPM (Portland cement only), SFPM (containing silica fume), FRPM (containing fibre), NCPM (containing nano-clay). In their study, two different methods for the shapeability “layer settlement” and “cylinder stability” were proposed. The experimental results showed that the nano-clay and the silica fume enhanced the shapeability of the fresh mixture, whereas little improvement was noticed in the printed part with the addition of polypropylene fibre.

In the study by Rushing et al. (2017), the mix design for extrusion printing was prepared as shown in Table 3. 8. It was noticed that mixture B3 had the best mix extrusion. An examination of short fibres in the concrete revealed that the short fibre did not decrease the flow and, in most cases, the fibre enhanced the shape stability of the fresh concrete.

Table 3. 7 Mix proportion of the different proportion materials used for 3DP

Mixture ID	Fine aggregate kg/m ³	Portland cement kg/m ³	Water kg/m ³	w/c	Silica fume kg/m ³	Fibre kg/m ³	Nano-clay %	HRW RA%	VMA %
PPM	1379	600	259	0.43	0	0	0	0.05	0.11
SFPM	1357	540	259	0.48	60	0	0	0.16	0
FRPM	1379	600	259	0.43	0	1.18	0	0.06	0.10
NCPM	1379	600	259	0.43	0	0	0.3	0.15	0

Table 3. 8 Non-conventional extrusion mixture proportions, kg/m³

Mix No.	Water	Type I/II cement	Limestone sand	Limestone 3/8 in.	RMA (rheology modifying admixture)	Additive type	Additive amount
B0	215	430	1290	430	5.4	None	-
B1	215	430	1290	430	5.4	0.5in metal fibre	39
B2	234	426	1278	426	5.4	0.5in nylon fibre	5.3
B3	215	429	1287	429	5.4	SP	4.3
B4	215	344	1290	430	5.4	Fly Ash	86
B5	232	422	1267	422	5.3	Bentonite	21
B6	215	387	1290	430	5.4	Silica Fume	43

According to the study performed by Shakor, Renneberg, et al. (2017), the proportion of concrete in the mixture could be prepared based on the squeeze flow tests, compressive strength, the slump test and the Vicat test. Table 3. 9 shows the pivotal trials for the concrete mixture. In the study by Shakor, Renneberg, et al. (2017), various cementitious mixes, namely, mortar mixes with various ratios of water and chemical admixture, were used. This could significantly alter the flowability of the concrete. In the study, twenty-two trials were conducted for the preparation of concrete printing. Further, three of these trials were chosen for the squeeze flow, mechanical characteristics and flowability tests. It was determined that the triple layers in trial five, which consisted of a mortar mix, had less displacement than the mix containing a coarse aggregate.

Table 3. 9 Mix proportion of the different proportion of materials used for extrusion printing by 6 degrees-of-freedom robot.

Trials that have been prepared using extrusion for cement mortar by (Shakor, Renneberg, et al. 2017)									
No.	Cem (g)	FS(g)	Water (ml)	Ret (ml)	Acc (ml)	SP (ml)	WR(ml)	NT(mm)	
1	1000	0	360	8	4	10.4	-	Ø20	
2	1000	500	300	8	4	10.4	-	Ø20	
3	500	500	150	4	4	5.2	-	Ø20	
4	750	750	292.5	4	4	5.5	-	Ø20	
5	750	750	250	4	5	5	-	Ø20	
6	1500	1500	550	8	10	11	-	20×20	
7	1000	1000	361.6	5.33	6.67	6.67	-	20×20	
8	1000	1000	343	5.33	6.67	6.67	-	20×20	
9	1000	1000	350	5.33	6.67	6.5	-	20×20	
10	1000	1250	375	5	6	5	3	Ø10	
Cem: cement, FS: fine sand, Ret: retarder, Acc: Accelerator, SP: superplasticizer, WR: water reducer, NT: nozzle									
Trials prepared using the peristaltic pump, inner diameter (6.4) mm									
No.	Cem (g)	FS (g)	Water (ml)	Ret (ml)	Acc (ml)	SP (ml)	WR (ml)	NT(mm)	
11	2000	0	1200	80	100	0	0	Ø10	
12	2300	0	1200	30	40	0	20	Ø10	
13	1500	0	650	15	22.5	0	15	Ø10	
14	1500	500	675	15	22.5	0	20	Ø10	
15	1000	1700	700	15	22.5	0	30	Ø10	
16	1500	500	670	15	25	0	20	Ø10	
17	1100	333	494	10	17	0	18	Ø10	
18	1000	-	600	-	40	-	-	Ø10	
Trials using crushed coarse aggregate using extrusion									
No.	Cem(g)	FS(g)	Aggregate(g)	Water(ml)	Ret(ml)	Acc(ml)	SP(ml)	WR(ml)	NT(mm)
19	750	750	250	300	4	5	5	-	20×20
20	750	75	250	250	4	5	5	-	20×20

Table 3. 9 above present different mix proportions in 3DP and used different chemical admixtures to control the rheology of the materials. The different mix ratios resulted in different outcomes and different final shapes of the structural components. Moreover, many of the concrete mixes were cured using a specific procedure. However, each study had a different measurement for the setting time of the concrete slurry based on the w/c and admixture proportions.

In Table 3. 9, it can be seen that the w/c ratio of mortar is between (0.3-0.4). In most studies, the w/c ratio used was 0.4. The w/c ratio of the concrete mix in the experimental

study had a major effect on the mix flowability and shapeability of the printed concrete parts.

The set accelerator ratio has a similar ratio in most of the studies as did superplasticizer. The concrete/mortar mixing time is a vital part of the printing process. The concrete/mortar mixing time in each of the research studies was different, depending on the mix proportions and water to cement ratio. In the study by Kazemian et al. (2017), mixing proportions took 8 minutes, while in (Le, Austin, Lim, Buswell, Law, et al. 2012), the concrete for the printed specimens was mixed for 15 minutes. In the study by Shakor, Renneberg, et al. (2017), the average mixing time was 5-8 minutes.

The mix design of concrete and mortar has demonstrated the limitations of various mixes. Most of the mixes did not include the coarse aggregate due to the large particle sizes. Therefore, mortar or fine particle sizes was chosen to make it easily pumpable. Coarse aggregate is not suitable for use with all types of pumps. Further, the printed concrete using coarse particles did not have a good appearance after printing.

3.3 Benchmark Experimental Results

3.3.1 Powder-based (Inkjet Printing (Binder Jetting))

3.3.1.1 Formulation of the Powder for Inkjet 3DP

In the inkjet 3DP technique, the crucial factor before starting a print is adaptability and compatibility of the powder with the type of the printer. The printing application will be easy whenever the particle size, flowability, and wettability of the powder match the recommended powder of the printer manufacturer. Accordingly, the particle size analysis of the recommended materials is important to identify the closest range of the particles that are expected to result in a successful print.

In the previous studies by Shakor, Sanjayan, et al. (2017) and Shakor et al. (2018), the distribution size of the powder used in an inkjet 3D printer (Z-printer150, Z-Corporation, USA) was analysed and identified. The data were acquired using a particle size laser analyser (Cilas 1190), *Figure 3. 2 (a)*. The powder recommended by the manufacturer (ZP 151) contains major materials of plaster, carbohydrate and vinyl polymer. Descriptive values of the mean particle size for 10%, 50%, and 90% of the materials were D10, D50, and D90, respectively. The D values that were obtained were equal to 1.48 μm , 23.07 μm and 70.12 μm , respectively. The specific surface area for the ZP 151 powder was recorded as 0.999 m^2/g using the (BELSORP-max) machine.

Figure 3. 2 (a) shows the particle size distribution details of ZP 151 and cement mortar, which were used in the inkjet printing process. In *Figure 3. 2 (a)* the particle size of the cement mortar is shown to be distributed more to the right side of the graph, which means the particle size is slightly larger than the recommended powder (ZP 151) which, for D90 values, is approximately 80 μm for modified powder (cement mortar). From the graph, neither powder is perfectly matched, but they are similar enough that it helps to ensure the regular flow of the powder through the printer's feeder bin and the ability to print structural specimens smoothly.

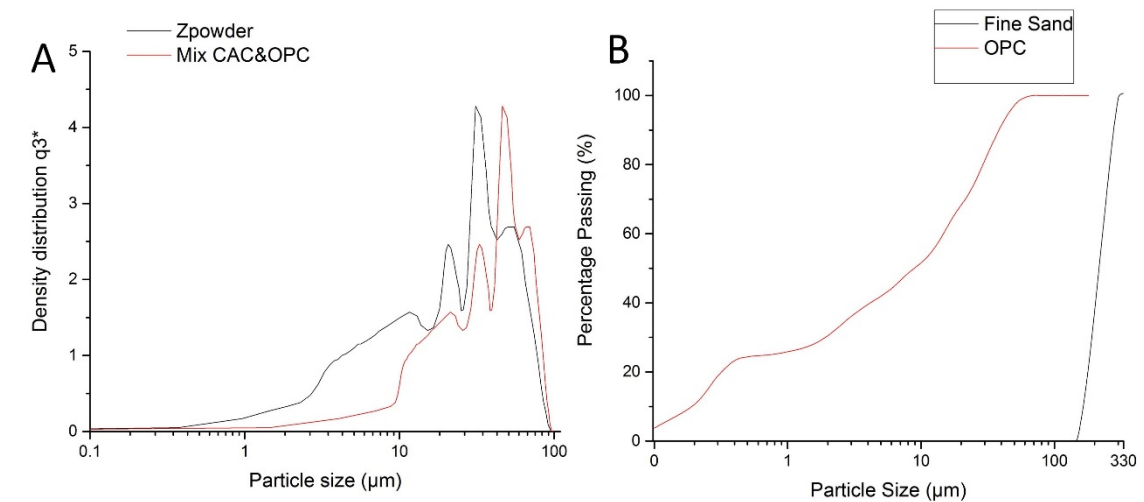


Figure 3. 2: (a) Particle size distribution of cement mortar and Zpowder (ZP 151) for the inkjet printing, (b) Particle size analysis of mortar versus percentage passing for the extrusion printing.

3.3.1.2 Specimen Preparation and Determination of the Water/Cement Ratio

The technique to print construction elements is inkjet printing (binder jetting) similar to an office printer in which, instead of printing on paper, the ink droplet drips on the powder materials. The D-shape printer also uses a similar process. In the binder jetting method, the powder is generally composed of a composite material. The liquid binder is mainly water, which is used as an activator to bind the powder. The printing process is conducted using a layer-by-layer application process. *Figure 3. 3 (a)* shows the cubic specimens under a uniaxial compression load. *Figure 3. 3 (b)* shows the core and shell of the specimens after the test. The saturation level is defined as the amount of liquid binder on the powder printed bed which is dropped out from the printhead (Miyajiri et al. 2016), as shown in the Equation below.

$$\text{Saturation level} = \frac{V_b}{V_p}$$

Where V_b is the volume of the binder and V_p is the volume of the powder after it has been rolled on the build chamber (enveloped powder).

Since the density and mass are known, then the Equation can be used to determine the w/c ratio for both materials. The different saturation levels in the liquid binder mean that the shell and core have a similar w/c ratio and similar saturation levels mean different w/c ratios inside the shell of the cube. The saturation levels in inkjet printing are based on the interior and exterior of the 3D printed part. The exterior part is called the shell and the interior part is called the core (Withell et al. 2011).

The files for the 3D printing objects are STL files which can be easily modelled and sent to the printer to print the segments (Cox et al. 2015; Hager, Golonka & Putanowicz 2016). STL has various backronyms names such as “Standard Tessellation Language, Standard Triangle Language”. In addition, STL is a file type of CAD software made by 3DSystems.

The printed part under a uniaxial compression load could be broken in various directions according to the direction of printing. In *Figure 3. 3 (b)*, in specimens of the same saturation, such as (S100 C100), a shell part under a uniaxial compression load detached from the core part of the specimens (Shakor, Nejadi, Paul & Malek 2019; Shakor, Sanjayan, et al. 2017). Further investigations are required to determine the reasons for the observed results, *Figure 3. 3*.

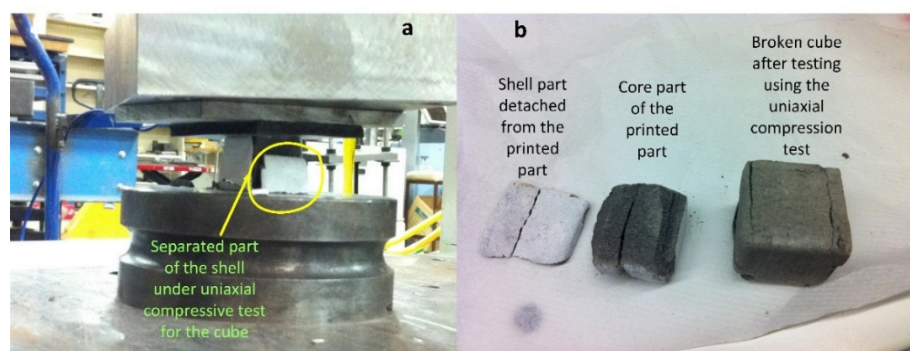


Figure 3. 3: Printed cementitious cube via inkjet 3D printer: (a) Compressed under a uniaxial load, (b) cracking and detaching of the shell and core parts.

3.3.1.3 Resolution and Surface Roughness of the Powder-bed

After preparing the materials and delivering the powders from the feeder, another parameter that should be investigated is the surface roughness of the powder and roughness of the specimens. This parameter is mainly related to the bed-powder preparations. One of the methods that can be used to assess the roughness of the powder is a visual inspection of the powder-bed in the build bin of the printer. The visual inspection of different types of gypsum has been performed in the studies by Zhou et al. (2014), which compared coarse and fine powders and also investigated the density of both powders. The distribution of the powder particles, uniformity of powder and the hygroscopic properties in the powder make a major contribution to the final printed product. Each of the powders has different properties for electric conductivity and microstructural strength development in the materials.

The modified material (cement mortar) is more capable of absorbing water and exhibiting hydration reactions. This is due to the main ingredient of powder being calcium aluminate cement, which undergoes an amorphous phase that results in the growth of an interlocked crystal of dense microstructure. Therefore, the high early strength in rapid-setting of the calcium aluminate cement was identified. On the other hand, the development of too many crystals causes a porous microstructure that will lead to a reduction in strength and durability (Sugama and Carciello, 1991).

In general, the hygroscopic properties and agglomeration in cement powder cause a poor powder-bed packing in the build chamber of the printer. Thus, the powder needs to be properly mixed and fluidised before printing any objects.

In inkjet printing, there is a clear difference between cement powder and the recommended gypsum powder in the build chamber of the printer. However, Shakor et

al. (2018) observed a significant number of porous, voids and roughness in the cement mortar powder. Consequently, this produced a weak printed sample and led to a reduction in the mechanical strength of the printed specimens. For that reason, it is highly recommended that the materials are mixed well before commencing the print process. Fresh cementitious powder should be used in addition to controlling the temperature and humidity in-vitro. There are other methods that reduce the moisture content of the materials and increase strength. Glass fibre has been used in other studies to increase the flexibility and strength of the printed structural members (Shakor, Pimplikar & Ghare 2011; Shakor & Pimplikar 2011).

3.3.2 Selective Laser Sintering

The SLS test was undertaken for the cementitious paste. This test was arranged to determine the reaction of materials under the heat of the laser beam and infusion between the particles.

Limited quantities of cement and water were prepared, with 630 g of cement and 282 ml of water, respectively, and a w/c ratio of 0.45. The thickness of the paste on the tray was 6 mm. This thickness has been chosen based on the printing process of concrete in 3D printing which usually ranges between from 6 mm to 20 mm. Secondly, the laser sintering could not solidify very thick materials. Finally, due to materials ingredients, which is only cement-paste materials. Cement-paste has a limited thickness in construction applications due to materials compositions. In this trial test, the paste was prepared on the flat tray so that the light of the beam could easily pass over the paste on the tray. The laser was applied to the cementitious paste to harden it and to dry the slurry of concrete, as shown in *Figure 3. 4* and *Table 3. 10*. It is noticeable that laser sintering did not significantly affect the cement paste and react with the slurry. The laser was also tested on different

powers and at various locations on the cement paste, resulting in a slightly dried stain on the surface of the cement paste. These trials were executed using the Voxeljet VX1000 machine. As shown in *Figure 3. 4*, the first line on the tray was cut by the laser light with a spot size of 1 mm. The spot size was then increased to 24 mm, which had no noticeable drying effect on the paste, due to the large size of the spotlight. In the fourth line, the spotlight was decreased to half (i.e. 12 mm). This dramatically changed the cementitious paste to a yellowish colour, which means it was burnt. The rest of the lines became dried and dehydrated with various ratios of spot sizes. For example, line nine became moderately dry compared with the other lines (Shakor, Nejadi, Paul & Malek 2019).

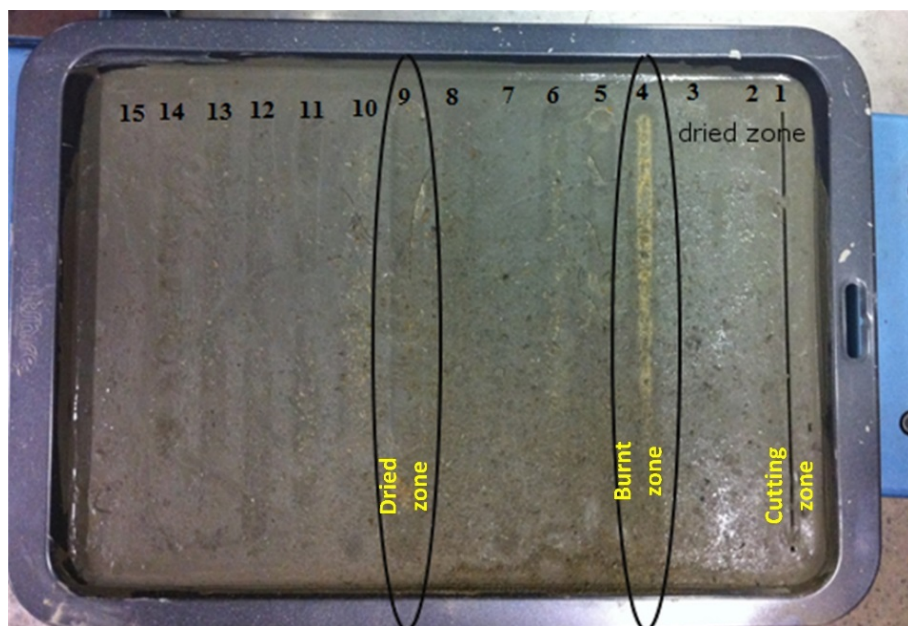


Figure 3. 4: Using laser sintering (SLS) for cement paste using different powers (Watts).

Table 3. 10 demonstrating the ratio of feed mm/min, the spot size (mm), power (watts), and temperature (°C). It is clear that the speed of axis and temperature are crucial factors in the SLS process and they both influence the resulting cementitious paste.

Table 3. 10 Demonstrating the speed, spot size, power and temperature for each line in Figure 3.4.

No.	Speed(Feed)mm/min	Spot Size	Power(Watts)	Temperature(°C)
1	300	1	207	30
2	300	24	207	60
3	300	24	500	85
4	300	12	700	95
5	300	12	1000	165
6	500	12	800	90
7	500	12	1000	40
8	300	12	1200	45
9	300	12	1500	180
10	500	12	1300	88
11	500	9	1300	55
12	300	9	1300	45
13	300	9	1500	45
14	300	9	1700	50
15	300	12	1700	55

3.3.3 Extrusion Printing

3.3.3.1 Mix design for Cementitious Materials

In a pilot study, Shakor, Renneberg, et al. (2017) used different concrete mixes and various nozzle sizes with an industrial robot to print cement mortar. The robot was also programmed to print any complicated geometries, as shown in *Figure 3. 5*. Currently, extrusion printing is one of the most common methods in construction applications. Extrusion printing (e.g. concrete printing (Le, Austin, Lim, Buswell, Gibb, et al. 2012), contour crafting (Khoshnevis et al. 2001)) has already been established in the construction field.

The methodology in Gosselin et al. (2016) was upgraded from a 3DOF (Three-Degree Of Freedom) which is called design of 2.5D printing (Le, Austin, Lim, Buswell, Law, et al. 2012) to a 6DOF (6-Degree Of Freedom) using an industrial robot. The 2.5D printing process uses the 3 axes of the printer instead of 6 axes, but this has limited ability to manoeuvre the print head. However, 3D printing is known as a complete application

process using six degrees of freedom robot which can be smoothly moved with a minimum of boundary limitations.



Figure 3. 5: (a) Printed mortar via extrusion printing, (b) Printed mortar using robot extrusion dried in ambient temperature for one day.

Figure 3. 5 shows how after the drying of the printed lines, shrinkage cracks occurred at the locations where the pump became clogged. This can occur when the delivery pipe does not have enough supply materials coming out of the nozzle. However, the shrinkage cracks can be eliminated by adding fibres such as glass fibre or polypropylene fibres (Shakor & Pimplikar 2011) and slightly increasing the w/c ratio or by adding a wire (308LS stainless steel) to increase the tensile strength of the printed objects (Laghi et al. 2018). Another limitation that was faced when printing the concrete was the oscillations experienced by joints 4 and 6 of the industrial robot when the robot approached singular configurations. This problem was initially exacerbated since these joints were experiencing the majority of the motions and changes in velocity. However, this oscillation could be solved by applying the Damped Least Squares (DLS) method for robot singularity avoidance as explained in earlier work (Shakor, Renneberg, et al. 2017). Sieve analysis and particle size distribution of the mortar have a major impact on the flow of the materials and the slump of the mortar. *Figure 3. 2 (b)* shows the passing percentage

of the particles from the sieve for fine sand and ordinary Portland cement versus the logarithmic particle size for extrusion printing. It is obvious that the particle size of dry powders is not greater than 300 μm . However, the particle size can be increased to larger particles, such as 1.0 mm, as a coarse sand to improve the strength of the mortar and reduce shrinkage cracking in the printed objects.

3.3.3.2 Extruder Adaptation and Delivery System

Extruder adaptation and delivery systems have the most significant influence on whether or not extrusion printing will produce a satisfactory printed object. A satisfactory outcome of the printed objects generally means a good mechanical property of the materials and good shapeability of the printed parts. *Figure 3. 6* shows the developed model in this study for the extruded part that has been designed to mount to the end-effector of the 6-DOF robot.

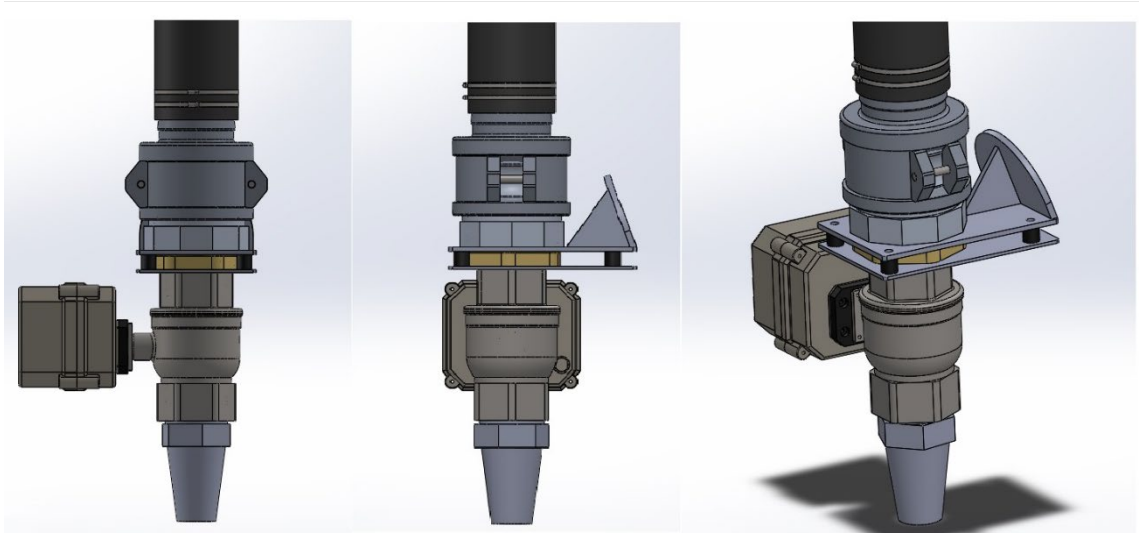


Figure 3. 6: Extruder mounted to the end-effector of the robot.

The joints of the robots that have been predominantly used during the printing process are joints 4 and 6. These two joints are used frequently to rotate and move the print nozzle

through the desired path in order to print the members. For that reason, oscillation appeared mostly in those two joints.

Nozzle shape and size are considered to be additional effective factors contributing to the mechanical strength and shapeability of the printed mortar objects. Therefore, these two factors should be taken into account in the design of the nozzle.

The delivery system is another parameter that needs to be considered. The delivery system has a major impact on printing outcomes such as the shapeability and slump of the concrete or mortar. Pumps are the most common delivery system used in printing applications. Pumps are of different types and use different mechanisms to deliver the material from the source to the end-effector of the printer. In 3DP using concrete, various pumps have been used, such as progressive cavity pumps (Shakor, Renneberg, et al. 2017), peristaltic pumps (Gosselin et al. 2016), pneumatic pumps (Bos et al. 2018), and piston pumps (Malaeb et al. 2015). Each of the pumps had limitations such as pressure, flow rate and heat transmission to the slurry. Thus, none of the pumps is perfect with 100% efficiency. Losing energy and transforming heat into the slurry makes the pump warmer and also warms the concrete. However, some pumps have fewer cavities and air voids than others such as pneumatic, or centrifugal and peristaltic pumps. The aforementioned types of pumps allow less air to enter due to the working principle of the turbine and easy-place dampeners in such pumps. The design of progressive cavity pumps results in cavities and voids which lead to air being discharged at the end of the rotor with materials. Moreover, when the operating time increases in the pump, the flow rate of the pump decreases dramatically by contrast with the flow rate in the rotary lobe which stays steady and constant (Boring 2016).

3.4 Summary and Discussion

Inkjet printing is the second best-known printing process in the construction field after extrusion-based printing. It consists of a powder and a binder. The powders could be any usable materials, which can easily react with the binder.

Chua & Leong (2014) and Low et al. (2017) referred to large printers such as Voxeljet and ExOne, which can print large parts up to $(4 \times 2 \times 1)$ m. Voxeljet is a German company which specialises in 3D printing system services. ExOne is an American company that has similar services to Voxeljet, the only differences being some technical specifications. For instance, the ExOne has two build chambers and can print at the same time but Voxeljet has only one chamber. The build chamber sizes of Voxeljet are larger than ExOne and reach $(4 \times 2 \times 1)$ m, but the maximum dimensions of ExOne reach $(2.2 \times 1.2 \times 0.6) \times 2$ m.

Nowadays, the main competition between these printers relates to resolution, speed and materials' properties, which have a significant role in the appearance and the mechanical behaviour of the manufactured parts. Chuang (2017) claimed that when the cartridge mounting angle changed from 1.1 to 90° , the resolution of inkjet printing changed from 5080 to 100 dpi. The outcome was increased drop spacing from 5 to 254 μm . The printed dots have an undesirably large overlap when the drop spacing is too close (short), causing a large spread of the ink because of efflux of the ink. On the other hand, a non-uniform width line or a separated dot occurs when the drop spacing is too great to overlap each dot.

One of the limitations of inkjet printing is the high porosity which makes the sample more fragile and permeable (i.e. water will easily pass through it). Therefore, extra post-

processing is required, such as curing with heat or with pressurised water steam (Dikshit et al. 2018).

On the other hand, the high porosity makes the 3D printed part very light and easy to handle and this could be very beneficial when printing structural components. It reduces the weight in the building and could be very effective for seismic zone regions.

Zhou et al. (2014) studied the density of the powder over the build chamber, which is called the in-process bed density. This density is usually lower than the true density and higher than the bulk density in magnitude. However, the enhancement could be implied by the type of packing of the bed powder on the chamber by changing the mechanical force applied on the powder bed. This can increase the required force of the roller on the bed layers which helps to reduce the voids within the powder particles. The outcome will be higher density and less porosity which will, in turn, eliminate or reduce extra post-processing.

Table 3. 11 explains the printer settings of an inkjet printer, extrusion printer and selective laser sintering.

Table 3. 11 Explanation of settings of printing and printing methods.

Printing Settings	Inkjet Printing (Binder Jetting)	Selective Laser Sintering (SLS)	Extrusion Printing (Extrusion based process)
Speed	The print head is mounted to the Fast Axis Assembly (FAA). It can print 2-4 layers per minute. This process takes longer than extrusion printing. The speed of the print head axis is identified as a speed of binder (drop of water) which impacts the layered powders.	Speed and resolution of SLS at industry averages have tolerance of 0.1mm. Due to the relatively slow fabrication speed, this method is suitable only for low volume production runs for small, precise parts. This process takes longer than the other two processes.	Extruders and nozzles are held by the arm of the robot, allowing the extrusion of materials through the nozzle. The speed of extrusion depends on the materials' rheology and size of the nozzles. The velocity of the print varies between 39mm/s to 60mm/s depending on the mixing types. The speed of the robot arm and the pump velocity are essential to discharge the constant slurry through the nozzle. If the robot arm speed more than slurry discharge, it will affect the air gap between the ingredients.
Strength	Inkjet printing has lower strength and lower density than extrusion printing. Inkjet printing leaves a significant number of voids inside the printed parts.	This type of additive manufacturing could not work properly with concrete fabrication; it reaches the point where it burns all particles and evaporates the water inside the concrete.	In extrusion printing, the concrete slurry can gain higher strength than with the other types of printers. Concrete can, therefore, gain higher strength and density than in other techniques of additive manufacturing.
Accuracy	Inkjet printing has lower accuracy than sintering because the liquid distribution is not distributed evenly on to the powder. However, it has better accuracy than extrusion printing.	This technique has higher precision than other processes.	This process has lower accuracy compared to the other types of printing.

Table 3. 12 Explanation of settings of printing and printing methods(continued).

Printing Settings	Inkjet Printing (Binder Jetting)	Selective Laser Sintering (SLS)	Extrusion Printing (Extrusion based process)
Resolution	<p>This printer has higher resolution than extrusion printing. Recently, different types of printer have been developed with different resolution, such as Zprinter resolutions Zprinter®150 (300×450) dpi and Zprinter®650 (600×540) dpi. The water/cement ratio controls the resolution of the printer and affects the resulting printed part. The number of drops per inch is the main factor on the powders to make the printed specimens higher resolutions or better shape.</p>	<p>The resolution of SLS is superior to the other two types of printer because the laser light can precisely print onto the exact spot on the powder. Furthermore, it does not leave any marks in surrounding areas and the adjacent side of the powder.</p>	<p>The resolution in extrusion printing is lower than it is for the other two printers. This system needs to have good finishing for the surface or the addition of a trowel to smooth the surface, such as contour crafting. The resolution of the printed parameters depends on the maximum particle sizes in the slurry, the height which slurry impacts on the platform and the water to cement ratio.</p>

SLS has broad applications in other fields but it has limited use in the construction field. The main materials used in this process are powders. Most powders consumed in this application are a polymer (nylon). In the SLS process, the powders are fused or react together using a laser. If the powders do not react using a laser, it is not an effective method.

In some studies, the SLS technique and conventional processes have been used in dental work. In the casting process, the gap in SLS production is greater than in conventional casting in all measured fields (Kim et al. 2013). Thus, the methodology of SLS is similar to the inkjet printing process, which produces similar voids among particles.

Another limitation in SLS is its low resolution due to the restrictions of the powder-base materials, which result from the agglomeration of fine particle sizes (Cao et al. 2015).

Extrusion printing has the greatest potential for use in the construction field compared with other techniques of additive manufacturing. There are particular limitations in extrusion printing that can be addressed, based on the scale of the project and the printing materials (Wu, Wang & Wang 2016).

Berman (2012) demonstrated that rapid prototyping is the most successful process for manufacturing small parts of the scaffold.

A question that has been frequently asked is whether 3DP could print at a larger scale for components in construction with durable mechanical properties. This question has been answered in recent decades with the development of additive manufacturing. For instance, the WinSun company in China has built precast components with dimensions of $150 \times 10 \times 6.6$ m (Feng 2014). However, the degree to which these 3D printed elements can withstand severe environments and weather conditions has not yet been proven.

Pumping speed and the velocity of the moving arm or nozzle (delivery mechanism) were found to have a crucial impact on the printed objects and the resolution of the samples. Shakor, Renneberg, et al. (2017) conducted a comprehensive experimental study examining various concrete mixes with regard to the speed of the robot, as shown in *Table 3. 13*. The optimum velocity of the robot printhead for the specific mix design was 39.36 mm/s for the total length of the printed line (1580) mm. However, when using the auger motor, speed in the adapted extruder was 15-19 volts. Thus, when the mix design was slightly modified, the speed approximated 35~45 mm/s, which could be the optimum speed.

Table 3. 13 Explanation of the time and velocity of the printed concrete outcomes.

Trial No.	Auger motor speed (volts)	Robot arm speed			Total length of printed line (mm)	Time (s)	Velocity mm/s
		Teach pendant %	MATLAB (GUI) %	Over all%			
1	-	10	30	3	940	-	-
2	14-15	10	30	3	940	25.13	37.4
3	-	10	30	3	-	-	-
4	-	10	30	3	1580	41.59	37.98
5	15-19	10	30	3	1580	40.14	39.36
6	25	10	30	3	3180	75.49	42.12
7	19	10	30	3	3180	75.49	42.12
8	-	10	30	3	3180	75.49	42.12
9	29	10	30	3	3180	75.49	42.12
13	-	10	30	3	3090	73.68	41.94
14	-	6	10	1.6	3090	488.0	6.33
15	-	5	20	2.5	-	-	-
16	-	5	20	2.5	1230	96.65	12.7
17	-	5	20	2.5	1230	96.65	12.7

The study by El Cheikh et al. (2017) explored the speed of the horizontal plane shifting with a constant speed (V_p) equal to $50 d/s$, where d/s is the diameter of the tube per second. The study by Hambach & Volkmer (2017) obtained a print speed of 30 mm/s by adjusting the layer height to 1.5 mm. Kazemian et al. (2017) used a linear printing speed of 60 mm/s. However, Shakor, Renneberg, et al. (2017) proved in their study that the most

appropriate robot arm speed suitable for printing concrete was (35~45) mm/s for their mix design.

The printing speed to extrude materials depends on several factors: the rheology of the materials, the size of the nozzle, the shape of the nozzle, the distance between the nozzle and printed platform and the distance between the delivery method and the extruder.

CHAPTER FOUR

4. TECHNIQUES AND METHODOLOGY

4.1 Powder-based (inkjet) Printing Technique

In this chapter, a review of the most advanced technology using modified materials for powder-based 3DP has been presented. A powder-based 3DP is a controlled method by a CAD model to fabricate objects by dropping a fluid binder into a powder bed to create a green part (Vaezi & Chua 2011). To determine the mechanical properties of the printed parts, it is necessary to include not only the printing process but also the formulation of the powder particles and liquid binder to enhance the success of a specific 3DP process (Utela 2008). A major mechanical property is the mechanical strength of 3DP parts which depend widely on the suitability of the materials including metals, ceramics and polymers, (or any other materials which could be used as a depositable powder with a suitable range of particle sizes e.g. cement-based mortar) (Utela 2008). Developing of 3DP parts with different modified materials, requires a number of stages: (1) selecting a suitable size range of powder particles; (2) selecting a suitable binding method; (3) selection of a suitable fluid binder to interact with the powder; (4) printing procedure (application) and affecting parameters; and (5) specification of any post-processing procedures.

4.1.1 Delivery System

Powder-based (inkjet) 3D printing is an additive manufacturing technique in which powder particles are bound together by dropping liquid droplets into the specific region. This process is called the binder jetting 3DP process (Lee, An & Chua 2017).

The inkjet 3DP consists of three main parts: a feeder chamber, build chamber, and feeding container (*Figure 4. 1*).

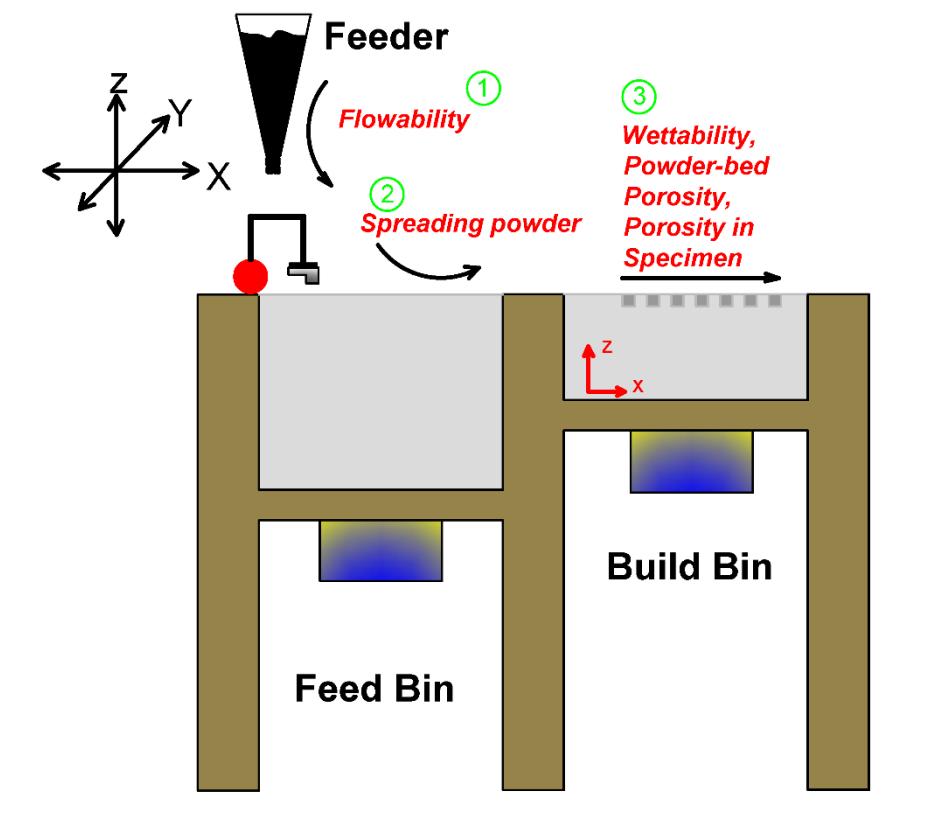


Figure 4. 1: Schematic illustration of powder-based 3D printer with relationship between flowability, wettability, powder-bed porosity and porosity in the specimen.

The powder particles flow as a result of gravity assisted by the rotating rotor in the feeder tank, see *Figure 4. 2*. In the feeder container, the rotor rotates in both clockwise and anticlockwise directions at a speed of 30 RPM (Revolution Per Minute). The length of the rotor shaft, which consists of 4 parallel stainless-steel bars, is 290 mm, as shown in *Figure 4. 2*. Inside the feeder container, there are 21 rectangular holes with dimensions of 4.5×1 mm. The particles of the powder flow down to the feed chamber through these holes (see *Figure 4. 2*). This process is initiated by the flow of powder particles from the feeder tank.

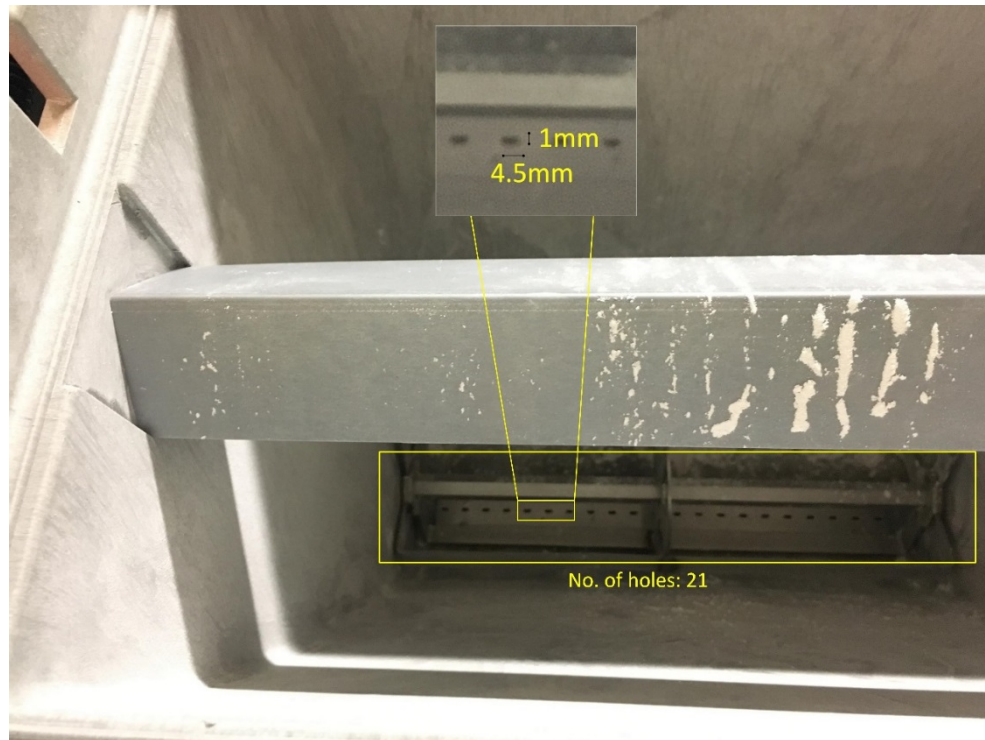


Figure 4. 2: Inside the feeder container showing the number of holes in the bin.

Subsequently, the powder particles on the feeder chamber are pushed by the fast axis roller, see *Figure 4. 1*. The process of spreading powder on the feeder and build chambers continues until the bed filling in the build chamber is complete. Then, the printhead, which is attached to a gantry, starts dropping the drops along the fast axis onto the powder bed.

Printheads are generally divided into two major types: continuous inkjet (CIJ) printing and drop-on-demand (DOD) inkjet printing. CIJ, which is used mostly for coding and marking purposes, uses a liquid which has diameters usually between 10 and 150 μm , while DOD is used for graphics and text printing with liquid diameters typically between 20 and 50 μm (Antohe & Wallace 2002).

The printhead is manufactured to drop the droplet of liquid binder bonding agent onto the powder. This process continues to print the next layer after spreading a new layer and dropping droplets onto the powder. The benefits of the binder jetting (inkjet) process are

a high speed printing process offering design and fabrication freedom, its freedom from formwork and support, its ability to build in large volumes, and its comparatively low cost (Lee, An & Chua 2017). Examples of machines utilising inkjet 3DP processes include Voxeljet, 3DSystems and ExOne production printers. The ExOne has various types of printers (Exerial, S-Max, S-Print, M-Print and M-Flex machines). These printers can use a variety of materials such as cement, ceramic, glass, sand, metal, and polymer which are suited to the inkjet printing technique.

The delivery system in this technique is gravity, and the rotor and fast axis roller are major contributors to the delivery of the powder into the build chamber and to the completion of the printing production.

4.1.2 Printing Applications

Recently, inkjet 3DP has advanced to a stage where it performs vital roles in many applications, such as art and design, biomedical applications, medicine, architecture and construction. There are also a few corporations using 3DP to produce new 3DP machines.

In the current scenario, 3DP processes are finally approaching their full potential, and are being used in the manufacturing and medical industries, as well as by sociocultural sectors which facilitate 3DP to become successful commercial technology.

Generally, a 3D model for 3DP parts is created in CAD software such as SolidWorks. This model is then converted into an (STL) file, the most common file used by most prototyping machines. This file defines the entire object in layers (slices) allowing the object to be constructed in sequence. This information is sent to the 3DP to indicate the location on the powder-base where the printhead should drop the droplet. A process of repeating the layering procedure completes the entire object. After a few hours, the complete object dries and hardens into a solid form (Buswell et al. 2007).

Powder-based (inkjet) 3DP is capable of printing a range of geometric shapes and sizes. The binder jetting process uses the inkjet head (IJH) technique for the printing process. In this method, the print heads play a major role in the production of high-quality products. A liquid binder passes through the nozzles (304 nozzles in ProJet 360 and ZPrinter 150). The ink-drop is 18 pl (picoliters). These ink-drops are ejected onto a thin layer of powders (0.1mm) which has been driven by software in order to create an object (Kullmann et al. 2012).

Inkjet 3DP is well-known in the pharmaceutical and tissue engineering fields (Huang et al. 2007). For instance, Spiritam® (levetiracetam) is the first 3DP medicine approved by the US Food and Drug Administration (FDA). Zipdose® technology produced a highly porous tablet (Goyanes et al. 2015). The tablet is quickly dissolving when fluids make contact with it due to its high porosity, occurring even at a high dose rate (Gupta 2010). This technology has less application to soft materials such as in food industry. However, recently this application has been used in ceramic and cementitious uses (Holman et al. 2002).

4.2 Extrusion Printing Technique

Extrusion 3D printing is a procedure that is typically initiated by printing parts layer by layer to construct a full scaffold of polymer materials (Wangler et al. 2016). Nowadays, this method is widely used in most industrial applications, including in the construction industry. The technique begins with a digitally controlled end-effector which consists of the nozzle and hose. These parts are usually connected to the pump or delivery system to deliver the concrete or mortar to the end-effector. The procedure is a layer by layer process. During the last few years, concrete printing has been investigated broadly by many researchers and companies. Prof. Khoshnevis, who is a pioneer of extrusion

printing, established a method called Contour Crafting in early 2004 at the University of Southern California (Khoshnevis et al. 2001; Khoshnevis & Dutton 1998). The idea was to construct a house on the moon using lunar soil (Leach et al. 2012; Wangler et al. 2016). In 2010, a researcher from Loughborough University conducted a similar project using a method called free form construction (Buswell et al. 2007; Lim et al. 2012). This type of 3DP concrete requires a large scale gantry or robotic frame as such a scale is required to print a whole structure. Issues currently being faced include: the size of the layers is no greater than a few centimetres; cold joints between layers; and the use of small particles of fine aggregate in the application. The utilisation of steel bars and reinforcement are still a major issue: how can the steel be bent or placed; and what type of steel or rebar reinforcement could be used for printing applications. There are a few studies addressing the problem of how the hollow structure has to be made and how afterwards the steel or rebar can be placed before infilling the structures with concrete and creating a connection to the whole printed structure (Asprone et al. 2018). There are other ideas, such as using the tendon bar while printing as it has higher flexibility than steel rebar and is easily adaptable for concrete reinforcement (Ma et al. 2019).

4.2.1 Delivery Systems

A cement-based mortar could be developed for mortar printing. The major points that need to be considered in the application of concrete or mortar in additive manufacturing processes include the fresh state of the mortar/concrete related to pumpability and the shapeability of the printed objects (Lim et al. 2012).

The following four points detail the key parameters of wet-process extrusion printing:

1. Pumpability: Easy flow and consistency of materials allowing them to travel through the delivery system, such as a pump;

2. Printability: The consistency of easily discharging materials through end-effector devices such as hoses and nozzles;
3. Buildability: The capability of the deposited slurry materials to control distortion and deformation under pressure and self-weight; and
4. Open-time: The time period for all the above characteristics is reliable and within accepted tolerances.

For each of the above mentioned points, different materials and admixtures are required to assist in the control of extrusion printing slurry. Using enough water and superplasticizer in the mixture to make the concrete pumpable and flowable helps the materials flow through the delivery systems easily. Printability is most related to the delivery system and its ability to deposit the materials in an appropriate way. Both water and superplasticizer have a major influence on the printability of the product. Buildability is most related to the admixture in the slurry, such as an accelerator, which helps the concrete or mortar materials set fast so it is capable of bearing the load deposited on top of the existing layer. This also helps to control the slump of mortar or concrete deposited on the printed platform. Open time refers to the use of a retarder which either prevents the mortar from setting or delays the setting time in the pump to maintain the consistency of the concrete/mortar (Jianchao et al. 2017).

The extrusion 3D concrete printing (3DCP) procedure for construction applications is shown in *Figure 4. 3*.

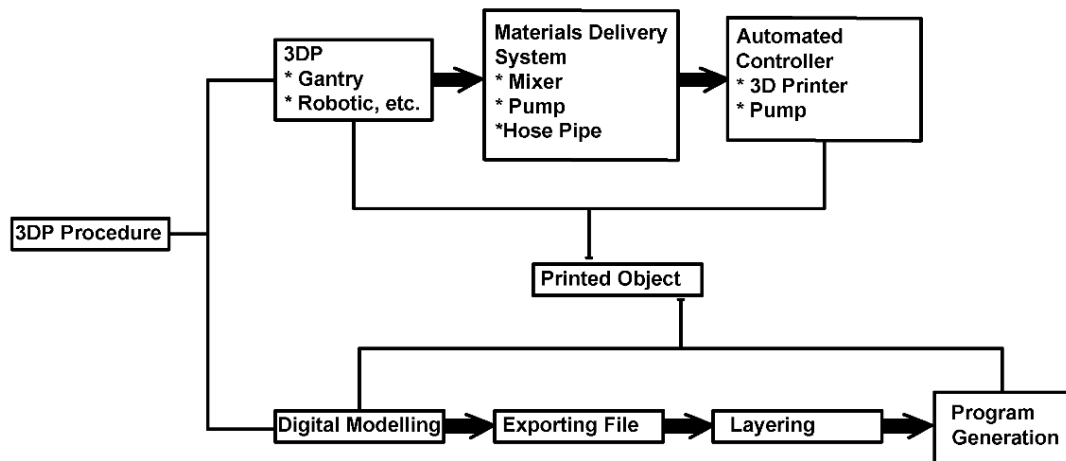


Figure 4. 3: 3DP concrete procedures for construction applications (reproduced after Paul et al. 2018)

The whole extrusion 3DP procedure consists of two processes. The bottom section of *Figure 4. 3* describes the software process; the top section of the figure describes the printed outcome process. In the first stage, a software file is prepared by SolidWorks to create an STL. This file can be exported for generation after slicing/layering. The CAD file can be easily programmed using MATLAB or Grasshopper to model the printed objects. This file is transferred to the robotic arm or gantry to create motion and start printing on the platform. To print an object, the materials are delivered through a hose which connects the pump to an integrated printer (robotic or gantry). At the end of the integrated printer, the end-effector, such as a nozzle orifice/head, is connected to the robot to deposit the materials layer by layer. A controller is always used to control the speed of the pump and flow of the slurry from the initial point until the end of the printing process (Paul et al. 2018).

The delivery system could be different according to the type of materials, mix design proportions and slurry type. In this study, different delivery systems for printing mortar, such as an adapted auger extruder, a peristaltic pump and a progressive pump, were used.

4.2.1.1 Adapted Auger Extruder

The extruder was made to attach to the end-effector of the industrial robot (Denso VM6083) and was based on the design by (Anell 2015). The extruder consists of the following parts:

- Y-Pipe (diameter 110mm) (Holman 100mm PVC 45 degree and female plain junction)
- Truck wiper motor (24 Volts)
- Auger (diameter 80mm)
- Nozzles of various sizes: circle (10, 20 and 30) mm, and square (10, 20 and 30) mm, (Figure 4. 4, Figure 4. 5).

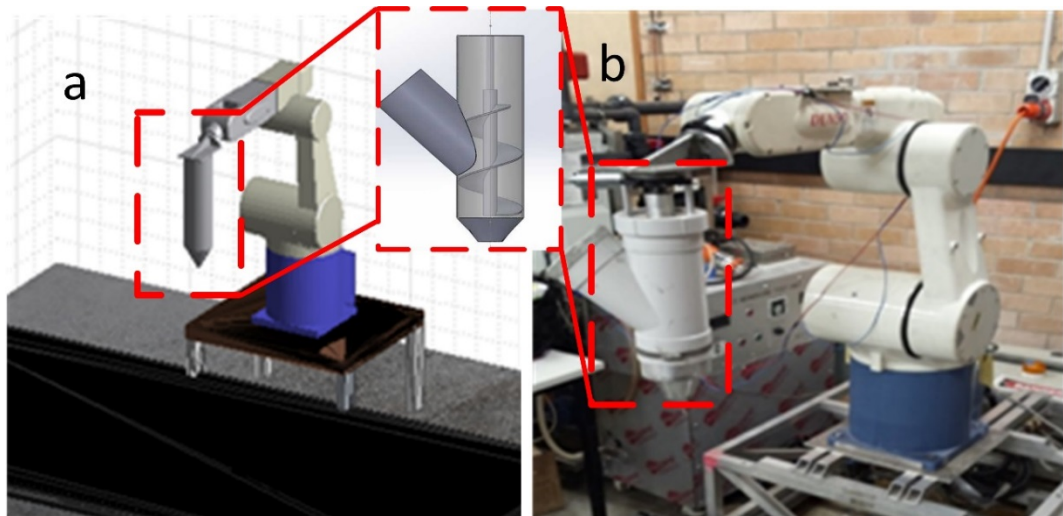


Figure 4. 4: (a) Simulated Robot with a print nozzle assembly attached, to demonstrate and check motion plans and paths. (b) Real world robot and auger nozzle assembly.

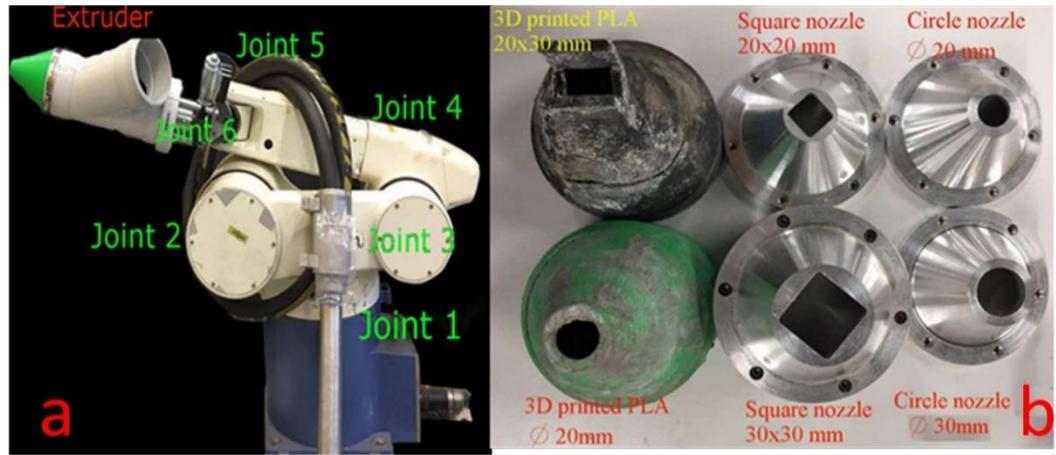


Figure 4. 5: (a) Extruder joined to the Denso Robot. (b) Nozzle types made with Aluminium and PLA.

A successful printed mortar using an adapted auger extruder is shown in Figure 4. 6. Printing mortar through the adapted auger had many limitations and challenges such as inconsistency in printing, creating voids among particles in the adapted pipe, and incapable wiper motor for heavy materials and viscous slurries.



Figure 4. 6: Resultant Print of successful print yielding a stable mortar and decent slump slurry. Issues with the auger delivery struggling to consistently push out materials.

4.2.1.2 Peristaltic Pumps

This pump, commonly known as a roller pump, is a type of positive displacement pump that can be used to pump different types of fluids and slurries. These fluids and slurries are enclosed in a stretchy pipe/tube fitted into a rounded pump case (linear peristaltic pumps). The external perimeter of the rotor compresses the stretchy pipe/tube which is attached to a number of "shoes", "wipers", or "lobes", forcing the fluid through the pipe/tube. As the rotor turns, the portion of the tube being pressed is pinched closed (or occludes) (Kommu, Kanchi & Uttarkar 2014), *Figure 4. 7.*

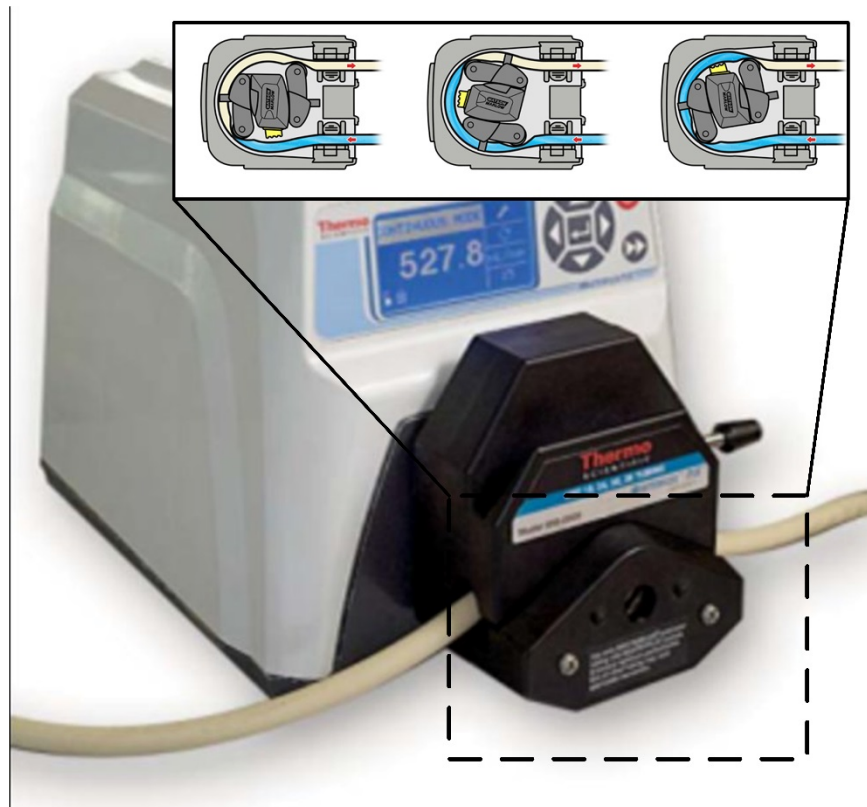


Figure 4. 7: Peristaltic pump with an explanation of the pumping process.

The mortar slurry printed with a peristaltic pump had a fine particle size due to the small hose diameter. Therefore, to push the materials easily through the pump requires a workable mortar property, *Figure 4. 8.*



Figure 4. 8: Printed cement mortar using a peristaltic pump with a 7.9mm diameter.

Any industrial 6-axis robotic arm could be used for printing purposes in construction applications. Such applications could be processed into designed structural members. It can be mounted to the end-effector of the robot as well as using pumps as a delivery system. For instance, two peristaltic pumps have been used by (Gosselin et al. 2016), one for delivering the accelerating agent and the other one for delivering the premix mortar. The end-effector and pumps were controlled by an Arduino Mega 2560 micro-controller using a program that could control the end-effector and pumps according to the building path (Gosselin et al. 2016).

4.2.1.3 Progressive Cavity Pumps

A progressive cavity pump is also a type of positive displacement pump called a progressing cavity pump, eccentric screw pump or cavity pump. This pump can transfer most viscous liquids and some types of slurries by means of progressive procedures. As the pump rotor turns, liquids or slurries pass through a short section of the tube of a specific shape, see *Figure 4. 9, Figure 4. 10*.

Small amounts of shearing are applied to the pumped liquid and the bidirectional rotation rate results in a proportional volumetric flow rate.

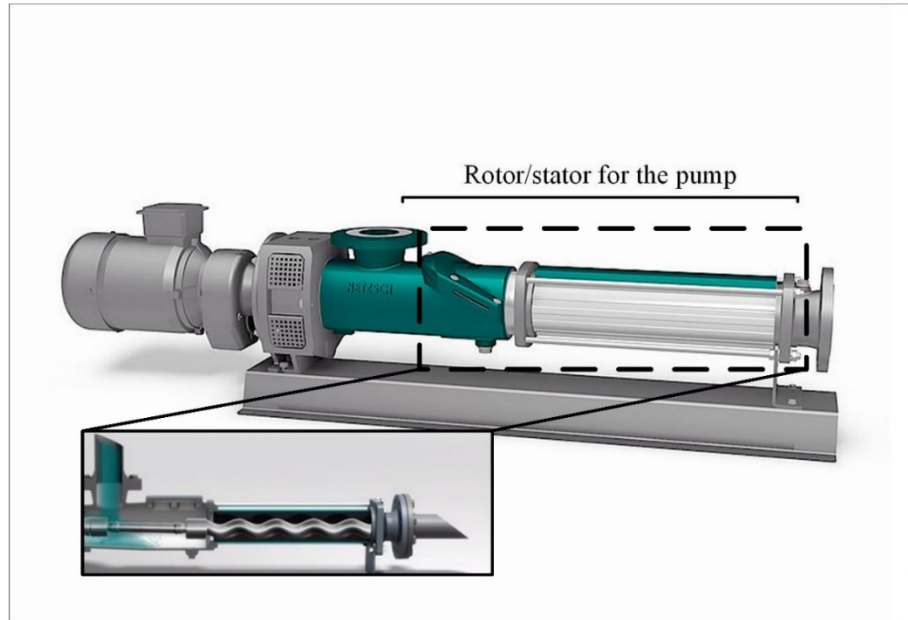


Figure 4. 9: Schematic illustration of the progressive cavity pump with the detail of the pumping system.



Figure 4. 10: Product of the progressive cavity pump using a 20 mm circular nozzle.

4.2.2 Printing Applications

Over the last ten years, the extrusion printing technique has been investigated broadly by several research companies and universities. The innovator of concrete 3D printing Prof. Khoshnevis, developed a process called Contour Crafting in early 2004 (Khoshnevis et al. 2001) (Khoshnevis & Dutton 1998). There are similar methodologies such as the free form construction project conducted at Loughborough University in 2010 (Lim et al. 2011). The approach in both is based on the layer by layer process. An issue in 3DP, it is a conjunction of steel rebar in the printing applications. This issue could be addressed by printing hollow structures and inserting the rebar afterwards. The process of placing the rebar is called a 'stay-in-place' formwork production process.

These two revolutionary projects have had a marked influence in the field of concrete 3DP applications, resulting in several companies and industries producing precast printed elements. One such company, WinSun in China, successfully printed a whole house within 24 hours by fabricating the construction members and assembling numerous portions of the structure (Wangler et al. 2016). The printing project by WinSun company faces many limitations such as off-site construction components, brittleness of the printed components and excluded from electrical and plumbing integration (Wu, Wang & Wang 2016).

Another example is a company named Total Kustom, owned by Andrey Rudenko who produced a 3D printed hotel in the Philippines (Rudenko3DPrinter). The Total Kustom has issues in terms of operating due to the limitation of the nozzle opening 30×10 mm (Bos et al. 2016). Another project, WASP, involved printing a 12 m tall hexagonal structural shape (3dWASP), WASP could print sustainable materials but challenged in terms of the strength capability for structural components. One more Chinese company,

HuaShang Tengda, recently printed a 400m² villa, with the goal of eliminating one of the major challenges in 3DP concrete, namely, the use of a horizontal extrusion-based technique. The whole villa was printed within 45 days to withstand a magnitude 8 earthquake (HuaShangTengda). HuaShang Tengda faces some issues such as erecting the steel frame on-site, it also considering slump behaviour in terms of the printer geometry (Bos et al. 2016). ConPrint3D at TU Dresden and 3D Concrete Printing at TU Eindhoven, have established material-based methods in their recent projects in conjunction with the XTreeE group in France (3DConcretePrinting ; CONPrint3D.In:TUDresd). These groups have developed their own trajectories in the sake of printing concrete on-site. Obviously facing some problems such as the nozzle dimensions and speed of the printhead.

CHAPTER FIVE

5. EXPERIMENTAL PROGRAM

5.1 Experimental Program

This chapter is divided into two major sections. The first section comprises a discussion of the experimental investigations of the Powder-Based (Inkjet) 3D Printing Technique. The second section discusses the Extrusion Printing Technique. The specific focus in this chapter is to optimise the powder and slurry materials, saturation level, and speed of the printing processes to fabricate objects with high quality and improved mechanical strength in the minimum processing time and with the best possible geometric accuracy.

5.1.1 Powder-Based 3D Printing Technique

In general, the most common method in civil engineering is to cast in place or use precast procedures to construct structural members. These structural members are cast using different materials such as concrete and masonry (Haroglu 2010). Given the ever-increasing need for speed, quality and bespoke design in the construction industry, and due to the advances in rapid prototyping, the procedures for constructing structural members need to change direction and upgraded.

Based on the earlier studies, three main techniques for 3DP powder-bed technique have been recognised (Lowke et al. 2018): selective binder (cement) activation; binder jetting; and selective paste intrusion (Shakor & Nejadi 2017; Shakor, Renneberg, et al. 2017). The selective binder (cement) activation (see *Figure 5. 1*), which is usually known as powder-bed printing (binder/inkjet printing) Shakor, Sanjayan, et al. (2017); Shakor et al. (2018) is the process that is described in this section (refer to Appendix A).

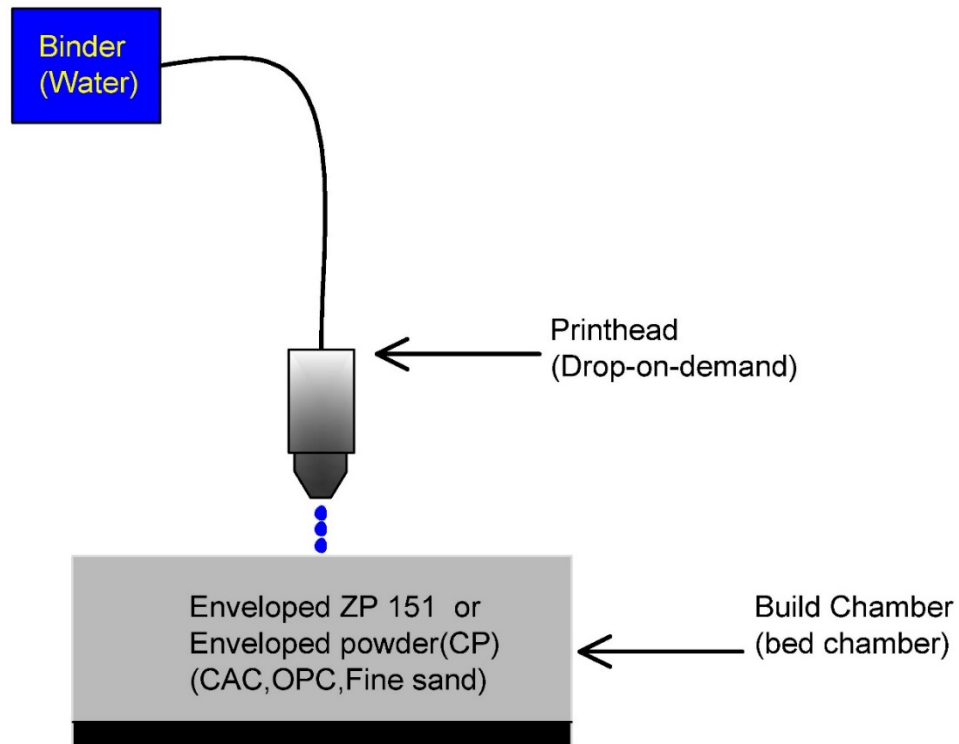


Figure 5. 1: Schematic illustration of the selective binder (cement) activation technique in inkjet 3D printing.

Inkjet printing is a layer-by-layer procedure to complete the entire scaffold using powder-based materials and an activator such as water, see *Figure 5. 2*.

In additive manufacturing techniques, powder-bed 3DP is a promising technique that could produce free-form fabricated concrete/mortar members without the need for support or formwork (falseworks) (Shakor, Nejadi, Paul, Sanjayan & Aslani 2019; Shakor, Sanjayan, et al. 2017). The only support provided while printing is the unbounded powder surrounding the printed specimens. Concrete members are usually optimised to obtain the required strength to withstand the load and resist climatic conditions. Hence, using such technologies in the construction industry, particularly for concrete and mortar materials, the number of duplications can be easily increased, thereby enabling the application of different geometries without having any complicated and expensive

formwork. This technique would be cost-effective, easy to apply and environmentally acceptable. It is also advantageous as it can reduce the use of different types of formwork.

Figure 5. 2 shows the technique that inkjet 3DP uses to construct a specimen, layer over layer, by spreading powder within thickness 0.1mm of the previous layer and adding water to make a bond between the layers.

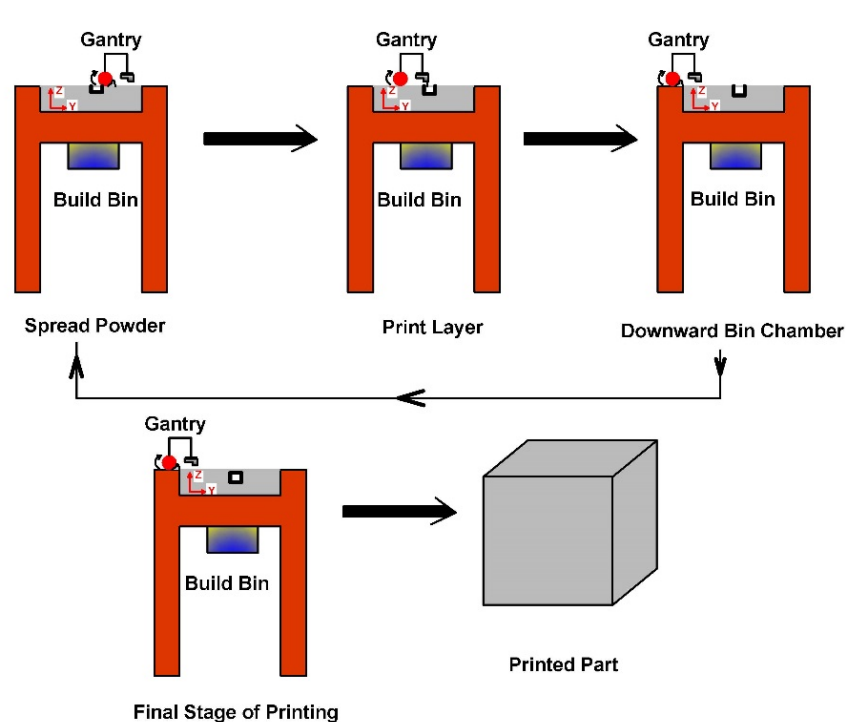


Figure 5. 2: Schematic depiction of powder-bed printing (layer technique) in inkjet 3D printing.

Powder-based 3DP is a promising printing technique which could print large members for construction with high precision. In order to make durable and strong construction members in 3DP, it is necessary to know the mechanical behaviours of the printed specimens. (ZP 151) is the recommended material provided by 3D-Systems (3DSYSTEMS 2013). This powder is ground powder with good consistency and homogeneously mixed to make it easily flow through the feeder tank. Therefore, it is essential to have a powder with similar characteristics to ZP 151. The investigation by Shakor, Sanjayan, et al.

(2017), Shakor et al. (2018) identified the cementitious powder, with characteristics similar to ZP 151, which can be used for the construction applications.

In inkjet 3DP, there are many limitations when printing objects. For example, Farzadi A. et al. (2014) discussed several limitations in 3DP such as binder selection, powder reactions, post-processing bed manipulations and depowdering. One of the major limitations in 3DP is the orientation angle, which has been discussed in the prior studies for plastic and poly-jet materials by other researchers (Dizon et al. 2018).

In the following subsections, the mechanical strength of the recommended powder (ZP 151) and the modified powder in this study cement mortar (CP) are examined and compared. Furthermore, the printed part is monitored and studied for different orientation angles. For the tensile and flexural strength tests, the highest observed and recorded results for both CP and ZP 151 are reported. In addition, Porosity, flowability, wettability, dimensional accuracy, delay printing are investigated and discussed. Finally, the conclusions of the experimental study are presented and proposed future work is discussed.

In the experimental program of powder-based 3DP technique, the following processes were conducted:

1. The powder based materials were formulated from the recommended materials by the supplier utilizing cement-based materials (cement mortar).
2. The water/cement (w/c) ratio or saturation level in the inkjet 3D printing was determined for the modified powder and compared with manual prepared modified powder.
3. The w/c or saturation level of the 3DP solid objects was optimised.

4. The medium curing and elevated temperature for the 3DP samples were optimised.
5. The delaying time between printed layers of cement mortar samples was optimised.
6. The porosity in the powder-based enveloped chamber and apparent porosity in the printed solid specimens was monitored and determined.
7. The flowability of the powder particles for the recommended materials and cement mortar materials were determined.
8. The dimensional accuracy of the cement mortar materials was identified and compared with the CAD-model sample.
9. The mechanical strength and mechanical properties for the printed cement mortar samples were measured with and without E6-glass fibre reinforcement.
10. The strongest plane (direction) in terms of mechanical strength was determined.
11. The effect of size on the printed specimens was compared and discussed.

5.1.2 Extrusion Printing Technique

Automation has contributed greatly to industrial fabrication and the economic segment of production. The construction industry has limited automation processes when compared with other industrialised sectors such as manufacturing. By developing Additive Manufacturing (AM) processes, construction companies can potentially increase revenue and productivity whilst simultaneously improving safety. There is evidence that automated machinery plays a crucial role in regulating time management and it is less costly and more eco-friendly (Buswell et al. 2005).

The extrusion printing technique consists of an extruder which extrudes cementitious slurry through a nozzle attached to a frame to print a structural member (Shakor, Renneberg, et al. 2017), refer to *Figure 5. 3*.

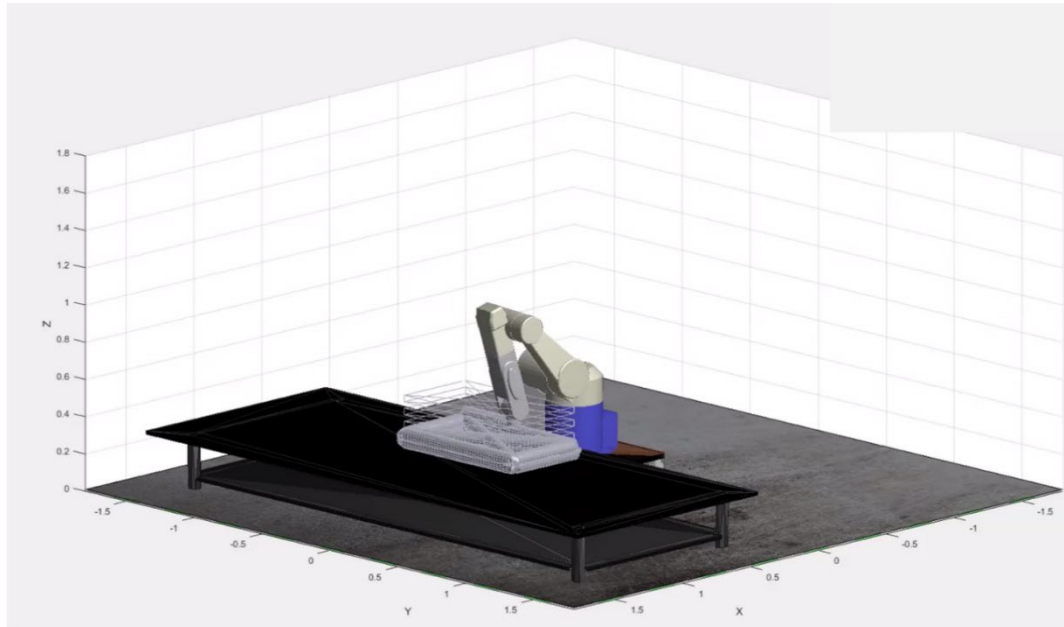


Figure 5. 3: Schematic illustration of the robotic arm movement to print a hollow-column using MATLAB software.

This study focuses on validating the optimum mix proportion which can be delivered through different delivery sources to print the cementitious slurry (refer to Appendix B). Furthermore, the most suitable type of fibre, which easily flows with slurry, was selected. The study compares the mechanical behaviours of the printed mortar with and without fibre reinforcement. In this chapter, we also discuss the optimum mix design of the cementitious material when utilising different types of fibre reinforcement. The two key findings of this section are: (a) using fibre mitigates shrinkage cracks and increases the flexural strength and buildability of the mortar; and (b), by increasing the number of layers the flexural strength reduces slightly.

In the experimental program of the extrusion-based 3DP technique, the following processes were conducted:

1. Designing and fabrication of the adapted nozzle for the extrusion-based 3DP concrete
2. Comparing the rectangular and circular nozzles in the result of the printed specimens.
3. Optimising and selection of the hose for the printed specimens
4. Optimising the used materials to print with and without the E6-glass fibre reinforced mortar.
5. Printing the prism and cubes in different layers with and without the E6-glass fibre reinforced mortar.
6. Optimising the required slump for the layer by layer printing and the time gap between the layers.
7. Regulating the speed of the pump and speed of the robot with the discharge of the slurry.

5.2 Experimental Program for the Powder-based 3D Printing

The particle size distribution of powder used in the 3D printer (Z-printer150, Z-Corporation, USA) was acquired using a particle size laser distributor (Cilas 1190). The results of the powder's particle size are shown in *Figure 5. 4*.

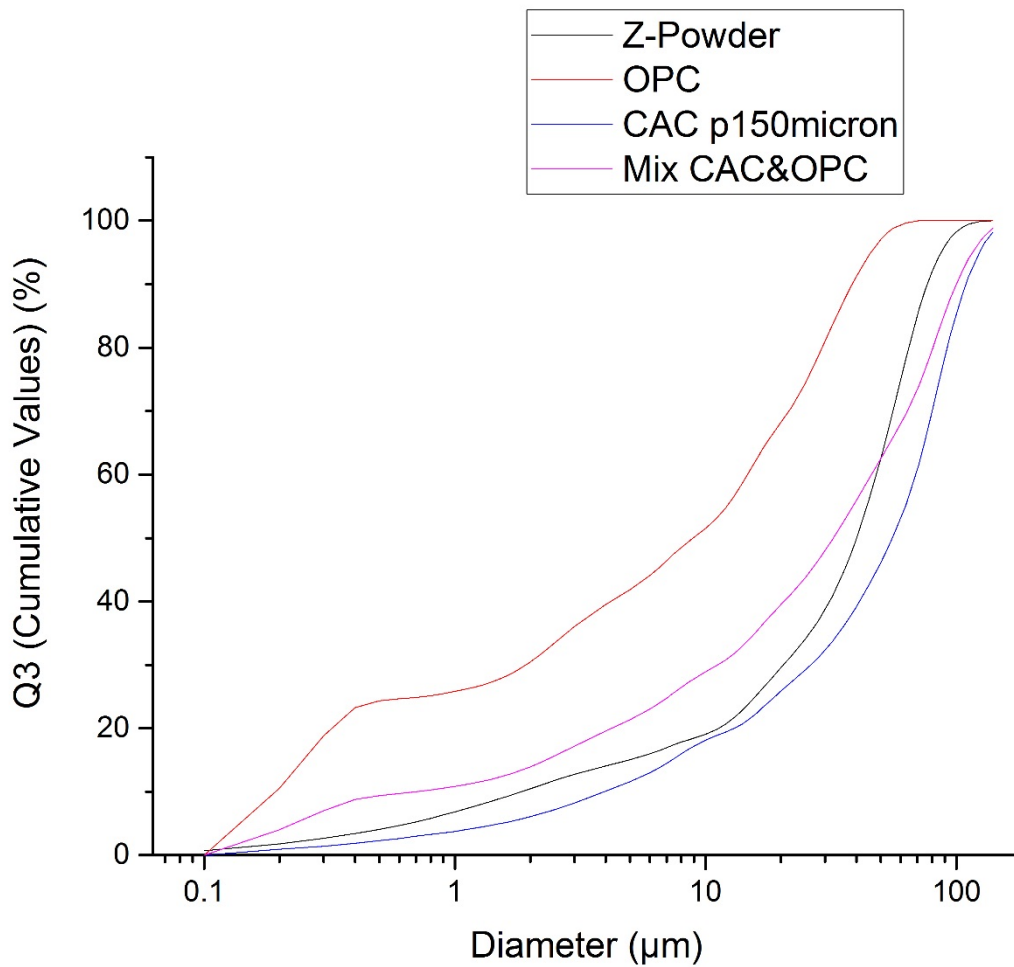


Figure 5. 4: Particle size distributions for Z-printer powder, OPC, CAC and combination of CAC & OPC.

Furthermore, the graphs can be presented logarithmically the particle size value (X-axis) versus the density distribution value (Y-axis), *Figure 5. 5*.

The homogeneity and consistency of the powder are vital factors that have to be controlled when seeking superior resolutions and results (Hiremath & Yaragal 2017). Hence, the speed of the mixer and, the time of blending are considered to be the main contributors to the homogeneity of the powder and production of better quality 3DP objects, *Figure 5. 6*.

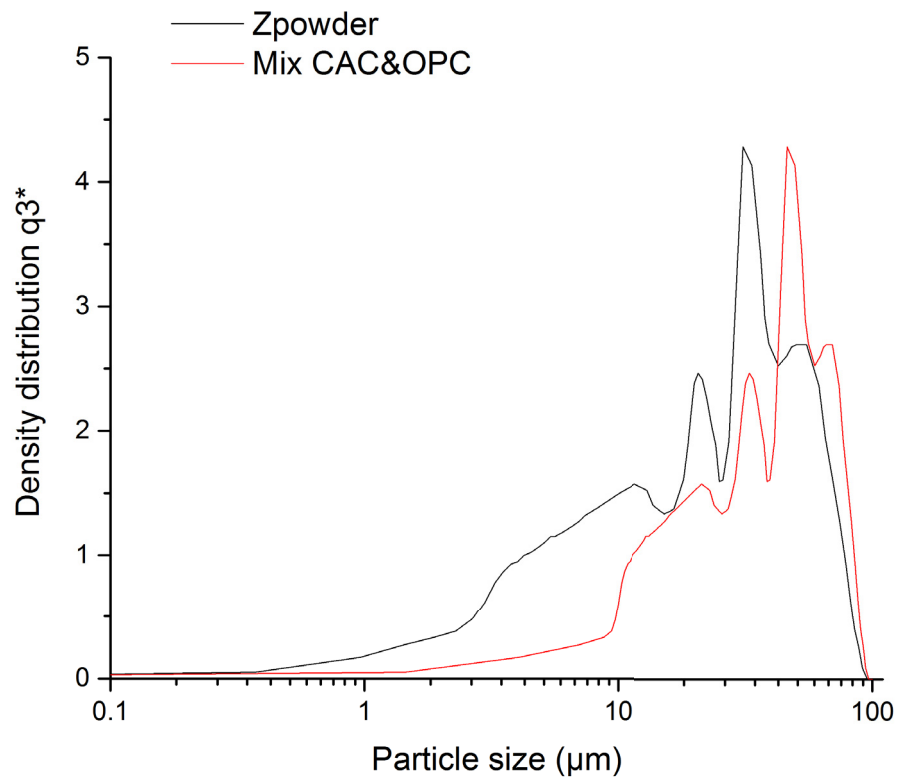


Figure 5. 5: Particle size distributions of Zpowder and CAC&OPC powder. *q3 is the unit standing for the logarithm of the percentage of total particles.

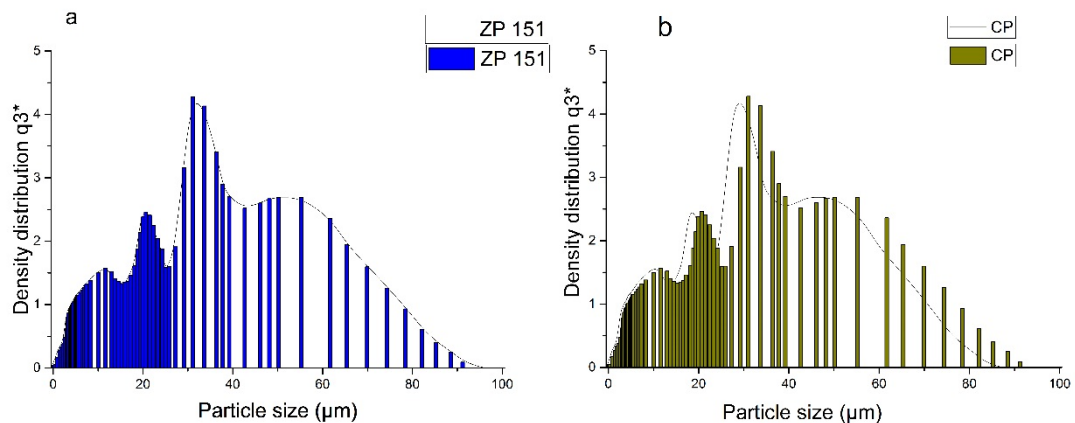


Figure 5. 6: Histogram and curve of particle size distributions of ZP 151 and CP powder. *q3 is the unit representing the density distribution of the total particles.

Figure 5. 7 shows the modified mix proportion of powder (cement mortar CP), which replaced the original powder ZP 151. The modified powder was mixed thoroughly by employing a Hobart mixer at a speed of 1450 revolutions per minute (rpm).

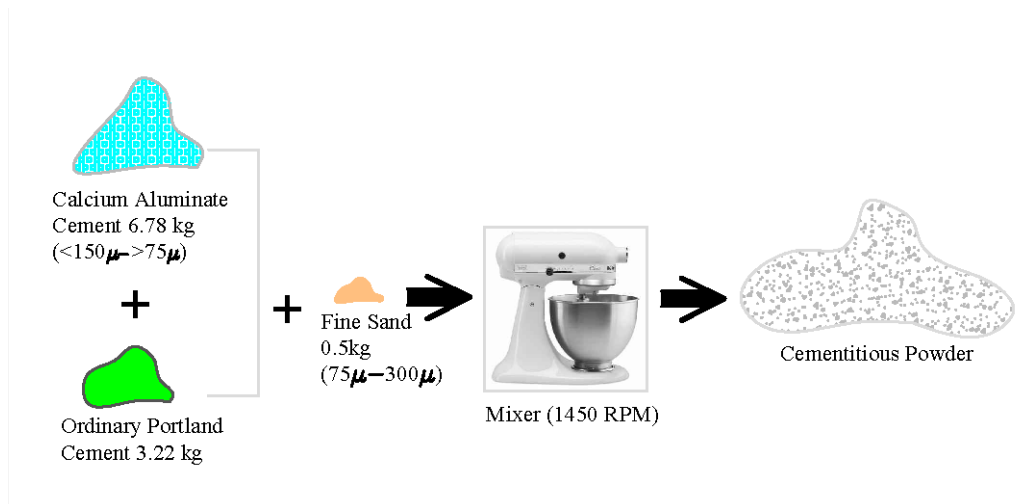


Figure 5. 7: Schematic illustration of the process for preparing cementitious powder.

The Z-printer powder consists of plaster, vinyl polymer and carbohydrate. D10, D50, and D90 values were found, these D values are representative of the mean particle sizes for 10%, 50% and 90% of the materials, respectively. Using particle size distribution (PSD) method, the particle size (D) values were 1.48, 23.07 and $70.12\mu\text{m}$, respectively. The specific surface area of Z-powder was $0.999\text{ m}^2/\text{g}$ when tested (BELSORP-max).

The two main materials used in this study were ordinary Portland cement (OPC) (Geelong cement) and calcium aluminate cement (CAC) (Ciment Fondu, Kerneos). Portland cement is a conventional cement type used worldwide, consisting of calcium, silica, alumina and iron. CAC is another type of cement comprising hydraulic calcium aluminates. It is also known as “aluminous cement”, “high-alumina cement” and, in French, “Ciment Fondu”. This type of cement is utilised in specialised applications (e.g. urgent repairs and foundation construction, a ductile iron pipe for wastewater, concrete pipes for sewerage, the petrochemicals industry and the rehabilitation of man-accessible sewer infrastructures).

Particle size distributions (PSD) for 10%, 50% and 90% of OPC are 0.19, 8.93 and $38.46\mu\text{m}$, respectively. For CAC they are passed through $150\mu\text{m}$ sieves of 3.38, 79.93 and

127.11 μm , respectively. These PSD are the most suitable distribution of particles to flow easily through the printer. The sieving of CAC is between 75 and 150 μm . The bulk particle densities for CAC and OPC are 1.23 and 0.92 g/cm^3 , respectively, while the specific surface area for the mixture of both kinds of cement is 1.021 m^2/g , tested by (BELSORP-max) as shown in *Table 5. 1*. The mixed ratio of powders contains 67.8% CAC and 32.2% OPC. For comparison purposes, 4.5% of the total mix was replaced by lithium carbonate (lithium carbonate, reagent grade, ACS) as an agent to accelerate the setting time of the cement (Lin et al. 2015). Also, it can produce rapid setting, low cost, high early strength, excellent adhesion and stability. The particle size of the ZPrinter powder has a similar size to 67%CAC and 33%OPC powders. The most widely used method to describe PSD is a “D value”. D90 values are equal to 127.11 μm for CAC and 38.46 μm for OPC powders. The surface area and bulk density of both powders are shown in *Table 5. 1*.

The surface area test for the powder specimens was performed with a multipoint surface area analyser (Microtrac BELSORP-max, USA) and the bulk density was determined according to (ASTM C29/29M 2007).

Table 5. 1 Properties of powders for starting Z-powder and CAC & OPC materials.

Powder properties	Z-powder	CAC & OPC powder 67.8 : 32.2
D10 (μm)	1.480	1.010
D50 (μm)	32.07	14.46
D90 (μm)	70.12	56.92
Bulk particle density ($\text{g}\cdot\text{cm}^{-3}$)	0.912	0.79
Specific surface area ($\text{m}^2\cdot\text{g}^{-1}$)	0.999	1.021

The CAC was sieved using 150 to 75 μm sieves and shaken for approximately 5 min. It was then blended with OPC using a Hobart mixer. Lithium carbonate was added and the mixer was operated at a rotation speed of 1450 rpm for 10 min. Since the CAC and OPC

powders have different particle size distributions (i.e. OPC is finer than CAC), these two types of cement powders were mixed to obtain one powder with a distribution of the target powder similar to that used in the ZPrinter 150 and ProJet 360.

5.2.1 Experimental Program and Curing Conditions

The specimens were made using the 3D ZPrinter 150 and ProJet 360 manufactured by Z-Corporation and 3DSYSTEMS with an HP11 (4810A) nozzle. The 3D printer consists of a build bin and a feed bin. The 3D samples are constructed in the build chamber (bin) and a roller mounted together with the print head on the gantry spreads the powder to create the 3D samples layer by layer. The feed bin is filled entirely with powder. The print nozzle moves and applies the binder onto the powder at specific locations to make the specimens layer-by-layer to create the sample. The container of a 3D printer is filled with the mixed CAC and OPC powders. The roller spreads a new layer on the bedded layers in the build bin with powders from the feed bin. The build bin moves downward the thickness of one layer so that the new layer can be constructed. When the layer is fully spread, the nozzle release the liquid to form a new layer. These actions are repeated until the sample is completely constructed.

In the 3D printing process, there are three axes along which the printer prints the samples, as displayed in *Figure 5. 8*. Feng et al. (2015) stated that the X-axis is the direction the nozzle moves to drop the binder onto the powder. The Y-axis, perpendicular to the X and Z axes, is the vertical direction, as shown in *Figure 5. 8*.

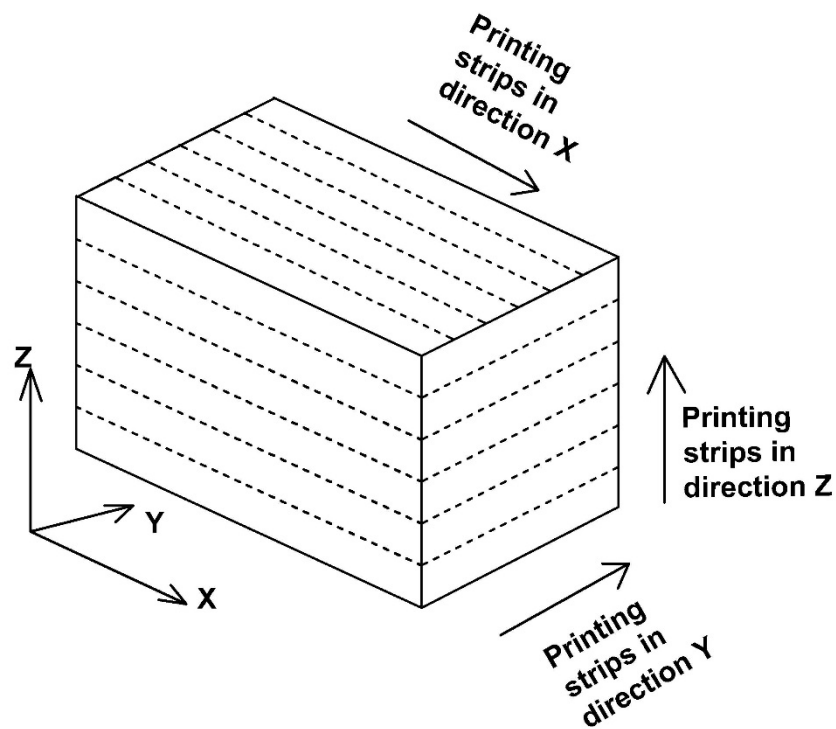


Figure 5. 8: Directional depiction of the 3D printing process.

This printing technique used various temperatures for curing (at 40°C, 60°C, 80°C, 90°C and 100°C). Curing at elevated temperatures was applied using various processes, for example, using only tap water, using tap water and then drying in an oven, or drying in an oven and then adding tap water before drying in the oven again, *Figure 5. 9*.

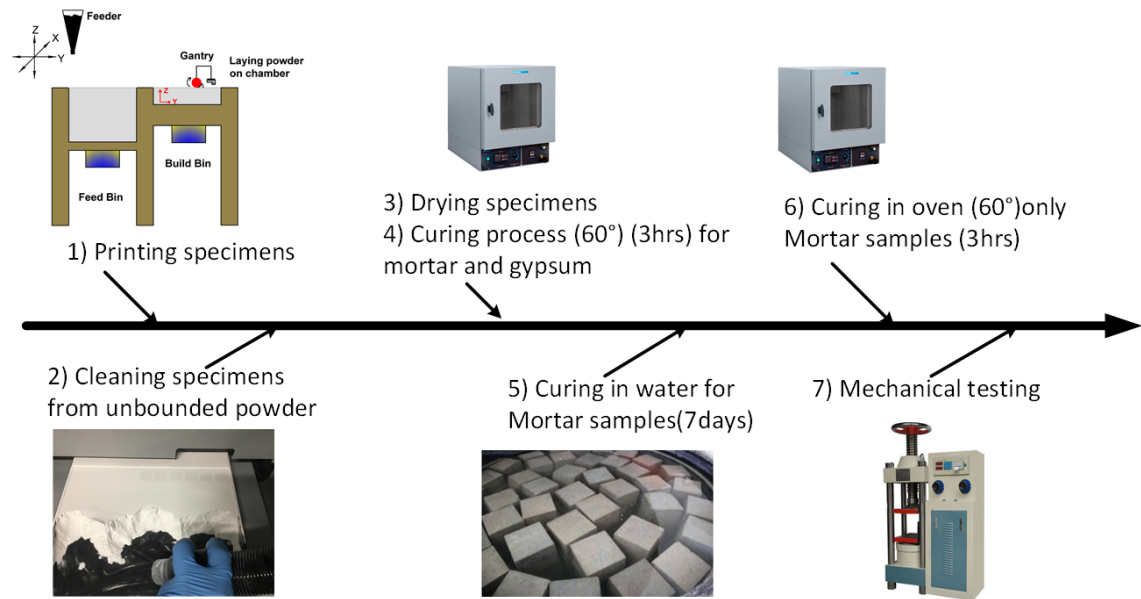


Figure 5. 9: Schematic diagram of the 3D printing process and curing process.

5.2.1.1 Compressive Strength Test

Initially, cubic specimens with the dimensions of (20×20×20)mm were fabricated to measure their compressive strength and determine the PSD of the 3D printed powders. Samples were prepared in three primary batches: 1) CAC and OPC with lithium carbonate produced by the 3D printer; 2) CAC and OPC without lithium carbonate produced by the 3D printer, and 3) CAC and OPC with lithium carbonate produced manually (hand mixing) (see *Table 5. 2*). Hand mixing is the manual combination of precisely measured components with water. In ZPrinter150 and ProJet 360 3D printers, the maximum saturation level for the shell and core are 170% and 340%, respectively.

Table 5. 2 Numbers of 3DP cubic specimens at different saturation levels with lithium carbonate (Li_2CO_3).

Sample designation	Saturation level (%)		No. of samples	Cementitious mixture	Curing condition	Weight (g) /cubic
	Shell	Core				
S75-C75-LC	75	75	2	CAC,OPC, Li_2CO_3	$\text{Ca}(\text{OH})_2$ and water	<9.0
S75-C75-OW	75	75	1	CAC,OPC	Water	
S100-C100-ZN	100	100	1	Zpowder	Not cured	9.2
S100-C100-LC	100	100	2	CAC,OPC, Li_2CO_3	$\text{Ca}(\text{OH})_2$ and water	
S100-C100-OW	100	100	1	CAC,OPC	Water	
S125-C125-LW	125	125	1	CAC,OPC, Li_2CO_3	Water	9.7
S125-C125-OW	125	125	1	CAC,OPC	Water	
S150-C150-LW	150	150	1	CAC,OPC, Li_2CO_3	Water	10
S150-C150-OW	150	150	1	CAC,OPC	Water	
S170-C170-LC	170	170	2	CAC,OPC, Li_2CO_3	$\text{Ca}(\text{OH})_2$ and water	10.9
S170-C170-OW	170	170	1	CAC,OPC	Water	
S75-C150-LW	75	150	1	CAC,OPC, Li_2CO_3	Water	9
S75-C150-OW	75	150	1	CAC,OPC	Water	
S100-C200-LW	100	200	1	CAC,OPC, Li_2CO_3	Water	9.5
S100-C200-OW	100	200	1	CAC,OPC	Water	
S125-C250-LC	125	250	2	CAC,OPC, Li_2CO_3	$\text{Ca}(\text{OH})_2$ and water	10.89
S125-C250-OW	125	250	1	CAC,OPC	Water	
S150-C300-LW	150	300	1	CAC,OPC, Li_2CO_3	Water	11.81
S150-C300-OW	150	300	1	CAC,OPC	Water	
S170-C340-LW	170	340	1	CAC,OPC, Li_2CO_3	Water	12.62
S170-C340-OW	170	340	1	CAC,OPC	Water	

Therefore, the saturation levels using the shell were between 75% and 170%, and for the core between 150% and 340%, *Figure 5. 10*.

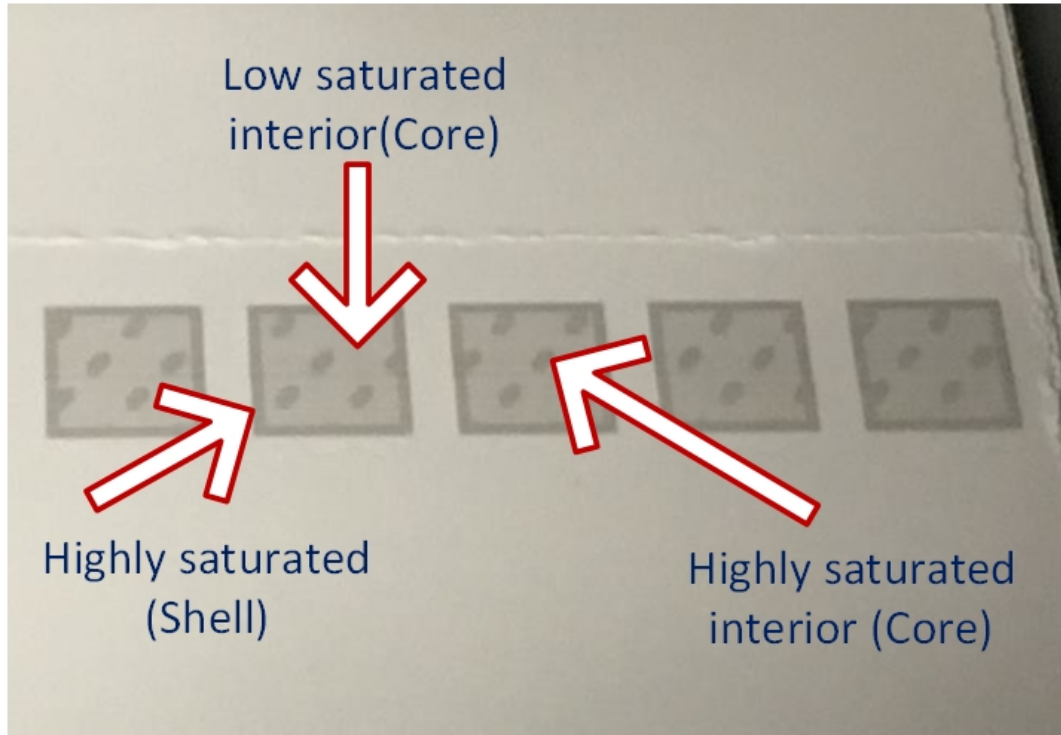


Figure 5. 10: Interior (core) and exterior (shell) for same saturation levels in 3DP sample.

The cubic samples were tested perpendicular to the X-axis and parallel to the Z-axis for different ages and curing saturations. The samples were tested as a green part, meaning that the cubic sample was taken directly from the 3D printer without curing (see *Figure 5. 11*). Following the above-mentioned procedure, samples were cured in water at room temperature for 1, 7 and 28 days. Other samples were cured in water which contained 2% $\text{Ca}(\text{OH})_2$ (calcium hydroxide).



Figure 5. 11: Morphology surface of cubic specimens (left) (Olympus BX61 Microscope-10×) and samples of CAC, OPC with Li_2CO_3 prepared by 3D printing (right).

The water/cement (w/c) ratio was determined on the basis of the binder/powder mass ratio (M_b/M_p) which is available in 3D printer software (Equation (5.1)) with the results shown in Table 5. 3.

$$\frac{M_b}{M_p} = \frac{\rho_b \cdot V_b}{\rho_p \cdot V_p} \quad (5.1)$$

Where M_b and M_p are the mass of binder and powder, respectively; ρ_b and ρ_p are the density of binder and powder, respectively; and V_b and V_p are the volumes of binder and powder, respectively.

Table 5. 3 The different levels of saturation converted into w/c ratio.

Saturation level	Binder/Volume Ratio		w/c ratio
	Shell(S)	Core(C)	
S100-C200	0.244	0.244	0.310
S125-C250	0.305	0.305	0.385
S150-C300	0.366	0.366	0.460
S170-C340	0.415	0.415	0.520
S100-C100	0.244	0.122	-
S125-C125	0.305	0.152	-
S150-C150	0.366	0.183	-
S170-C170	0.415	0.207	-

This test comprised 29 samples in three batches. The first two batches were created using 3D printer and the third batch was manually mixed. There were massive differences between the hand-mixed and 3D printed specimens due to the way the samples were formed. The compressive strength of samples utilised 3D produced batches was weaker than the manually mixed cementitious samples, which also had higher porosity.

Then, powder preparation was modified by adding fine sand into the mix to become mortar. The samples were fabricated by mixing CAC (6.78 kg), OPC (3.22 kg), fine sand (0.5 kg) and lithium carbonate (0.45 kg), which comprised the total weight of the powder. Two types of cement, calcium aluminate cement ($\text{Al}_2\text{O}_3 \geq 37\%$, $\text{CaO} \leq 39.8\%$, $\text{SiO}_2 \leq 6\%$, $\text{Fe}_2\text{O}_3 \leq 18.5\%$), ordinary Portland cement conforming to the Australian Standard, AS 3972 general purpose type (C_3S , $\text{C}_2\text{S} > 70\%$, $\text{C}_3\text{A} > 4\%$, $\text{C}_4\text{AF} > 10\%$) and fine sand ($\text{SiO}_2 > 90\%$, Australia - maximum size of approximately 300 μm), were used to create a total of fifty-four specimens for the compressive tests (see *Table 5. 4*).

Table 5. 4 Details of the 3D-printed specimens for compressive strength

Specimens	CAD dimensions (mm)	Curing method	Number of samples		
			1 Day	7 Days	28 Days
Green Part	(20×20×20)	—	3	3	3
S100C200	(20×20×20)	water	3	3	3
S125C250	(20×20×20)	water	3	3	3
S150C300	(20×20×20)	water	3	3	3
S170C340	(20×20×20)	water & $\text{Ca}(\text{OH})_2$	0	9	9

Lithium carbonate (Li_2CO_3) (American Chemical Society reagent grade) was mixed to accelerate the setting time of the mortar. The prepared specimens were divided into two batches of fifty-four samples for the compressive strength test, with the data for each being shown as an average (\pm corresponding standard deviation). For each test, 3 specimens were printed, being the minimum requirements for making and curing samples according to the Australian standard (AS1012.8.3 2015). The mixture ratio used was

closest to the ZPrinter powder. The ZPrinter powder is the recommended powder that is supplied by the Zcorp for the ZPrinter® 150 (Inkjet 3DP). In the present study, the Zpowder was compared with the cement mortar (modified powder). It should be noted that the ZPrinter powder was chiefly calcium sulfate hemihydrate ($\text{CaSO}_4 \cdot 0.5\text{H}_2\text{O}$), also known as plaster of Paris (Zhou et al. 2013). The ZPrinter powder® 150 was used for the delicate models. The powder was a combination of carbohydrate (<10%), vinyl polymer (<20%) and plaster (<90%) which was applied without further sieving.

All powder samples were measured three times to determine the D10, D50 and D90 values, meaning that 10%, 50% and 90% of the particles were small than those sizes. A layer thickness of approximately 0.1mm was set as the default for the 3D printer, thus determining the thickness of each layer when being spread by the roller (see *Figure 5.12*).

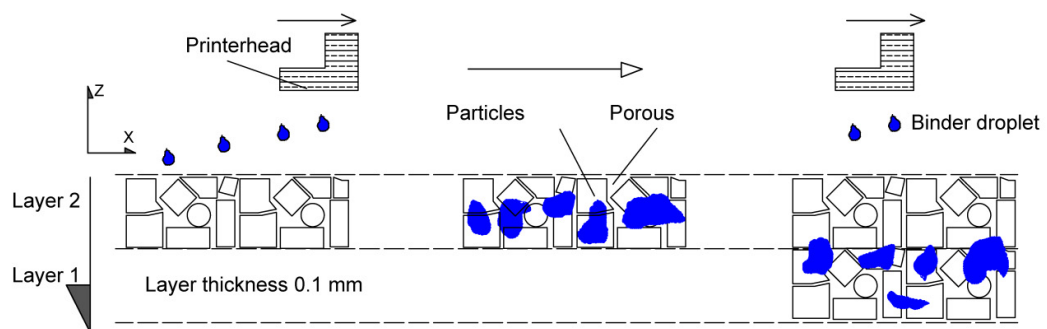


Figure 5.12 Layer explanation and powder/binder interaction between layers.

A fluid solvent (Zb® 63) was utilised as an adhesive during the 3DP process. The binder was a clear liquid solution with a viscosity close to pure water. The formation of the binder was 2-Pyrrolidone with mostly water (Farzadi et al. 2014).

The inkjet 3DP (ZPrinter® 150) could be adjusted only for different saturation levels (binder/volume ratio) or the w/c ratio. Recently, new ZCorp products have made it possible to adjust the sample thickness layers in addition to saturation levels. The thickness and saturation levels of the specimens had a significant effect on the porosity and stability of the samples' green parts. The appropriate time to remove a green part from the unbounded powder depends on the duration of drying in the powder bed and saturation levels. The green part (uncured object) can be defined when a binder (liquid) is added to the powder and reacts to build a printed scaffold (Gibbons et al. 2010). In addition, evaporation of the printing liquid plays a crucial role. The saturation levels of the printer can be adjusted according to the outer and inner scaffold, which are known as the shell and core, respectively. The ratio of binder to powder materials influences the degree of unification and consolidation. In addition, the layer thickness determines the infiltration and final resolution of the printing liquid. The saturation levels are presented in *Table 5. 5*.

Table 5. 5 Description of the saturation levels, consumed binder and time taken to build a cubic (20×20×20)mm sample

Sample Name	Sample Description	Binder/Volume ratio	Binder (mL)	Duration (minute)
S100C200	Shell: 100, Core:200	0.244	3.24	8.55
S125S250	Shell: 125, Core:250	0.305	3.74	8.66
S150C300	Shell: 150, Core:300	0.366	4.24	8.88
S170C340	Shell: 170, Core:340	0.415	4.66	9.00

Lee et al. (2007) studied the compressive strength values in different Rapid Prototyping (RP) machines. Fused deposition modelling (FDM) and the inkjet 3DP were assumed to be rapid prototype machines. Anisotropic characteristics were revealed in the compressive strength results of the specimens.

According to Lin et al. (2015), the extrusion 3DP samples could achieve a compressive strength of approximately 10-20 MPa after 2 hours and approximately 50-60 MPa after

28 days. The setting time of concrete was between 20 and 60 minutes after using lithium carbonate as an accelerator. However, the main differences observed in powder-based printer samples, compared with extrusion printing, were the saturation levels for the core and shell of the structure. Szucs & Brabazon (2009) claimed that an increase in the saturation level of printed samples could improve the mechanical properties of the structure. Based on the same study, the stiffness and compressive strength of the 3DP samples rise at higher sintering temperature. Furthermore, sintering can reduce the specific surface area and increase the porosity of the sample. Szucs & Brabazon (2009) discovered that the mechanical properties achieved were still not sufficient for load-bearing applications. In this study, to harden the powder for the cubic samples, a higher saturation level was utilised to produce a 3DP part. It was expected that the customised powder would be stronger than the commercially available powder.

From the literature review, it is evident that existing research recognised the critical role played by layer thickness and binder saturation level. For instance, Lu & Reynolds (2008) created a complex shape from TiNiHf Shape Memory Alloy (SMA). They found that a printed sample with a particle diameter of 35 μ m and a 170% binder saturation level had the highest structural mesh integrity. In general, a printing layer thickness of 35 μ m and binder saturation level of 170% were found to be the optimum requirements when printing samples using a TiNiHf 3D mesh scaffold.

The curing process and curing conditions are also important aspects of 3DP for construction applications. The final process of printing is post-hardening. Post-hardening in 3DP has three alternatives: wax, Z-bond™CynoAcrylate and ZMax™epoxy. These could be applied as a dip, drizzle and spray, respectively. However, there are different processes for curing the cementitious powder. In this study, water was used. Some

samples were cured with 5% calcium hydroxide ($\text{Ca}(\text{OH})_2$) dissolved in the total weight of water. *Table 5. 6* summarises the dimensions and weight of the S170C340 sample in the different curing scenarios using water and 5% calcium hydroxide. As shown in *Table 5. 6*, the specimens in water increase their dimensions when they were cured for 7 days and 28 days. Specifically, if a sample was cured in water with 5% calcium hydroxide after drying in an oven for approximately an hour at 40°C , the original dimensions changed by 2 ± 0.22 mm, which means the dimensional rate increased by 6%. According to the study of Pfister et al. (2004), when comparing 3D Bioplotting with 3DP, the maximum elongation was found to be four-times greater and the maximum flexural strength was three-times greater. The swelling of the 3D Bioplotting (to print biological organs) matrix was 14% less than in 3DP using water. In another study, Seitz et al. (2005) used hydroxyapatite (HA) powder to fabricate 3D-printed specimens. They found that the printed parameter dimensions were 3% smaller than the dimensions of the CAD model.

Table 5. 6 Curing method of S170C340 in water and 5% of $\text{Ca}(\text{OH})_2$ after drying at 40°C in an oven

Sample description	Curing method	Dimensions (mm)		Weight (g)	
		7 Days	28 Days	7 Days	28 Days
S170 C340	Water(40°C)	(20.94 × 20.64)	(21.53 × 22.07)	15.85	16.55
	Water & 5% $\text{Ca}(\text{OH})_2$ (40°C)	(22.37 × 22.19)	(22.05 × 22.1)	16.60	16.85
	Green parts	(21.12 × 20.83)		12.64	

One of the common factors that can be used to assess the durability of the concrete and mortar is compressive strength (ASTMC39 2001). Thus, the compressive strength test was performed for the 3DP samples according to the ASTM standard (ASTMC39 2001). The specimens for the compressive strength test were prepared at different orientational angles because changing the orientation and the directional axis is a much easier process than conventional casting. Therefore, a total of 30 samples were tested, including 3

samples for each of the orientation angles. The speed rate of the loading in the test was 0.833kN/s.

Figure 5. 13 shows the cubic samples printed in different orientation angles, Figure 5. 13 (a). They were printed at (0° , 30° , 37.5° , 45°). The figure also shows the orientation angle of prepared specimens with regard to the X, Y and Z planes in the 3DSystems software, Figure 5. 13 (b). A mould ($20 \times 20 \times 20$)mm was used for casting the comparison samples. All the samples for compressive and flexural strength tests were prepared using a similar process. These samples in Figure 5. 13 was tested only in the XZ plane.

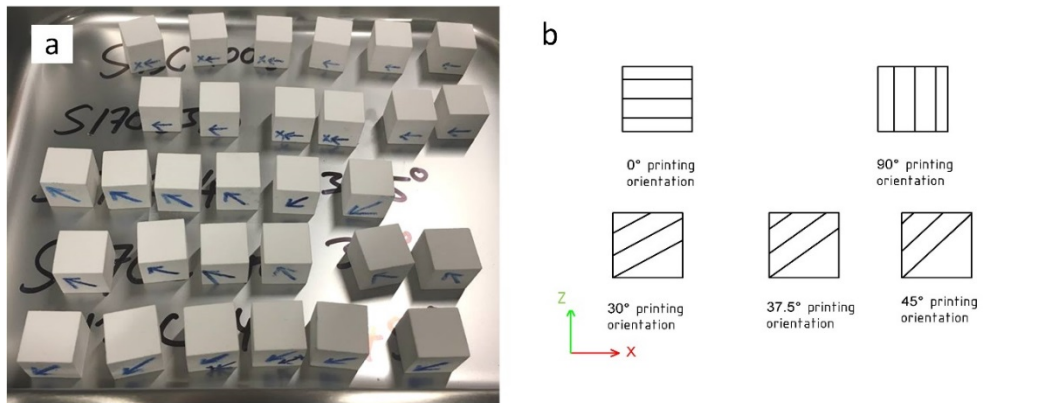


Figure 5. 13: (a) Real-world 3DP cubes in (0° , 30° , 37.7° , 45° , 90°) orientation (b) CAD file of 3DP cubes in (0° , 30° , 37.7° , 45° , 90°).

The orientation angles in 3DP can be used in inkjet printing to create different geometries, optimise the mechanical strength of structural parts, and optimise the number of layers to print an object.

Next, samples were printed in the presence and absence of glass fibre and were cured at five different temperatures (40, 60, 80, 90, 100) $^\circ$ C for 7 and 28 days. The samples were then cured in tap water. They were again dried in an oven at the same corresponding temperatures. Samples with dimensions of ($20 \times 20 \times 20$)mm and ($50 \times 50 \times 50$)mm were prepared for the compressive strength test. Samples with dimensions of ($160 \times 40 \times 40$)mm

were prepared for the flexural strength test. Six samples were prepared for each test, *Table 5. 7*.

Table 5. 7 Detailed number and dimension of samples

Sample description	CAD dimension (mm)	Printed direction plane
Compressive strength test	(20×20×20)	XY, XZ, YZ
Compressive strength test	(50×50×50)	XY, XZ, YZ
Flexural strength test	(160×40×40)	XZ

The glass fibre used in the printing fabrication was E6-glass fibre (high-performance E6 enhanced glass fibre). *Table 5. 8* describes the physical properties of the glass fibre.

Table 5. 8 Physical properties of chopped strand E6-glass fibre

Fibre type	Length (mm)	Thickness (µm)	Filament diameter (mm)	Specific gravity (g/cm ³)	Tensile strength (MPa)	Tensile modulus (GPa)	Expansion coefficient (10 ⁻⁶ K ⁻¹)
E6-Glass fibre (Trojan)	6 ±1	100	13±1	2.62-2.63	2500-2700	81	6

5.2.1.2 Flexural Strength Test

The specimens for the flexural strength test were sketched using SolidWorks software (2015 Edition) for printing using inkjet 3DP (56 samples). In *Figure 5. 14* and *Figure 5. 16*, the cubic samples with dimensions of (20×20×20)mm and two prism specimens with dimensions of (60×5×5)mm and (70×10×4)mm, are shown.

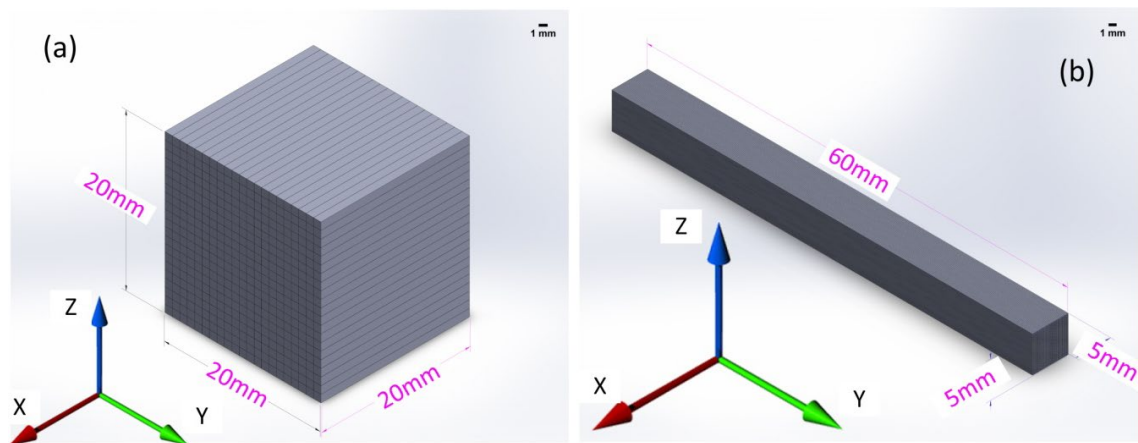


Figure 5. 14: (a) cubic specimens (20×20×20mm), (b) prism specimens (60×5×5mm).

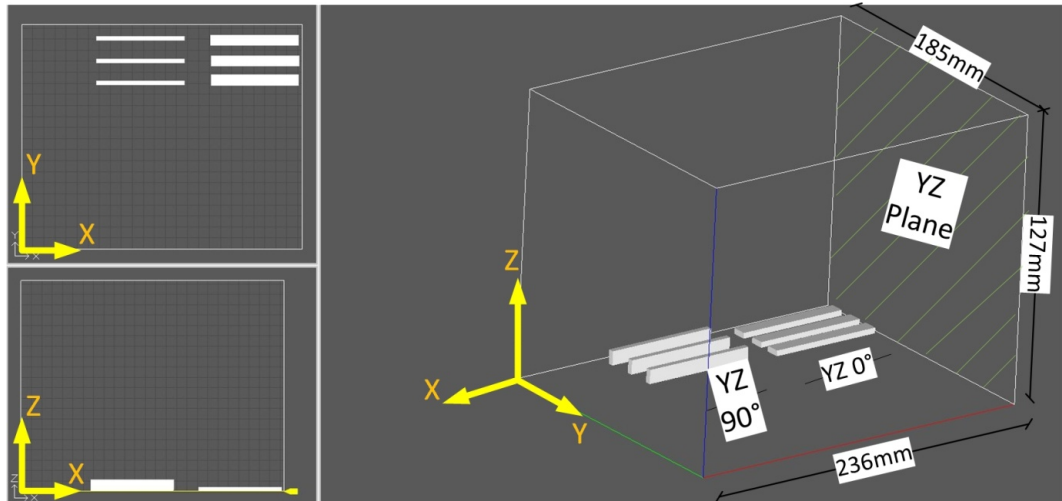


Figure 5. 15: Different planes in the 3DP software for each axis (X, Y, Z), the prism($70 \times 10 \times 4$ mm) presented in the plane of YZ 0° and YZ 90° .

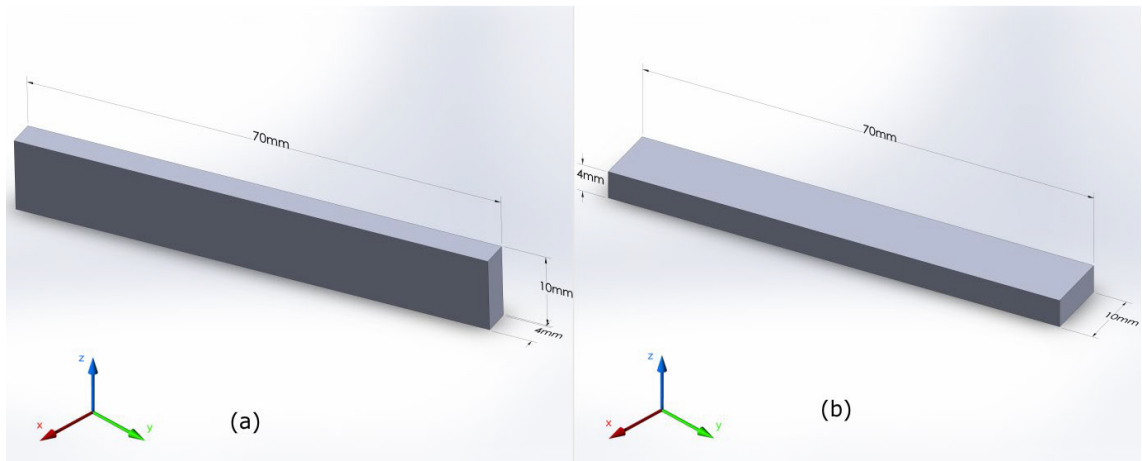


Figure 5. 16: (a)-prism specimen ($70 \times 10 \times 4$ mm) (YZ 90°) degrees, (b)-prism specimen ($70 \times 10 \times 4$ mm) (YZ 0°) degrees.

Table 5. 9 presents the flexural strength of specimens with dimensions of ($60 \times 5 \times 5$)mm.

Table 5. 10 presents the flexural strength details of specimens with dimensions of ($70 \times 10 \times 4$)mm.

Table 5. 9 Details of the 3D-printed & manual mix specimens (60×5×5mm) for flexural strength

Specimens	CAD dimension (mm)	Printed direction	Number of samples	
			7 Days	28 Days
S100C200	(60×5×5)	X,Y,Z	1	3
S125C250	(60×5×5)	X,Y,Z	1	3
S150C300	(60×5×5)	X,Y,Z	1	3
S170C340	(60×5×5)	X,Y,Z	1	3
S100C200	(60×5×5)	Manual mix	1	1
S125C250	(60×5×5)	Manual mix	1	1
S150C300	(60×5×5)	Manual mix	1	1
S170C340	(60×5×5)	Manual mix	1	1

Other specimens, with dimensions of (70×10×4)mm, were also fabricated for flexural strength at the same saturation levels of shell and core (see *Figure 6. 16*). They were printed in two orientation degrees in the YZ plane when (i)-YZ 0° (width of scaffold parallel to X-direction of the printer) and (ii)-YZ 90° when it was rotated 90° (thickness of scaffold parallel to X-direction), see *Table 5. 10* and *Table 5. 11* for more details.

Table 5. 10: Details of the 3D-printed specimens (70×10×4mm) for flexural strength

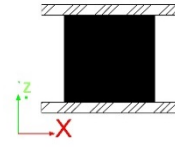
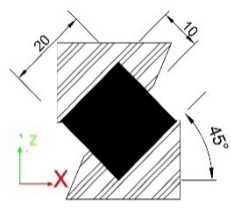


Specimens	CAD dimensions (mm)	Printed sample in YZ plane		Number of samples in (YZ 0,90°) directions	
		YZ 0°	YZ 90°	7 Days	28 Days
S100C200	(70×10×4)	YZ 0°	YZ 90°	2	6
S125C250	(70×10×4)	YZ 0°	YZ 90°	2	6
S150C300	(70×10×4)	YZ 0°	YZ 90°	2	6
S170C340	(70×10×4)	YZ 0°	YZ 90°	2	6

An HP11 cartridge was used as a print head by the ZPrinter®150 with a surface tension of 45 dynes/cm and viscosity of 1.35 cP, similar to the work conducted by (Utela et al. 2008). *Figure 5. 15* illustrates the different planes and directions of the printed samples for the flexural strength test.

Similar to the tests of compressive strength, specimens for the flexural strength test were prepared at different orientational angles. A total of 36 samples were printed using the

manual mix, including 3 samples prepared for each orientation angle. The speed rate of the loading in the test was 426 N/min according to the ASTM standard (ASTMC293/C293M 2002). *Table 5. 11* shows the details of all different printed samples.

Table 5. 11 Tests with respect to the number of samples, dimensions and building orientations.

Tests	No. of Samples	Dimensions (mm)	CAD Drawing
Compression test	30	20×20×20	
Shear test	30	20×20×20	
Three-point bending test (flexural strength)	36	167×17×7	
Tensile test	36	205×30×6.5	

Then, samples were prepared for flexural strength with dimensions of (160×40×40)mm, six samples were selected for each test, *Table 5. 7*. These samples were both printed with 1% E-glass fibre and without E-glass fibre, *Figure 5. 17*.

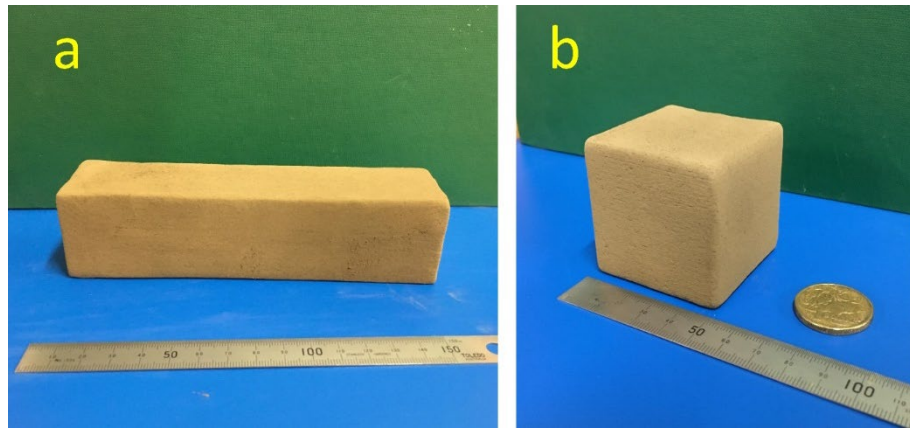


Figure 5. 17: (a) Green part of 3DP cement mortar prism, (b) Green part of 3DP cement mortar cube.

5.2.1.3 Tensile Strength Test

The specimens for the tensile strength test were prepared according to ASTM type III (ASTM:D638 2014). There were 36 samples for the tensile test. For each of the orientation angles, 3 samples were prepared, see *Table 5. 11*. The speed rate of the loading in the test was 426 N/min.

5.2.1.4 Shear Strength Test

The samples were placed between the two loading plates to test shear resistance. The upper and lower boundaries were unrestrained in the horizontal trend, in a similar manner to that in the study by (Cao et al. 2018). The displacement loading rate was fixed at 0.2mm/min. *Figure 5. 18* shows how the samples were positioned between two inclined die blocks at 45° relative to the horizontal direction. All specimens were loaded until they reached failure, and the load-displacement diagram was plotted and recorded through data collection equipment. The compression samples were tested with a uniaxial testing loading machine.

There were 30 samples for the shear test. For each of the orientation angles, 3 samples were prepared.

The shear stress, (τ) along the surface of the specimens can be found using Equation (5.2);

$$\tau = \frac{Q}{S} = \frac{P}{S}(\sin\beta - f\cos\beta) \quad (5.2)$$

Where Q is the normal shear force, S is the shear area, which is equal to the cross-sectional area of the specimen. P is the axial force on the specimen and f is the friction coefficient between the shear case and the shear load platform. In this investigation, the friction coefficient (f) was zero, as the shear case was directly connected to the load platform. Finally, β is the shear angle, which was 45° .

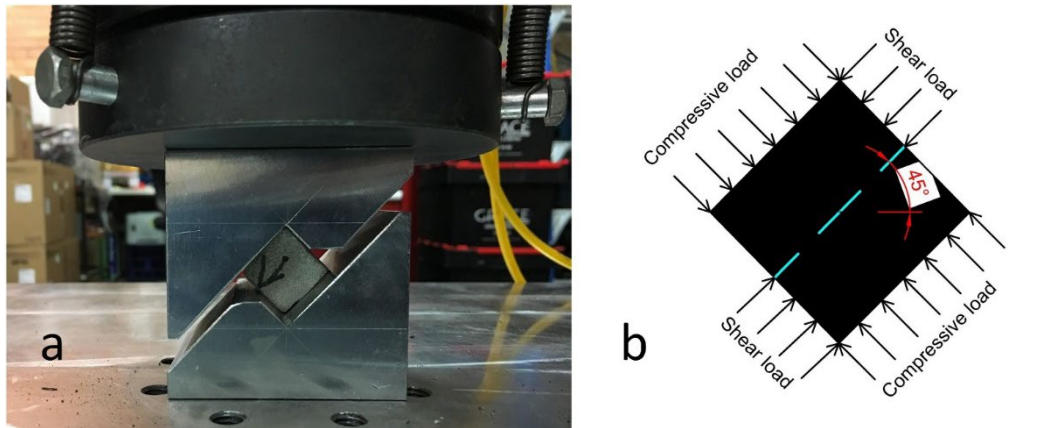


Figure 5. 18: a) Loading layout in X-axis (0° orientation) on the CP sample; b) Experimental principle for setting up the specimens and applying the load.

5.2.1.5 Porosity Test

Apparent Porosity tests were conducted on the samples shown in *Table 5. 12* according to the Australian Standard (AS1774.5:2014 2014). The tests were conducted in vitro for cubic samples. The samples were dried in an oven (Vtech, XU 225) at $110\pm 5^\circ\text{C}$ for approximately 2 hours and left to cool down to room temperature. Sample weight at this stage is designated as dry weight (m_1). Samples were then inserted into a porosity and bulk density tester (XQK-03) and the air was sucked inside the tester for approximately 10 min. Water was later poured into the bucket until the water covered the samples by approximately 5 cm. There was a waiting period of 10 min to ensure that the samples

were completely saturated by water. The weight of the samples in soaked water was then measured on the scale (m_2), followed by rolling the four sides of the samples on the damp cloth and measuring again (m_3). From this, the apparent porosity of cubic samples was calculated using Equation (5.3):

$$P_a = \frac{m_3 - m_1}{m_3 - m_2} \times 100 \quad (5.3)$$




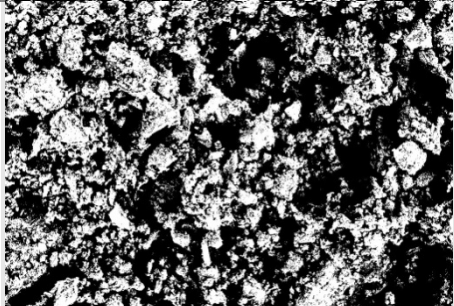
The obtained SEM images were analysed by Image J software and then compared with the porosity test conducted in the laboratory (see *Table 5. 12*).

There were some differences. Analysis using Image J was not precise due to SEM focusing on a specific area in the cubic samples. It does not, therefore, represent the whole sample. The difference between the analysed images using Image J software, and the test at vitro, was approximately (3-10)%.

The tests were prepared using the Accupyc II (gas pycnometer) to measure true density. True density (ρ_{true}) and bulk density (ρ_{bulk}) of the powders was measured according to Australian Standards (AS1774.6-2001(R2013) 2013) and Australian Standard (AS1774.2-2001(R2013) 2013), respectively. Equation (5.4) was used to calculate the powder-bed porosity in the build bin of the printer;

$$P_{\text{bed}} = 1 - \frac{\rho_{\text{bed}}}{\rho_{\text{true}}} \times 100\% \quad (5.4)$$

Table 5. 12 Porosity with different saturation levels of CAC & OPC without Li_2CO_3 analysed using Image J.

Sample Name	Porosity %	Image J analyse
S100-C200	66.37	
S125-C250	65.15	
S150-C300	63.64	
S170-C340	62.29	

In-process-bed-density (ρ_{bed}) that was suggested by (Zhou et al. 2014) measures the density when the powder particles are embedded in the build chamber. To ensure high-quality printing it is vital to have a high-quality inkjet 3DP process.

5.2.1.6 Flowability Test

Powder flowability can be defined as the ability of the powder to movement. It is measured by ranking the flowability (from flow to nonflow) (Prescott & Barnum 2000). A previous study by Utela et al. (2008) indicated that the most important property of 3DP is the shape and size of particles. Therefore, the 3DP powder can be released in either a wet or dry state. In the wet or dry state, a particle size smaller than 5 μm can be deposited through the feeder container's holes, but in the dry state, it is preferable that particles are larger than 20 μm . Asadi-Eydivand et al. (2016) stated that ZP150 powder D10, D50, and D90 particle size distributions are 0.64, 27.36 and 68.83 μm , respectively. D10, D50 and D90 represent the range (diameter of particles) and a midpoint of the particle size that is based on sieve analysis results which calculate the represent for 10%, 50% and 90% of the mass, respectively.

To deposit the powder in the build chamber, enough powder must be packed in the bed so that it is homogeneously spread through the build chamber. Powder flowability is the most important factor in this procedure to ensure an adequate spread over the feeder and build chamber. Major factors that influence the flowability include particle size, the surface area of the powder, surface roughness and the printed layer thickness. Using Jenike's method (Jenike 1964), this experiment used the powder flowability test, with confirmation of the test involving the use of the feeder tank of the printer as a flowing test machine.

5.2.1.7 Wettability Test

Wettability is measured by the contact angle, which is the angle between the solid surface and the liquid drop, whereas a fluid/liquid touches a solid surface. Wettability could be quantified for a solid surface and a fluid using Young's equation (Lander et al. 1993).

This test was conducted using two different methods. One used the contact angle goniometer method, while the other used a high-resolution camera to investigate the penetration time of the drop of liquid on the powder bed of the printer. *Figure 5. 19* shows how the contact angle goniometer KSV CAM200 was used for this investigation, to capture image frames of each test at a rate of 60 frames/s. In *Figure 5. 20*, the second approach used a high-speed video recorder, operating at 240 frames/s, to capture images of the path a single binder droplet as it penetrated the powder bed. For each of the powders and methods, the test was replicated three times.

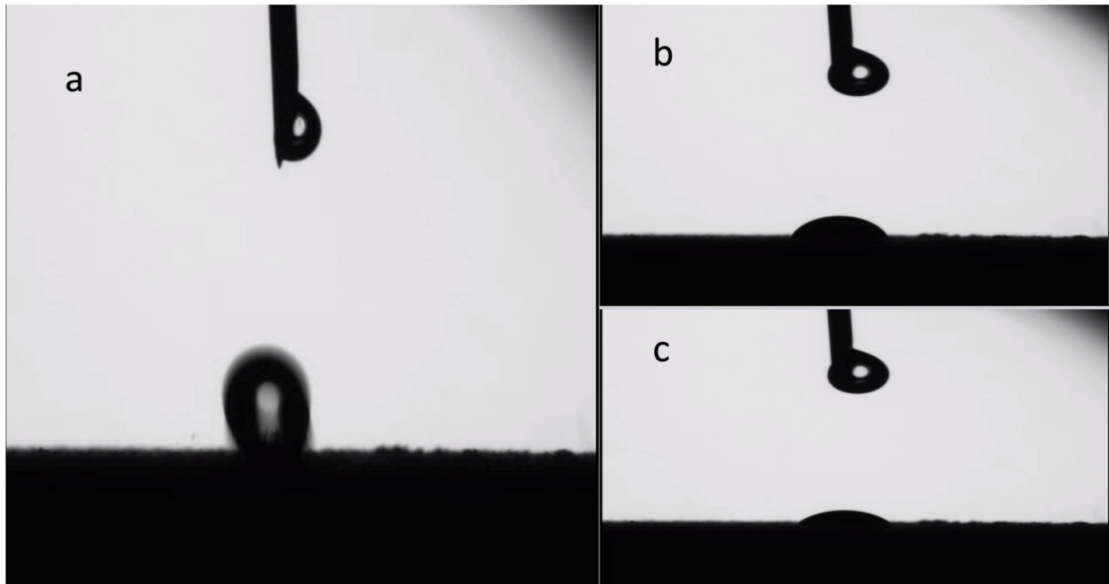


Figure 5. 19: Steps of the penetration of Zb63 liquid into Zpowder, (a) impact time of droplet on the surface of the powder, (b) penetration process of liquid on the powder after 16 seconds, (c) absorbing most of the liquid into the powder.

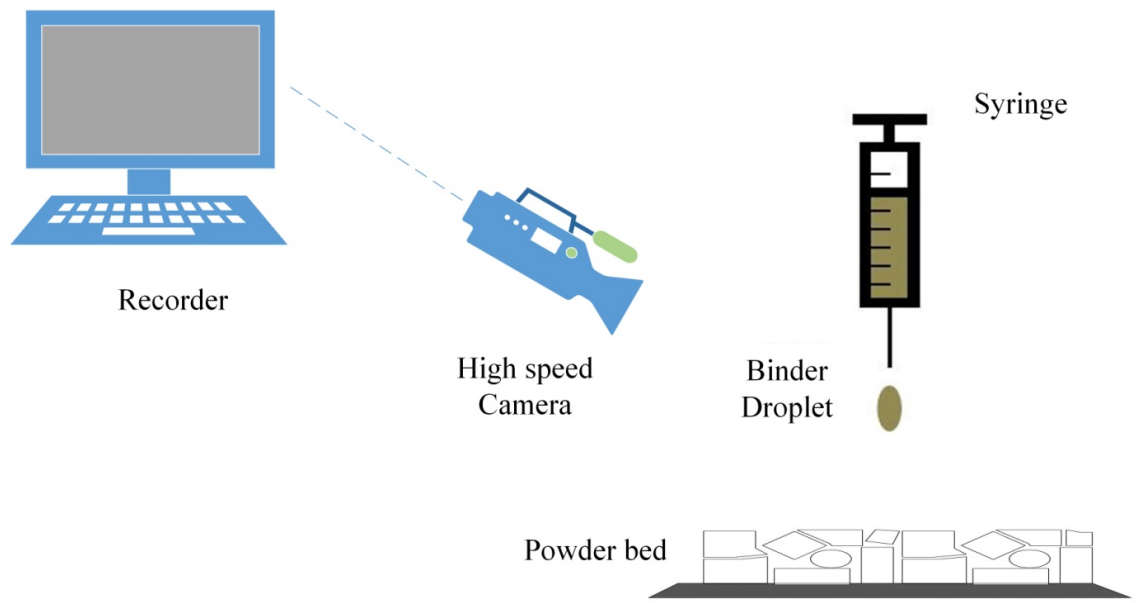


Figure 5. 20: Illustration of the drop penetration test setup.

A single droplet of binder (Zb63, ZCorp) was used to deposit and, consequently, penetrate the powder bed. Powder beds were prepared in the printer before the process of drop fall and penetration. After the process was completed, the build chamber was removed from the 3D printer and was used to conduct the drop penetration test. A binder (Zb®63) droplet with a volume of approximately 60 μl was dropped by a 1-mL medical syringe (25-gauge needle), which was placed over the powder surface.

Frame-by-frame shots by a high-speed camera were used to determine the drop penetration time as well as to examine the complete drop penetration process, as for previous studies (Hapgood et al. 2002; Nguyen, Shen & Hapgood 2009; Zhou et al. 2014). The starting point was indicated as an impact point to the surface when the droplet first touched the powder bed surface. Thereafter, the end-point was determined as the time when the liquid completely disappeared under the surface of the powder bed.

Table 5. 13 shows the surface area for ZP 151 and CP. It is obvious that the surface area for CP was higher than the surface area for ZP 151, which suggests that a greater reaction

could possibly occur for CP than for ZP 151. It also shows more particles on the surface of the powder. This is directly related to the wettability of the powder. However, the layer thickness on the build chamber has a major impact on the binder penetration and the spreadability of the binder over the packed powder.

As shown in *Table 5. 13*, the bulk density of ZP 151 was greater than the bulk density of CP, which means the porosity in ZP 151 was lower than it was for CP. This is consistent with the study by Zhang et al. (2013) in which increasing bulk density in the powder significantly decreased porosity in the powder.

Table 5. 13 Properties of ZPowder (ZP 151) and cementitious powder (CP)

Powders properties	ZP 151	CP
Surface area (m²/g)	0.999	1.021
Bulk Density (g/cm³)	0.912	0.79

5.2.1.8 Dimensional Accuracy Test

The dimensions of the printed specimens were not as accurate as those designed by the SolidWorks software. The standard deviations were between 0.09 and 1.79 mm (Asadi-Eydivand et al. 2016). Measurements of all samples are summarised in *Table 5. 14*, with all samples measured after 28-days curing in tap water. The results were that most of the samples with saturation levels greater than 100% were oversized. This may be due to unbounded powder that was not completely removed during the depowdering process, or that the samples had swollen due to the higher rate of water permeability penetrating the samples. Samples with 75% saturation levels, (S75-C75) and (S75-C150), were smaller than the SolidWorks model as a consequence of insufficient hydration between the particles and their lower density.

Table 5. 14 Measurement of 3D printed (green part) cubic specimens

Saturation levels	Cubic dimensions (mm)	
	OPC & CAC & Li ₂ CO ₃	OPC & CAC
S75-C75	(19.77×19.57)	(19.88×19.65)
S100-C100	(19.55×19.81)	(20.09×20.13)
S125-C125	(20.49×20.76)	(21.1×20.52)
S150-C150	(21.16×21.41)	(21.01×21.37)
S170-C170	(21.48×21.86)	(21.62×21.91)
S75-C150	(19.89×19.51)	(19.91×20.12)
S100-C200	(20.71×20.55)	(19.86×19.81)
S125-C250	(21.03×21.3)	(20.3×20.78)
S150-C300	(21.79×21.42)	(21.45×21.17)
S170-C340	(21.58×21.46)	(20.21×20.37)

The key features that distinguish powder-based (inkjet) 3DP specimens from those created by the conventional casting method are the accuracy and dimensional precision of 3DP specimens. The dimensions of the green specimens (directly after completing the print) for 10 samples were measured using digital callipers with an accuracy of 0.01mm in each direction. The height was measured using a MeasumaX and a Mitutoyo (LH-600E), which have an accuracy of $\pm 0.04\text{mm}$ and $\pm 0.00122\text{mm}$, respectively.

5.2.1.9 Delay Printing Time

Inkjet 3DP is a layer-on-layer procedure that creates an entire scaffold using powder-based materials and an activator such as water. The default pause time between layers can be changed to introduce a short delay after each layer is finished and before the next layer is started.

The CP powders were put into an inkjet 3DP instead of the original ZP151 powder. The ProJet360 uses a binder liquid passing through the HP 11 printhead into a powder, one layer upon another layer, from the bottom of the build chamber until the object is complete. Table 5. 15 shows the scaffold specifications of the printed specimens designed

by CAD software and the 3DP parts. The mechanical properties of five cubes of (20×20×20)mm were examined at each printing delay time. The printing process was prepared using a binder/volume ratio of 0.415 (shell) and 0.415 (core), which is a saturation level of 170% (shell) and 340% (core). The binder/volume ratio values for shell and core regions were assumed to be constant. After completing a print, the printed object was dried in the build chamber for approximately 90 minutes before being removed from the powder bed. Compressed air was then used to remove any unbound powders from the printed specimens.

Table 5. 15 Features and different time delays in layer printing of specimens.

Name of specimens	Saturation level	Number of samples		V_b/V_p	Delay in layer printing (ms)	Specimen size (CAD) dimensions (mm)
		3-days	7-days			
S100		5	5		100	
S200	S170C340	5	5	0.415	200	(20×20×20)
S300		5	5		300	

The printed cubic specimens (20×20×20)mm were prepared by the inkjet 3DP as explained in the paper by (Shakor, Sanjayan, et al. 2017). In the current study, after specimens were taken from the printer, the post-processing consisted of using an oven to dry the specimens for 3 hours at 60°C. The specimens were then cured in tap water for 3 days and 7 days (*Table 5. 15*). Once the specimens were removed from the water, they were dried in the oven for 3 hours at 60°C. This procedure was applied to all specimens. Curing in the oven had a significant effect on the mechanical strength of specimens (Shakor et al. 2018) (Shakor, Nejadi, Paul, Sanjayan & Nazari 2019).

5.2.1.10 Utilising Three-Dimensional Scanning and Scanning Electron Microscope

Three-Dimensional Scanning (3D scanning) and scanning electron microscope (SEM) were used for various experimental investigations in this study. The 3D scanner was used to show the effect of water curing on the printed sample, and the surface roughness of both the recommended printer powder and the cement mortar powder. The 3D scanner was also used to scan the build-chamber powder for both the recommended powder and the cement mortar powder. It was further used to show the orientation of the E6-glass fibre in the powder bed, as well as to precisely check the dispersion, diameter and length of the glass fibre filaments in the printed specimens. Surface roughness and the comparison of both powder materials have been discussed in chapter 6. The scanner microscope was also used to show the printed line on the surface of the printed objects. Because the printed part was printed at different orientation angles, the 3D scanner was able to show the printed line in fine detail.

The SEM was also used to show the reaction and hydration process among particles on the surface of the printed objects. It showed the clear porosity among particles, indicating reacted and unreacted particles on the green samples.

5.2.1.11 Mechanical Characterization of Glass Fibre Reinforcement in Inkjet 3DP Specimens

Concrete commonly provides sufficient fire resistance for most normal applications. Nevertheless, the strength of concrete declines at elevated temperatures due to chemical and physical changes (Kodur 2014). At high temperatures, the spalling of conventional concrete occurs as a result of rapid layer-by-layer loss of the concrete surface, significantly caused by the exposure of the reinforcement bars in the concrete to fire (Sanjayan & Stocks 1993). Numerous studies have been conducted on the different types

of binders at different temperatures to identify the optimum strength and optimum heat resistance of concrete. The use of fibre reinforcement in concrete and mortar to achieve better mechanical behaviours, as found in earlier studies (Li & Maalej 1996; Shakor, Pimplikar & Ghare 2011; Shakor & Pimplikar 2011).

The main objective of this study was to experimentally scrutinise the performances of 3DP mortar when used in the inkjet printing technique under elevated temperatures and with fibre reinforcement. This investigation also studied the effects of sample sizing on the printed mortar. Bending and compression mechanical strength tests of the printed mortar were also conducted in different curing media and at different elevated temperatures.

Homogeneity and consistency of the powder before and during the printing process are important factors that must be controlled in pursuit of superior resolutions (Hiremath & Yaragal 2017). Hence, the speed of the mixer and, therefore, the blending time are considered to be the main contributors to the homogeneity of the powder and production of greater quality 3DP objects.

Samples with dimensions of (20×20×20)mm, (50×50×50)mm and (160×40×40)mm were prepared for the compressive and flexural strength tests. Six samples were produced for each test, see *Table 5. 7*, *Table 5. 8* and *Figure 5. 17*.

5.3 Analytical Relationships for the Mechanical and Material Properties (Powder-based 3DP)

In this section, we explain the analytical relationships of the mechanical properties of the powder-based materials. The results show significant differences in all three planes of the printed objects (XY, YZ, XZ).

5.3.1 Compressive Stress-Strain Relationship

The compressive stress-strain diagram is used to determine the resistance of the printed cement mortar materials to the applied load on the structure and elements. *Figure 5. 21* also shows the energy dissipation of the printed object in response to the applied load.

The (50×50×50)mm size and all three planes are shown in *Figure 5. 21*. In the inkjet 3DP samples, the results are different from those for conventionally cast mortar or concrete. It is clear that cast concrete/mortar has a uniform result in all planes and directions. Further, increases in the size of the cast specimens reduce the compressive strength results (Hamad 2017; Thomas & Peethamparan 2017).

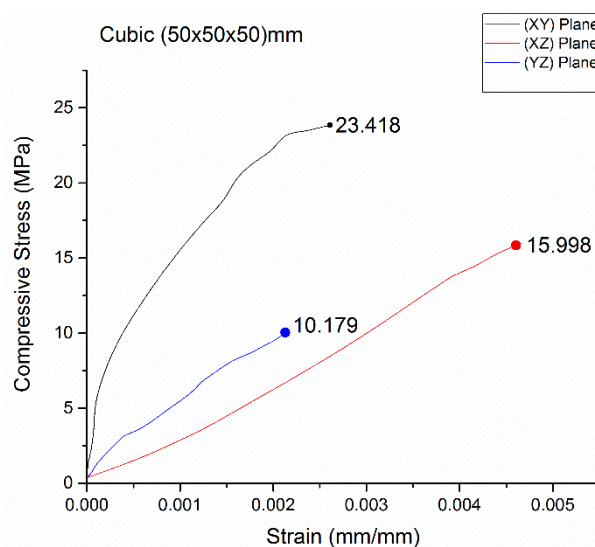


Figure 5. 21: Maximum Compressive stress-strain diagram for the printed cubic (50×50×50)mm.

5.3.2 Porosity-Saturation Level Relationship

Durability is the ability of materials to resist different environments for a long period without significant deterioration. For concrete, durability is dependent on five major factors: curing, compaction, cement content, permeability and cover. These factors are discussed in more detail in the following sections.

Curing or post-processing plays a major role in the durability of the printed specimens. The common curing process for ordinary concrete is to place it in a moist environment or in water. However, for the 3D printed specimens, we used different methods, such as keeping them in water only or curing in water for 28 days and then drying them at 40°C in an oven for an hour. The results of these experiments are explained in the results and discussion (material composition) section. The main enhancement in mechanical properties was found to occur when drying in an oven, with the compressive strength increasing twice as much as normally cured specimens.

Proper compacting or vibration increases the density and durability of concrete. This function is unattainable in the 3DP application in which the powder is spread only by a roller. The spreading of the powder by the roller, called in-process bed powder preparation, slightly compacts the bedded powder (Zhou et al. 2014). The density of the 3DP cementitious mortar has been measured and has a density less than normal concrete due to the lack of vibration and high porosity among particles. The density of the 3DP part is $1764 \pm 60 \text{ kg/m}^3$, see *Table 5. 6*, compared with normal concrete which has a density of 2400 kg/m^3 .

Another factor which affects durability is the cement content. The materials comprising the printed structure contained a high amount of cement and a limited amount of sand (5% of cement weight). The mechanism used to build printed specimens is totally

different from that for ordinary mortar. The nozzles of the printer are located in specific areas to deposit water droplets on the bedded powder. Thus, the entire part of the printed specimen cannot be saturated sufficiently. Furthermore, the mechanical properties of the 3DP specimens are weaker compared with normal concrete. This needs further investigation to achieve stronger mechanical properties in 3DP specimens.

Permeability is another factor which should be taken into account with 3DP specimens. This is linked to the porosity of the specimens, which was explained in chapter 6 concerning the porosity test. The minimum porosity level for the 3DP specimens was approximately 62%, which means that the printed specimen was a permeable medium. As a result, post-processing has a major influence on improving 3DP permeability. The curing process in 3DP uses a different technique which depends on the type of materials. For instance, for the Zpowder samples, infiltration is normally used for the curing process or it is cured in an oven for a few hours. The infiltration method consists of applying a specific resin on the printed part in order to achieve higher strength and improve the mechanical properties. The Zcorp company also provides several post-processing products such as wax, resins and epoxy. This production improves specific characterizations of the specimens such as mechanical ability, and colour vibrancy, see *Figure 5. 22*.

Figure 5. 23 clearly shows the fluctuation of porosity versus saturation level. When increasing the w/c ratio, porosity reduces significantly. However, when porosity is reduced, it improves the mechanical compressive strength of the specimens. Having a high rate of porosity makes the concrete weaker.

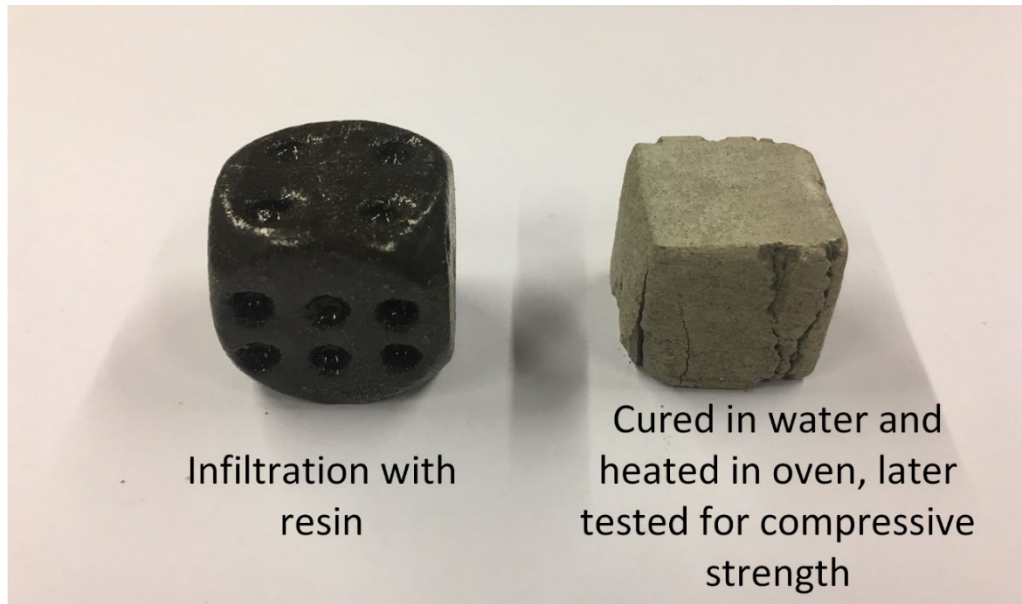


Figure 5. 22: 3DP specimens are cured using different agents

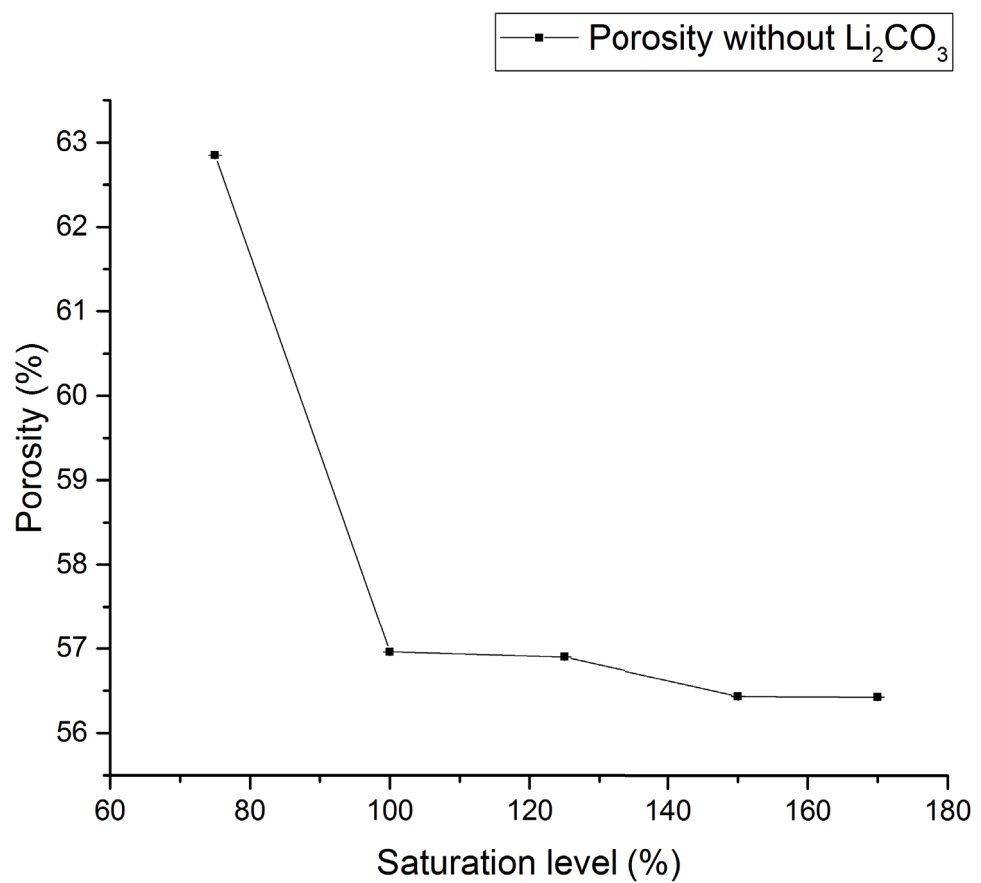


Figure 5. 23: Porosity versus saturation levels for CP specimens without lithium carbonate.

5.3.3 Compressive Strength-Saturation Level Relationship

Figure 5. 24 clearly shows the fluctuation of compressive strength while increasing the w/c ratio. Compressive strength also increases slightly.

Generally, 3DP specimens do not display any shrinkage cracks. To better understand this, further work needs to be done to check the microcracks inside the samples. The morphology of the 3DP specimens was studied for the purpose of observing particle size. Figure 5. 11 shows the morphology of the powders before printing. It reveals that the cementitious powder has a heterogeneous arrangement compared to the Zpowder. Therefore, both powders would have a different percentage of porosity and different microstructure composition.

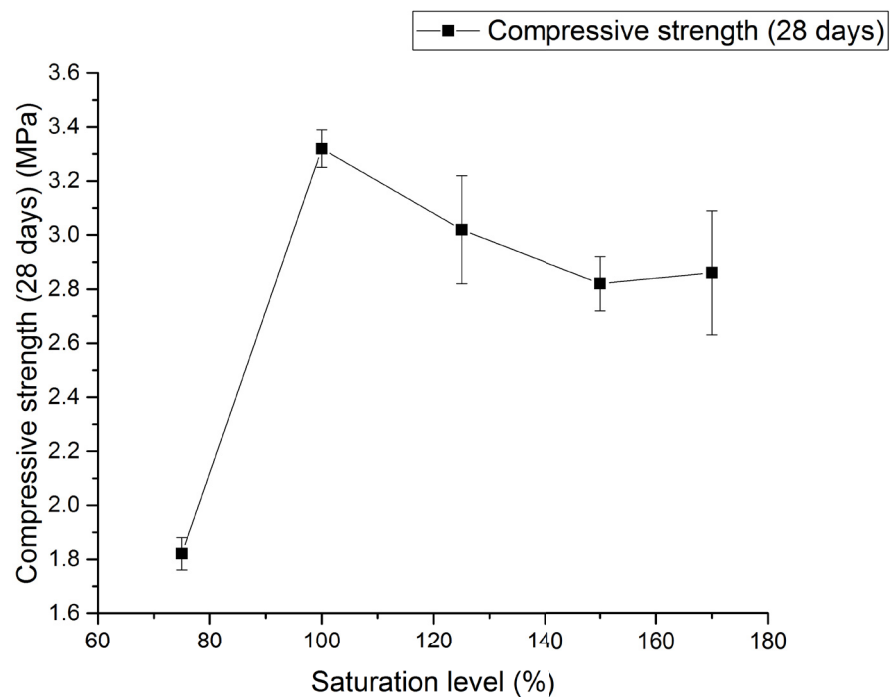


Figure 5. 24: Compressive strength versus saturation levels for CP specimens without lithium carbonate.

5.4 Experimental Program for Extrusion Printing

The extrusion printing method includes depositing slurry materials from an orifice connected to a frame to print layers of a structural member (see *Figure 5. 25*), for example, concrete printing, designed by (Le, Austin, Lim, Buswell, Gibb, et al. 2012) and contour crafting, established by (Hwang & Khoshnevis 2004). Le, Austin, Lim, Buswell, Law, et al. (2012) studied high-performance printed concrete properties which were deposited from an orifice 9mm diameter. They revealed that the printed samples in different directions have a compressive strength results between 75 and 102 MPa. They also proved that the perpendicular load direction had the maximum compressive load, while in a normal cast cube, compressive strength was roughly 107 MPa.

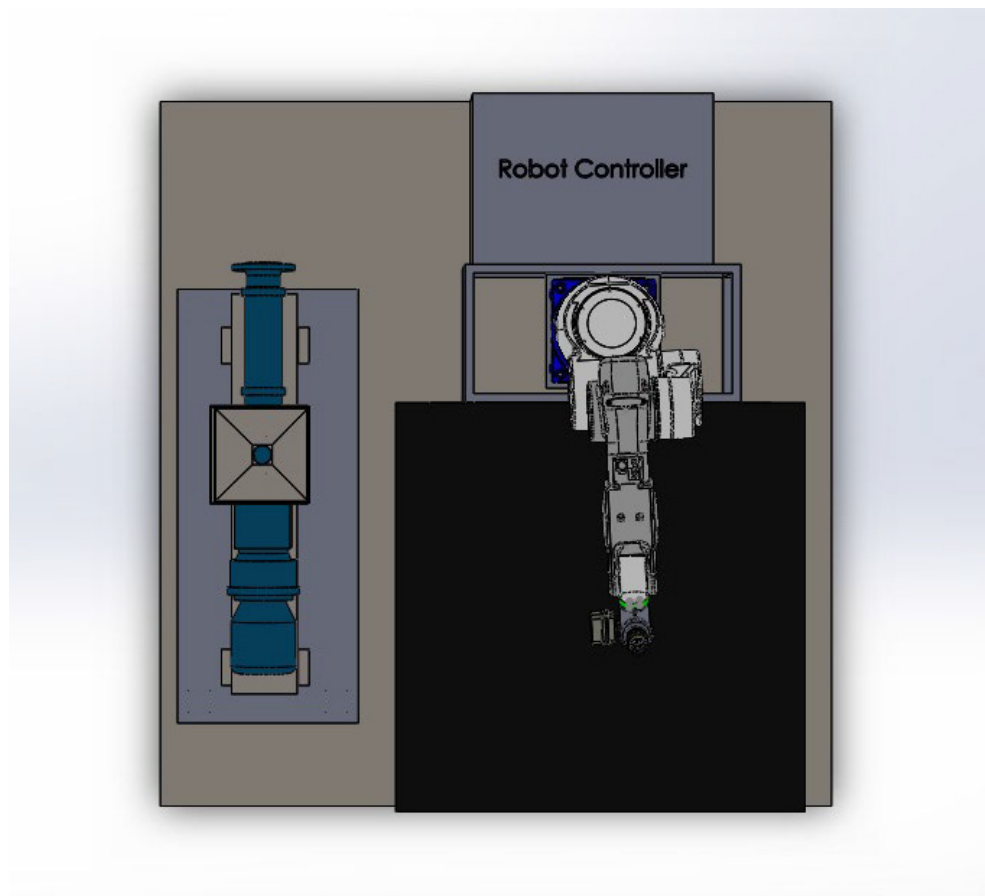


Figure 5. 25: Top-down view of the 6-DOF robotic arm and pump setup.

5.4.1 Experimental Program and Curing Conditions

Materials play a crucial role in 3DP of objects for construction applications. When the properties of the materials are optimised, the printing process will have a better result. In the present work, the materials consisted of fine sand (Sydney Sand) from Australian Native Landscapes, ordinary Portland cement (General Purpose cement) from Eureka and chemical admixtures such as superplasticizer (SikaPlast®3 in 1), accelerator (Sigunit L80AF), and retarder (Retarder N). Particle size mesh analysis was conducted for the fine sand with a maximum particle size of 300µm. The particle size analysis distribution was prepared using a sieve mesh and particle size analyser (Shakor, Nejadi & Paul 2019). The fibre used was polypropylene (PP) (6mm) (Elasto Plastic Concrete) and E6-glass (G) fibre from Trojan, *Table 5. 16*.

Table 5. 16 Mechanical properties of the PP fibre and G fibre that were used in the mortar mix.

Fibre type	Length (mm)	Thickness (µm)	Specific gravity (g/cm³)	Tensile strength (MPa)	Tensile modulus (GPa)
Polypropylene	6	100	0.91	1300	7.2
E6-glass	6	100	2.62-2.63	2500-2700	81

Figure 5. 26 (a) shows particle size distribution versus the percentage of passing particles of ordinary Portland cement, fine sand and *Figure 5. 26 (b)* coarse aggregate which was used in the slurry mix.

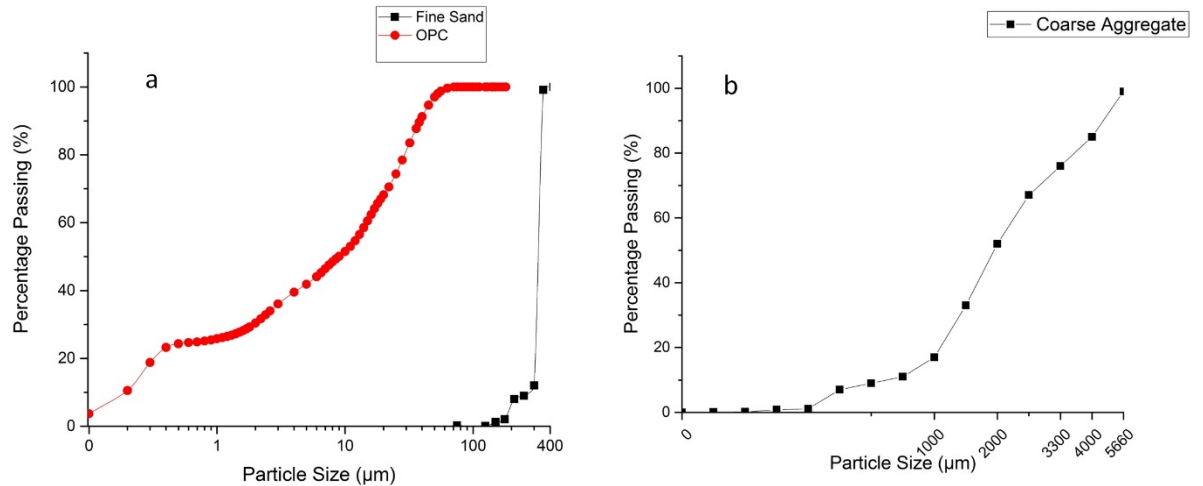


Figure 5. 26: (a) Fine sand and Ordinary Portland Cement particle size distribution, (b) Coarse aggregate particle size distribution.

The extruder for the printed mortar shown in Figure 5. 27 was designed so that it could be mounted to the end-effector of an industrial robot. The design incorporated improvements to increase the efficiency of printing cementitious materials.

The pump was used to appropriately deliver material to the extruder. The extruder consisted of the components shown in Figure 5. 27.

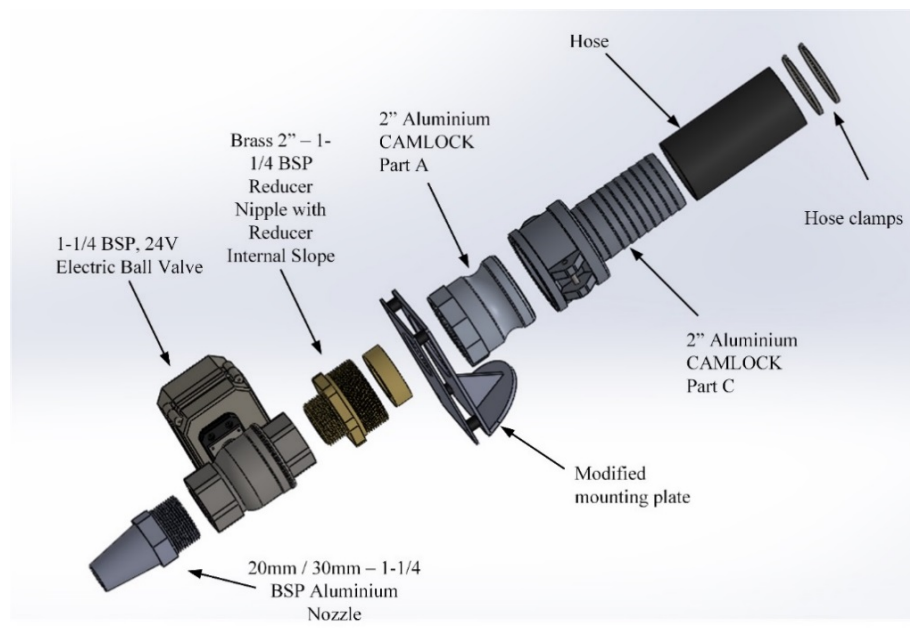


Figure 5. 27: Exploded view of the extruder assembly that is connected to the progressive cavity pump and is attached to the end of the robot.

A caulking gun was used with different sized nozzles (14mm, 20mm, 35×10mm). The caulking gun has been used in previous work by (Al-Qutaifi, Nazari & Bagheri 2018; Soltan & Li 2018). The caulking used as a mechanically actuated gun to print the cementitious mortar.

Figure 5. 28 shows the connections of the pump to the end-effector. The progressive cavity pump connected to a tube with an inner hose with diameters of 20mm and 30mm, refer to Figure 5. 28.



Figure 5. 28: The final system with the progress cavity pump connected to the robot.

Several trials for the cement mortar were prepared to check the optimum printable cementitious mortar. Fabrication and mix designs were examined, based on the previous investigation (Shakor & Nejadi 2017; Shakor, Renneberg, et al. 2017) and further mixed trials were implemented to improve smooth pumpability through the pump and delivery systems. Several studies were also prepared for concrete fabrication and printing members. Until now, 3DP concrete and mortar in the construction industry have not been technologically advanced enough and have not been thoroughly investigated on a large-scale.

The present study fills a gap in the literature. It used different mixes until an optimum mix was obtained which could be more compatible with the different delivery system. This optimum mix was obtained through printing the specimens by trial and error process. This study also investigated a suitable delivery method for printed mortar, while using different mortar mixes to obtain the optimum mix design. Two techniques were adopted to deliver the mortar, namely, using a caulking gun and a cavity pump.

The mix of mortar with various agents and chemical admixture has an important effect on the amount of air in the mix, leading to a lot of residual air. Agents such as superplasticizer, accelerator, retarder and water reducer, affect the amount of air according to the type of medium and the delivery system. However, for these mixes, the setting time and shapeability of the mortar were considered.

For the caulking gun (internal diameter of nozzle circular 14mm, 20mm, rectangular 35×10mm), several trials are presented in *Table 5.17*. Mixing times of 5 to 6 minutes were found to be the most suitable. Due to the inconsistencies in extrusion, printing heights were taken as an average measurement for caulking gun printing. However, the printing height for mortar printing via a robotic arm was fixed according to the diameter of the nozzle, where the diameter of the nozzle was equal to the height of the end-effector from the printed platform. *Table 5.17* shows the selected mix proportion from previous work (Shakor, Renneberg, et al. 2017), which has excellent performance while printing (Shakor, Nejadi & Paul 2019).

Table 5. 17 Mortar mix design with 1:1 and 0.5:1 ratio (cement:sand) with/without PP fibre.

Trial No.	Fine Sand (g)	Cement (g)	Coarse Aggregate (g)	Retarder (ml)	Accelerator (ml)	Water (ml)	Superplasticizer (ml)	PP Fibre
T5	375	375	-	2	2.5	125	2.5	0%
T5*	375 187.5	375 375	-	2	2.5	125	2.5	1%
T8	500	500	-	2.66	3.3	171.5	3.33	0%
T12	375	375	125	2	2.5	125	2.5	0%

*selected mix using polypropylene fibre.

The mix design was then changed slightly according to the delivery system and nozzle of the end-effector to improve the slump and flow of the cement mortar. Table 5. 18 shows the optimum amount of mortar slurry which can pass through the pump and delivery system. Glass fibre replaced polypropylene fibre due to its easy flow through the delivery system and its ability to be properly mixed with the cement mortar. PP is difficult to mix with mortar with clogging sometimes occurring at the end-effector of the delivery system.

Table 5. 18 Mortar mix design for 1:1.2 (cement: sand) ratio with/without glass fibre

Fine Sand (g)	Cement (g)	Retarder (ml)	Accelerator (ml)	Superplasticizer (ml)	Water (ml)	E6-Glass Fibre
6075	5062.5	27	33.75	25.31	1890	0%
6075	5062.5	27	33.75	30	2000	1%

5.4.1.1 Programming of the Robot and Control Methodology

To maintain a consistent flow, it is important to implement an efficient method of planning to provide a stable path for the end-effector to follow. Using a combination of Damp Least Squares (DLS) paired with Resolved Motion Rate Control (RMRC) to plan

and control the robot's path, it is possible to create a steady 3-dimensional print which is completely customizable with an integrated MATLAB and C++ interface.

It is important to consider, when planning transitions between multiple joint states, how the robot will reduce the impacts of singularity on the system. Singularity refers to any given joint state of formation which reduces or even limits the degrees of freedom of the end effector. Typically, this occurs when two connected links form a straight member. The conventional method of calculating inverse differential kinematics results in a destabilization of the transitions between joint states. This appears, as described by Chiaverini, Siciliano & Egeland (1994), as a sudden increase in joint velocities over large control deviations. It is possible to apply the DLS method (also known as Levenberg-Marquardt stabilization) in order to mitigate the impacts of singularities. This method reduces subsequent oscillations on the system as the joints approach an unreachable position. The DLS solution, as it appears in (Buss 2004), can be described by the following Equation (5.5),

$$\Delta\theta = (J^T + \lambda^2 I)^{-1} J^T e^{-\rightarrow} \quad (5.5)$$

Where the change in angular displacement, $\Delta\theta$, is minimised to stabilize the joint velocities when approaching a singularity. The damping constant, λ , must be adjusted (Buss 2004) according to the systems' parameters in order to perform efficiently. Ahmed & Pechev (2009) outline how the stability of the rotational velocities depends heavily on the 'exactness' of the damping factor and that the damping constant can be found using the following Equation (5.6):

$$\lambda = \lambda_0 \left(1 - \left(\frac{w}{w_0}\right)\right), w < w_0 \quad (5.6)$$

where, λ_0 , refers to the initial damping factor predetermined by (Ahmed & Pechev 2009) 'user requirements', and w refers to the measure of manipulability and w_0 refers to a threshold number of minimum manipulability before DLS is to be used.

For any given joint angle ($\theta_i, i = 1, \dots, 6$) for all joint positions of the calculated path, a measure of manipulability of the system can be taken to determine whether or not the system is approaching a singularity.

From Yoshikawa (1985) we use the following Equation (5.7),

$$w = \sqrt{\det(J * J^T)} \quad (5.7)$$

Where, J , is the Jacobian of the system, and J^T , is the transpose of the Jacobian, the measure of manipulability is compared with the predetermined threshold value represented by epsilon, ϵ (equal to w_0), which allows the system to apply reactive coding to dampen the effects of singularity on the joint velocities, for instance, where the measure of manipulability, w , is less than ϵ .

The Jacobian of the system relates to the kinematic properties that are present during a transition at any given joint state. Acquiring the most appropriate joint velocity (Altuzarra et al. 2008), for each individual joint involves using a Jacobian that relates both active and passive joint velocities acting in the system. As the robot is 6DOF, the system's Jacobian, J yields a 6×6 matrix. For any given path, the program will determine the required total joint positions by using inverse kinematics which yields the rotational joint positions q_i . The program stores these values in an n×6 matrix (where n is the number of joint positions required to transition through the given path), and then J is found by passing in q_i .

Depending on w at q , DLS will alter the way the Inverse Jacobian is calculated. When the manipulability is less than the threshold value represented by ϵ , a pseudo inverse Jacobian must be found in order to continue planning. This pseudo-inverse Jacobian is designed to handle stabilization issues associated with singularities, where the conventional method tends to perform poorly. The inverse Jacobian, J^+ is used to handle the approach toward singularity as Equation (5.8):

$$J^+ = J^T (JJ^T + \lambda^2 I)^{-1} \quad (5.8)$$

When considering a robot's joint motions, there are multiple joint paths the robot can use in order to transition between consecutive end-effector poses (Clifton et al. 2008). For any given test represented by a series of joint states, RMRC trajectory planning was used to create linear transitions between joint states. It allows the system to use the most optimal path between two points in space for where the robot's end-effector will transition with the best possible motion. Utilising the calculation of error for both the rotational and translational displacements, the program updates the stored joint rotational values, $\dot{\theta}_{i=1 \rightarrow 6}$, in order to maintain a near linear trajectory. This also helps to maintain the end effectors' 'downwards' orientation during transitions.

Determining the joint velocities as shown in (Ko 2015), drives the position of the end effector with a velocity which can be described as,

$$\dot{x}_e = (\dot{x}_e, \dot{y}_e, \dot{z}_e, \dot{\theta}_r, \dot{\theta}_p, \dot{\theta}_y) \quad (5.9)$$

Since the end effector's Roll, $\dot{\theta}_r$, Pitch, $\dot{\theta}_p$, and Yaw, $\dot{\theta}_y$, are at fixed values, any change in velocity impacting on the end effector's change in position occurs linearly in the x, y, and z plane. The change in displacement is found using the following equation and is stored as dx for each joint state, i , in any given transition:

$$dx = x_{i+1} - x_i, y_{i+1} - y_i, z_{i+1} - z_i \quad (5.10)$$

To maintain a fixed end effector roll, pitch and yaw, the rotational error of the end effector is calculated as,

$$d\theta = r_{i+1} - r_i, p_{i+1} - p_i, y_{i+1} - y_i \quad (5.11)$$

It is then used to correct the end effector's orientation as it transitions. The properties of both (6) and (7) are used to formulate the properties of (5), thus:

$$\dot{x}_e = (dx, d\theta) \quad (5.12)$$

Hewit & Love (1983) described the basis of RMRC as,

$$\dot{\theta} = J(\theta)^{-1} * \dot{x} \quad (5.13)$$

The calculated end effector velocity, \dot{x} , is found in (5.12). Depending on whether DLS is implemented, the inverse Jacobian, denoted by $J(\theta)^{-1}$, with the end effector velocity will give the required rotational velocities, $\dot{\theta}$, for each joint.

The robot uses the angular velocity, $\dot{\theta}$, to apply RMRC to update the next joint state parameters based on the current joint positions. This method applies an element of self-correction to the path planning to ensure that the end-effector maintains the same direction.

Finding the actual velocity of the end-effector is essential for maintaining an effective extrusion rate at the end-effector. Note that, despite the use of RMRC in the planning of the robot's path, the actual joint step completion time is determined by the controller. Given the maximum joint velocities of each joint, it is possible to calculate the maximum 'actual' velocity of the end effector at any given time. Equation (5.13) can be re-arranged to give the following:

$$\dot{x} = J(\theta) \cdot \dot{\theta} \quad (5.14)$$

Essentially, calculating the product between the Jacobian for a given joint state and the rotational velocities will give the velocity components of the end effector. By accounting for the percentage multipliers imposed by the controller pipeline, (5.14) is expressed as:

$$\dot{x} = P_M * P_{TP} * (J(\theta) \cdot \omega) \quad (5.15)$$

Where P_M and P_{TP} are the percentage values of maximum speed dictated by the software interface and the robot's end-effector, respectively. Finding the magnitude of \dot{x} gives the controlled peak velocity. For the experiments, these values were heuristically determined by measuring both the displacement of a given path and time to complete the path.

5.4.1.2 Compressive Strength Test

Several experiments were conducted to assess the mechanical and hardened properties of materials after completed the print and at the hardened state of the components. It is essential to print the small structural members before printing at a larger scale. These tests were prepared based on the mortar materials' behaviours. The mechanical properties of the printed objects are derived by the measurement of the materials' behaviours, which can be used to indicate the yield strength, deformation of the materials and resistance of the materials. Three samples were used for each of the trial and mix designs. Table 5. 19 presents the number of samples and batches. The small hollow column with 7 layers was prepared, 3 samples with 1% PP fibre and other 3 without fibre. Then, after 28 days were tested for compressive strength under the uniaxial testing machine (UH-500kNJapan). The printed column was performed via a robotic arm (Denso) using cavity pump as a delivery system. The printed hollow column prepared without any time lapse between printed layers and without wet curing for the printed specimens.

The printed specimens of flexural strength and compressive strength were printed by delivering systems of the caulking gun and cavity pump.

Based on *Table 5. 20*, the cubic specimens and prism specimens were produced in various layers (1 layer, 2 layers, 4 layers, 6 layers) to print specimens with/without E6-glass fibres. *Table 5. 20* shows the number of specimens that were produced in the laboratory using a 6DOF robotic arm.

Table 5. 19 Details of the prepared samples with/without presence polypropylene fibre

Sample description	Number of the samples	Size of samples (mm)	Delivery method
Hollow column	6	(300×300)	Cavity pump
Printed without Fibre	6	(160×40×8)	Caulking gun (35×10mm)
Reinforced mortar	6	(160×40×16)	
Reinforced mortar	6	(160×40×24)	
Reinforced mortar	6	(160×40×32)	
Printed with/without Fibre	6	(160×14×12)	Caulking gun (14mm)
Reinforced mortar	6	(160×14×24)	
Reinforced mortar	6	(160×14×36)	
Reinforced mortar	6	(160×14×48)	
Printed without Fibre	6	(160×24×18)	Caulking gun (20mm)
Reinforced mortar	6	(160×24×36)	
Reinforced mortar	6	(160×24×54)	
Reinforced mortar	6	(160×24×72)	
Casted prisms	18	(160×40×40)	Conventional method
Casted cubes	18	(50×50×50)	Conventional method

Table 5. 20 Prepared specimens with glass fibre/without fibre

Type of Specimen	1 layer	2 layers	4 layers	6 layers
cubic	6	6	6	6
prism	6	6	6	6

To evaluate the mechanical properties of various mortar mixes, a uniaxial compressive strength test was conducted to check the suitability of the sample under compression before printing the complete components. The cubic specimen dimensions of (50×50×50)mm were prepared according to the Australian standard (AS1012.9:2014 2014). The loading rate was 0.833 kN/s. The testing machine used was from Shimadzu (UH-500kN XR 500kN, Japan).

5.4.1.3 Flexural Strength Test

To assess the flexural strength of the specimens, a three-point bending test was conducted to all the main mortar mixes according to ASTM standards (ASTMC293/C293M 2002). The prisms, with dimensions of (160×40×40)mm, were cast as for a conventional mortar mix. The various layers were printed using a caulking gun for the three-point bending test. The caulking gun can print with the dimensions of; (160×20×18)mm for one layer; (160×20×36)mm for two layers; (160×20×54)mm for three layers; and (160×20×72)mm for four layers. All used a 20mm circular nozzle. Thus, only the thickness of the sample changed. A similar prism was cast for one, two, three and four layers with a circular nozzle of 14mm. Three samples for each printed layer were prepared. These batches were prepared with PP fibres and without fibres, see *Table 5. 19*. The uniaxial testing machine from Shimadzu (AGS-X 50kN, Japan) was used for this test.

According to *Table 5. 20*, the prism was prepared in various layers (1 layer, 2 layers, 4 layers, 6 layers) with/without E6-glass fibres reinforcement using a robotic arm with an optimum mortar mix. *Table 5. 20* describes the number of specimens that were conducted in vitro.

5.4.1.4 Squeeze-flow Test

The squeeze flow test was prepared according to the Brazilian test (ABNT-NBR15839 2010). For this test, the uniaxial testing machine, Shimadzu (AGS-X 50kN, Japan), was used to check the resistance of three main mixes (see *Table 5. 17*) while in a fresh state. The displacement speed was 0.1 mm/s (see *Figure 5. 29*). The surface roughness for this test was conducted using a portable profilometer (Taylor Hobson Surtronic 3+). This test was conducted for single layers, double layers and triple layers.

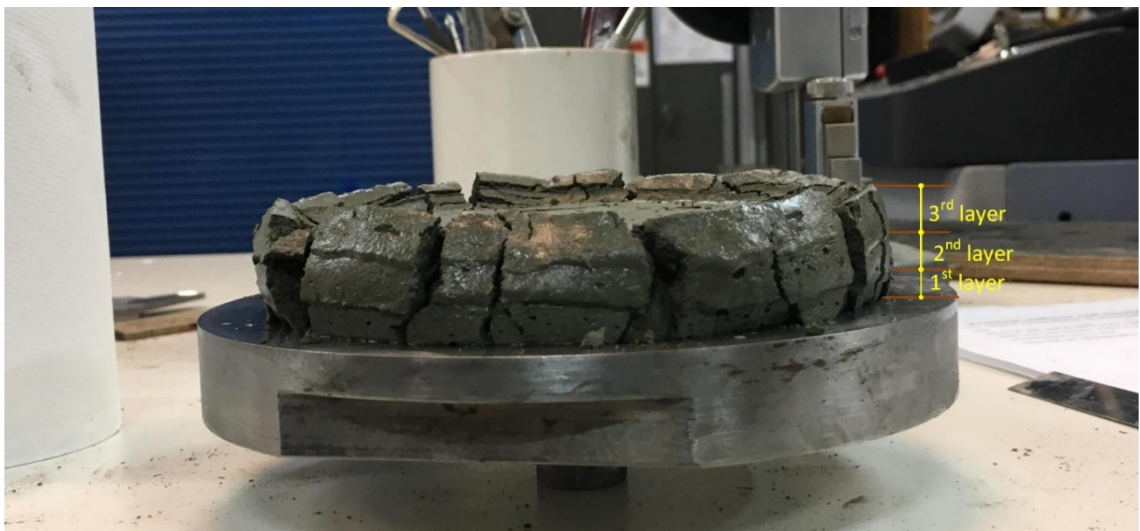


Figure 5. 29: Triple layers of the mortar after squeezing under a uniaxial compression load.

5.4.1.5 Slump and Spread-flow Test

The slump tests (spread-flow tests) were prepared according to (ASTMC1437 2015) to determine the flowability of the mortar mixes. This test was performed using a mini cone of (100×70×50)mm. The first step of the slump procedure involved pouring fresh mortar into the mini cone mould and then tamping it slightly, for settling down and levelling purposes, with a manual tamper for approximately 20 tamps.

The mini cone was then filled with the second and the third layers using fresh mortar. The second and third layers were poured and tamped afterwards using the same procedure as

the first layer. Lastly, the remaining mortar at the top of the conical mould was flattened and scraped. After flattening the third layer, the mini cone was raised and the height of the fresh mortar specimen was measured. Next, the fresh mortar was tapped 25 times. When the fresh mortar was spread, the diameter was measured in two perpendicular directions. Next, the relative slumps could be calculated using Equation (5.16):

$$rp = (d/d_o)^2 - 1 \quad (5.16)$$

Where rp represents a relative slump, d is the measured diameter as an average value of the spreading mortar, and d_o equal 100 mm (which is the base diameter of the mini cone).

5.4.1.6 Setting Time Test

The Vicat test was used to validate the layer setting-time of the cementitious materials. In this study, three trials of mortar mix (T5, T8, T12) were selected. The outcomes are presented in the results section.

The measurement for the Vicat test was implemented according to (ASTMC191-13 2013; Sleiman, Perrot & Amziane 2010). The diameter of the needle (on a movable rod) was 1mm and had a fixed weight of approximately 300g. A sample of normal uniformity fresh mortar was prepared and placed in a container 40mm in height. The test consisted of the measurement of the needle penetration, which falls due to gravity, to a required depth. The initial setting time was at 15-minute intervals. The first 15-minute recording of the needle penetration was 39 ± 0.5 mm. The final time recorded less than 0.5 mm penetration. The setting time test for each printing trial using the caulking gun and the real height and width of the printed layer are listed in the results section. The outcomes and further interpretations are also presented in the results section.

All the tests and trials were mixed using a Hobart mixer (A200) at speeds of 1 and 2 for the entire mixes. The speeds of the mixer (A200) are divided into three categories: Low, Intermediate, and High (A200MIXER), see *Table 5. 21*.

Table 5. 21 Speed of the Hobart mixer (A200).

	Speed	Agitator (RPM)	Attachment (RPM)
1.	Low	107	61
2.	Intermediate	198	113
3.	High	361	205

The materials were placed into the mixer and mixed in a dried state for approximately 1 minute. The mix was then mixed for approximately 4 minutes in a wet condition. The mix commenced with the speed number set at 1 (107 rpm) for approximately 1 minute and then paused for 1 minute. A paddle was used to scrape the sides and bottom of the bowl. Next, the mixer was set at speed number 2 (198 rpm) for 75 seconds, and the sides of the bowl were scraped. The mixer was set again on speed number 2 for another 75 seconds.

5.5 Analytical Determination of the Mechanical Properties

Mechanics of materials is dealing with the behavior of materials which subject to stresses, the mechanics of materials can be investigated in the fresh state or hardened state. Further, the mechanical strength test in the presented investigation was conducted to measure the fresh state slurry of the mortar and hardened state of the mortar.

There are two major factors that have a significant effect on the final shape result of the product are (a) the number of printed layers, and (b) the discharging of mortar slurry through different nozzle shapes and sizes.

It is logical to assume that an increase in the number of layers in a specimen will increase the load that acts on the lower layers of that specimen. This causes to having a larger displacement in the height of the printed sample. According to the Hertz Theory: Contact of Spherical Surfaces Wang & Zhu (2013), Yang (1997), and de Vicente et al. (2011), the contact between two spheres could be described as the total height is considered to be h so that h can be expressed as:

$$h = 2 N_{pc}(\alpha - \delta) \quad (5.17)$$

Where N_{pc} is the number of particles in a chain, α is the radius of the particle and δ is the indentation depth.

The normal force, F , acting on the plate is expressed as:

$$F = N_c f \quad (5.18)$$

Here, N_c is the number of chains, and f is the force between the particles. The force between particles increases as the number of layers increase, based on equation (5.18). However, this is a controversial concept because the normal force incrementations are dependent on the type of slurry or paste, distribution of the particles on the previous layers, the time between the two printed layers, and the viscosity and moisture content between particles.

Figure 5. 30 explains the change in width, which is specified as $(W+\Delta W)$, while the thickness is expressed as $(T-\Delta T)$. *Figure 5. 31* shows that the extruded layers changed into their original shapes. The width and thickness of the first printed layer also changed after loading the next layers. The first layer also experienced a change in its shape after the printing of the third layer. This change is possibly continuous until the shape has reached stability in its form and has set sufficiently. The last layer of the component did

not encounter any modifications and changes because no further layers were added, so it retained its own shape, *Figure 5. 31*.

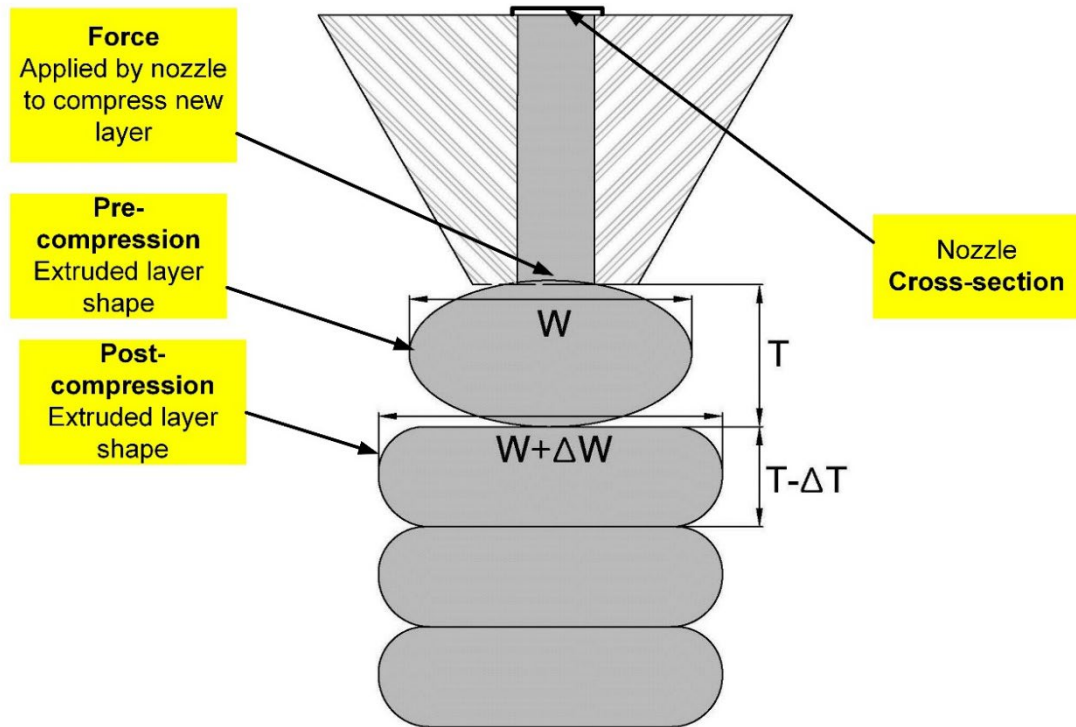


Figure 5. 30: Schematic illustration of the prediction of the printed mortar passed through the circular nozzle.

Where W is the true width and ΔW is the trace width error. T is the true thickness and ΔT is the trace thickness error. Therefore, the area of the object will change at the pre-compression and post-compression stages according to the rheology of the mix proportions and the forced impact of the next layers which are printed. *Figure 5. 30* shows that the area of the layers will vary according to the printing height, nozzle types, the mixing time and the setting time of the materials. Therefore, the true area of each cross-section printed layer is equal to $(W+\Delta W)*(T-\Delta T)$.

However, there could be a different result when the time intervals between layers change.

When a slight decrease in the time intervals occurs between layers, the rate of penetration

between layers increases due to the viscosity and shear thickening properties in the concrete. This is consistent with research by Cyr, Legrand & Mouret (2000), which found that the shear thinning of the concrete could be changed to shear thickening by adding superplasticizer to the paste of the cementitious materials. Shear thickening is defined as the proportion of the shear stresses to the viscosity of materials which can be increased gradually. This phenomenon emerged during the pumping of the mortar. The mortar had resisted downward pressure and the viscosity also greatly increased. For this to occur, a mixer in the hopper needs to move continuously in the container. In this study, a different ratio of superplasticizer was used. This had a significant effect on the setting time of the mortar and the viscosity of the mortar. The ratio of superplasticizer to cement materials was (0.67% to 1%).

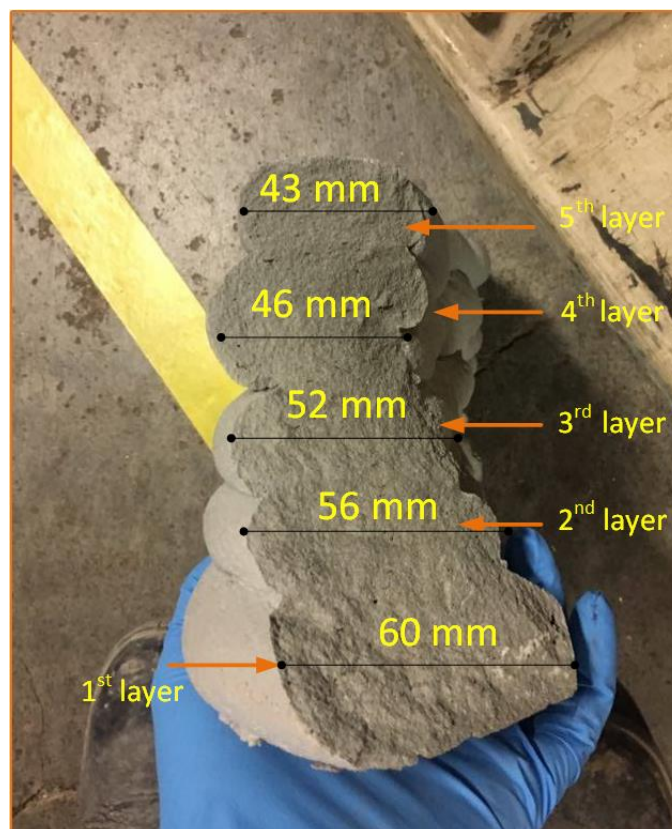


Figure 5. 31: Cross-section of the details of the printed layers after crushing under a uniaxial compression load, using a cavity pump as a delivery system (nozzle Ø50mm).

The shape of the nozzles has an effect on the printability, shape and flowability of the slurry. The study by Li et al. (2017) asserted that intercepting shocks are significantly changed according to the shape of the nozzles. The study found that square shaped orifices are faced with higher interception than the other jets due to the four corners exiting at the nozzle. In addition, the penetration between two layers increased while the w/c and the number of layers incremented proportionally. Furthermore, the shape of the nozzles also affected the percentage of penetration between the two layers. If the nozzle shape was circular, the penetration rate increased slightly. This was due the previous layer being laid down as a concave rather than a flat shape. The application of the spherical particles and square particles theory could be applied to the circle and square nozzles in terms of the shape and load applications. *Figure 5. 32* shows that the load in the square nozzles is distributed equally due to the radius of distribution in the square shapes. This distribution area is smaller in circular nozzles (Cwalina, Harrison & Wagner 2016). Böhmer et al. (2006) found that in the inkjet printing technique the diameter of the droplet, which contains 0.3% polyvinyl alcohol solutions, was larger than the diameter of the nozzle. They used a different concentration of polymer solution with the three different nozzle diameters. As a result, at a constant polymer concentration, smaller droplets were produced initially by the smallest nozzle diameter that, in turn, also led to smaller particles. Consequently, this could be similar to concrete/mortar slurry where a higher flow of slurry is produced with increasing nozzle sizes.

Cwalina, Harrison & Wagner (2016) stated that the particles with spherical and cubic shapes produce different results. The squeeze flow and load distribution between two cubic particles and two spherical particles with equivalent radii-lengths are illustrated in *Figure 5. 32*.

For particles at the centre of the line, moving with velocity, V , the characteristic half-width of the line, R , viscosity of the fluid as a Newtonian, ηf , the force measurement for the spheres and cubes, are measured as (Cwalina, Harrison & Wagner 2016);

$$F_{spheres} = \frac{6\pi V \eta f R^2}{h} \quad (5.19)$$

$$F_{cubes} = \frac{3\pi V \eta f R^4}{h^3} \quad (5.20)$$

In the two equations, (5.19) and (5.20), it is obvious that the reaction force between two particles increases when the shapes change from cubes to spheres. This result will be similar for printing when square or circular nozzles are used. The printed shape will replicate the shape of the nozzles. The particles used in this experimental test were mostly spherical with some irregular shapes. As a result, the printed slurry was a similar shape as it passed through the nozzle. The different shapes and sizes of the nozzles were also investigated in this study. The shapes used were circular and rectangular, with diameters of (20)mm and (35×10)mm. The forces were distributed evenly over the greater surface area in the square and rectangular shapes than in circular shapes. Consequently, the printed layers of the square or rectangular nozzles withstood more layers than those printed using circular nozzles. It should be noted that the same mix ratio was used for the printed object utilizing different nozzle types. It was found that the nominal width in a rectangular shape was larger by 2 ± 0.85 mm than its reduced width (layer surface contact). Conversely, the nominal width of a circular shape was larger by 3.1 ± 0.75 mm than its reduced width.

Considering the forces applying to differently shaped particles, the higher forces emerged between flat cubic particle surfaces compared with the curved surface characteristic of spherical particles.

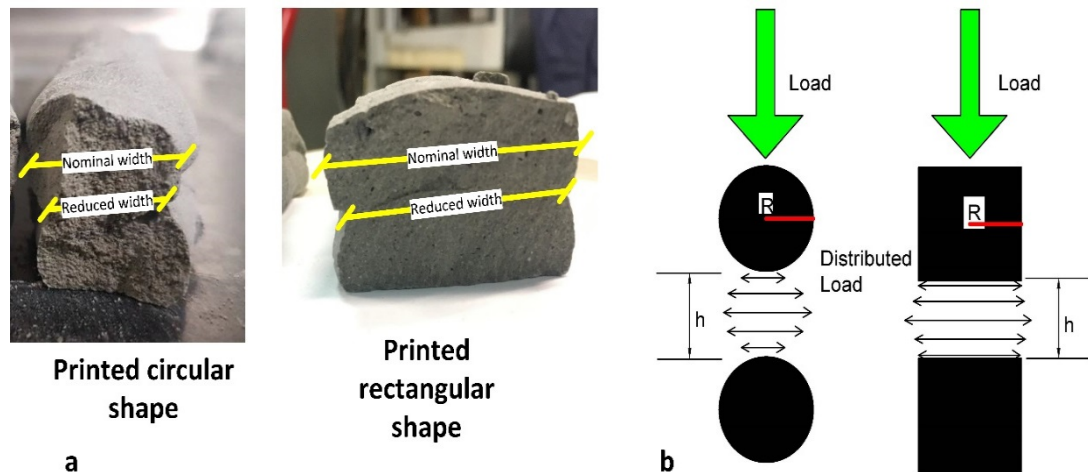


Figure 5. 32: (a) Real printed circular and rectangular shape; (b) Lubrication squeeze flow between two spherical particles (left) and two cubic particles (right) with an identical characteristic half-width, R (reproduced by (Cwalina, Harrison & Wagner 2016)).

Figure 5. 33, shows an object where one layer had two layers printed onto it. It was printed to measure its dimensional geometry and test its mechanical behaviour.



Figure 5. 33: (a) Three layers of the printed object; (b) One layer of the printed object.

For a printed object larger than 120 mm (more than 7 layers), the oscillation at the arm of the robot increased in the end-tip of the arm which is most related to joints 4 and 6 of the robot (Shakor, Renneberg, et al. 2017). Figure 5. 34 shows how the printed layers collapsed after 10 layers of printing.



Figure 5. 34: The movement of the robot arm has a major effect on the printing process, particularly when the height of the object increased to more than 7 layers.

Another challenge that was faced during the printing process was the use of a flat-based hopper, as shown in Figure 5. 35, where core-flow (rat-holing) occurred during the printing of the specimens. Some of the slurry close to the wall of the bucket is in a static state, while other parts of the slurry are in a mobile state.

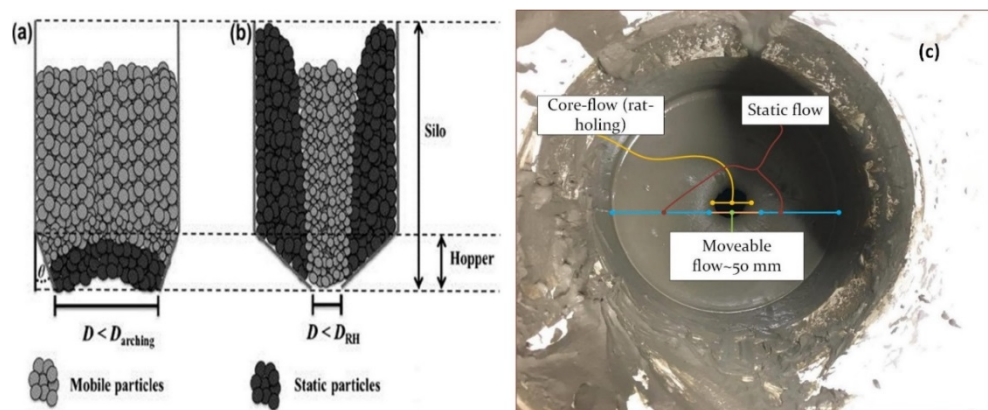


Figure 5. 35: Schematic illustration of flow problems encountered in hoppers, namely, arching and rat-holing, during (a) mass-flow and (b) core-flow, respectively, where D = outlet diameter, $D_{arching}$ = minimum arching diameter, D_{RH} = minimum rat-hole diameter and θ = hopper half angle (Crowley et al. 2014), (c) pictorial illustration showed the rat-holing flow in the bucket above the pump during pumping.

Figure 5. 36 shows a modified hopper angle of $\theta 45^\circ$ to improve flowability in the hopper. Generally, fresh concrete poured in place behaves as a liquid slurry (a viscoplastic

fluid with high yield stress). However, the internal structure of slow casting concrete/mortar when in a rest state leads it to flocculate. It also has the ability to resist the load from concrete cast over it without increasing lateral stress, despite the nature of the mould. Feys, Verhoeven & De Schutter (2009) explained that the (hydro-) clusters are assembled together and become moulded from certain shear stress on the critical shear stress. By increasing the shear rate, the viscosity of concrete increases proportionally. This state of fresh concrete/mortar is called shear thickening. When the temperature rises, the workability and slump of the concrete decreases. This is another reason that the mortar could not pass through the hopper effortlessly. The longer concrete or mortar remains in the hopper, the more advanced the reaction and the higher the increase in temperature, which subsequently leads to an increase in the viscosity of the mortar. A temperature rises from 21°C to 35°C was measured after 30 minutes of the mixing process.

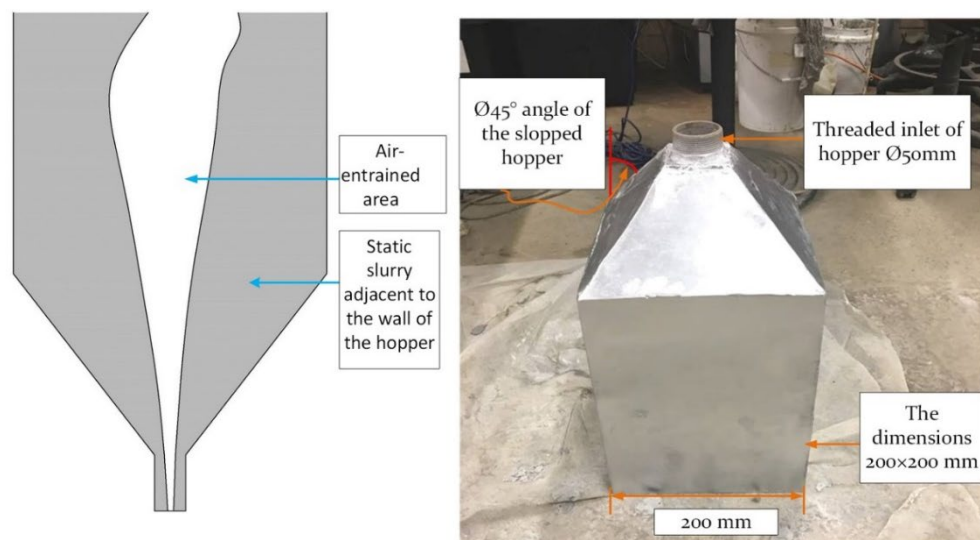


Figure 5. 36: The hopper with an angle of $\text{Ø}45^\circ$ and the core-flow concept.

Earlier studies explained the two types of powder flow pattern in the hopper: mass-flow and core-flow (Crowley et al. 2014). The most noteworthy is the core-flow that emerges while feeding the concrete through the pump to the robot. According to Fitzpatrick, Barringer & Iqbal (2004), the moisture content has a high impact on powder particles in

terms of flowability. Consequently, the surface forces between the powder particles or slurry and the wall surface have a major influence on the nature of the powder flow, see *Figure 5. 35*.

Figure 5. 36 shows a hopper with an angle of $\varnothing 45^\circ$, which reduced rat-holing but did not eliminate it completely. This rat-holing phenomenon happens due to the flocculates of the particles and maintains particles in the static state. Improving this situation requires consistent mixing in the hopper.

For most of the trials that were prepared in the experimental program, a set of prisms and cubes were prepared to validate the mechanical behaviour of the mixing property. The printed prisms were created by selecting trial 5 cementitious mortar as the mix proportion. The mortar printed with a caulking gun was tested for each of the layers from (1 to 4).

The outcomes suggest that waiting time between layers of 10 minutes is necessary due to surface moisture between layers (Marchment & Sanjayan 2018).

The printed part is shown in *Figure 5. 37*. Shrinkage cracks appeared on the printed part after one day (24 hours) of curings in the laboratory temperature environment. This crack has been observed after 12 hours. Further study is required to observe the occurrence of the crack. In addition, digital image correlation would be helpful to indicate the location and size of the crack. To reduce the cracks so the printed materials are stronger and exhibit fewer shrinkage cracks, chopped strand fibres (polypropylene and glass) were introduced.

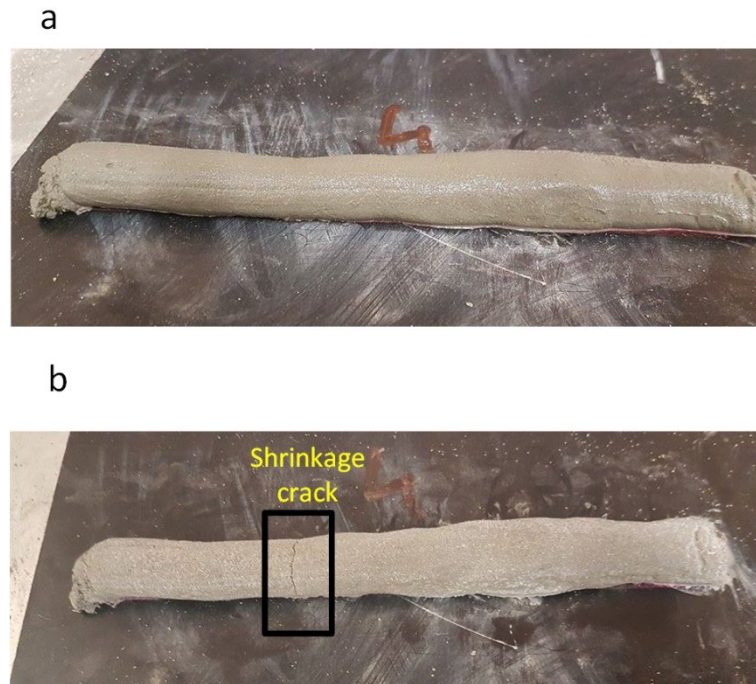


Figure 5. 37: (a) The printed part immediately after printing; (b) The printed part after one-day drying.

5.5.1 End-Effector Speed-Slurry Discharge/Line Width Relationship

Vision-based sensing has been incorporated into systems for 3D printing with a robotic arm. Using image analysis techniques, a map of the printed structure is generated throughout the process, allowing comparisons to be made between the computed path of the robotic arm and the actual location of the material placed (Sutjipto et al. 2019). The Sutjipto et al. (2019) study would be useful in mortar and concrete printing to measure the accurate distance, discharge the slurry flow and speed of the robotic arm in different angles of orientation. However, this particular technique requires further investigation to discern the effects of robot end-effector travel speed and trajectory shape, as well as feed pump properties (Lim et al. 2011; Tay et al. 2017; Teizer et al. 2016; Utela et al. 2008). Therefore, this must be studied to identify the safe zone based on the robot's speed. According to the study by Beauchamp et al. (1991), the safe zone for the time necessary

to reach the stop button for the total overrun distance is 100 mm/s for a 1 second period per 200 mm total distance.

It is important to work in a safe environment given that the robotic arm, as artificial intelligence, involves in human life. The study of Beauchamp et al. (1991) explained the safe zone of the robotic arm motion. They identified that the motion speed of 100 mm/s in a robot overrun distance was almost in the safe zone (below 200 mm) when the reach time was equal to or less than 1 s. Therefore, our study adopted a safe zone of less than 100 mm/s (> 40 mm/s). In this study, we adopted a speed limit of 34.99 mm/s to print the prismatic and cubic specimens. Therefore, all the parts were printed in a safe zone of less than 100 mm/s.

The main transition path is taken by the robot-mounted extruder referred to as the 'horizontal and vertical test', is shown in *Figure 5. 38*. The path was determined by the desired thickness of the layer which is reflected in the choice of the mortar mix proportion, speed of the end-effector and the pump flow rate. It consisted of a series of rows of approximately 330mm in length printed next to each other for the prism specimens and 100mm length for the cubic specimens.

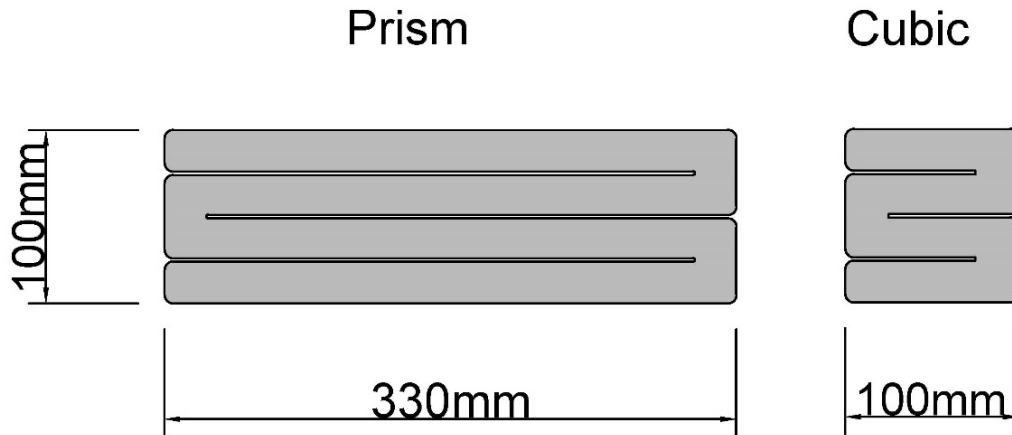


Figure 5. 38: Horizontal printed path cross-section “four lines printed specimen”.

Based on the examined specimens, we observed that the structural outcomes were also influenced by the motion of the end-effector. A discussion of the result of the end-effector velocity in relation to the slurry discharge and the width of the printed lines is presented below.

Figure 5. 39 shows the corresponding print outcomes for various defined speeds. It was observed that end-effector velocities of 34.99 mm, 46.56 and 60.32 mm/s yielded ideal specimens when considering the shapeability and continuity of the print line. The corresponding printed line width of each end-effector velocity can be seen in Table 5. 22.

Table 5. 22 End-effector velocity for the robotic arm for the printing mortar

GUI speed (%)	End-effector speed (%)	End-effector velocity (mm/s)
20%	2%	11.96
20%	4%	23.78
20%	6%	34.99
20%	8%	46.56
20%	10%	60.32
20%	12%	70.97
20%	14%	81.88
20%	16%	98.88

It was observed that an end-effector speed of 60.32mm/s exhibited slight shrinkage of the specimen, resulting in cracks on the surface of the fresh mortar sample. Consequently, this speed was not ideal for this system setup. The ideal end-effector speeds for the mortar mix design explored in this study were in the range of 34.99 mm/s to 46.56 mm/s. *Figure 5. 39* demonstrates that end-effector speeds below 34.99mm/s and greater than 45.56mm/s resulted in specimens with cracks, discontinuous print segments and undesired structural shapes. These results support the work undertaken by Thrane, Pade & Nielsen (2009) and Buswell et al. (2018), who postulated that specimens have a close plastic viscosity and yield stress (21.1 Pa.s) and (0.27 kPa), respectively.

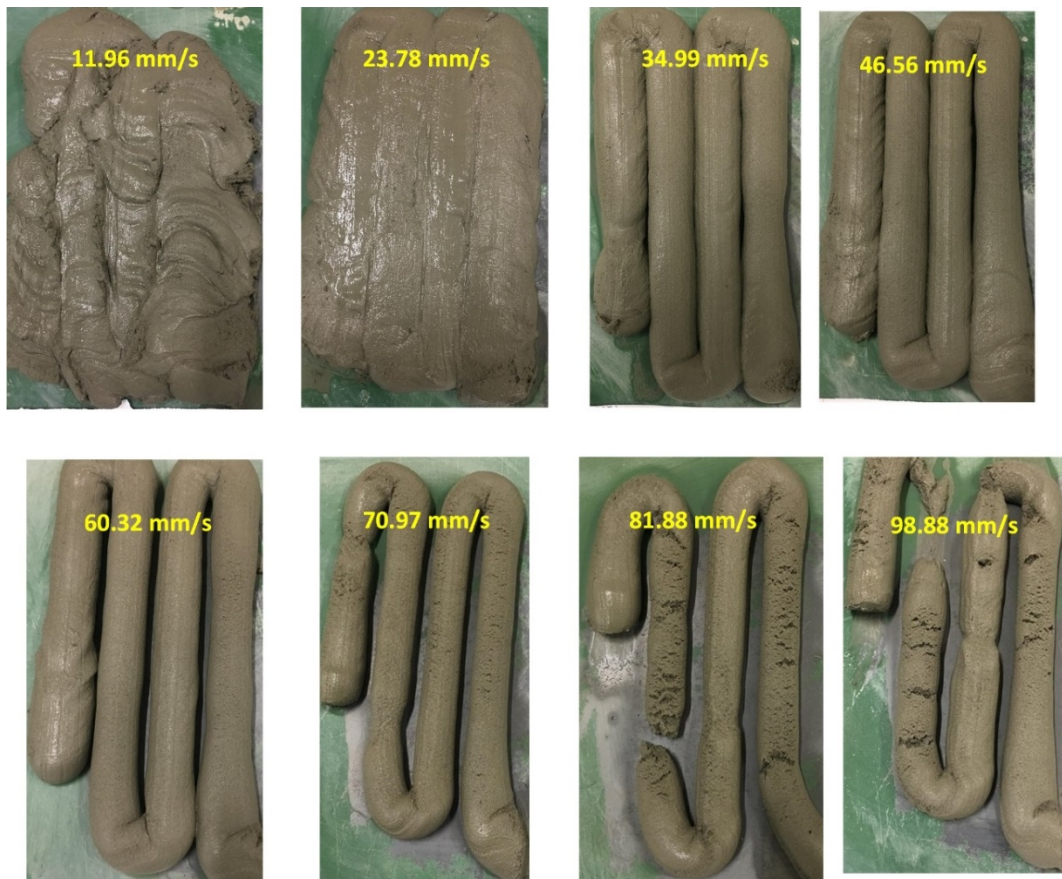


Figure 5. 39: A series of photographs showing the results of the various speed of end-effector, resulted in various shape in the printing line outcomes.

5.5.2 Regression Relationship for Velocity and Slurry Discharge

The regression relationship is significant in showing the region (window) of printability of mortar materials versus the velocity of the robotic arm while the pump velocity is steady. *Figure 5. 40* shows the power regression relationship for the velocity and slurry discharge at the end-effector of the robot. The best fit relationship for the velocity and slurry discharge of mortar from the nozzle can be defined by a power regression relationship. This is become the best fitting trendline due to the R^2 which is 0.98. R-squared is a data measurement displayed as a fitted line. Its closeness to the regression line is then examined. It is also identified as a determination coefficient. In regression, a fitted line value closer to 1 predicts a precise fit. This term is corrected after comparing the residual values with the fitted value plot. The ideal value for the slurry output mass can be determined using Equation (5.21):

$$Y = 28996 * X^{-0.884} \quad (5.21)$$

Where Y describes the slurry output mass (g) from the nozzle, and X describes the velocity (mm/s) of the end-effector of the robot. In the regression model in non-linear allometric model type (power regression), by increasing the velocity the slurry output decreases non-linearly which makes it more suitable for printing of concrete and structural components.

This study demonstrated the effect of the robot end-effector velocity on the printed mortar line width and slurry output mass. It also highlighted the effect of glass fibre on printed mortar specimens.

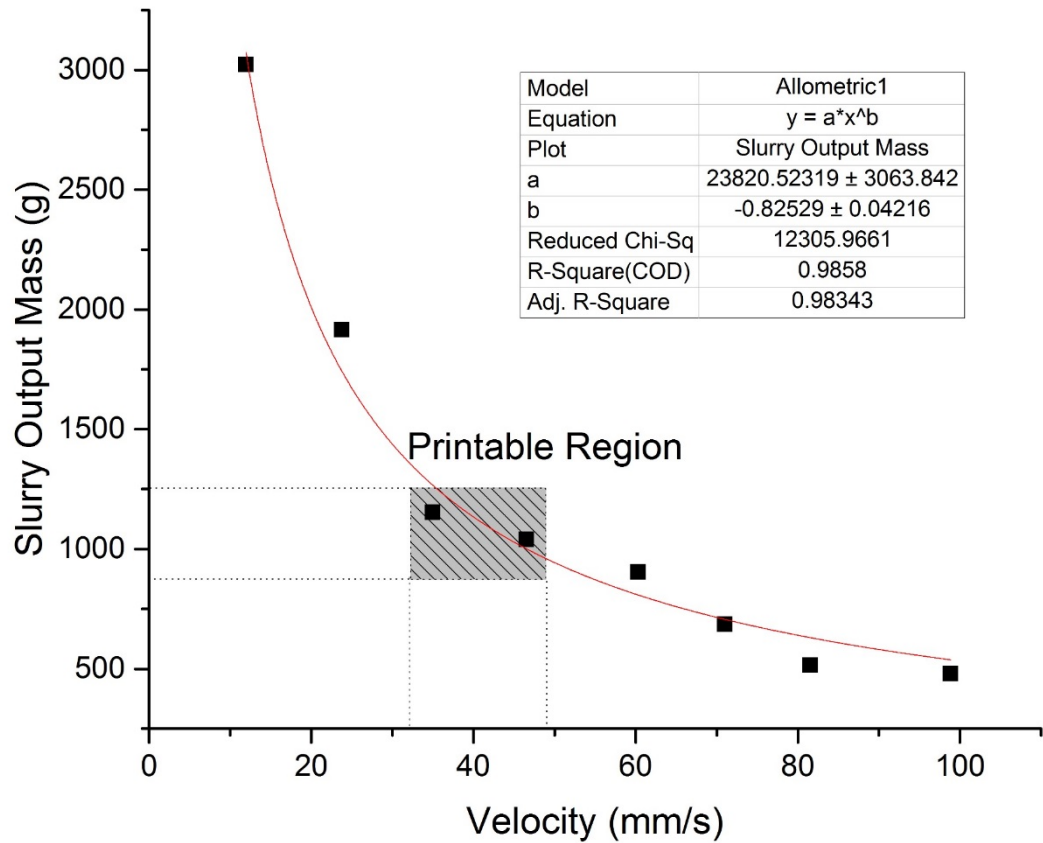


Figure 5. 40: Power regression relationship between velocity and slurry output mass of the mortar for the printed line.

To sum up, this chapter explained the experimental methodology of the two printing technologies for construction applications. The mechanical behaviour and materials properties of the cementitious materials in the fresh-state and hardened-state have been investigated in detail by using both powder-based and extrusion-based 3D printing technologies. The analytical relationship of the material properties and robot planning program have been discussed also in this chapter.

CHAPTER SIX 6. EXPERIMENTAL RESULTS AND DISCUSSIONS

6.1 Results and Discussions - 3DP Parts

An extensive experimental program has been performed for both powder-based and extrusion-based 3DP techniques and the printed specimens were monitored under the test. This chapter contains a discussion and interpretation of the experimental program results for both the powder-based and extrusion-based 3DP techniques.

6.1.1 Powder-based (inkjet) 3D Printing Materials

Powder-based 3DP objects which were printed in this study were subjected to various tests, one of which including the compressive strength test. The compressive strength test results of the cubic samples are illustrated in *Figure 6. 1*. The sample description appears in *Table 5. 2*. The results show that when the shell and core had similar saturation levels, the compressive strength of 3DP specimens increased gradually when the saturation level increased (*Figure 6. 1*). This is quite different from the results obtained by manual mixing of cement with water, which resulted in lower strength at a high w/c (saturation level) ratio. All the tests were conducted using a Tecnotest machine (300 kN, Italy) and Shimadzu machine.

At the same saturation level (shell and core) of the sample (S100-C100-LW), 100% to (S170-C170- LW) 170% compressive strength increased incrementally from 3.08 MPa to 8.26 MPa over a 28-day period, (refer to *Table 5. 2*). This is almost 37% higher than the lowest saturation level of 100%. It could be linked to porosity because, when porosity increased, strength declined. Such large open pores affect the strength of specimens while they are being cured in water, which made weaker bonds among particles. However, there was not enough reaction between the cement particles when specimens were being

printed. Furthermore, CAC contains a large amount of alumina filler that leads to a demand for more water and hydration on a quicker basis (Klaus, Neubauer & Goetz-Neunhoeffler 2016). As a result, those particles are unbound from the printed specimens due to not properly hydrated.

The maximum saturation level in the ZP150 and ProJet360 printer was 170% for the shell and 340% for the core (S170-C340) and this saturation level could not be increased. Hydration, therefore, could not increase between the cement particles. Maier et al. (2011) claimed that the limited amount of water released from the printer head means that the process will not achieve sufficient strength for the specimen. The 3DP samples had less strength than the hand-mixed samples, as shown in *Figure 6. 1* and *Figure 6. 2*.

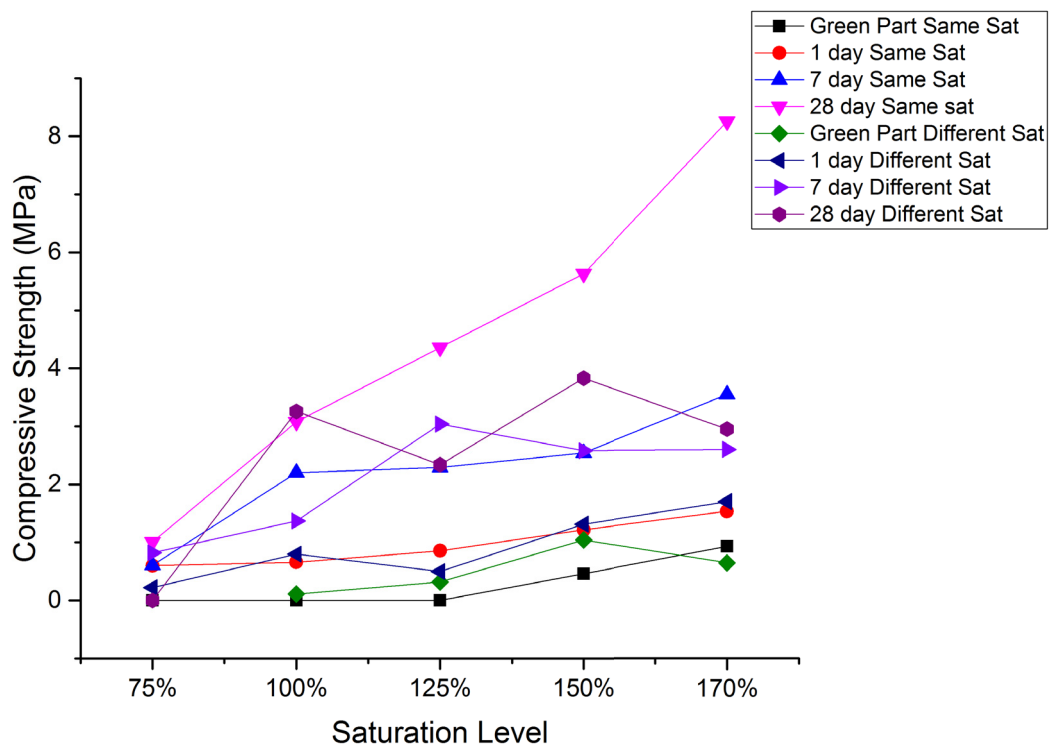


Figure 6. 1: Compressive strength of 3DP cubic samples with lithium carbonate.

It is obvious from *Figure 6. 1* that, for different saturation levels, the optimum strength is 3.83 MPa at the saturation level of the sample (S150-C300-LW) in 3DP samples cured for 28 days. This may be due to the level of porosity between particles where the

saturation level is minimal. As shown in *Figure 6. 2*, lower water ratios for hand-mixed samples resulted in greater strength. The tests were applied at all saturation levels after the ratio of saturation levels was converted to the w/c ratio.

Figure 6. 2 shows that at the saturation level of w/c 0.31 for the sample S100-C200, the highest compressive strength was obtained as 19.05 MPa. According to Feng et al. (2015), in 3DP of the samples in different directions have an impact on compressive strength. They contend that the speed of printing in the X-direction is faster than the other directions.

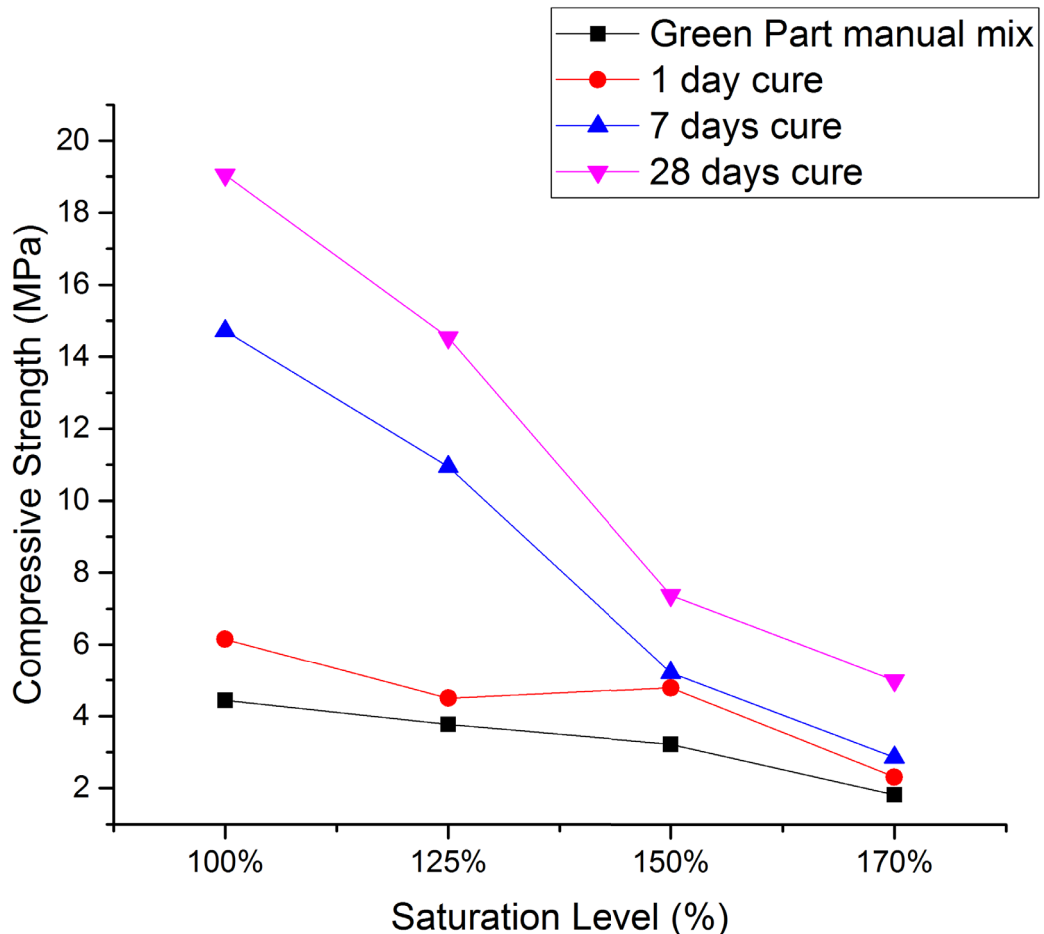


Figure 6. 2: Compressive strength of hand mixed cubic samples.

Furthermore, the time taken to print adjacent layers in the Y-direction is shorter than printing adjacent layers in the Z-direction. The level of the bond between two parts of the

particles is thereby higher for shorter print times, resulting in higher strength in a continuous strip rather than the strip in between. In this study the load was parallel to the Z-direction and, when this load was applied, cracks passed through the interior strip in the vertical direction *Figure 6. 3*. It was also found that in the 3DP cubes the lateral sides became spalled and ruptures occurred due to crushing.



Figure 6. 3:(50 × 50) mm diagonal crack inside the Z-powder specimen.

Table 5. 2 shows that using different curing agents, such as calcium hydroxide $\text{Ca}(\text{OH})_2$, did not alter the specimens' strength. The results for compressive strength are similar to results for samples cured in water. Tests were conducted to assess the compressive strength of CAC & OPC without lithium carbonate, as shown in *Figure 6. 4*. The same saturation levels of the shell and core of the samples S75-C75-OW to S170-C170-OW (see *Table 5. 2*), increased the materials' strength from 1.065 to 3.33 MPa after curing for 28 days, respectively. This is three times higher than the minimum saturation level. However, the optimum strength at different saturation levels after 28 days curing for the

sample S100-C200-OW recorded the highest compressive strength as 3.32 MPa. It is obvious that these differences were due to changes in the saturation levels of the 3DP specimens.

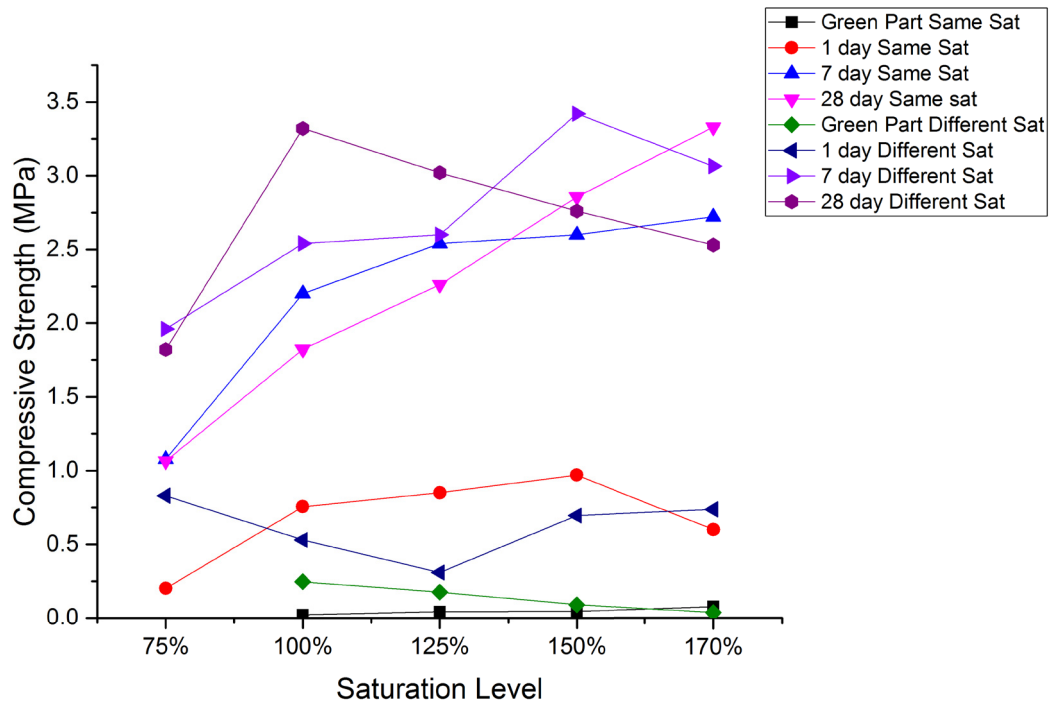


Figure 6. 4: Compressive strength test of 3DP cubic specimens without lithium carbonate (Li_2CO_3).

The porosity of the cubic samples was checked according to the Australian Standard (AS1774.5:2014 2014). The results show that by increasing the saturation level, total apparent porosity decreases in 3DP specimens. Maier et al. (2011) stated that capillary pores and other large holes are mainly responsible for the reduction in elasticity and strength. They also found that, after curing for 72 hours, an intermixed crystal network develops and this fills up the pore spaces and minimises the total porosity. Figure 6. 5 illustrates the variation of porosity in 3D printed samples at different and/or similar saturation levels when using lithium carbonate and without lithium carbonate. The lowest level of porosity was recorded at the different saturation levels of samples at S170-C340-LW, details of the samples in Table 5. 2.

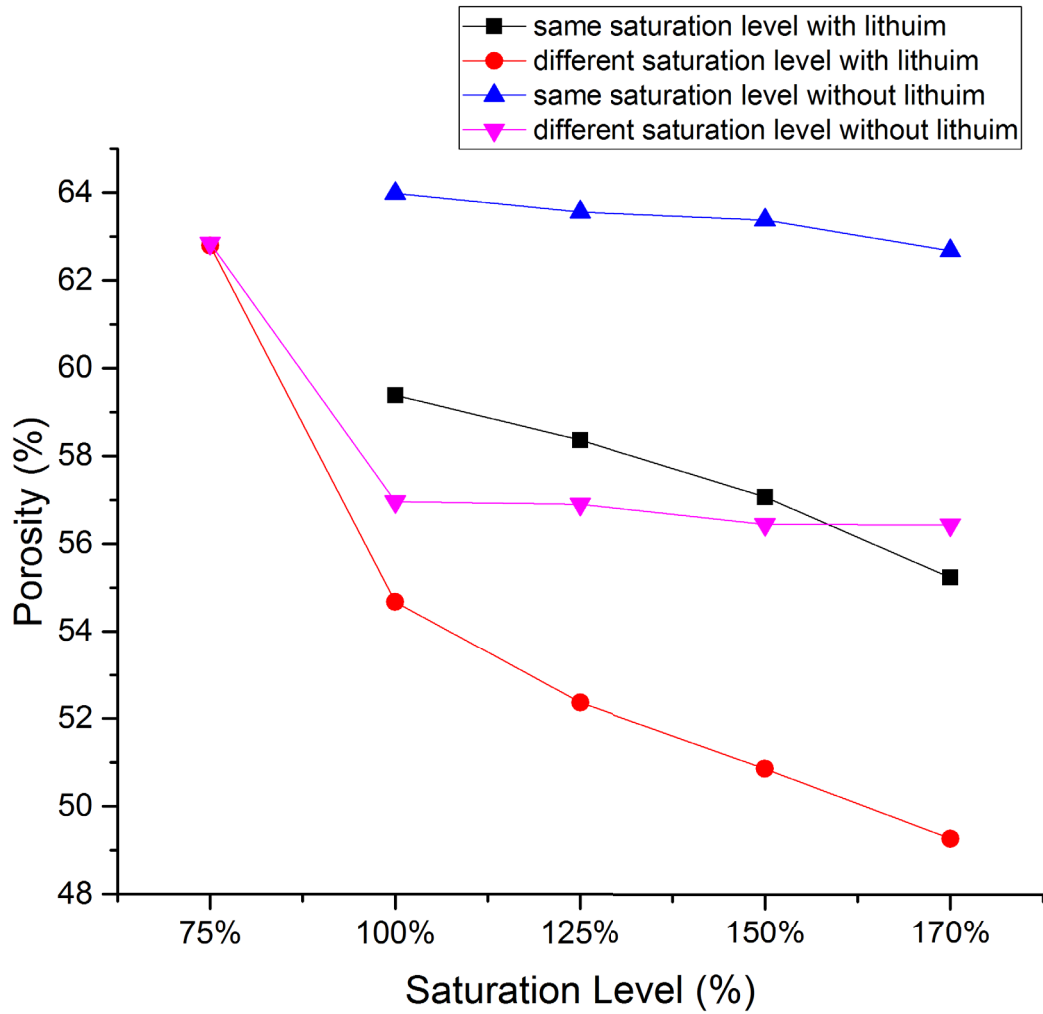


Figure 6. 5: Porosity of 3D printed samples.

Figure 6. 6 shows the results of the Scanning Electron Microscope (SEM). It exhibits the porosity between particles of the printed cubic specimen. Plate-like large crystal growths occurred, with some other unreacted particles on the surface of the specimens. Furthermore, deep holes and incohesive particles on SEM can be seen on the left and right side of Figure 6. 6. It is evident that hydration was not completed between the cement particles.

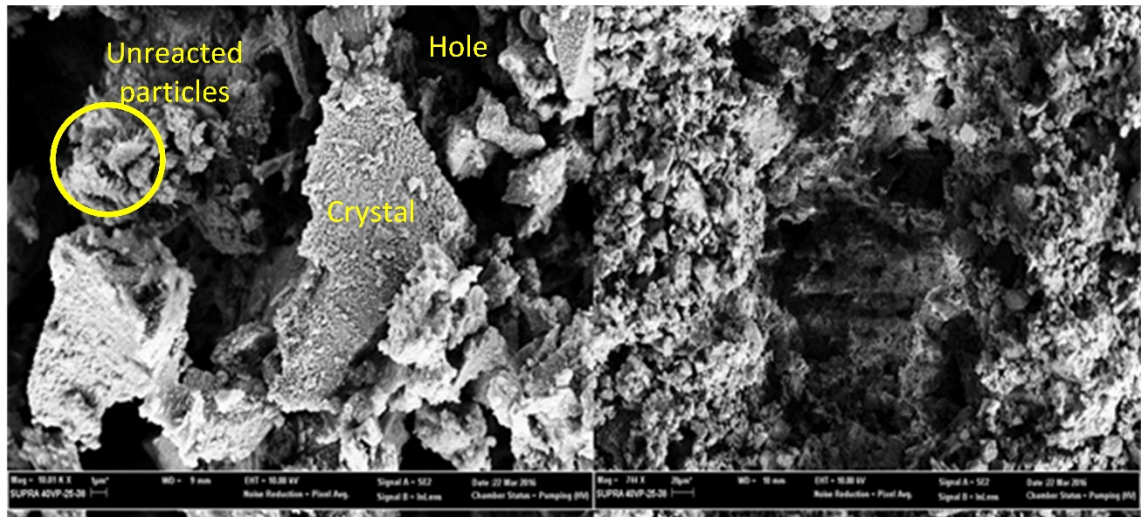


Figure 6. 6: SEM image of 3D printed samples (left (1 μm) right (20 μm)).

3D profiling detected the porosity of specimens. As shown in *Figure 6. 7*, different saturation levels of specimens with different magnifications were tested to explore the porosity and surface roughness of the samples. The test was conducted employing 3D profile Veeco (Dektak) at the following magnifications: 2.5 \times , 20 \times and 50 \times . The clear porosity and haphazard surface shape of the 3D-printed specimens are visible in *Figure 6. 8*. The same sections of the samples were monitored in the side layer (Z-direction, the vertical direction in 3DP) for the green part and the cured samples in water. After 7 days the cured samples in water were scanned using the 3D profile and showed pits (porous holes) on their surface area. The topographical shape of height distributions changed dramatically. It shows the value of skewness (Ssk) after curing, with most samples having positive signs. This means many high spikes appeared on the surface. The Ssk parameter correlated with load bearings and porosity. According to Petzing, Coupland & Leach (2010), the Ssk is zero when the height distribution has a symmetrical surface. This is validated by the centre line for symmetrical and unsymmetrical purposes. So the direction of skew is differentiated above the mean line (negative skew) or below the mean line (positive skew). *Figure 6. 8* shows that the samples released and left many particles, with clear pits on the surface of samples cured in water.

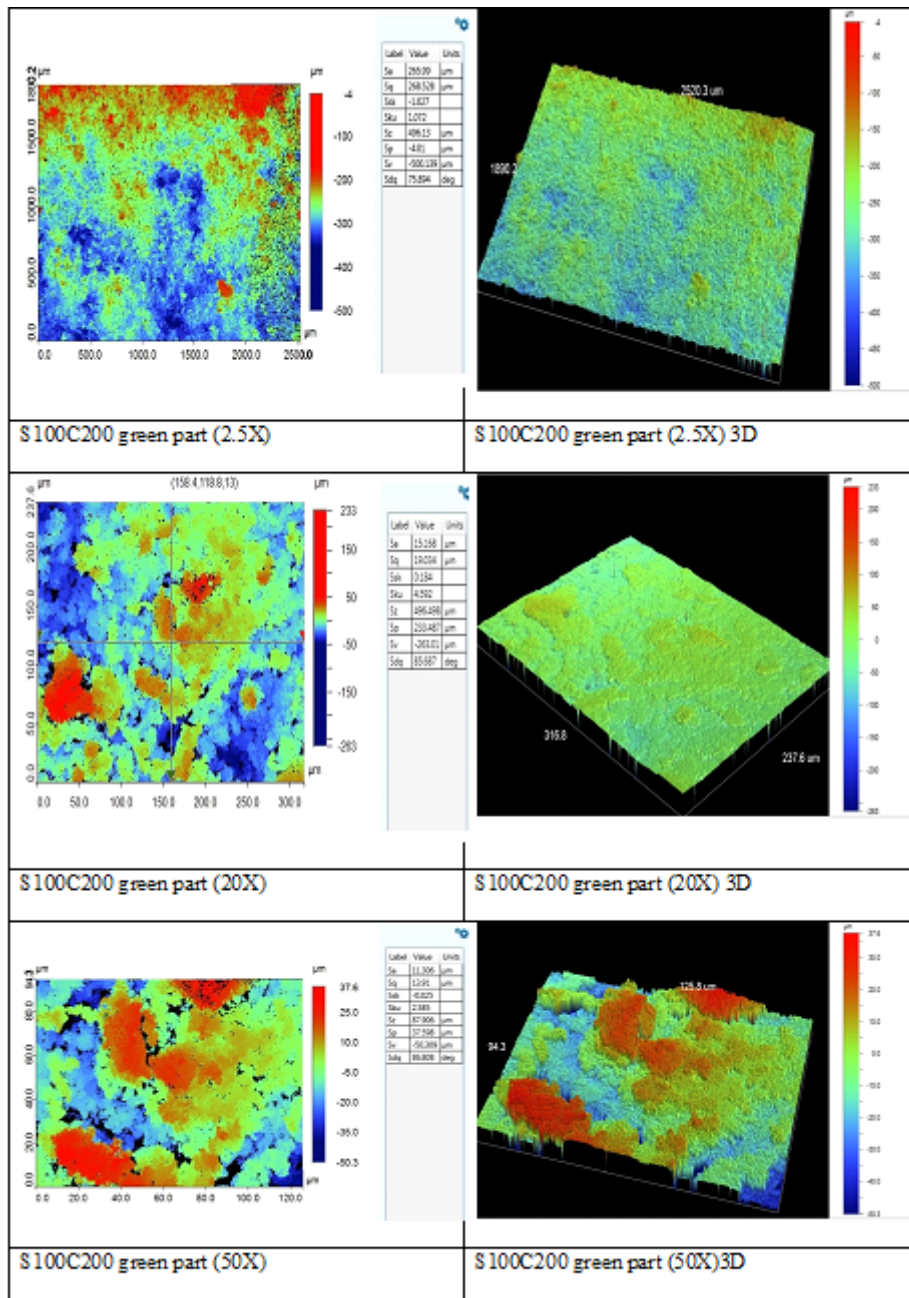


Figure 6. 7: 3D profiling for 3D printed samples.

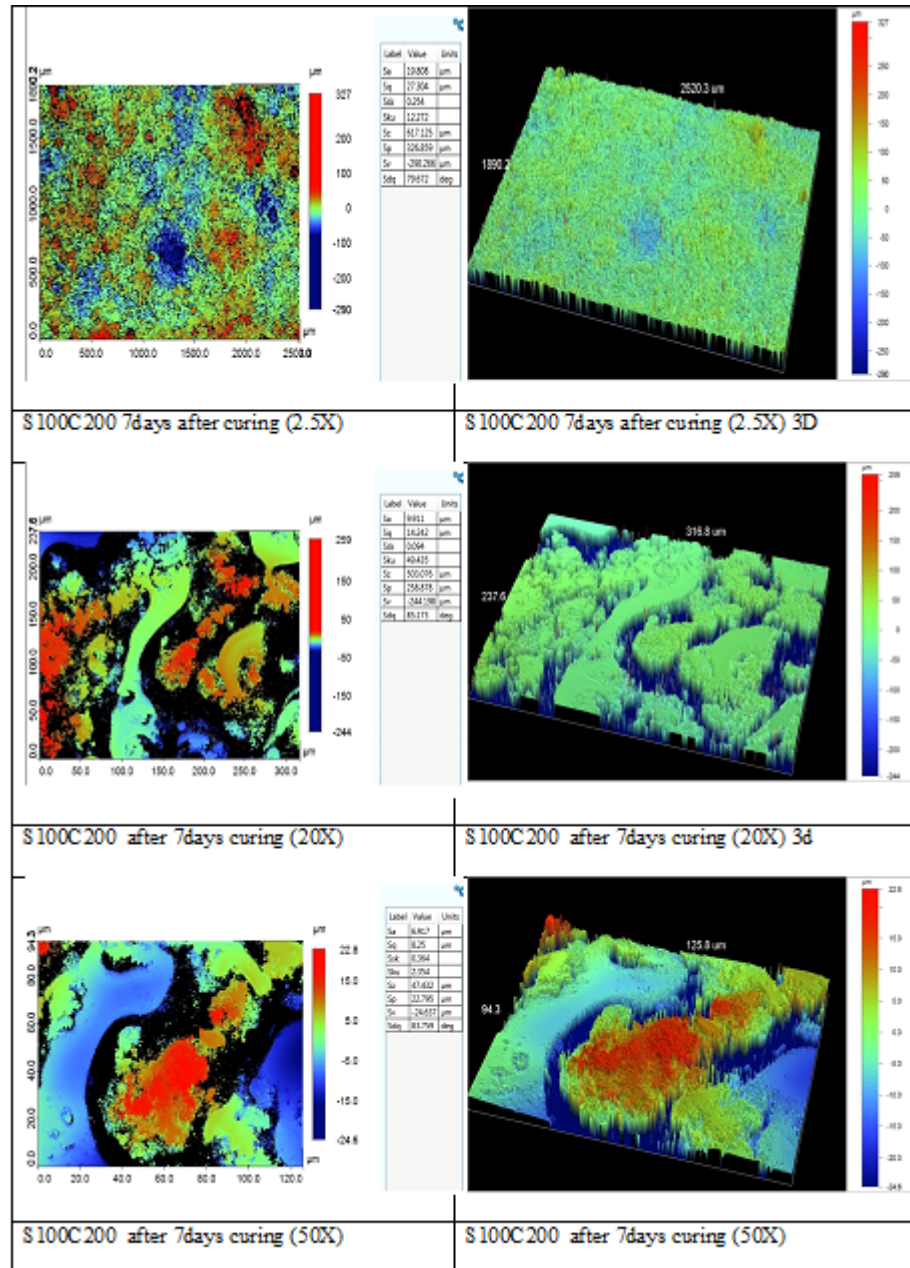


Figure 6. 8: 3D profiling for 3D printed samples after 7days curing.

In general, the 3DP process is complex and many studies continue to focus on the formulation of different materials. According to this study, the 3D printed cubic specimens did not produce high compressive strength due to open pores between the layers and strips which were not completely filled. This led to less compressive strength. Neither the powder consisted of CAC passing through a sieve of 150µm and OPC has achieved enough strength in 3DP specimens.

One reason may be that the amount of water (binder) from the printer was not sufficient to hydrate all particles of the material. The morphology of the particles and the presence of interparticle pores could be another reason. Furthermore, fine particles of cement increase the contact angle and reduce the powder's wettability (Kirchberg, Abdin & Ziegmann 2011).

It should also be noted that the binder was not pure water as it included about 5-10% of polyvinyl alcohol or glycerol (humectant) or methanol (20% volume of binder). The research of Sun et al. (2013) used nozzles of 30 mm to print the layers of ink on glass to control ink solidification and used solvent materials in water evaporation (boiling point 100°C) during the printing process to induce partial solidification, while ethylene glycol (b.p. 197.3 c) and glycerol (b.p. 290 c) acted as humectants. That humectant is not suitable for use as a mixed water-based binder because it reduces the compressive strength of cementitious materials.

This research was also developing a method to fabricate a stronger sample. However, in the authors' earlier study, Shakor, Sanjayan, et al. (2017), the ZPrinter powder was modified and the w/c ratio for the manual mix was investigated. It was found that it is not possible to obtain consistent and acceptable mechanical properties in the produced printed samples for construction applications. In the previous study, it was also found that the maximum compressive strength can achieve up to 8.26 MPa after 28 days when the samples were cured only in water. In the current research, we changed the curing medium of the printed sample to obtain better outcomes. Although the green samples should have enough strength to hold their shape while handling and removing the excess material. Dimensional accuracy was another concern. The 3DP samples did not have the exact dimensions of the original CAD design model. To examine and monitor the overall parts

of the fabricated cubic and prism specimens for compressive and flexural strength, the external dimensions of each sample were measured accurately using a digital calliper with an accuracy of 0.01mm. The weight of the specimen was also measured on a precision scale with an accuracy of 0.001g.

This research also investigated how the saturation settings influenced the strength of the cement component powder. It was revealed that the flexural strength in the X-direction had the highest strength (approximately 6.21MPa) since it required the least number of layers to be constructed in this direction compared with the other directions (axes) (refer to *Figure 5. 16*). This is consistent with the study by (Farzadi et al. 2014) and was due to the acceptable coincidences between layers in this direction where the movement was parallel to the printer head. As an illustration, Castilho et al. (2011) stated that 3DP scaffold stiffness decreased when the number of elementary units (layers) increased. This suggestion was also proposed by (Vaezi & Chua 2011). Therefore, in the present study, a similar thickness was used. The literature also supports the case that a higher saturation level leads to a higher compressive strength (Shakor, Sanjayan, et al. 2017). Experimental work by Vaezi & Chua (2011) found that increasing the binder saturation level from 90% to 125% increased the sample's flexural and tensile strengths and this was also confirmed by the present study (Shakor, Nejadi, Paul, Sanjayan & Nazari 2019).

The existing work used a print layer thickness of 0.102 mm. Most of the particle sizes used were less than 0.1 mm. According to Withell et al. (2011), an increase in the layer thickness requires a higher saturation level to ensure complete cohesion between the layers. In this work, the fast-axis mounted print head, which was set on a default speed, could build 2-4 layers in 60 seconds. The three-point bending test equipment was custom made to test the flexural strength of 3DP specimens by ignoring friction. According to

ASTMC293/C293M (2002), flexural strength is approximately 10-20% of the compressive strength value. This depends on the size, volume and type of the coarse aggregates that are used. The samples of (60×5×5)mm were put on a simply supported edge with the exact dimensions of 50 mm centre to centre. To evaluate the flexural strength of printed specimens, manually-mixed samples were prepared with the same dimensions and compacted. It is noted that flexural strength in the manual mix at a saturation level of (S125C250) was recorded as the highest result among all the specimens, at approximately 9.77 MPa (see *Figure 6. 9*). This result suggests that, due to sufficient vibration in the normal mix, the outcomes were higher than for the 3D printed samples. The dimensions of the specimens were found to have a significant impact on the results. The specimens were produced in accordance with printer constraints, similar to those of Feng, Meng & Zhang (2015) who produced their samples in a similar way.

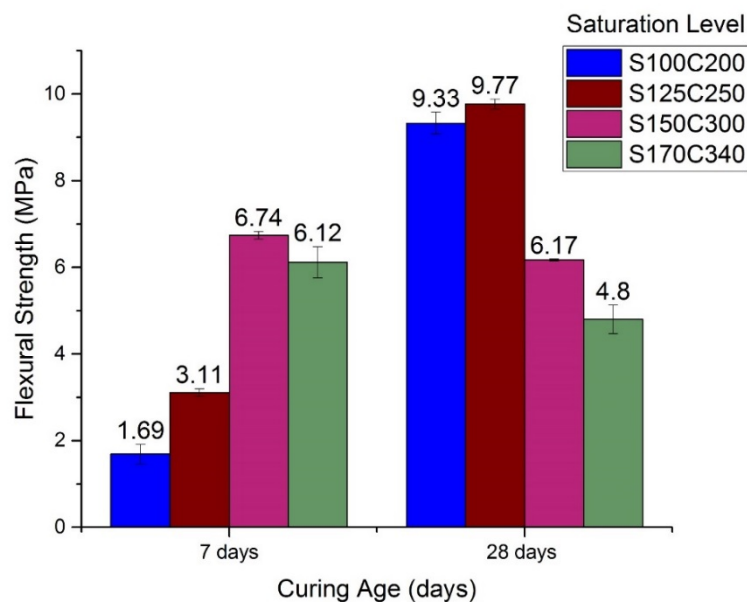


Figure 6. 9: Flexural strength of manual mixture cementitious prism specimens.

The specimens of (60×5×5)mm were tested for flexural strength (results are shown in *Figure 6. 10*).

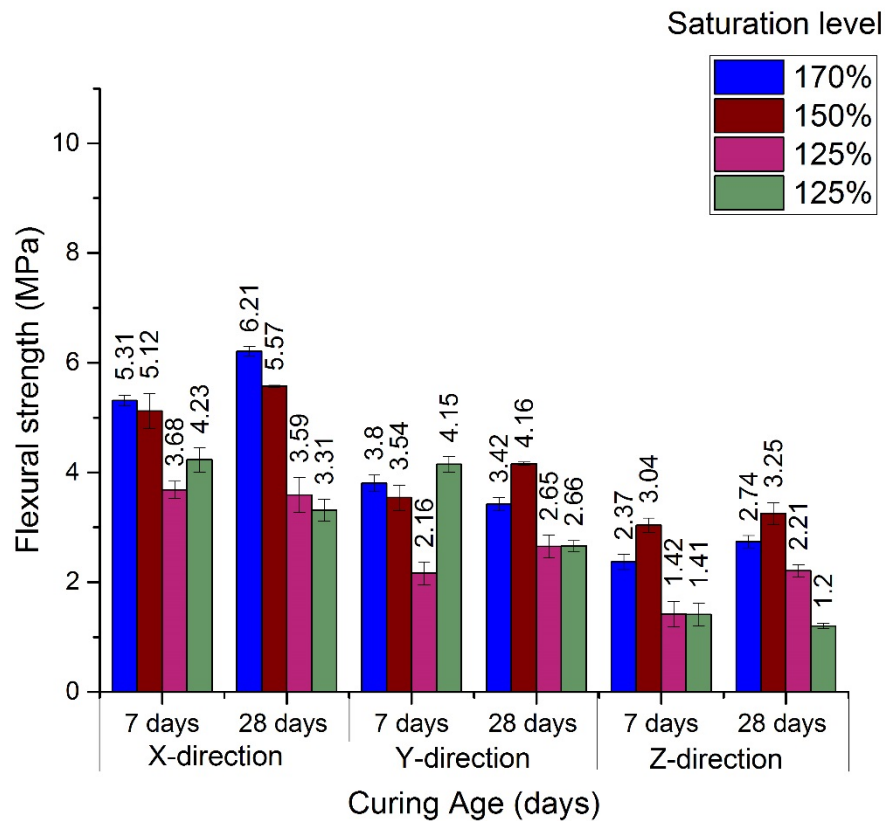


Figure 6. 10: Flexural strength of cementitious printed prism tested in different directions (X, Y, and Z) and saturation levels.

Other samples with dimensions of (70×10×4)mm were also subjected to the three-point bending test to measure their bending strength. In Figure 6. 11 and Figure 6. 12 the results of the bending strength test are illustrated, with the sample in the YZ plane at 0° (termed YZ 0°), see Figure 5. 15. The sample was then rotated 90° in the YZ plane (YZ 90°). The finding of the preliminary flexural strength test for the (YZ 0°) samples was that the strength of bending increases when the saturation level is increased.

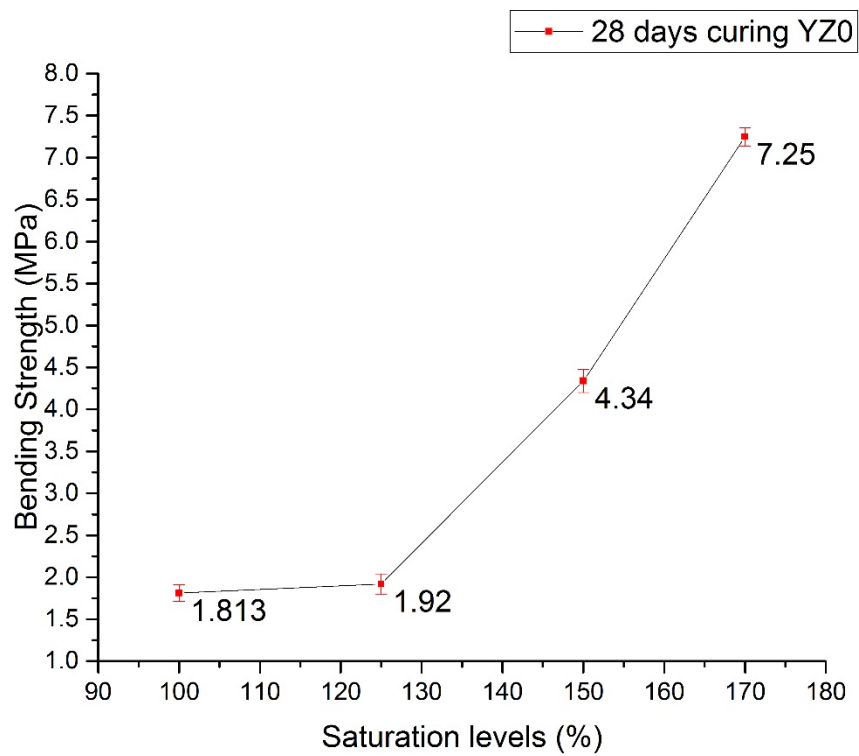


Figure 6. 11: Flexural strength of cementitious prism samples when it tested in (YZ0°).

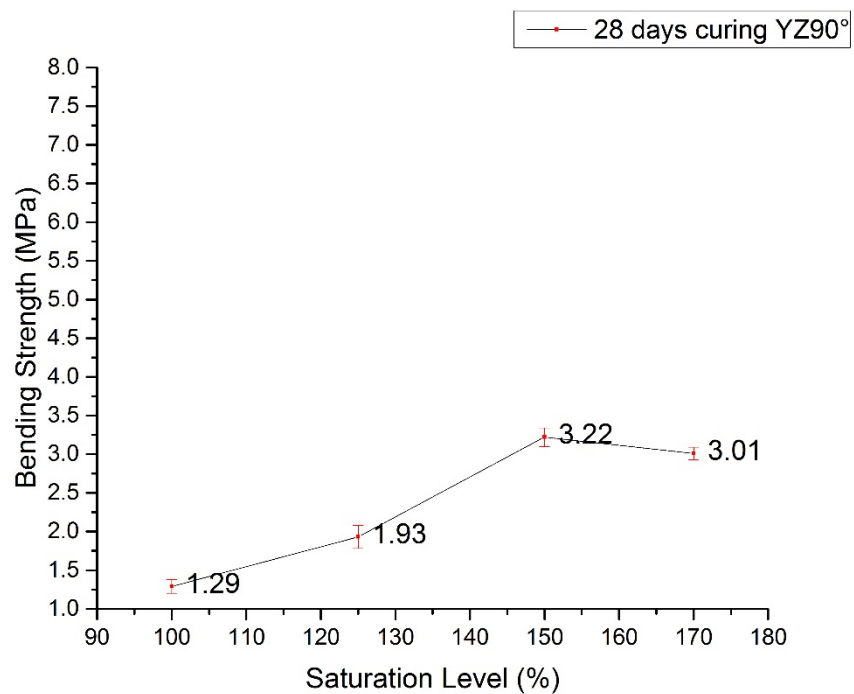


Figure 6. 12: Flexural strength of cementitious prism samples when it tested in (YZ90°).

Figure 6. 13 shows that the maximum peak point of bending strength of (YZ 0°) was (7.25±0.11 MPa). It can be seen that the sample printed in the plane (YZ 0°) could resist more bearing loads because it needed less time to print the samples than those that were printed in (YZ 90°). Furthermore, the largest part printed in the X-direction or plane of (YZ 0°) had stronger mechanical properties than when printed in the other directions. Previous work by Withell et al. (2011) is consistent with the finding that the X-direction (YZ 0°) has the best results for flexural strength.

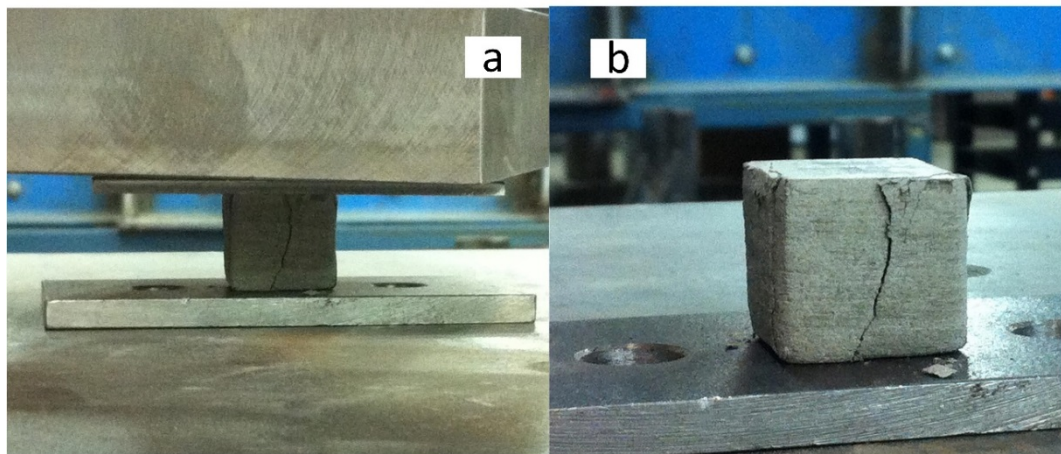


Figure 6. 13: Cementitious cube (a) sample under uniaxial compressive strength test, (b) after removal from the uniaxial compressive strength test.

Figure 6. 12 illustrates the optimum bending strength (YZ 90°) at S150C300. It was recorded as the highest point of deflection (3.22±0.12 MPa) however, overall, it still had less strength than (YZ 0°). It was noted that this specimen was more fragile than specimens printed in the other plane. This was because printing in (YZ 90°) took longer and left a large number of voids between the particles of the powder.

Research by Vlasea, Pilliar & Toyserkani (2015) found that the different layer orientation had an effect on the mechanical properties of the printed scaffold. Similarly, Miguel et al. (2013) produced almost the same results. In the present work, all the cubic samples were

tested parallel to the X-direction (0°), except for the prisms, which were tested in different directions.

The present research found that the curing parameters had a significant impact on the mechanical properties of the materials' composition. All the tests used the Tecnotest machine (50kN, Italy) and Shimadzu machine (50kN, Japan) as shown in *Figure 6. 13*.

Figure 6. 14 shows how the 3DP samples changes in conditions of high temperature in two types of curing scenarios. Compressive strength was tested according to ASTM (ASTMC39 2001).

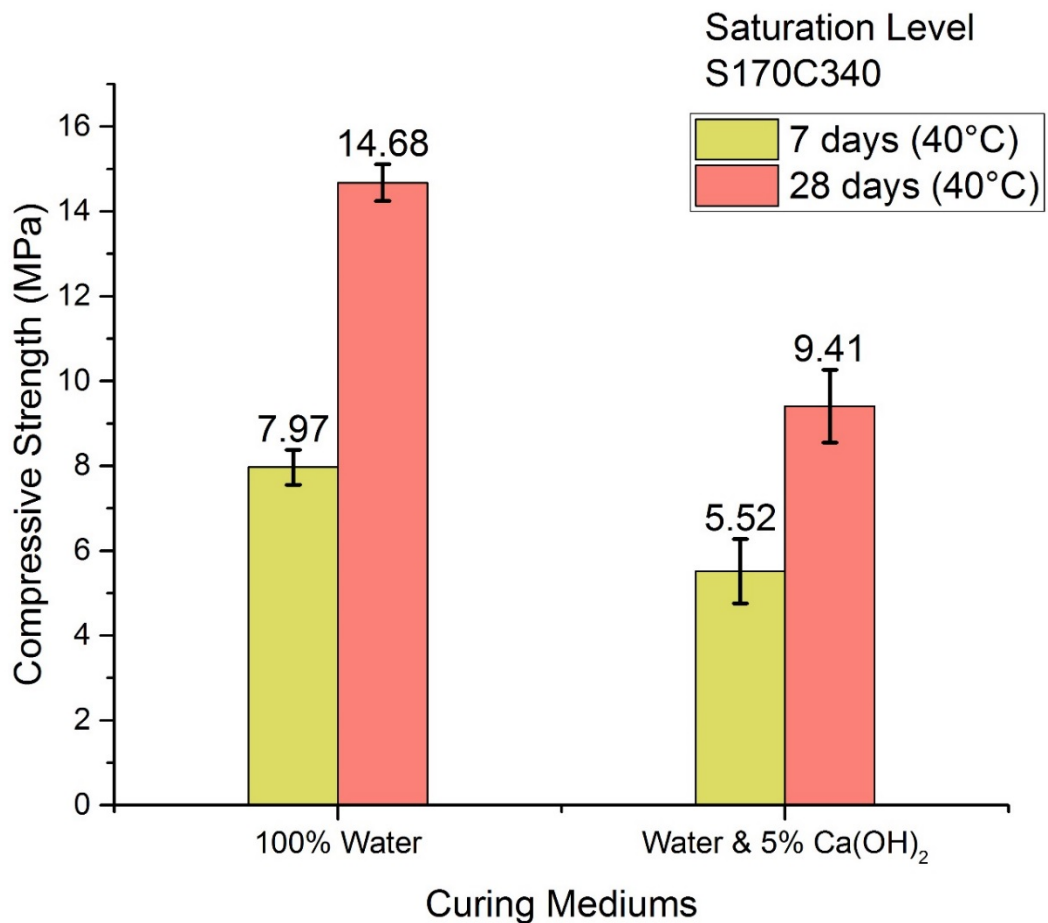


Figure 6. 14: Compressive strength of cementitious cube at different curing conditions and saturation level S170C340.

In the present study, the highest compressive strength was recorded as 14.68 ± 0.43 MPa when compared with other recorded samples that were cured without drying at a high temperature which was recorded as 4.81 ± 0.86 MPa. This is presented in more detail in *Figure 6. 15*. Boxes represent the mean \pm standard deviations.

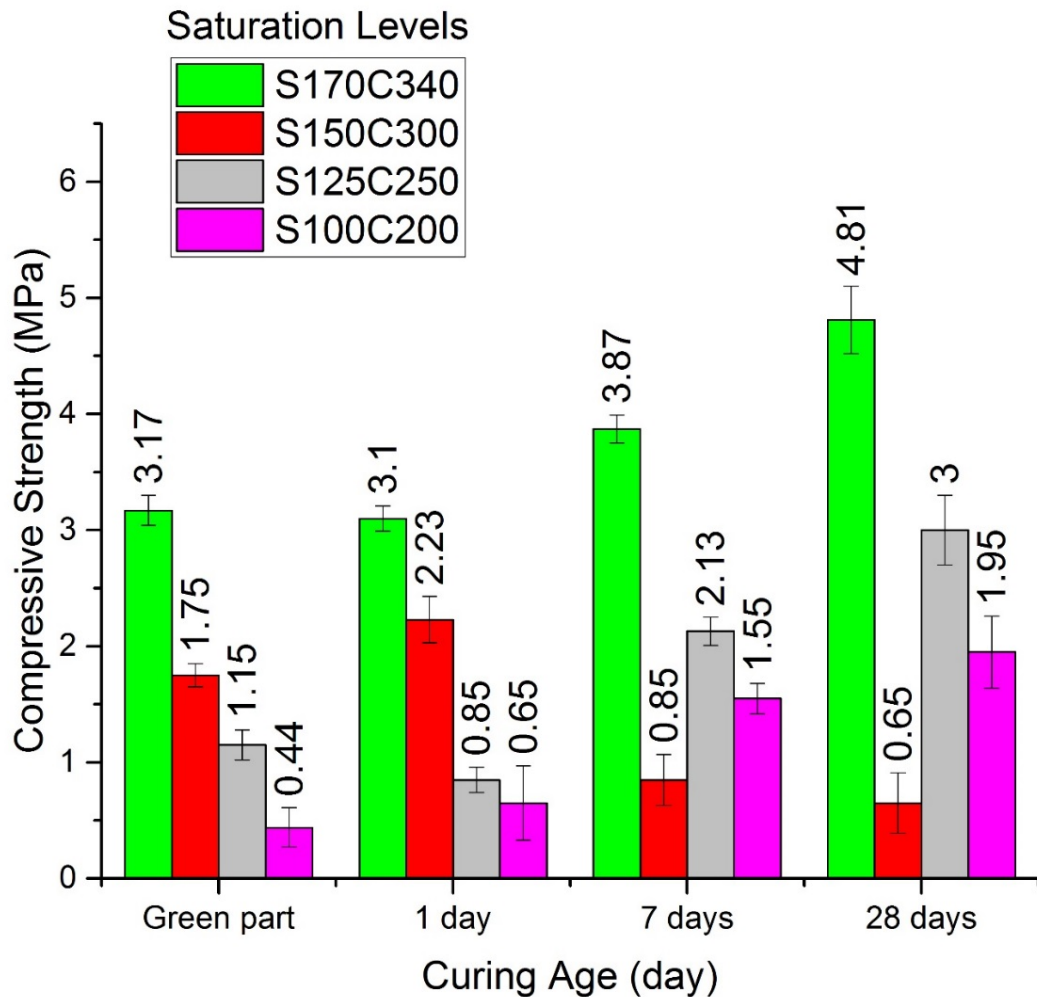


Figure 6. 15: Compressive strength of cementitious cube at different saturation level and curing in normal temperature water.

For instance, in the study by Ma et al. (2015), carbon powders with small particle sizes were used as a solution binder. It was found that the bending strength of the samples was very low but, after pre-sintering, this doubled.

Sample (S170C340) had the highest result in compressive strength when cured for 28 days in water and then dried for approximately one hour at 40°C in the furnace (Vtech,

XU 225) and then left to cool to room temperature. Samples in the experiment were cured for 28 days in water blended with 5% Ca(OH)_2 which yielded weaker compressive strength than the samples that had been cured in water only. This might be due to the Ca(OH)_2 not contributing to filling the gaps between the particles. As shown in *Table 5.6* the sample cured in Ca(OH)_2 had larger dimensions and heavier weight. This means that the samples cured in Ca(OH)_2 became larger, increasing the voids and not providing any reactions with the Ca(OH)_2 . Goto & Roy (1981) found that the curing temperature and w/c ratio influences the pore size distribution, the porosity and the permeability of the cement paste. However, the samples of Goto & Roy, which were cured at 60°C , had a smaller total porosity than the samples cured at 27°C . Goto & Roy (1981) also claimed that Tricalcium Silicate (C_3S), when cured at a higher temperature, becomes larger than when cured at a lower temperature at an early age. In addition, Sandor (1986) found that the compressive strength of the sample is improved when the exterior holds less wetness than the interior.

Figure 6. 15 shows the compressive strength of the cubic specimens (S100C200, S125C250, S150C300, and S170C340), which used different saturation levels at the same curing conditions. It was observed that the maximum compressive strength was 4.81 ± 0.79 MPa when not dried in the oven. Hence, this reveals that high-temperature curing has a more significant effect on the mechanical behaviour of materials.

There are several factors that controlled the compressive strength results, as shown in *Figure 6. 15*, where some specimens did not develop effectively in the 7-day and 28-day curing periods. Firstly, because the binder used in this preparation was not pure water. As a result, the final mechanical properties of the mortar was affected. Secondly, the samples had orthotropic properties despite being isotropic material. Furthermore, porosities were

prominent among the particles due to their free-flowing nature. Layer processes made complete shapes which also created open pores between layers. Another point to consider is the hydration process. *Figure 5. 10* shows how, at the same saturation level, all particles did not hydrate at the same time because the dispersion of the binder on the powder was not distributed evenly (some parts of the powder were wet, and others were still dry). Accordingly, it was observed that when they were put in the water for curing, the unhydrated particles released from the hydrated particles. The combined particles resulted in better bonds, and the C-S-H bonds became stronger. However, they did not have enough strength for structural purposes. This is further evidenced when the samples of Parr et al. (2005), Patel, Bland & Pool (1996) achieved better mechanical strength after being heated in the oven since it helped the C-S-H or C-A-H to form a better bond.

Furthermore, normal cement mortar is usually cast under conditions of compaction or vibration, resulting in higher strength than the 3DP samples due to the removal of voids. In the 3DP process, there was no such compaction.

Most notably, CAC (6.78kg) and Lithium carbonate (0.45kg) in the powder quickly set the sample at an early age with a higher strength than normal cement. However, as shown in *Figure 6. 15* and corroborated by Ann & Cho (2014), the development of later age strength (28 days) is negatively affected.

Two sizes of 3DP samples are presented in *Figure 6. 16*. The result shows that the (20×20×20)mm samples have a slight difference in their compressive strength from the standard (50×50×50)mm mortar cube sample. This study needs further investigation to identify the differences in all three axes when compared with conventional mortar mix. Due to the consistency of the printing layer and binder distribution on the powder bed, there was little difference in stiffness between the two printed dimensions. However, the

compressive strength results in the conventional mix for the different dimensions of cube mould can make an enormous difference due to the compaction, porosity and particle size distribution, as explained by (Hamad 2017; Majeed 2011). For the 3DP specimens, the compressive strength increased by 14% when the 3DP cube changed dimensions from (20×20×20)mm to (50×50×50)mm, which is contrary to that for the conventionally prepared mortar cube. To further understand the anisotropic properties of the 3DP cube requires further examination and study. In addition, the 3DP scaffold produced was found to continuously change its properties and dimensions over time or in a variable environment such as medium conditions, temperature and humidity (Farzadi et al. 2015).

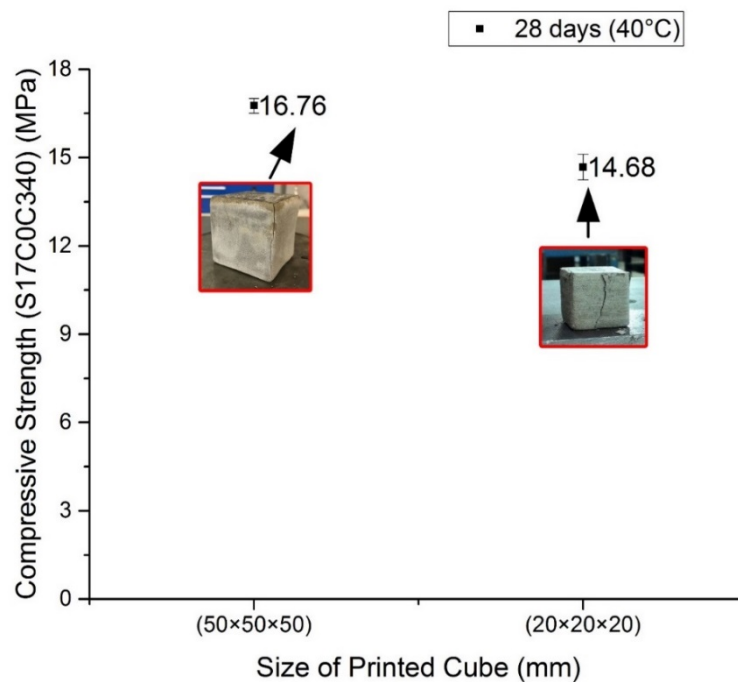


Figure 6. 16: Comparison of the compressive strength of 3DP cement mortar cube at different sizes

In the previous study conducted by Shakor, Sanjayan, et al. (2017) and Shakor, Nejadi, Paul, Sanjayan & Nazari (2019) the porosity and voids in the cubic samples were investigated. The findings and optimum saturation level were used in this thesis to print and prepare all the scaffolds at the same saturation levels.

Figure 6. 17 shows the porosity of the specimens at various w/c ratios, where the highest saturation level (w/c) resulted in a reduction of the porosity percentage for both powders (CP) and (ZP 151). According to the study by Popovics & Ujhelyi (2008), the relationship between w/c ratio and porosity can be described by Equation (6.1);

$$p = 0.001a + \frac{w/c}{w/c+1/G} \quad (6.1)$$

Where p is the total porosity for the fresh cement, a is the air content by volume, G is the specific gravity of cement and w/c is the water/cement ratio by mass. Consequently, an increase in w/c ratio means an increase in porosity of the sample and results in a reduction in the strength of the sample. However, this equation cannot be applied to the 3DP cementitious powder (CP) or gypsum (ZP 151). The printing of (CP) and (ZP 151) is completed as a layer-by-layer process. This technique is completely different from the manual-mix process, which involves mixing the powder with water within one batch and vibrating it in the casting mould. The process of printing and post-processing has various effects on the mechanical properties and durability of the printed object. For example, the hygroscopic property of the powder and electrostatic charge on the surface of the powder has a significant influence on the capability of powder to absorb moisture from the air. This leads to an increase in the cohesion and a reduction in the flowability of the powder. This property in the powder would also affect the size of the specimen and change its mechanical properties. Accordingly, it is clearly shown in *Figure 6. 17* that an increase in the w/c ratio in the 3DP specimens reduced porosity and led to an increase in the mechanical strength of the 3DP part.

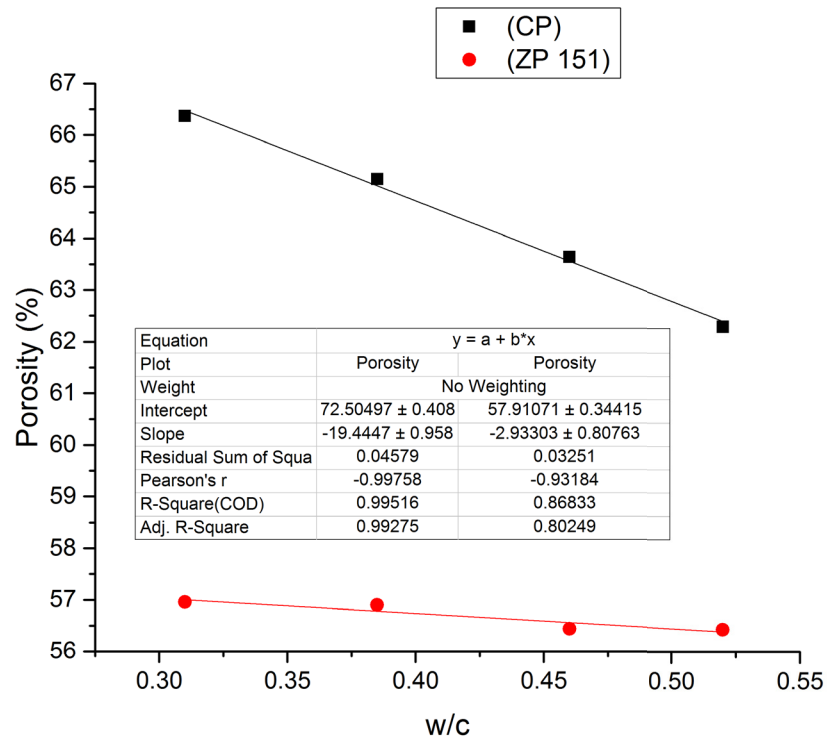


Figure 6. 17: Linear regression relationship between porosity versus w/c ratio in the 3DP scaffold.

The goodness of fit is displayed in Figure 6. 17, the regression coefficient R^2 for the CP scaffold is 0.87, while the correlation coefficient R^2 for ZP 151 increased to 0.99. Equations (6.2) and (6.3) are the line of best-fit equations, for each of the powder CP and ZP 151, respectively.

$$P = -2.933 \times w/c + 57.911 \quad (6.2)$$

$$P = -19.445 \times w/c + 72.505 \quad (6.3)$$

Where P represents the porosity % and w/c represents the water/cement ratio.

Figure 6. 18 illustrates the compressive strength of the specimens for the saturation level of S170C340. This saturation level is equal to a w/c of 0.52 in CP and 0.46 in ZP 151 at all orientation angles. In addition, it shows the orientation angle of (0°) gives the highest value 14.73 ± 0.12 MPa for CP after curing in an oven for 3 hours before and after wet-curing, and 7-day curing in water. This value is enough to build a structural member which is cured for only 7 days. According to the ACI code, curing for 7 days contributes

65% of the strength of mortar or concrete (ACI308R-01 2001), while the compressive strength of mortar or concrete increases to about 99% strength in 28 days.

The highest recorded result for ZP 151 (11.59 ± 1.18 MPa) at an orientation angle of (0°), (i.e. with printhead parallel to the X-axis) was reported by (Asadi-Eydivand et al. 2016). This study also recorded 11.78 ± 1.19 MPa at an orientation angle of (90°) for ZP 151, which is change the plane in the 90° of angle orientation.

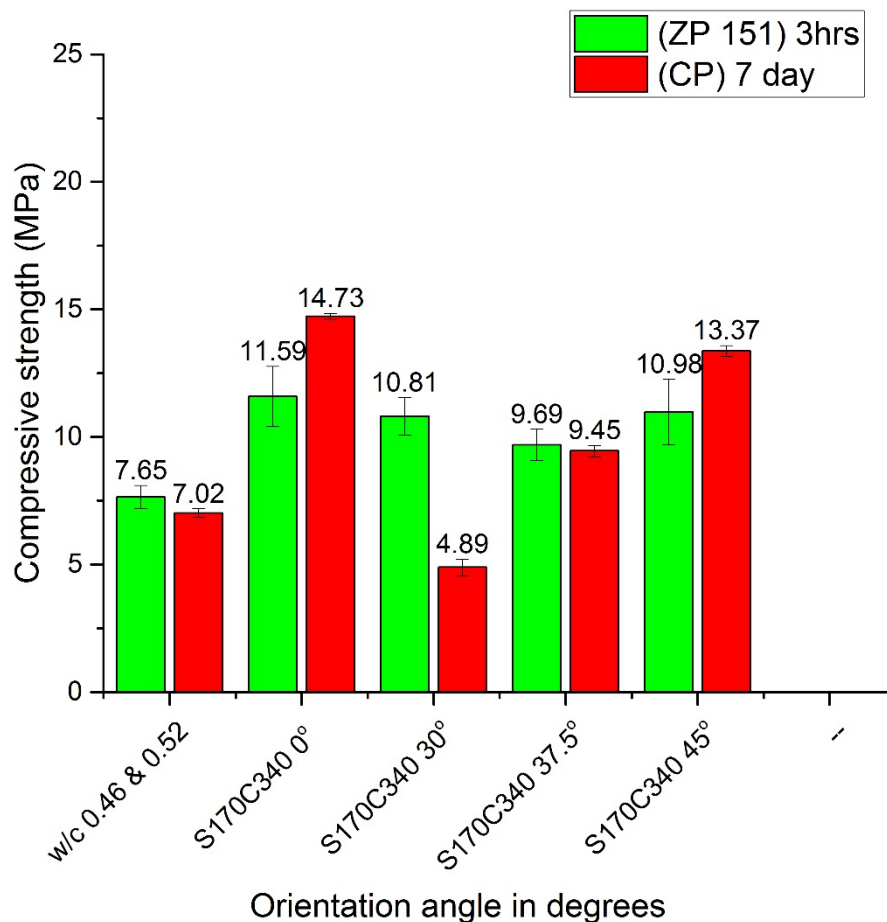


Figure 6. 18: Compressive strength for the ZP 151 cubes and CP cubes (average \pm standard deviation) at saturation level S170C340 in different angles.

It is worth noting that curing for 3 hours in an oven at 60°C before immersing in the water medium resulted in a significant increase in the compressive strength of the sample and in fewer particles dispersing in the water, see Figure 6. 19. According to the investigation by Dias (2000), air-dried OPC concrete results in an increase in weight and a reduction

in absorption by keeping it longer in the water medium. Another study confirmed that relative humidity has a major impact on the concrete porosity and air permeability of the specimens as well as a significant effect on the mechanical strength of concrete and mortar (Parrott 1994). It also showed that drying the concrete at 50°C for 1.3-3 days would still have 80% of relative humidity for their specific specimens. That amount of humidity would be enough to achieve minimal porosity in the specimens.

It is clear from the experimental results that the printing orientation angle had a major impact on the mechanical strength of the specimens, particularly in the cement mortar specimens. As shown in *Figure 6. 18* the printing orientation of (0°) recorded the highest compressive strength value, which means that the optimum strength in the XZ plane for cement mortar was in a perpendicular direction. However, the results for gypsum were slightly different since angle (0°) achieved maximum compressive strength. The results of the two angles are very similar to each other, with differences only in the decimal range. Thus, it is highly recommended that the print occurs with a 0° orientation angle for CP to achieve the highest compressive strength whilst also aiming to increase the flexural strength. This is further explained in the following subsection.

Figure 6. 20 shows the results under different curing conditions for the (20×20×20)mm cube for 7 days and 28 days. The X-axis of the figure shows the curing procedure in sequence, (60°C, water, and 60°C), namely, dried in an oven for 3 hours at 60°C, then placed in water for 7 or 28 days, and then dried again in the oven for three hours at 60°C. Studies of the procedure (water and 40°C) have been conducted by Shakor, Sanjayan, et al. (2017), where specimens were cured in water for 7 or 28 days, then dried in an oven for an hour at 40°C. The results are positive since the procedure led to a proportional increase in the compression strength of specimens when the temperature of the drying

process was increased to 60°C. Therefore, it is highly recommended that printed specimens are cured in the oven for 3 hours and at 60°C. The 28-day result of the printed part shows the strength is sufficient to use in construction applications in the construction industry that currently use precast members.

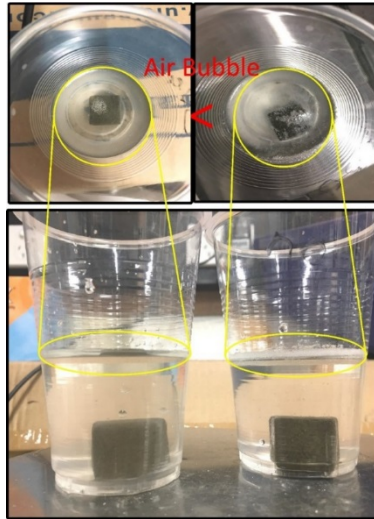


Figure 6. 19: The difference between: (left) curing in an oven for 3 hours then submerged in water; and (right) not cured in the oven but instead submerged directly in water. The air bubbles (voids) are more pronounced on the (right) than the (left).

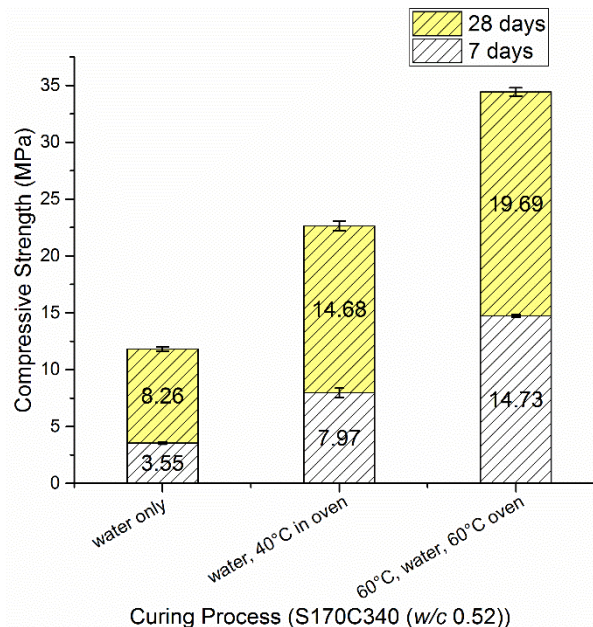


Figure 6. 20: Compressive strength results in the different curing process, all results for a printed part (20×20×20)mm at an angle of (0°) in the XZ plane only.

All dogbone samples underwent the tensile test. The orientation angle had a major impact on the tensile result of the printed product for both materials. *Figure 6. 21* displays the results from the manually prepared sample for an angle from 0° to 90° . The experimental results show the maximum tensile strength for the ZP 151 was achieved at 0° (4.49 ± 0.15 MPa) and required that samples were manually prepared. The lowest result emerged at 37.5° . At 45° , samples of ZP 151 and CP broke before the applied load test because the rate of deflection was too high, hence, samples could not be grasped firmly by the end of the gripper before applying the load. This also occurred to the CP samples at an angle of 37.5° . The manually-prepared CP samples presented in *Figure 6. 21* recorded the highest result 2.35 ± 0.14 MPa, while the highest tensile strength 1.61 ± 0.28 MPa was recorded at 0° among printed CP samples. However, samples at 37.5° and 45° were brittle and broken before the load could be applied by the machine. Overall, the 0° orientation demonstrated more acceptable and reliable results in tensile strength for both materials. Thus, it is suggested that the optimal orientation angle to be used in future works is to print at 0° in the X-direction parallel to the movement of the printhead.

Figure 6. 22 presents the different patterns of dog bone ruptures. A non-uniform rupture can be seen at the fractured tips of the different orientation angles of the dogbone samples.

It is obvious that the rupture occurred in the lower portion of the specimens where the printing orientation angle was smaller, due to the high quantity of powder that settled in that portion (see *Figure 6. 22*), which subsequently led to a weakening in the narrow section of the dog bone specimens.

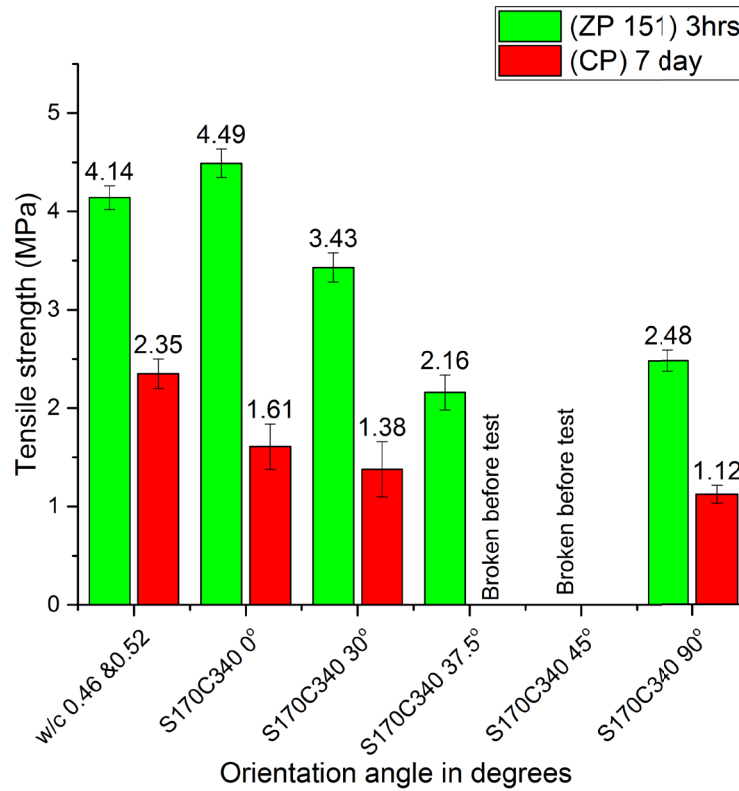


Figure 6. 21: Tensile strength results for the ZP 151 specimens and CP specimens (average \pm standard deviation) at saturation level S170C340 in different angles.

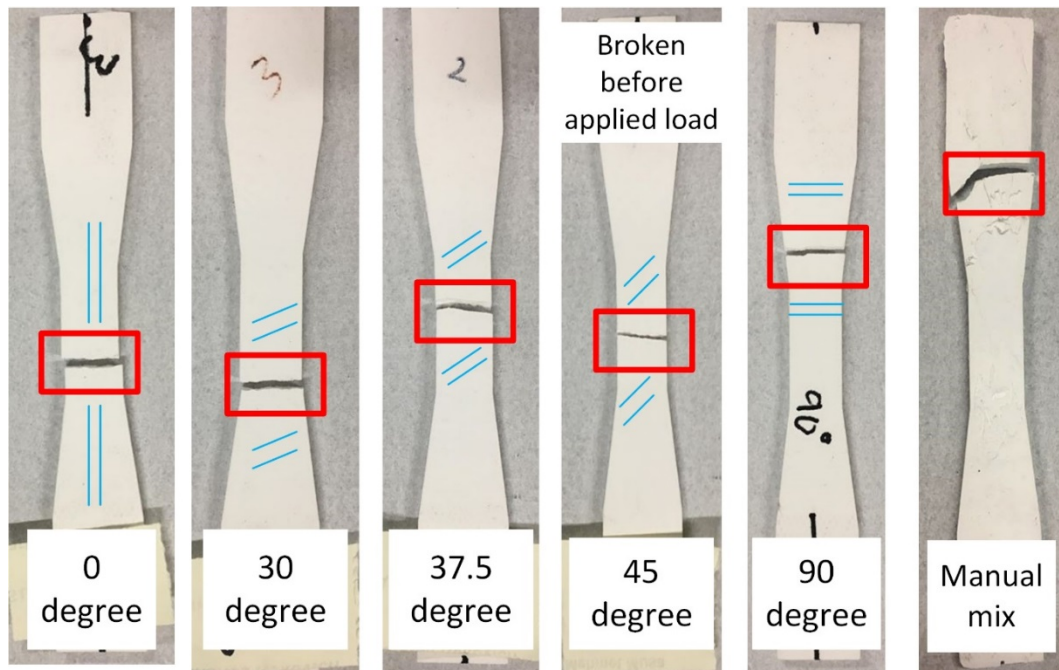


Figure 6. 22: Cracking present at the dogbone samples for ZP 151 at different orientation angles.

The shear strength test is another testing method used to induce a sliding failure parallel to the plane where forces are generally expected to be experienced. Generally, shear forces are where one part of the material is forced in one direction and the other part is forced in the opposite direction so the material is stressed in a sliding motion. *Figure 6.23* shows the shear strength of each sample printed using ZP 151 and CP powders. As shown in the graph, the highest value was recorded at 90° and 45° for the orientation angles in the CP cubes. However, the highest value was observed at 30° for the ZP 151 cubes.

It is worth noting that each powder has different characteristics at different orientation angles. With the print direction opposite to the directional load when applied to the specimens, angles of 45° provided more resistance. The value for the shear load for CP specimens at 45° was 20.28 MPa. The angle of 45° had a higher shear value due to the interlayer resistance at that angle and reached rupture later than it did for the compressive strength test. Thus, the shear strength achieved a higher value because of the changed orientation angle. For normal mortar, the cement to the sand ratio (1:6) achieved only 0.27 MPa after being coated with epoxy resin (Sarangapani, Venkatarama Reddy & Jagadish 2005). However, this was completely different for the 3DP specimens with cement to the sand ratio of (1:0.05), where the ultimate strength recorded in the 45° orientation is 20.28 ± 0.54 MPa. This result is somewhat optimistic, and the ratio of mixing could be changed if more care was taken to optimise the flowability of printing materials in the printer.

Conversely, the maximum shear load for the ZP 151 cubes was recorded in the orientation angle at 30° and 45°, which is 9.06 ± 1.74 and 8.85 ± 1.29 MPa, respectively.

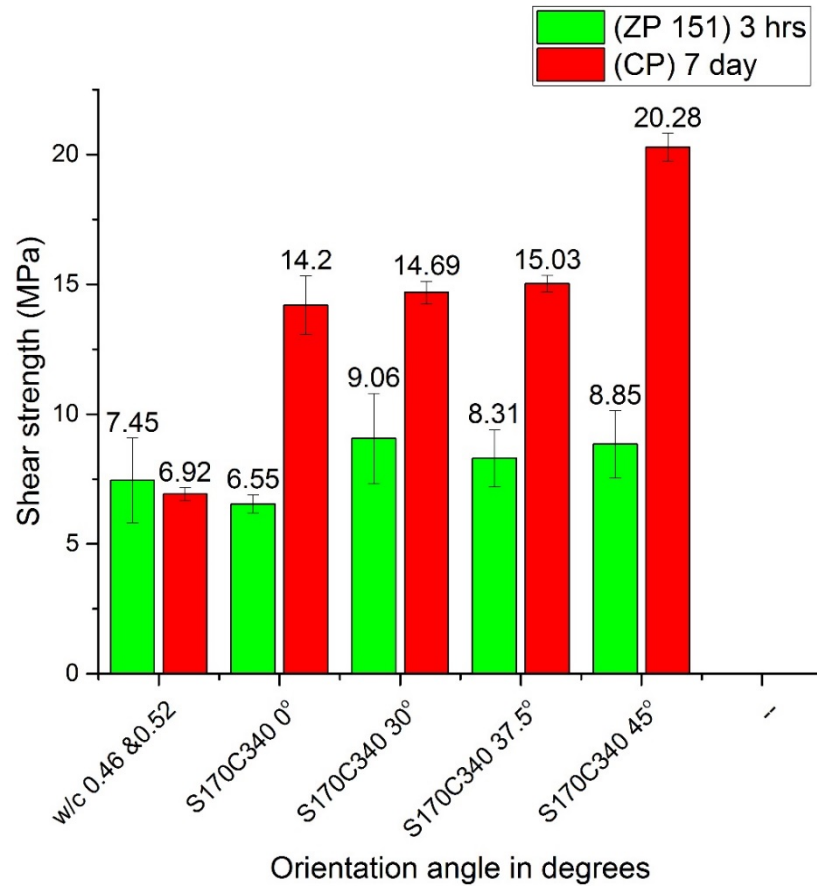


Figure 6. 23: Shear strength for the ZP 151 cubes and CP cubes (average \pm standard deviation) at saturation level S170C340 in different angles.

Figure 6. 24 shows the rupture between the interlayer of the printed specimens in the shear and compression tests. The fracture for the printed specimens is quite clear at the angle of 45°.

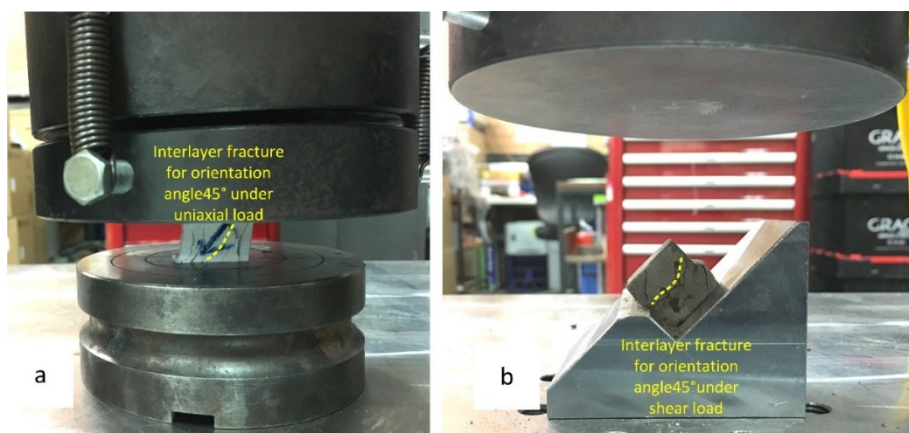


Figure 6. 24: Fracture in the printed 45° specimens in both (a) compressive test for ZP 151 and (b) shear test for CP.

Three-point bending tests were conducted to evaluate the flexural strength of the printed ZP 151 and CP specimens. *Figure 6. 25* shows that, in general, the flexural strength in gypsum is higher than in the cement mortar specimens. According to ACI330R-01 (2001), the flexural strength of concrete is approximately 10% to 20% of the compressive strength results. Likewise, the flexural strength result for CP after 7 days showed that it was approximately 14% of the compressive strength. However, this could be due to the medium of the specimens, type, sizes, the volume of the particle size and duration of curing.

Figure 6. 25 shows flexural strength results, which are basically the opposite of the compressive strength result for both materials. As shown in *Figure 6. 18* the highest result was in CP specimens. However, in *Figure 6. 25* the results for ZP 151 specimens have higher values than for CP specimens. Previous studies have found that using gypsum leads to an increase in bending and tensile strength (Ghosh & Subbarao 2006). The high percentage of lime content in fly ash with a high ratio of gypsum (1%), leads to a dramatic increase in the tensile strength (Ghosh & Subbarao 2006). Therefore, gypsum is acting as a flexible material and has great flexibility compared to the cement materials. In an earlier study by Lewry & Williamson (1994), it was found that the reaction of water with plaster (gypsum), which is similar to ZP 151, with a 0.6 w/c ratio, could gain about 12.2 MPa of flexural strength. This result is quite close to the manual mix of ZP 151 with a w/c ratio of 0.46 in this study 14.23 MPa. However, post-processing and purity of the materials have a significant effect on the result of the bending strength of gypsum materials.

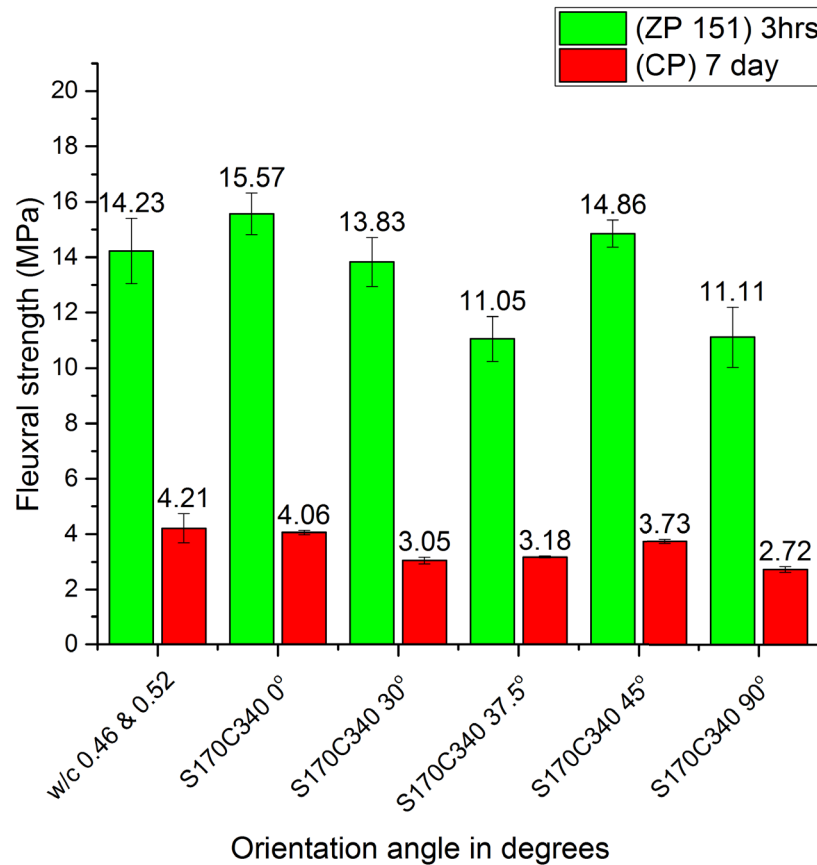


Figure 6. 25: Flexural strength results for the ZP 151 specimens and CP specimens (average \pm standard deviation) at saturation level S170C340 in different angles.

The highest bending strength results for the printed ZP 151 and CP samples were recorded at the orientation angle of 0°, whereas the manual mix of CP in bending strength was slightly higher than the printed angle of 0°. Therefore, in the present study when printing with CP, 0° and 90° were the optimum angles to print construction members because the highest results achieved for compressive strength were at a 90° angle and the highest results achieved for bending strength were at an angle of 0°. This could be improved by adding reinforcement and then using the members for the façade and cladding of a building (Shakor & Pimplikar 2011).

Figure 6. 26 displays the surface of the cubic cement mortar (CP) at different orientation angles. The photo was captured by both of the 3D microscope scanners (Olympus LEXT OLS5000 and Nikon iNEXIV). The photos were taken at low magnifications to show the

printed line for each of the different angles of orientation in the CP. Using the Olympus scanner at the lowest magnification ($5\times$), the working distance was 20mm. However, using the Nikon set to the lowest magnification ($3.5\times$) the working distance was 73.5mm. In the images, the printed line of the orientation angles is clearly visible. However, it can be seen that the inclined print parts, specifically at 30° and 37.5° , have many valleys and a higher roughness compared with other parts. Therefore, in some images, the blur appeared at angles of 30° and 37.5° due to the abundance of uneven surfaces on the mortar samples (CP).

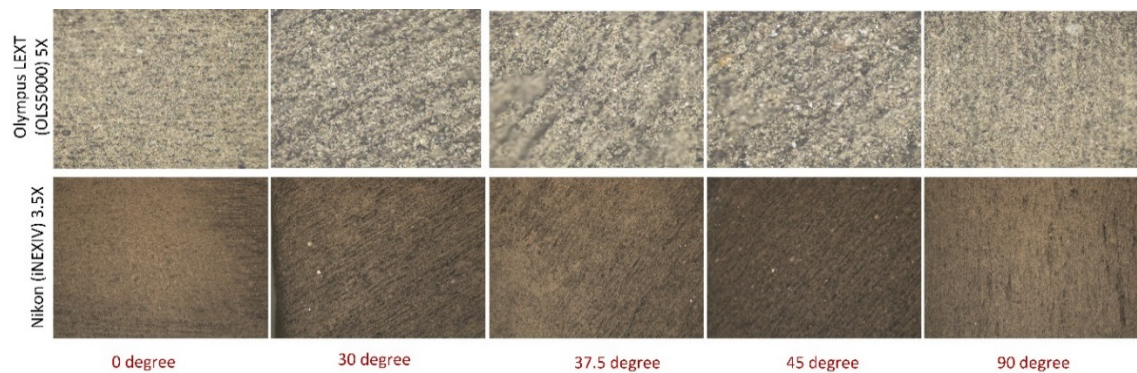


Figure 6. 26: Surface images of the cubic specimens of CP at orientation angles of (0° , 30° , 37.5° , 45° and 90°) by the Nikon and Olympus 3D laser microscopes.

Future work in 3DP using concrete or mortar is necessary to focus on the broader goal of printing large objects when using different techniques, such as extrusion and selective laser sintering, which are applied extensively in other manufacturing fields. This application could develop rapidly and could produce a strong and smart structure. This could be used easily in seismic areas due to the light weight of the 3DP part. Based on previous work, it is possible to numerically and theoretically develop a model of structural members with desirable characteristics that can be used for different applications in construction, such as in seismic zones as mentioned above, and to reduce the risk of cyclic loading.

Wettability and drop penetration tests were conducted for Zpowder and CAC&OPC powder (modified powder). It was observed that both test methods produced similar outcomes for the penetration time of the water-based droplet into the powder.

Figure 6. 27 shows the test results for the Zpowder and modified powder for both of the contact angle goniometer methodologies. It shows that drop penetration had an average value of 55.24 ± 5.4 seconds in Zpowder, while the absorption of the whole drop took less time in the modified powder (cementitious powder), where the average value was 3.70 ± 1.4 seconds. For each powder, the test was repeated three times. Each of the trials is identified using different coloured lines in Figure 6. 27.

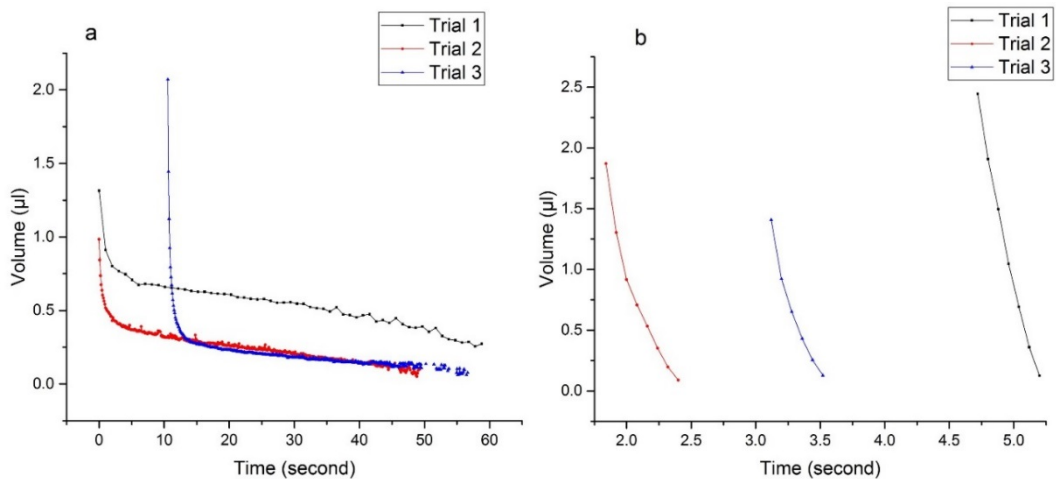


Figure 6. 27: (a) penetration time per volume (μl) consumes in Zpowder, (b) penetration time per volume (μl) consumes in CAC&OPC powder.

Figure 6. 28 shows the test results with the images of the droplet penetration taken by the high-speed camera for both powders. The results of the binder drop penetration in this method are similar to those of the goniometer method. In this approach, the drop penetration average value time in Zpowder was approximately 55.93 ± 0.66 seconds, while the drop penetration average value time for the modified powder was 1.28 ± 0.07 seconds. These experiments were also conducted by (Hapgood et al. 2002; Zhou et al. 2014). The significant differences in penetration time were the result of the agglomeration of the

modified powder, with Zpowder being more tightly packed in the bed of the printer than the modified powder. In other words, Zpowder was distributed as a homogeneous powder and the CAC&OPC (modified) powder was distributed as a heterogeneous powder during the preparation of the bedding layer and testing for droplet penetration.


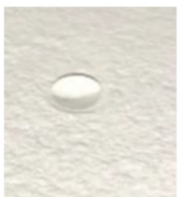



<i>Description</i>	<i>Time (sec)</i>		<i>CAC&OPC powder</i>	<i>Gypsum powder</i>
	<i>CAC&OPC</i>	<i>Gypsum</i>		
<i>Impact time</i>	0	0		
	1.24	1.24		
		56.1		

Figure 6. 28: Images from a video recording for the penetration time per drop of binder in Zpowder and CAC&OPC powder.

The earlier studies by Nguyen, Shen & Hapgood (2009) used two types of powder with different particle sizes for the hydrophobicity and hydrophilicity tests. They discovered that smaller-sized particles had hydrophobic properties. That study also found that the penetration time increased as a result of adding fine particle powders to the mixture powder. Hence, the findings of this research are consistent with the same study conducted by (Hapgood, Litster & Smith 2003). In all the previously conducted investigations into

penetration time, evidence shows that the hydrophobic phenomena will occur in the finer powder particles. The results in the literature are, therefore, consistent with the results presented in this chapter. In *Figure 5. 4* it can be seen that Zpowder had a smaller particle size than that of CAC&OPC.

As further evidence, Fuhr et al. (2013) showed that fungi penetration time increases with decreasing pore size in wood. In the present study, we observed that Zpowder has a smaller pore size than cementitious powder. Another study, conducted by Tschapek (1984), found that the porosity in the soil helps the water easily pass through the soil particles (hydrophilic soil).

Further study should be conducted to better understand the phenomenon for drop penetration through two different powders. Droplet penetration of the powder is highly dependent on the porosity between particles, with greater porosity resulting in the droplet penetrating the unpacked surface faster.

This experimental work revealed that the Zb63 droplet on Zpowder particles took longer to completely penetrate the surface.

The wettability test is utilised to discover how the nature of the structural form and its coherence with the printed part. The coherence of 3D printed objects is dependent mainly on the strength of the bond between particles and the way in which the droplet binds the particles. The coherence of the printed specimens is affected by the droplet of binding which drops through a tinny nozzle. Sometimes these nozzles are blocked or damaged, then this is the reason for reducing the water droplet on the powder particles. A recoating blade also affects powder particles spreading. Sometimes these spreading are not homogenous due to the humidity level of the powder. The morphology of the particles and the presence of interparticle pores could be another reason for differences

incoherence. Cement particles may provide an additional reason and, according to Kirchberg, Abdin & Ziegmann (2011), fine particles increment the contact angle and decrease the powder's wettability. *Figure 5. 5* clearly shows the peak particle sizes in Zpowder are likely to be finer than CAC&OPC powder.

Wettability or wetting is the ability of a fluid to maintain contact with a powder surface, as a result of the intermolecular interactions when the two are brought together. For example, fungi penetration time increases with decreasing pore size in wood (Fuhr et al. 2013), with the velocity of fungus depending on the relationship between depth penetration and time taken.

The study of the presence of macrovoids in unpacked powder by Hapgood et al. (2002) found that, for packed powder, the penetration will be easily and evenly distributed in the liquid. In their investigation, different liquid solutions were used with respect to time penetration. One of the liquids with similar properties to Zb 63 is a clear binder solution named 3.5% HPC (Hydroxypropyl Cellulose) and dye. The penetration time for this solution was 21.5 seconds in the Merck lactose powder ($d_{50}=64.8\mu\text{m}$).

Another study by Doerr (1998) explained the surface tension of water on soil. This study found that if a water droplet does not penetrate the soil, it means the surface tension of the soil is less than the surface tension of water 72.75 dynes/cm. Furthermore, the investigation stated that the porosity of the soil helps the water easily pass through the soil particles (hydrophilic soil) (Tschapek 1984). Earlier studies found that the porosity in the powder bed, fluid type and macrovoids all contribute to the wettability of the powder. *Figure 6. 29* explains the penetration of the binder (water) into the ZP 151 at different stages of penetration.

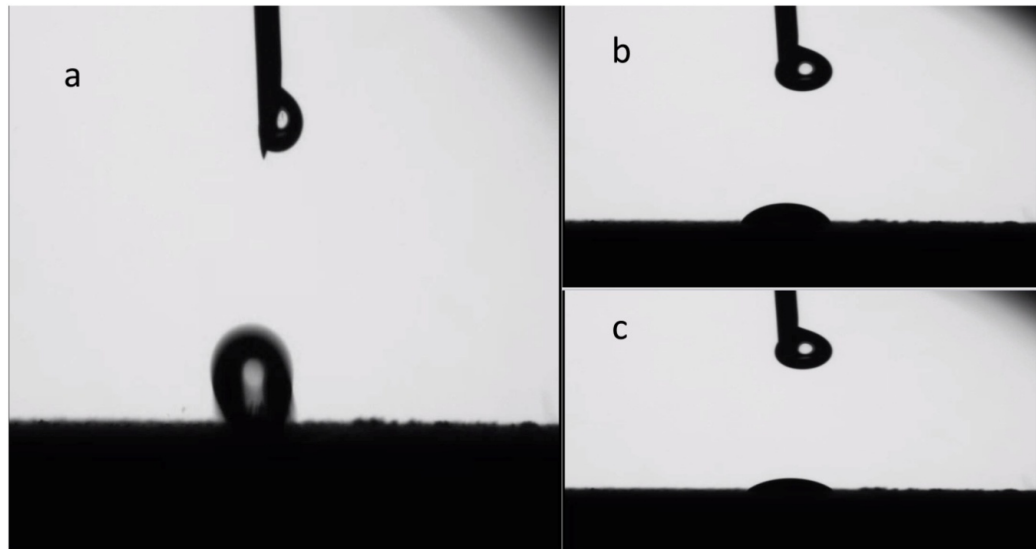


Figure 6. 29: Steps in the penetration Zb63 liquid into ZP 151, (a) impact time of droplet on the surface of the powder, (b) penetration processes of liquid on the powder after 16 seconds, (c) absorbing most of the liquid into the powder.

Table 6. 1 shows the highest spreading available in the CP so the penetration can be deduced as being due to the spreadability of the binder to the adjacent particle, rather than the depth of penetration into the powder. For example, Hapgood et al. (2002) explained how large macro voids would lead to a halt in the penetration of the droplet and instead result in spreading to the adjacent particles.

Table 6. 1 Penetration time, diameter of the droplet on the powder and depth of the penetration of the droplet

Powder Type	Droplet binder	Penetration time (s)	Diameter of the droplet (mm)	Depth of the penetrating droplet (mm)
ZP 151	Zb 63	55.24±5.40	2.40±0.09	1.25±0.03
CP		3.70±1.40	2.64±0.02	1.11±0.21

Figure 6. 30 explains the process of creating a bond between the two layers for ZP 151 due to the hydrophobic properties of the gypsum (ZP 151): the drop stays longer on the ZP 151 than CP. Figure 6. 29 displays the image 16 seconds after the falling of the drop and the new layer bonded well due to the drop. According to ZprinterManual (2012), the vertical build speed takes 2 to 4 layers per minute. Thus, the photo was taken after 16

seconds for the purpose of showing the drop as it is between layers. For this reason, the stopwatch timer and goniometer device were used for the printed specimens. The experimental results demonstrated the time between two layers for each printed specimen was approximately 16.64 ± 1.2 seconds. Therefore, taking the photo at 16 seconds is ideal to show the drop between the layers. The purpose of showing the binder drop between two layers in the ZP 151 is to show that the ZP powder has more powder pack on the build chamber than CP. The high number of voids in the cementitious powder (CP) allows the water binder to penetrate more quickly than in the recommended powder (ZP 151).

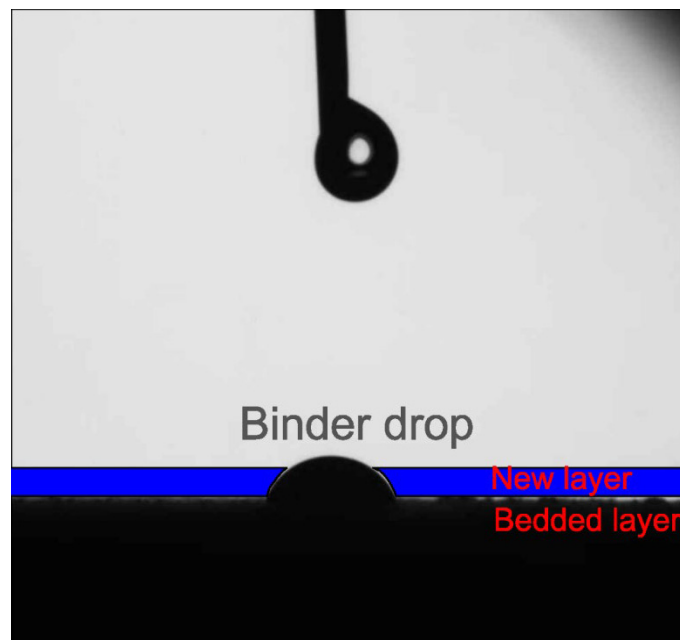


Figure 6. 30: Schematic explanation of the binder drop between two layers and binding two layers together, the schematic shows what happens at the 16 second mark.

Figure 6. 30 shows that the dropped binder (water) remained longer on ZP 151 due to the drop binding the layers more effectively.

In *Figure 6. 27*, the water drop could stay until the new layers of powder are deposited. It is clear from the graph that ZP 151 is more tightly packed than CP. In the graph, the volume of the water drop at 16.224 seconds is approximately $0.27 \mu\text{l}$ and the height is 0.25 mm. The height of each layer is 0.1 mm. The period taken for drop penetration into

each layer is approximately 16.3 seconds. Thus, the figure shows that the drop of water from the previous layer was still protruding when the roller deposited a new layer on the previous layer of powder. The printhead inkjet was then moving and the dripping of the binder over the powder continued. Overall, this study found that ZP 151 has a tightly packed surface and particles are distributed evenly on the bed. On the other hand, the CP has more voids and porous space between the particles due to the agglomeration between cementitious powder and is less free-flowing from the container to the feeder chamber.

The following graphs in *Figure 6. 27*, show the results of the three trials of contact angle goniometry on the ZP 151 and CP. These graphs show the time of penetration for each binder on the two different powders.

A measure of the contact angle is a proxy that can be used to measure wettability. For instance, Siebold et al. (2000) stated that the contact angle has a higher value at all times during capillary rise than is anticipated, and depends firmly on increasing velocity. They also explored how the capillary rise was carried out at a single capillary and in column-packed powder to determine the contact angle.

There are a few investigations of the type of powders and penetration, such as using two types of powder for hydrophobicity and hydrophilicity. Salicylic acid and Lactose of 100 and 200 grade, respectively, were chosen for the hydrophobic and hydrophilic investigations (Nguyen, Shen & Hapgood 2009). The Salicylic acid particle sizes are smaller than the Lactose particles. Regarding particle size, the finest particle size has hydrophobic properties (Hapgood, Litster & Smith 2003). They found that the penetration time increases with the addition of fine particles of salicylic acid to the powder mixture (Hapgood, Litster & Smith 2003), which agrees with the present study. The evidence on

penetration time is overwhelming and shows that hydrophobic properties will occur in fine powder particles.

The time between printing layers has a significant impact on the result of the printed part and correct wettability between printed layers. For example, Farzadi et al. (2015) discovered that printing layers with different printing delays have an impact on the physical and mechanical properties of the printed structure. When aiming for the optimum mechanical strength, it was found that the optimum time delay for print the specimens is 300 ms.

Hydration and released energy have also a high impact on the material characterisation of the printed object. That is due to the hydration of calcium silicate in the cement powder. Research has found that the thickness of the calcium silicate hydrate (C-S-H) rims in cement in 28 day-old pastes increased from 5 mm to 25 mm at 20°C and 80°C, respectively (Patel, Bland & Pool 1996). C-S-H is the basic product in the hydration of Portland cement and is mainly responsible for the strength in cement-based materials. Energy dispersive spectroscopy microanalyses revealed that the chemical structures of the different C-S-H rims depend mostly on the temperature at which they were made. The lighter C-S-H made at 90°C is able to have a greater attraction in regard to sulphate than C-S-H developed at 20°C (post- or pre-cured C-S-H produces). During the following storage at 20°C, the release of sulphate from the lighter C-S-H gel designates that SO_4^{2-} is not chemically stuck in the C-S-H scaffold but may be balanced and sorbed by Ca_2^+ in the C-S-H during heat curing (Famy et al. 2002).

There is a strong relationship between the surface roughness (Ra) of the materials and the contact angle (wettability) of the surface of the powder. Two situations should be taken

into account for the effect of roughness, namely, if the binder droplet leads to a groove in the surface or if air pockets are left between the droplet and the surface (BiolinScientific).

If the surface homogeneously becomes wet, the droplet is said to be in a Wenzel state. In a Wenzel state, wettability will be enhanced by adding surface roughness, which is affected by the chemistry of the surface (Wenzel 1936). The Wenzel relationship can be written Equation (6.4);

$$\cos(\theta_m) = r \cos(\theta_Y) \quad (6.4)$$

Where θ_m represents the contact angle, θ_Y is known as a Young contact angle and r is called the roughness ratio.

However, when the surface becomes heterogeneously wet, the droplet is said to be in a Cassie-Baxter state (Cassie & Baxter 1944). The most stable contact angle is considered to be related to the Young contact angle. This is the angle of a water droplet on the solid surface which measures the quantifying of wettability on the surface of powder. The contact angles were considered from each of the Wenzel and Cassie-Baxter equations and were found to be a reasonable assumption for the most stable contact angles with real surfaces (Marmur 2009). Thus, the most suitable equation for CP powder in inkjet 3DP, which could be measured as a heterogeneous wet surface, could be expressed as in Equation (6.5):

$$\cos \theta_w = f_1 \cos \theta_R - f_2 \quad (6.5)$$

Where θ_R represents the solid-water declining contact angle, and θ_w is the apparent receding contact angle for the porous surface. It should be noted that f_1 and f_2 in Equation (6.5) are designated by the advancing contact angle θ_A .

All the tensile and flexural samples were measured to determine the amount of the deflections in each orientation angle of 3DP samples. In the present research, the deflection of the tensile specimens is shown for each of the ZP 151 and CP scaffolds. The deflections occurred when the size of the samples was large and had a long shape with less thickness. This was observed more frequently when the samples were printed in an angular orientation, particularly in the XZ plane, except for orientation angles of 0° and 90° , which had minimum deflection.

Measurements were taken for three specimens at each of the different orientation angles. It was observed that the 45° orientation angle had the highest deflection compared with all the other orientation angles for both types of printed powders. *Figure 6. 31* shows that the deflections at the orientation angle of 45° for ZP 151 specimens were recorded as 1.77 ± 0.21 mm. However, the deflection for the CP specimens was recorded as the highest value, namely, 1.79 ± 0.11 mm at the 45° orientation angle.

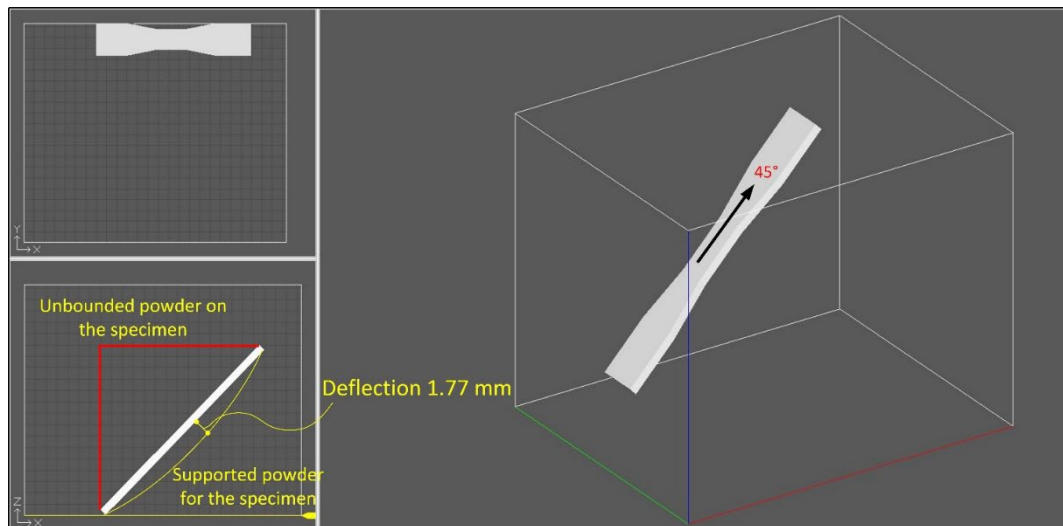


Figure 6. 31: Illustration of the deflection for the ZP 151 specimen (45°) in the build chamber of the 3DP.

Table 6. 2 details the mean and standard deviations of the deflections in millimetres (mm) for each of the 3DP tensile specimens. Specimens printed at orientation angles of 0° and 90° were found to exhibit the smallest deflections in the CP specimens, with values of

0.03±0.31mm and 0.04±0.12mm, respectively. It was noted that deflection also occurred during the preparation of the conventionally prepared specimens but within a limited and insignificant range (0.02mm).

Table 6. 2 Deflection in tensile specimens for the different orientation angle of the printed specimens.

Printed orientation angle	Deflection in tensile specimens (mm)	
	ZP 151 specimens	CP specimens
0°(XZ)	0.03±0.23	0.03±0.31
30°(XZ)	0.73±0.07	0.76±0.16
37.5°(XZ)	1.28±0.09	1.30±0.22
45°(XZ)	1.77±0.21	1.79±0.11
90°(XZ)	0.01±0.10	0.04±0.12
Manual mix	0.02±0.11	0.02±0.13

The dimensional accuracy of a fabricated member defines the grade of approval between the dimensions of the manufactured part and its designed specification.

The Dimensional Deviation Ratio (DDR) can be used to compute the dimensional precision of printed structures, as in Equation (6.6);

$$\text{DDR} = \frac{L_P - L_{CAD}}{L_{CAD}} \times 100\% \quad (6.6)$$

Where L_p is the real (printed) measured length value of the sample, L_{CAD} is the CAD length value designed model which is 20mm for all three sides of the cube.

Table 6. 3 presents the identified DDR value for all three axis orientations (X, Y, Z): the X-axis is the direction of the printhead that is parallel to the bed when it crosses the jet binder; the Y-axis is the direction of the bed that is perpendicular to the direction of the printhead, and the Z-axis is the direction of the next layer that is added on top of the previous layer. Each value is shown as an average (\pm) the standard deviation. As

mentioned earlier (subsection 5.1.1), the state of absorbing the binder liquid by the powder potentially affects the dimensions of the printed part. The dimensional accuracy of the fabricated part is affected by many factors such as wettability of the powder, surface morphology of the powder, binder reactivity with powder, powder components, printing delay, build orientation, resolution of the printhead, post-processing procedures, binder droplet volume, layer thickness and particle size of the powder. In *Table 6. 3* there is a significant change in the Y-axis due to the printhead, distributing in the fast axis, overlapping the binder in the Y-axis. Another possible reason for the Y-axis change relates to the penetration of the binder in the powder bed.

Table 6. 3 Difference between ZP 151 and CP in DDR for 3DP cubic samples saturation level (S170C340) (w/c 0.46 & 0.52)

Cubic samples	Dimensional deviation ratio (DDR) %		
	X- axis	Y-axis	Z-axis
ZP 151	3.75±0.55	1.10±0.60	2.25±0.95
CP	-1.15±0.11*	-3.9±0.12*	0.7±0.06

***(-) the value with meaning sample smaller than the original (CAD) drawing.**

The major advantage of the inkjet 3DP technique is the fabrication of structural components with complicated geometries without implementing costly formwork. The most vital aspect that distinguishes inkjet (powder-based) 3DP from the conventional casting method is the precision of printing.

Figure 6. 32 shows the results of the dimensional accuracy of the green cubic sample (green part) for the CP materials. Here, “green part” refers to a specimen that has been removed from the build chamber (build bin) prior to any post-processing. The negative values show that the printed specimens are smaller than the original size. This is due to unprecise water droplet distribution on the powder surface and also change of shape of water in high saturation dripping on the surface of the powder. The shrinkage is another reason in the high saturation level of the printed parts.

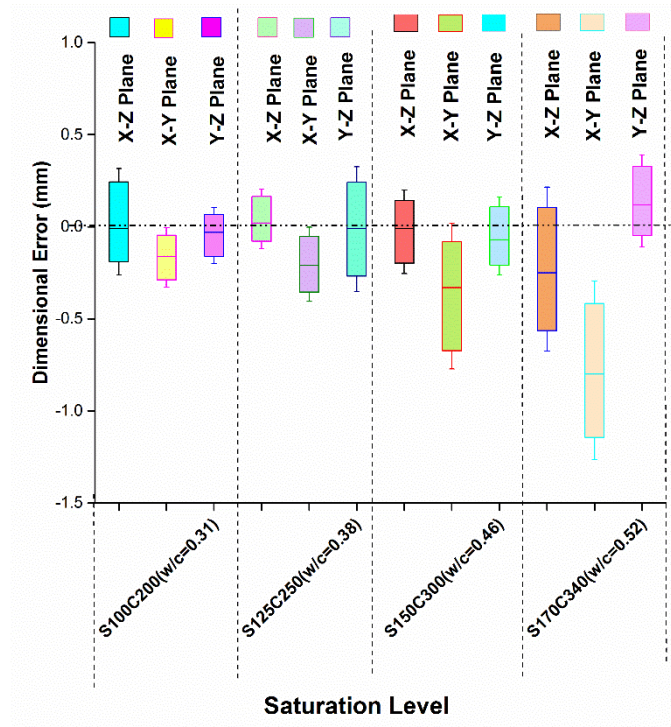


Figure 6. 32: The relationship between dimensional accuracy and saturation level (w/c) for printed green cube CP specimens (CAD $20 \times 20 \times 20$ mm), printed by ProJet CJP (304 nozzles). (Note: the box is the mean \pm standard deviation, and the whisker is \pm minimum and maximum)

The dimensional error for the mortar printed specimen can be found using Equation (6.7):

$$D_e = D_p - D_{CAD} \quad (6.7)$$

Where D_e is the dimensional error, D_p is an actual printed dimension, and D_{CAD} is the CAD dimension.

Figure 6. 32 also shows that, in general, the dimensional accuracy increased as the w/c was reduced for all planes. However, in the X-Y plane, a significant amount of undesirable deviation in the dimensional precision can be observed. These deviations are smaller than the nominal (CAD) dimensions due to the inaccuracy of the printhead nozzle and closeness of the nozzle. This inaccuracy could lead to overlapping and collision of the binder when it drops on the powder. Another reason may be the chemical and physical characterization of the powder-to-binder and the drop penetration ability of the powder.

In addition, the printhead located on the fast axis rails has a high rate of movement. This can be considered as another important factor contributing to dimensional accuracy. The gantry holds the binder supply system, which is located on the fast axis rails of the printer.

It is obvious that the dimensional accuracy in the 3DP parts is related to the orthotropic phenomenon, which has different mechanical strength results in each direction. The orthotropic properties of the printed objects are most related to the penetration of the liquid in the vertical Y-Z plane, which can be called the Z-direction of the sample (Shanjani et al. 2011). The X-Y plane has the highest variable error magnitude due to the effect of liquid spreadability on the surface of the X-Y plane.

In spite of the DDR shown in *Table 6. 3* for the ZP 151 sample, ZP 151 has better shape stability and a more regular cubic appearance than cement mortar (CP) samples. *Figure 6. 33* shows that the corners of each sample have different shapes. It is clear that the ZP 151 sample had a more accurate appearance than the CP samples. The filleting at the corners of CP samples meant that it did not imitate the real shape of the cubic samples. This phenomenon occurred in the CP specimens because of the shape of the powder particles in the CP specimens. Another reason is the powder spreadability on the build chamber and binder reactions in the CP specimens, which not only contain a greater number of voids but also because of their hygroscopic property. The reasons, which are explained in other subsections, are the flowability of powder, surface roughness and the apparent porosity of the samples.

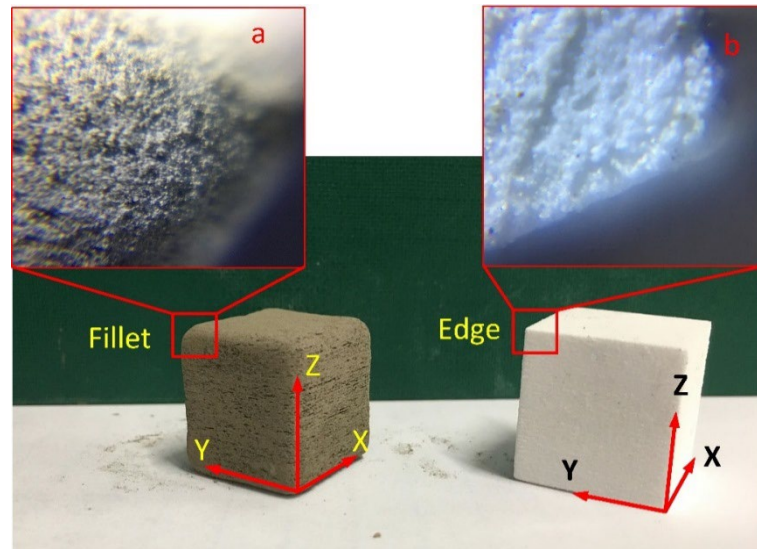


Figure 6. 33: Cementitious cube ($20\times 20\times 20\text{mm}$) (CP) printed by ProJet 360 (left), Gypsum cube (ZP 151) ($20\times 20\times 20\text{mm}$) (right)

By observing the laser microscope (*LEXT OLS5000*) images for the samples, the 3DP ZP 151 and CP samples included micropores in the microstructure because of the large spacing between the particles, which ranged from 10 to 75 μm . Therefore, the flow for each of the powder particles had fluctuated. *Table 6. 4* shows the surface roughness and topography of particles for each of the powders. The surface roughness of CP was much greater than ZP 151 due to the numerous valleys on the powder bed. The roughness is related to the flow of the powder and rate of particles flowing from the printer. Will, Detsch & Boccaccini (2013) stated that in the 3DP elements, the inter-agglomeration pores are generally formed in a size range from 1–100 μm , which is consistent with the observations of the present study.

Table 6. 4 Difference between ZP 151 and CP for the angle of repose for each of the powders

Bedded powders on build chamber	Surface roughness (Ra) μm
ZP 151	12.72 \pm 1.66
CP	19.83 \pm 2.43

Methods used to calculate the flowability of the powders include Angle of repose, Carr's compressibility index, Hausner ratio Flow through an orifice, the Shear cell method, and Cohesion Index (Geldart et al. 2006).

The angle of repose can be found using Equation (6.8);

$$\theta = \tan^{-1} \frac{h}{r} \quad (6.8)$$

Where θ the angle of repose, h the height of the pile, and r is the radius of the base of the pile. *Figure 6. 34* shows the angle of repose test for both powders. The results of the comparison of angles of repose of the original powder (ZP 151) and the modified powder (CP) are listed in *Table 6. 5*. Apparently, the regular process of the fluidization in the powder reduced the agglomeration and rate of the flowability issues in the CP powder. The fluidised bed process was verified with an initial trial and was consequently used as the standard powder preparation method for the study.

Yildirim (2001) stated that an increment in the surface hydrophobicity of talc powder would lead to a decrease in the values of total surface free energy (γ_s) and the other components (γ_s^{LW} (apolar component) and γ_s^{AB} (polar component)), attributing this to the exposure of more basal plane surfaces upon pulverization. The surface free energy for both CP and ZP 151 must be calculated, therefore, further investigation is required for that purpose.

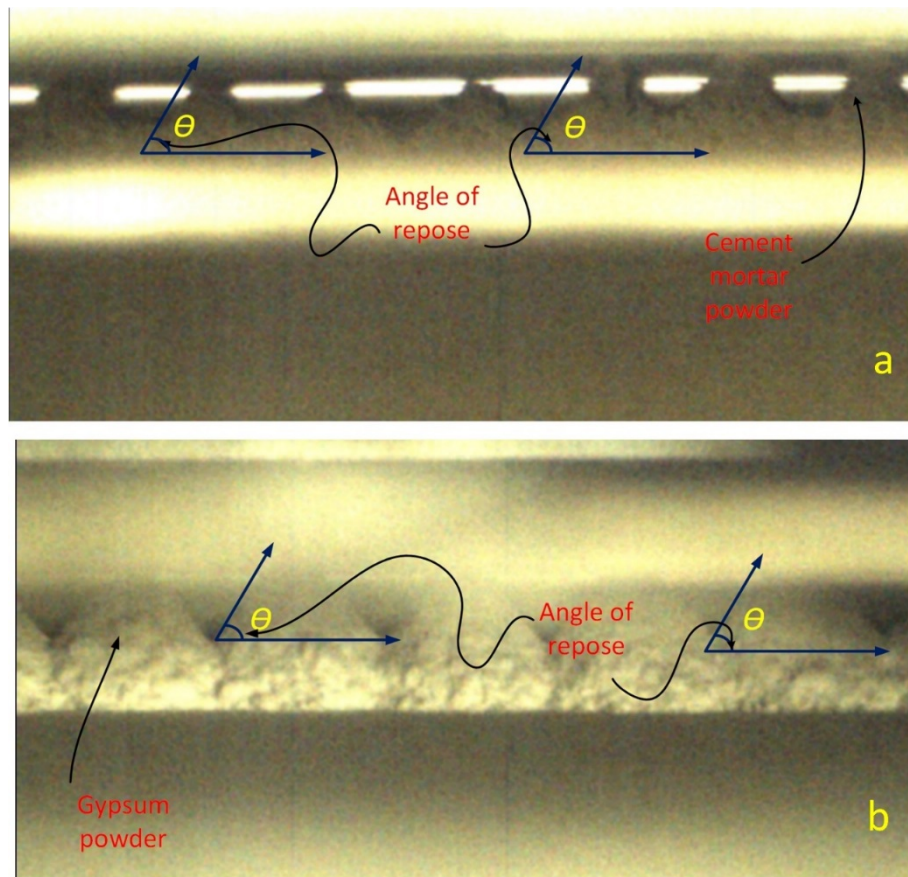


Figure 6. 34: Angle of repose for (a) CP powders after flowing from the feeder container of the printer, (b) ZP 151 powders after flowing from the feeder container of the printer.

There are several factors that decrease the flow of the powders: superficial adhesiveness, the shape of particles (spherical particles flow quickly while irregular shape particles flow slowly), the surface of particles (wrinkled surfaces have low flowability while smooth surfaces have high flowability), the presence of the electrostatic charge on the surface, and the hygroscopicity of the powders. The electrostatic charges occur inside the powder particle while flowing, particles exchange charge when contacting each other (Zhang, Bi & Grace 2015). The particles become charged with electrostatic forces as fluidised powder, with most of the particles likely to be charged negatively (Zhang, Bi & Grace 2015).

Table 6. 5 Difference between ZP 151 and CP for the angle of repose for each of the powders

Powders	Angle of repose (Θ)
ZP 151	53.90°
CP	70. 57°

There are other approaches to calculate the flowability and cohesiveness of the powder, such as the Hausner ratio and Carr's index (see Table 6. 6). Each of the approaches requires measuring the tapped density and tapped volume of the powders. The bulk density is measured by dividing the mass by untapped volume. The tapped density requires the mass to be divided by tapped volume. The Hausner ratio can be calculated using Equation (6.9);

$$H = \frac{V_t}{V_b} \quad (6.9)$$

Where H is a Hausner ratio, V_t is a tapped density, and V_b is a bulk density. A Hausner ratio of <1.25 indicates a powder that is free-flowing, whereas a ratio of >1.25 indicates poor flowability. For both powders, the Hausner ratio is greater than 1.25. However, the modified CP powder has a much higher ratio than ZP 151.

Another approach is Carr's index, which is used to measure the flow properties of the powders. Carr's index can be calculated using Equation (6.10);

$$I = \frac{V_t - V_b}{V_t} \times 100 \quad (6.10)$$

Where V_t is a tapped density, and V_b is a bulk density. A smaller Carr's Index means there are better flow properties. For instance, $5 < I \leq 12$ indicates "excellent", $12 < I \leq 16$ is "good", $16 < I \leq 23$ is "fair" and $23 < I$ is "poor" flow. Using this approach with both powders resulted in Carr's indices greater than 23, thereby indicating poor flow. Nevertheless, the CP powder has much higher cohesiveness and much poorer flow than the ZP 151 powder, recording 55.61% and 40.77%, respectively. It appears that both

powders have low flow from the feeder container to the feeder chamber. However, the result shows the flow for ZP 151 was better than for CP.

Table 6. 6 Densities, Carr's index and Hausner ratio for the ZP 151 and CP powders

Powders properties	ZP 151	CP
Surface area (m²/g)	0.999	1.021
Bulk Density (g/cm³)	0.912	0.79
Tapped Density (g/cm³)	1.54	1.78
Hausner ratio = tapped density / bulk density	1.68	2.25
Carr's Index = ((tapped density – bulk density)/ tapped	40.77%	55.61%

The process of determining powder bed porosity requires finding the in-process bed density. The in-process bed density (ρ_{bed}), proposed by Zhou et al. (2014), measures the density after the powder is spread on the build chamber. High quality in the powder-based 3DP process is important to ensure high-quality printing.

Figure 6. 35 shows the quality surface of ZP 151 and CP powders. The visual inspections and 3D laser scanning clearly show the porosity and voids on the surface of the powder. At the top of *Figure 6. 35* (a, b), the powder is bedded on the build chamber and the photo was taken for visual inspections to identify any differences between the powders. However, the bottom of *Figure 6. 35* (c, d), which illustrates the same final bedded layer after being scanned by the 3D laser scanner, clearly shows that the CP powder has a lower quality surface roughness and the powder is distributed unevenly.

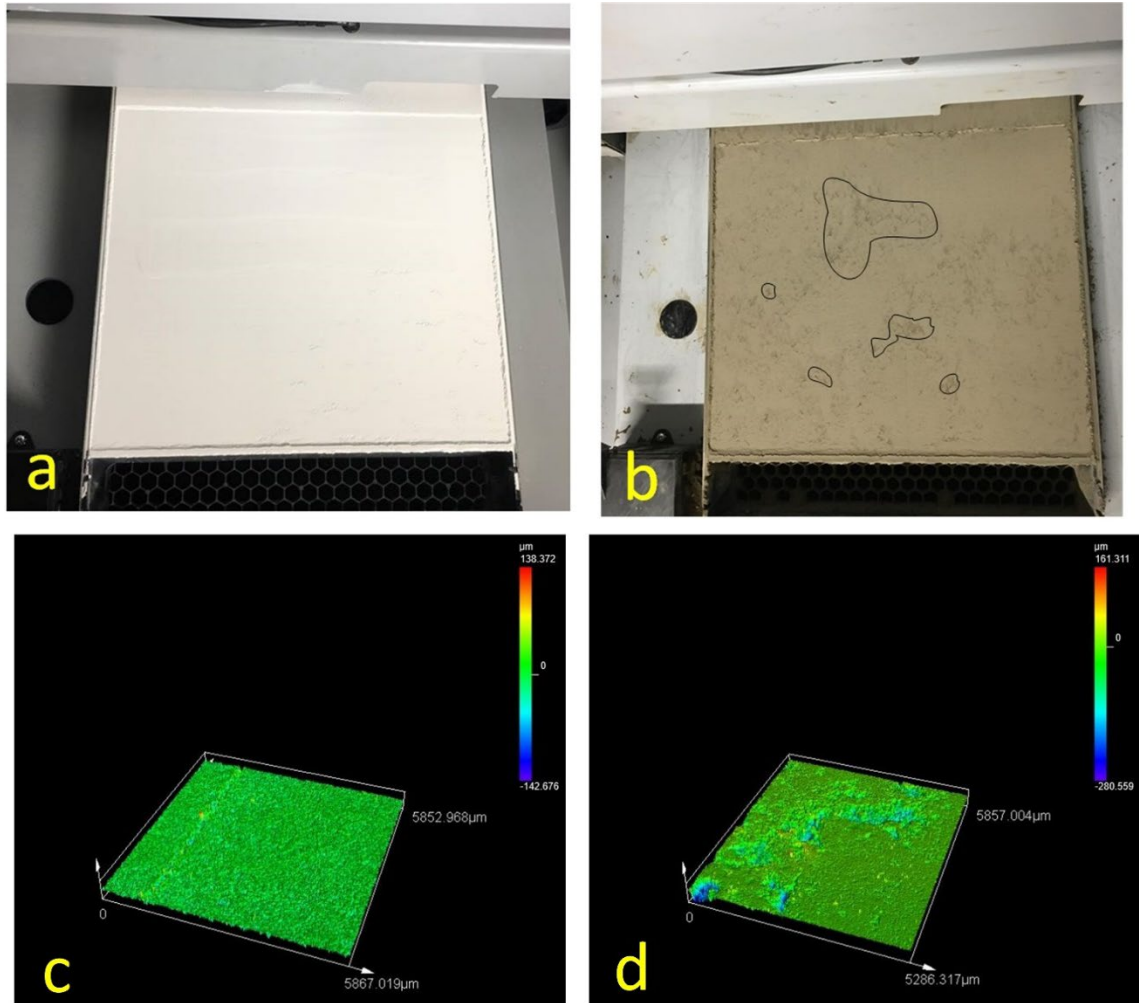


Figure 6. 35: The powder-bed on the build chamber: (a) ZP 151 (gypsum) the powder on the build chamber and (c) scanned of the bed by the 3D scanner (Olympus OLS5000), and (b) CP (mortar) the powder on the build chamber and (d) scanned powder bed by the 3D scanner.

The surface roughness of both powder-beds was measured using an Olympus (LEXT OLS5000), (see *Table 6. 4*). The results show that ZP 151 powder-bed surface roughness was approximately $(12.72 \pm 1.66 \mu\text{m})$ and the surface roughness for CP was approximately $(19.83 \pm 2.43 \mu\text{m})$. *Table 6. 7* shows the result of powder bed porosity, namely, 73.6% in CP and 64.9% in ZP 151. Therefore, the final CP printed specimens would have higher porosity than ZP 151. Hence, powder bed porosity has a great influence on the solid printed product, and the porosity of the powder bed is directly related to the printed specimens.

Table 6. 7 Bulk density, in-process density and powder bed porosity

Powder properties	ZP 151	CP
Bulk density (g/cm ³)	0.91	0.79
True density (g/cm ³)	2.65	3.07
In-process density (g/cm ³)	0.93	0.81
Powder bed porosity (%)	64.9%	73.6%

The previous subsection discussed powder bed porosity. This bed porosity directly affects the porosity of the specimens. *Figure 6. 36* illustrates the result of the porosity of 3D printed specimens for different saturation levels when using lithium carbonate and without lithium carbonate. The lower level of porosity was recorded at the different saturation levels of samples at S170-C340. *Figure 6. 36* shows that increasing lithium carbonate by a small amount had an impact on the porosity of the printed powder, however, the porosity at the highest and lowest saturation levels for both mixes was almost the same. The minimum porosity of the specimen was $55.23 \pm 0.25\%$.

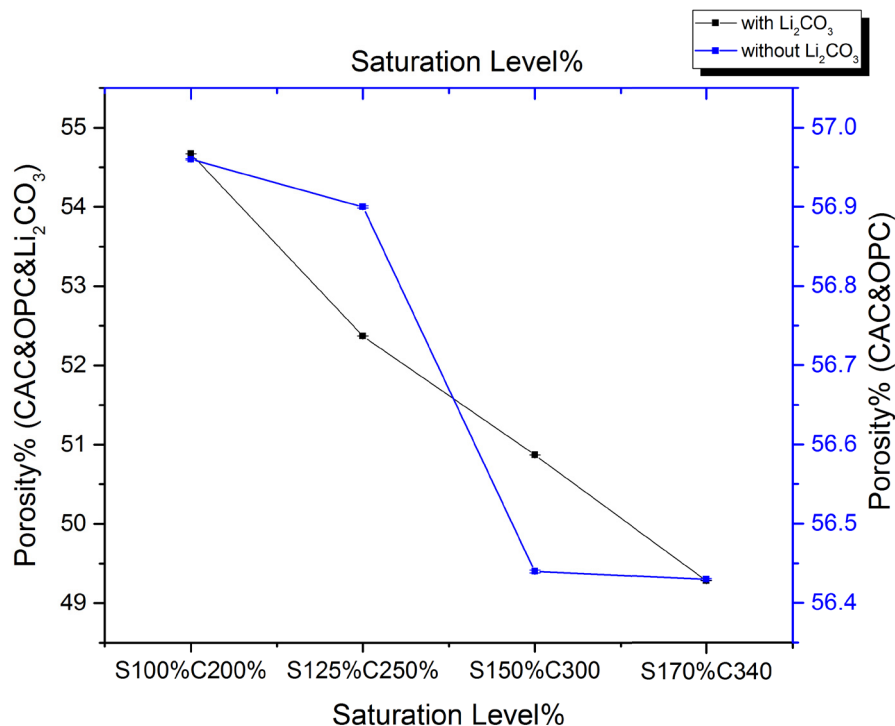


Figure 6. 36: Porosity versus saturation level for specimens CP with/without lithium carbonate.

Figure 6. 37 shows the fluctuation of porosity versus compressive strength while increasing the w/c ratio (Shakor, Sanjayan, et al. 2017). The compressive strength also increased slightly. Conversely, when porosity decreased, the compressive strength increased slightly, which was the expected result. Having a high degree of porosity weakens concrete strength. The results in Figure 6. 37 refer to a printed part without extra curings, such as heat curing. It shows that while the porosity reduced after the saturation level was reached (S150%C300%), the compressive strength increased again with the error bar value higher than the other samples. This is obvious due to the ratio of water (saturation level) increasing in the specimens, which then promotes recovery in the compressive strength of the specimens. However, the porosity in the 3DP specimens usually decreases with increased amounts of water in the printed specimens. This indicates that the part has been saturated fully and has enhanced the reaction among particles in a fully saturated state, as found in (Shakor, Sanjayan, et al. 2017).

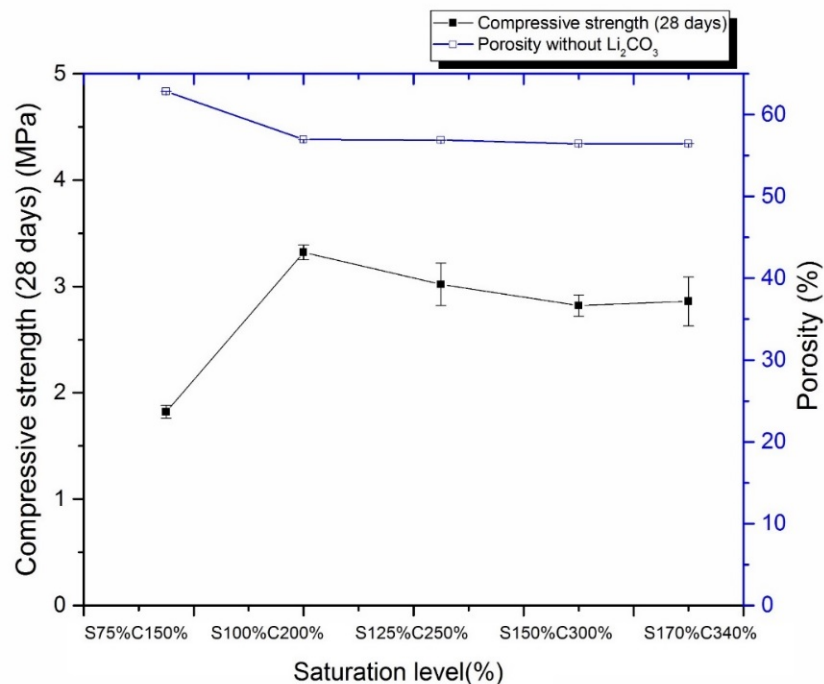


Figure 6. 37: Compressive strength versus saturation levels for CP specimens without lithium carbonate.

Figure 6. 38 illustrates the test executed using a Scanning Electron Microscope (SEM), which shows the porosity between particles of the printed cubic specimen. Plate-like large crystal growths occurred with some other unreacted particles on the surface of the specimens. It shows that there were deep holes and incohesive particles on SEM (left and right side of *Figure 6. 38*). It is obvious that the process of hydration had not completed between some of the cement particles. The 3D scanning profile assisted the identification of the porosity in the specimens.

Illustrated in *Figure 6. 38* is the test performed using the SEM. It shows the porosity on the surface of the printed cubic specimen and open pores among particles. Plate-like large crystal growths occurred with some other unreacted particles on the surface of the specimens. Furthermore, the SEM shows deep holes and incohesive particles (black colour number 2 in *Figure 6. 38*). It is evident that hydration was not completed between the cement particles and left many voids among particles. *Figure 6. 38* number 1 is a large crystal which represents the fine sand, and number 3 represents the crystal C-S-H formation of the cementitious materials.

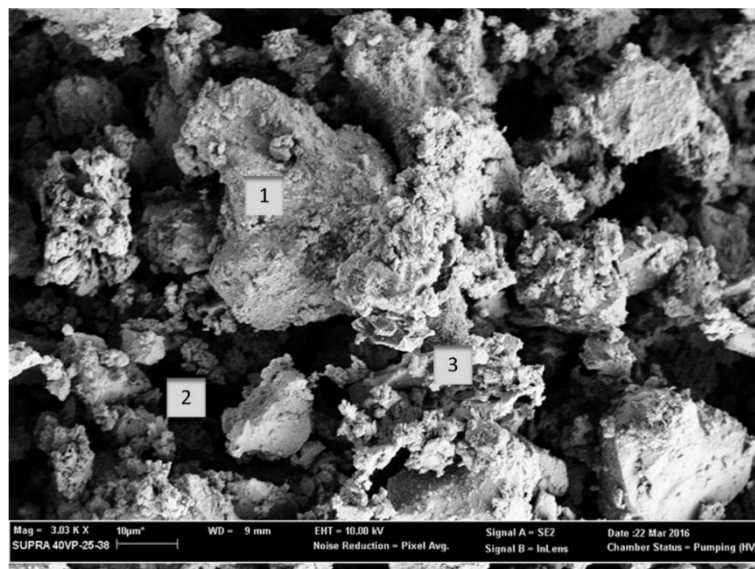


Figure 6. 38: Image of Scanning Electron Microscope (10µm) for the 3DP (green part) CP specimen.

As shown in *Figure 6. 39*, the different saturation levels of specimens at different magnifications were tested to explore the porosity and surface roughness of the samples. The test was conducted employing a 3D profile Veeco (Dektak) and Olympus (*LEXT OLS5000*) with 50× magnifications. The clear porosity and uneven surface shape of the 3D-printed specimens are visible in *Figure 6. 39*. The samples were tested and zoomed in on the side layer (XZ-plane) for the green part and the samples cured in water. However, after 7 days, the samples cured in water and tested using the 3D profile exhibited valleys (porous holes) on their surface areas. The topology and height distributions dramatically changed. This demonstrates that the value of skewness (*Ssk*) after curing had an asymmetric end extending out toward more positive signs, which means many high spikes emerged on the surface topography. The *Ssk* parameter correlated with load bearings and porosity. According to Petzing, Coupland & Leach (2010) when *Ssk* is zero this means that the height distribution at the surface is symmetrical. This is verified by the centre line for both symmetrical and asymmetrical purposes. The direction of each skew is differentiated from the one above the mean line indicating a negative skew or below the mean line indicating a positive skew, see *Table 6. 8*.

Table 6. 8 shows the *Ssk* values for a printed specimen (S100%C200%) at the same spot before curing and after curing in tap water (7 days). The value of skewness dramatically changed from negative skewness to positive skewness due to the water effect on the surface of the sample. It can also be observed in *Figure 6. 39* that many of the particles were released on the surface because of less than perfect reactions and hydration in the printing process, specifically at a low *w/c* ratio (saturation level).

Table 6. 8 Skewness value for the CP specimens before and after 7-days curing in tap water.

Sample Description	Ssk Value	
	Before curing (green part)	After curing in water (7-days)
S100%C200%	-0.025	+0.364

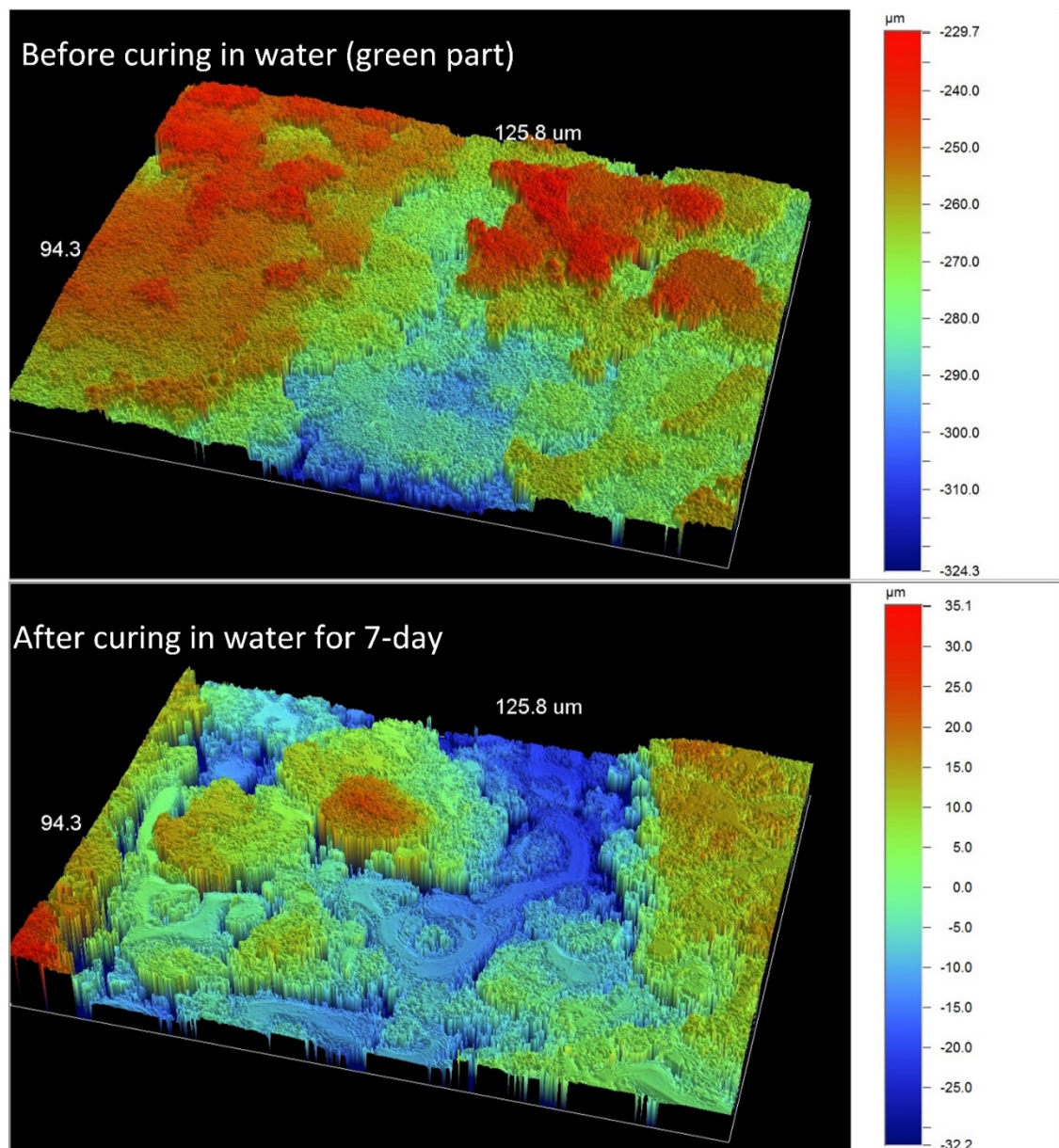


Figure 6. 39: 3D scanned image (50 \times) of the printed CP specimen before curing (green part) and after curing in water for 7 days.

Figure 6. 39 demonstrates that the samples released and split up many particles. Thus, valleys (porous holes) more clearly appeared on the surface of samples cured in water.

The porosity of CP is higher than that of ZP 151 because the penetration time was quicker, as found in the study by (Shakor, Sanjayan, et al. 2017).

Post-processing or curing has a major impact on the results of mechanical strength and the hydration process of the printed powder. *Figure 6. 19* shows that the air bubble in the uncured sample in the oven was higher than in the sample that was cured in an oven for 3 hours at (60°C). This is evidence that the curing process with heat resulted in improved printed specimens by reducing the voids and porosity between printed layers.

Table 6. 9 shows the weight results from the first until the third day of curing in water for both samples. The sample on the left was cured in the oven for 3 hours at (60°C), and the sample on the right was not cured in an oven. The results show that the water absorption in the non-cured sample in the oven was higher than the sample cured in the oven. This shows that the rate of porosity was greater in the non-cured sample than it was for the sample cured in the oven. Earlier studies found that curing concrete in a medium substituting 2% of TiO₂ nanoparticles significantly increased the flexural strength and reduced the percentage of water which is absorbed by the specimens (Nazari 2011). This means reducing the water absorption by the specimens has a positive effect on the mechanical behaviour of the specimens. Such studies need further investigation to determine the nature of the voids, such as close porous and open porous, in the samples.

A compressive strength test is commonly used to confirm that the concrete mixture meets the required strength of the construction application. The compressive strength of the 3D printed samples was calculated and compared for different delay times to identify the optimum delay time in printing. All samples were tested with similar parameters and setup conditions for delay printing times as mentioned in *Table 5. 16*.

Table 6. 9 Curing for 3 hours in oven compared with non-curing in the oven

Sample description	Medium of cure	Weight difference after water absorption (g)	Difference in weight for (non-cure minus cured sample) (g)	Note
0 day	Non-cure	3.71	-0.22	Both samples are kept for 3 hrs in water before weighing
	3 hours cure in an oven	3.93		
1 day	Non-cure	7.94	+0.49	Both samples are kept for 1 day in water before weighing
	3 hours cure in an oven	7.45		
2 days	Non-cure	10.29	+0.63	Both samples are kept for 2 days in water before weighing
	3 hours cure in an oven	9.66		
3 days	Non-cure	12.65	+0.62	Both samples kept for 3 days in water before weighing
	3 hours cure in an oven	12.03		

Figure 6. 40 shows the average values \pm standard deviation values for all five measurements, for each of the three delay times for 3 days and 7 days curing.

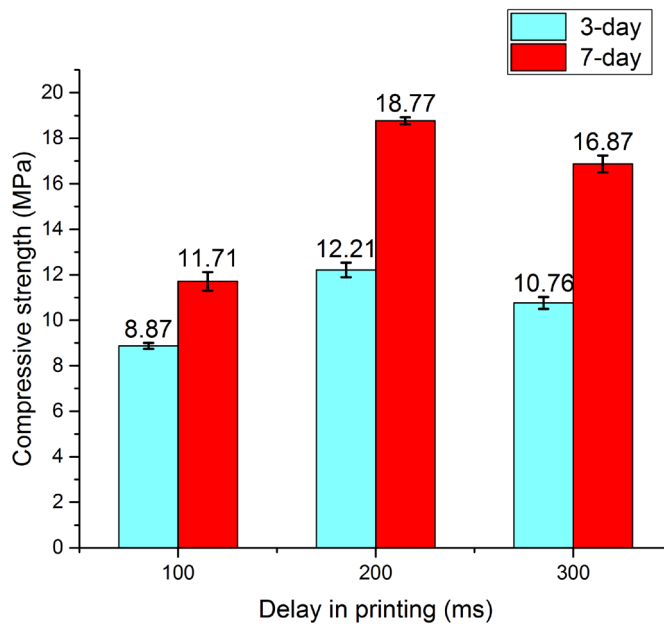


Figure 6. 40: Compressive strength in printed CP with a different delay in printing time.

Figure 6. 41 shows the stress-strain diagram in compression which begins with an initial non-linear toe region. Then, the main region is a linear region. Next, the concave region starts until it reaches the failure point. According to the compressive stress-strain diagram in Figure 6. 41, the samples (1 for each delay time) initially experienced elastic displacement then a failure in the whole body of the cube. Through the visual inspection, microcrack generation can be observed in the margin wall of the cubic structure vertically through the cube. Furthermore, the cracks sometimes extended through the middle of the cube in an hourglass shape. Thus, the internal structure of the core has an important effect on the mechanical behaviours of 3DP specimens.

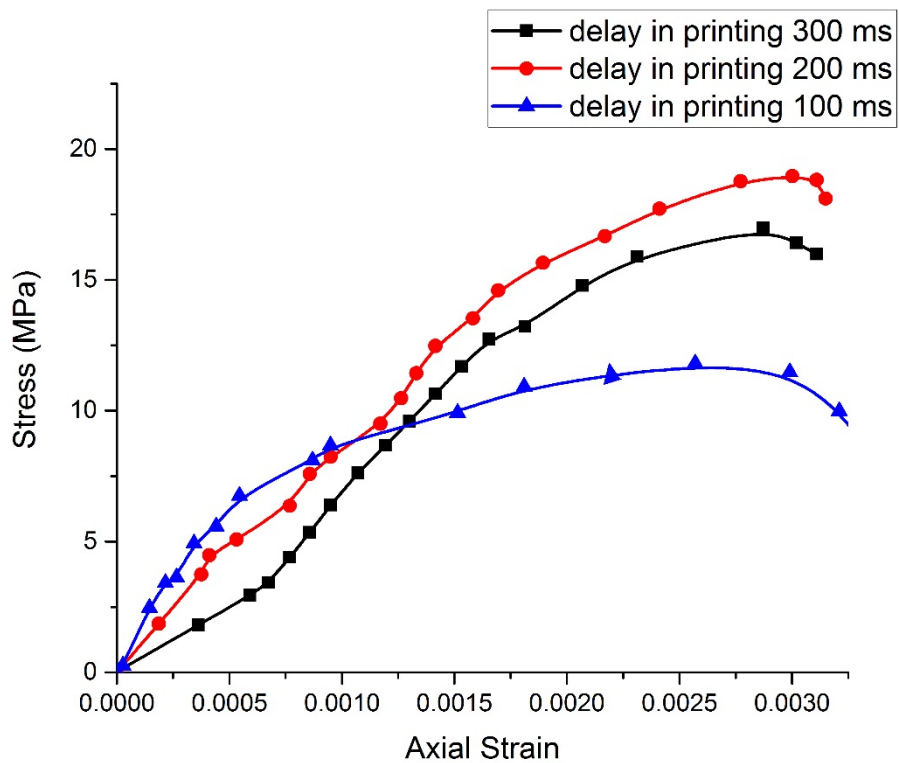


Figure 6. 41: Compressive stress-strain curve for different layer printing delay times of CP specimens for the maximum printed sample and with 7-day curing.

As shown in Figure 6. 41, a differential delay in printing between layers results in different values in compressive strength at 3 days and 7 days. S100 specimens were found to have relatively low compressive strength (refer to Table 5. 15). Incrementing the printing delay from 100ms to 200ms increased the compressive strength and toughness

of the printed structure. S300 specimens had higher compressive strength values compared with S100. However, S200 recorded the highest overall results among all printing layer delays. Thus, amongst the delay testing for the three (100, 200, 300ms) selected times, 200ms was the optimum printing delay between layers for CP materials.

In an earlier study, it was shown that when the saturation level of powder was high, the strength of CP specimens increased (Shakor et al. 2018; Shakor, Sanjayan, et al. 2017). Therefore, in this study, the optimum saturation levels were chosen. It was found that an increase in the delay time between layers resulted in better binder uniformity and spreading which, in turn, enhanced the strength. One noteworthy result shown in *Figure 6. 40*, is that for the same binder saturation, an increased printing delay (from 100ms to 200ms) led to an increase in compressive strength. This is because the delay enabled the sprayed binder to penetrate more efficiently in both lateral and vertical directions on the surface of the powder, hence, resulting in fewer voids between powder particles. This is consistent with a study by Vaezi & Chua (2011), which found that inadequate spreading of the binder vertically and laterally reduced sample strength and integrity. According to *Figure 6. 40*, the weakest average compressive strength was found in S100 specimens. Another reason for the weakness of S100 was due to weak compactions by the roller on the powder bed. The roller moves faster when the delay in printing time is reduced which, in turn, led to inconsistent and less compaction in the powder bed.

It was observed that as the delay in printing time between layers decreased, the fresh layer of powder was not spread homogeneously on the bed surface. This created voids in the bed-powder, making the printed specimen porous, and the final product inconsistent. In another case, the binder was not fully solidified and the following powder layers were placed on to the previous layer that had not completely hardened. Alternatively, the binder

may have hardened relatively quickly once it was placed, meaning that particles deposited from the new layer on the surface of the former layer were not subject to particle restructuring due to capillary forces. Further, a binder droplet on the surface layer may have reacted and penetrated entirely before the next layer was laid. In this way, the previous layer would be more coherently created and, as a result, the compressive strength would be improved.

Consequently, finding the optimum delay in printing time is crucial for printing different geometries in CP (Sachs et al. 1994). With regard to the delay in printing time, drop penetration depth, drop penetration speed and wettability ratios account for delays in layer printing and green part strength of the final 3DP product (Shakor et al. 2018; Zhou et al. 2014). Overall, the shearing of the layers during or after the printing process occurred when non-ideal (i.e. too high or low) printing delay times were used during the printing of structures. The factors discussed significantly influence the mechanical behaviours of the printed product.

Figure 6. 42 shows the results of the compressive strength tests of printed mortar samples. The results presented had all been cured in tap water only, (3-hour 40°C, 28 days water, 3 hours 40°C), (3 hours 60°C, 28 days water, 3 hours 60°C). After a sample was printed, the post-processing consisted of (a) curing in the oven for 3 hours; (b) curing for 28 days in tap water; then (c) drying in the oven for 3 hours. This same basic post-processing sequence was used for all samples, but at various temperatures, until the optimised maximum compressive strength of the printed sample was found.

Figure 6. 42 shows the compressive strength test outcomes for the sets of printed specimens that were cured for 28 days at five different temperatures. The bars with indicated values on top are the actual strengths and the error bars indicate the standard

deviations of the results. As is shown in *Figure 6. 42*, an increase in the curing temperature from 40 to 80°C led to a near-linear increase in compressive strength. This increased strength in the cement mortar proportional to the increase in temperatures was likely due to the greater reaction level of cement mortar at raised temperatures. Curing in an oven accelerates the reaction of the cementitious process. Fast hydration and a high early compressive strength have been observed to occur as the temperature increases (Lothenbach et al. 2007).

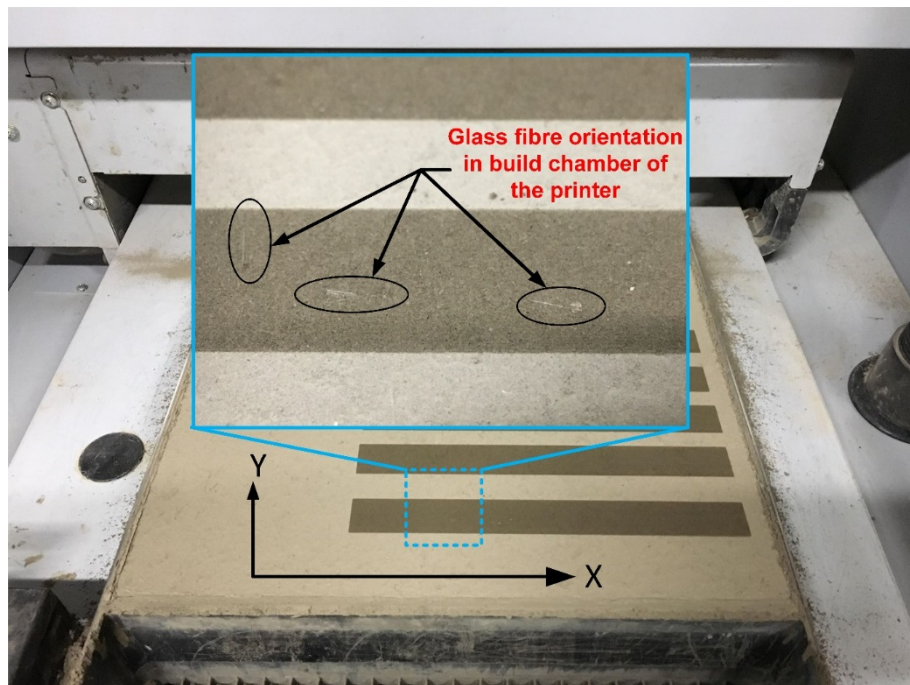


Figure 6. 42: Glass fibre orientation while bedding the powder on the build chamber of the 3DP.

The experimental results are consistent with a study by Abd elaty (2014) which demonstrated that the compressive strength of Portland cement concrete with a low w/c ratio at 50°C is higher than at lower temperatures (e.g. 10°C and 23°C). Early mechanical strength development for compressive strength and a trend towards increasing strength have been repeatedly observed, even at 91 days, for cement mortar at temperatures of 60°C (Amin et al. 2017).

Raising the temperature increases the rate of reaction and reduces the setting time (Shakor et al. 2018) since it accelerates the dissolving of alumina and silica particles from the unreacted particles of the powder and a greater amount of Alumina (Al_2O_3) and Silica(SiO_2) becomes available for the reaction process. The modified powder for 3DP contains a high proportion of Alumina due to the high levels of CAC in the main powder. In relation to the total mass, Al_2O_3 contributes approximately 70% in CAC, whereas it is only 5% in cement.

The binder has a significant effect on the result of compressive strength at high temperatures due to the main content of the binder, namely, isopropyl alcohol. The binder consists of humectant and water, where the humectant is 2-pyrrolidone (3DSystems 2012).

Despite the trend observed up to 80°C, a contrary trend was observed when temperatures rose beyond 80°C up to 90°C, as shown in *Figure 6. 46*. According to previous studies Altan & Erdoğan (2012), a threshold temperature for the cementitious reaction process will occur when temperature-controlled kinetics is inhibited. Extra Al_2O_3 and SiO_2 particles react when the curing temperature is above the threshold point. Mortar slurry forms rapidly and deposits on the surface of the unreacted powder, which will constrain further dissolution. Consequently, the compressive strength declines significantly. Hence, 80°C was nominated as the optimum curing temperature for cement mortar samples.

Figure 6. 46 shows the results of the compressive strength of printed mortar samples. The results are presented for all curing processes in tap water only (3 hours 40°C, 28 days water, 3 hours 40°C), (3 hours 60°C, 28 days water, 3 hours 60°C), etc. The post-processing involved curing the printed sample in the oven for 3 hours and then curing it for 28 days in tap water, then drying it in the oven for 3 hours. This process was used for

all samples at various temperatures until the maximum compressive strength of the printed sample was optimised.

In general, curing in tap water achieves low compressive strength test results, predominantly due to the slight reaction that occurs among particles. The small concentration of OH⁻ ions in tap water works as a reactive chemical agent in the cementitious process since it leads to ineffective dissolution and formation of hydroxyl substances (Bellego, Gérard & Pijaudier-Cabot 2000; Sagoe-Crentsil & Weng 2007). Consequently, low compressive strength will result due to the densify reaction not being established appropriately. It must also be noted that water-curing at high temperatures has been observed to adversely affect compressive strength, due to heat acceleration which leads to the leaching of Al₂O₃ and SiO₂ from the existing gel in the samples.

Samples for the compressive test were printed and tested in all three planes. The study was prepared to show the influence of the fibre effect and the plane direction in the sample *Figure 6. 42*. It is clearly shown in *Figure 6. 42* that most of the fibre strands are oriented in the Y-direction, with only a few of the fibre strands being bedded in the X-direction. This was also observed after removing the sample from the build chamber.

To observe the obvious embedding of the fibre strand in the cement mortar powder, the build chamber of the printer was removed and put under the 3D laser microscope (LEXT OLS5000) to identify the location and bedding of the fibre strand, *Figure 6. 43* and *Figure 6. 44*. It is clear that the Y-axis has more fibre strands bedded on the powder. Therefore, the orientation of printing is highly significant and has an effect on the mechanical strength of the printed object. This study contributes to determining the printing directions with fibre reinforcement and optimizing mechanical strength.

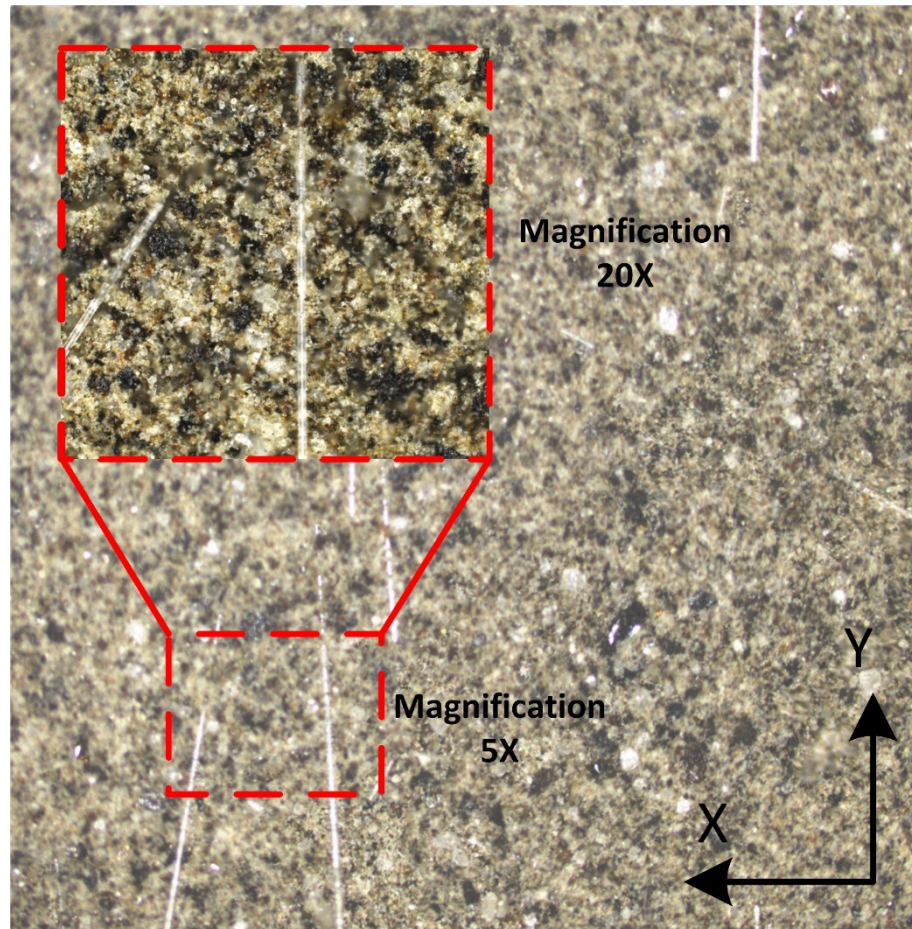


Figure 6. 43: Glass fibre bedding on the powder in the build chamber of the 3DP (3D laser scanning image LEXT OLS5000).

Figure 6. 44 clearly shows the orientation of the fibre strands after spreading on the build chamber. Most of the glass fibres are spread parallel to the Y-axis. The reason fibres are spread along that axis is that the fast axis roller pushes all powder and fibres in this direction. This is consistent with the work of (Christ et al. 2015).

3D laser scanning microscopy was used to capture the fibre strands in the printed object. Such close scanning detected the bedding orientation of the fibres and whether the fibres were damaged or not, see Figure 6. 45.

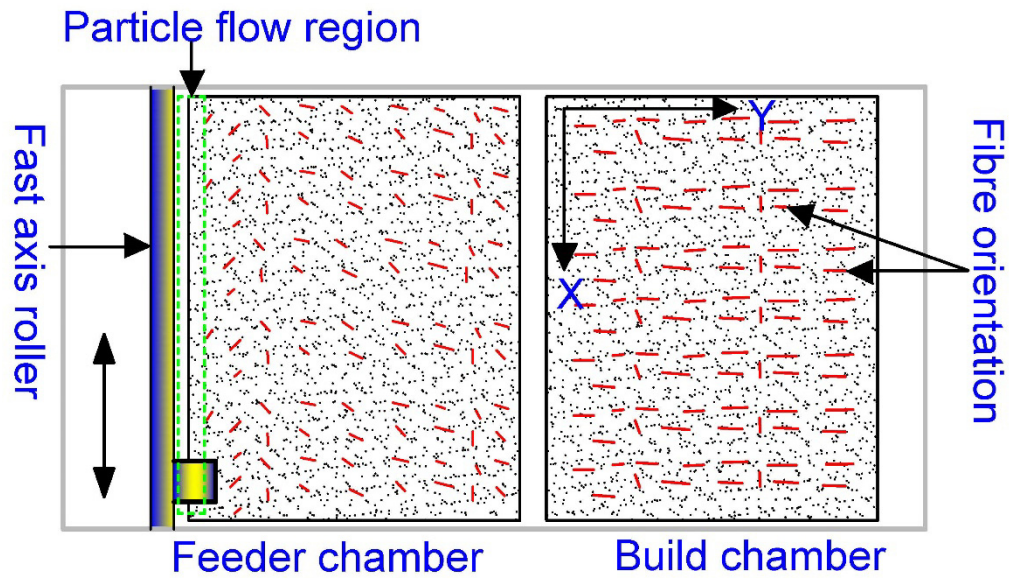


Figure 6. 44: Schematic illustration of the chopped fibres spread on the build chamber and feeder chamber.

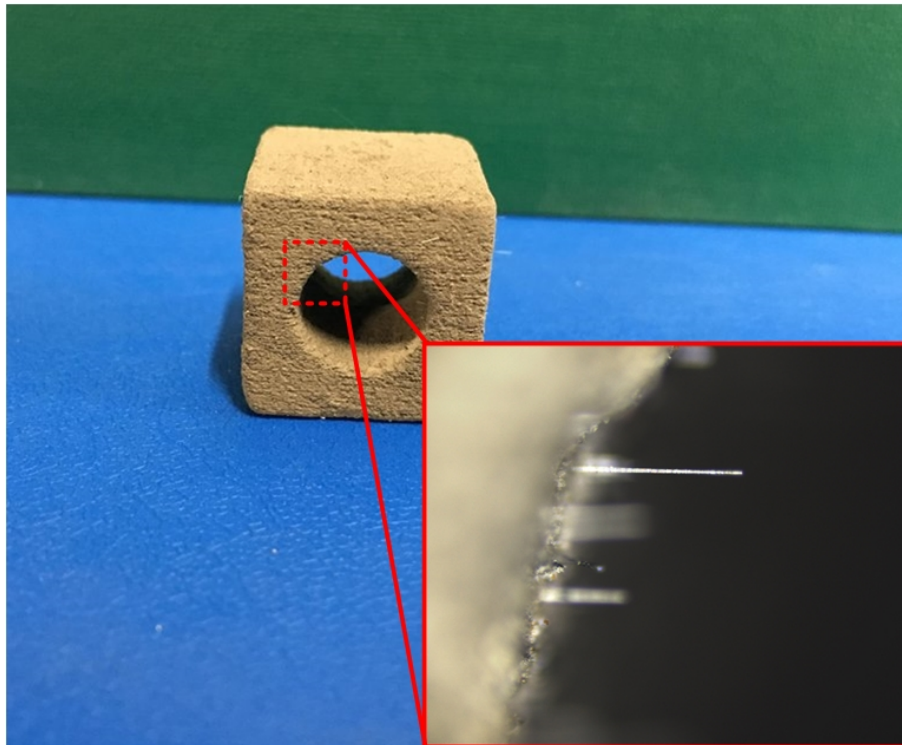


Figure 6. 45: Fibre bedded orientation by 3D laser scanning by (LEXT OLS5000).

Figure 6. 46 shows the compressive strength of the printed mortar using 1% E6-glass fibre as reinforcement when curing at different temperatures. Figure 6. 46 clearly shows that curing at 80°C recorded the optimum compressive strength for the printed mortar. It

was also found that the maximum strength was in the XY plane when the load was applied in the YZ plane. The compressive strength of mortar with 1% glass fibre was 37.88 MPa, which is strong enough for construction applications.

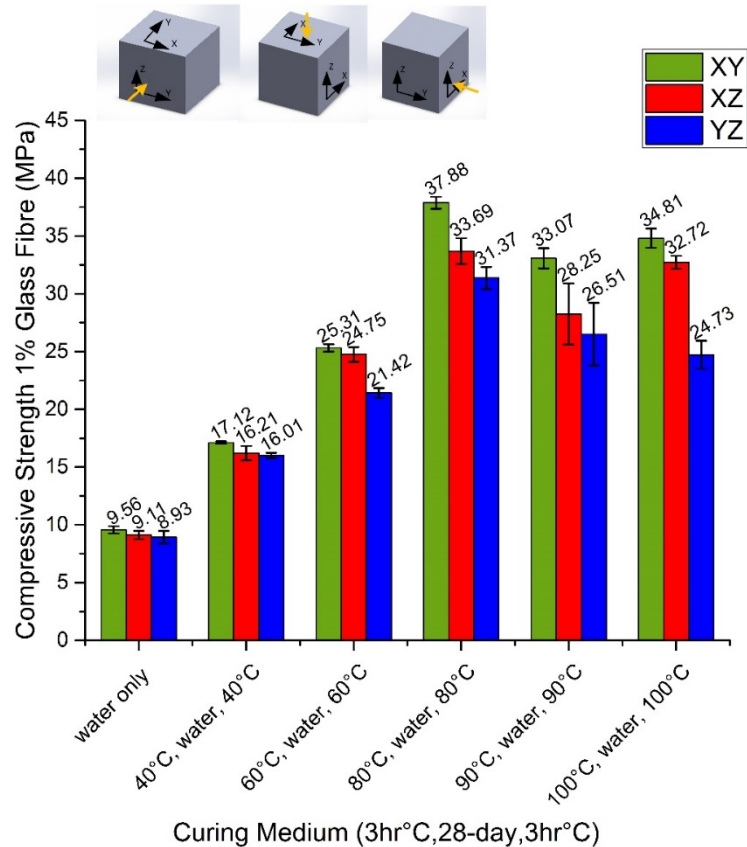


Figure 6. 46: Compressive strength of mortar sample ($50 \times 50 \times 50$)mm with 1% glass fibre using different curing medium.

These results are quite positive for the construction industry and precast construction applications. This study identified the optimum saturation level (which was selected from earlier studies of the authors (Shakor et al. 2018; Shakor, Sanjayan, et al. 2017)), the strongest plane and direction, and identified the optimum temperature which is most suitable for curing the medium to achieve the highest compressive strength. For long term durability and to check the quality of the materials, it is necessary to conduct further investigations such as monitoring the surface quality and mechanical strength of the materials.

Figure 6. 47 shows the compressive strength of the printed mortar cube without glass fibre in all three planes. It shows that the optimum compression strength was in the XY plane, however, the compressive strength was lower than the samples using glass fibre.

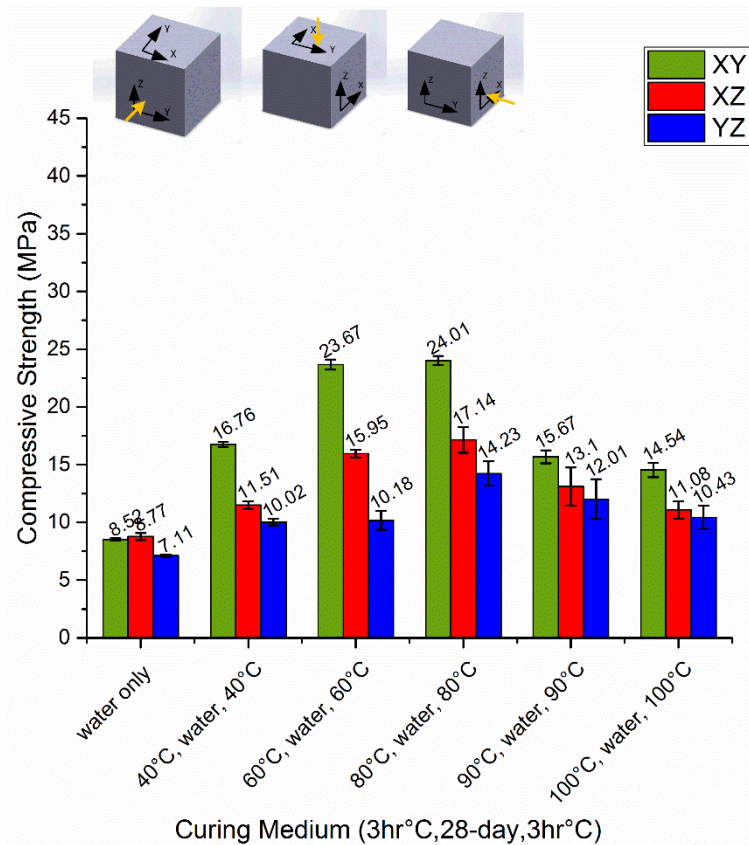


Figure 6. 47: Compressive strength of mortar sample (50×50×50)mm without glass fibre using different curing medium.

Figure 6. 48 shows the results of the compressive strength of printed mortar samples for specimen dimensions of (20×20×20)mm. The results are presented for all different curing processes in tap water only, (3 hours, 40°C, 28 days water, 3 hours 40°C), (3 hours 60°C, 28 days water, 3 hours 60°C), etc. Samples for the compressive test were printed and tested in all three planes. This study showed the influence of the plane direction of the sample.

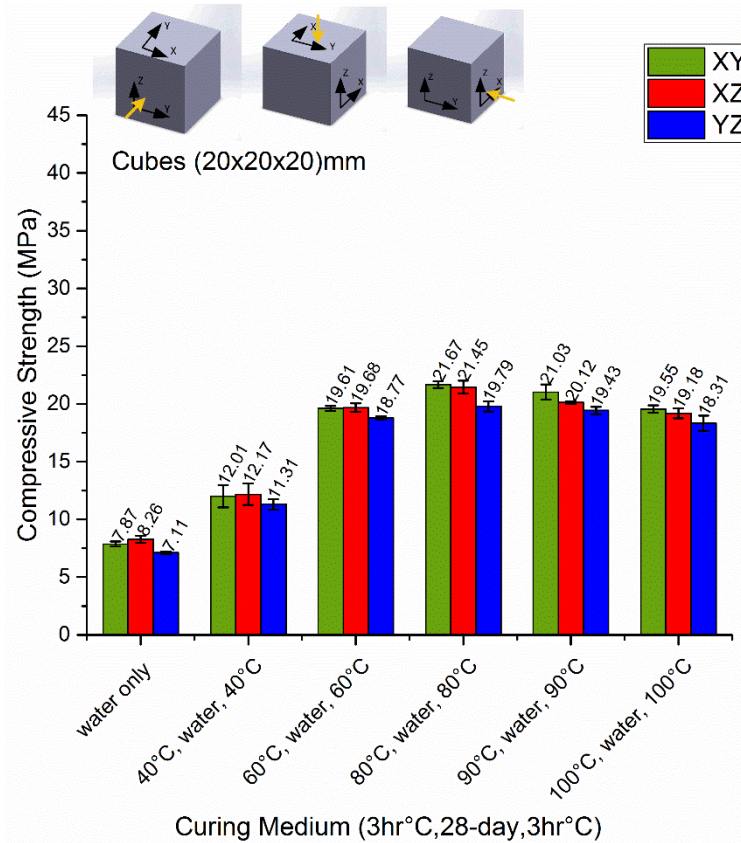
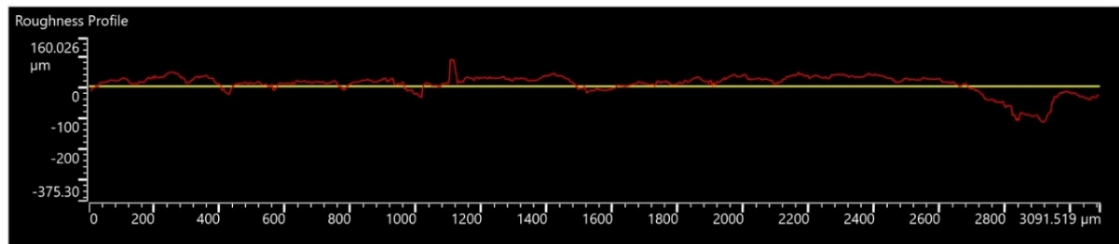


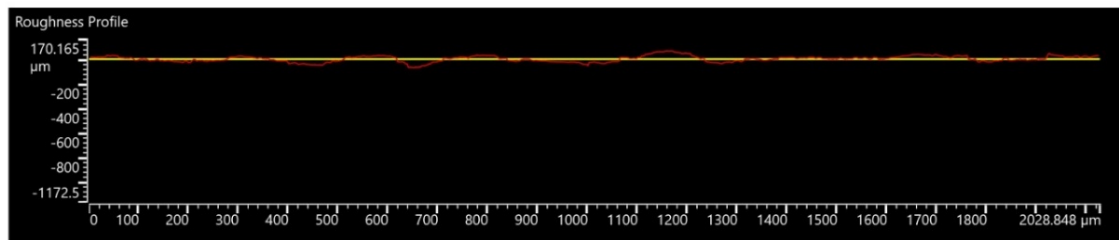
Figure 6. 48: Compressive strength of mortar sample (20×20×20)mm using different curing media without glass fibre.

The compressive strength results using 1% glass fibre significantly increased the strength values by approximately 37%. There was not only an increase in compressive strength but also in flexural strength. All samples, with and without glass fibre, were subjected to the same curing conditions. After the curing, however, fibre-reinforced printed samples showed significantly higher values compared with unreinforced samples. A fibre content of 1% was easily mixed in the feeder tank and passed through feeder holes. Flexural strength was increased by 46% at 60°C with this fibre content. A higher ratio of fibre content in the cement mortar made it difficult to flow through the feeder tank. Furthermore, the vacuuming of all materials back to the feeder was difficult due to the high fibre filament content.

The Porosity and Density of the composite materials had an impact on the mechanical properties of the sample. While the density of the printed scaffold was not affected by fibre reinforcement *Table 5. 8*, the porosity of the printed scaffold was reduced if the printed scaffold was reinforced with fibre, due to the well-distributed fibres on the powder-bed chamber. *Figure 6. 49* shows the surface roughness profile of printed specimens in the presence and absence of glass fibre. *Figure 6. 49* clearly shows the improvement in the roughness on the surface morphology of the cube. The surface roughness of the cube with 1% glass fibre was approximately $18.57\pm 1.35\mu\text{m}$; without using glass fibre it was $22.31\pm 3.72\mu\text{m}$.



Roughness Profile of Printed Cement Mortar Cube



Roughness Profile of Printed Cement Mortar Cube with 1% glass fibre

Figure 6. 49: Comparison between printed cement mortar specimens in the presence and absence of glass fibre.

Ra is a value describing the surface roughness of material surfaces. A substantial change occurred when we added glass fibre to the cement mortar. *Figure 6. 50* shows the roughness profile and the surface morphology of the printed specimens at different magnifications (20×, 50×, 100×) for a cement mortar cube without fibre. Obvious holes and valleys are visible on the printed specimens, as illustrated in *Figure 6. 50*. The blurred part occurred due to differential changes in height on the surface of the printed structures.

The average surface roughness on the printed cement mortar specimen was $22.31 \pm 3.72 \mu\text{m}$. The gypsum specimen was a few digits higher $13.76 \pm 0.95 \mu\text{m}$ than the cement mortar specimen. This means that the printed cement mortar had a rougher surface than the gypsum and had more valleys on the printed surface.

The roughness on the mortar surface varied from position to position due to the inconsistency in the distribution of cement mortar powders on the build-chamber. The distribution of the gypsum powder on the build-chamber was better and provided a higher resolution, leading to a better result for the printed part.

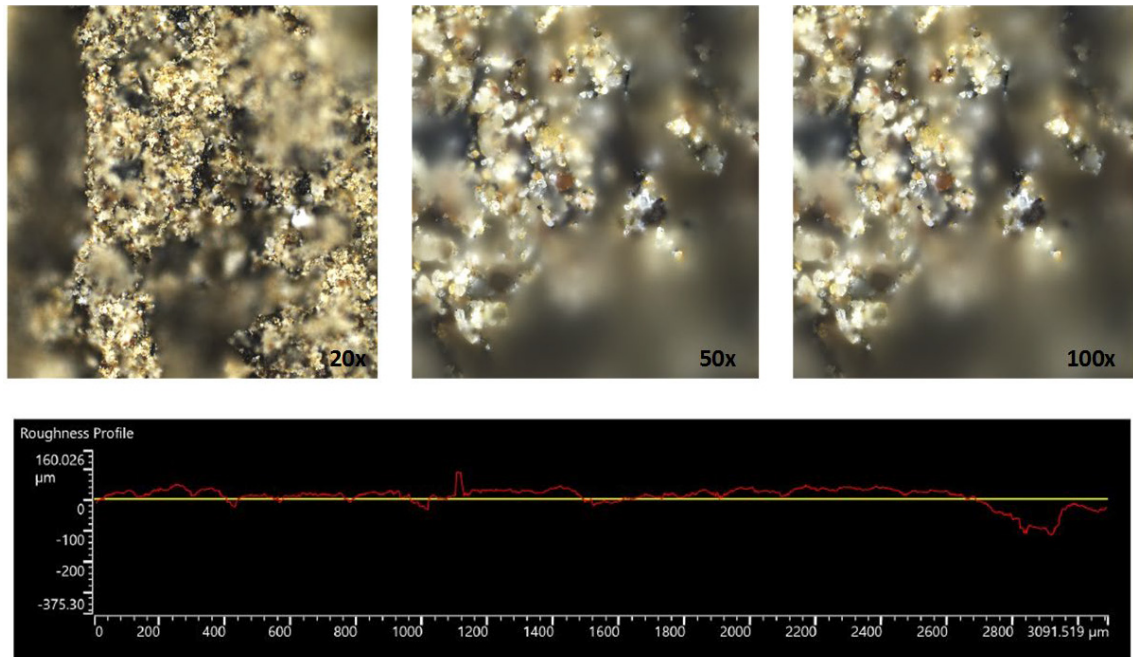


Figure 6. 50: Surface roughness profile and capture of the surface of printed cement mortar at 20 \times , 50 \times , and 100 \times .

3D laser scanning microscopy (LEXT OLS5000) was used to measure the diameters of the filaments and the spreadability of the chopped glass fibre in the printed specimens. The result shows that the diameters of the filaments were the same as that provided in the datasheet of the manufacturer of the E6-glass fibre, namely, $13 \mu\text{m} \pm 10\%$ with a length of $6000 \mu\text{m} \pm 1000 \mu\text{m}$ (JushiUSA). This means the fibre filaments were dispersed and bedded in the printed specimens without any damage.

Figure 6. 51 shows the 3D laser scan of the fibre filaments in the printed specimens, clearly showing the approximate length at the edge of the sample and the diameter of the sample. The approximate length of the filaments beyond the edge was approximately 400 μm , with the rest of the fibre's length inside the printed mortar. The diameter was approximately 13.49 μm . This is reasonable proof that the filaments were not damaged during printing and solidification.

In the study by Zortuk et al. (2008), different percentages of glass fibre (0%, 0.5%, 1%, 2%) were used in the thermoplastic resin to check the surface roughness and physical characterisation. They found an increase in mechanical strength in 0.5% and 1% glass fibre without any significant change in surface roughness and quality. This is consistent with the finding of the present research regarding the mechanical characterisation of the cement mortar printed part. A study by Farina et al. (2016) investigated two different types and textures of fibre/rebar of different sizes printed using electron beam melting (EBM). The macroscopic result showed that the smaller fibre/rebar had better pullout response after fracture, which confirmed the presence of fibre among mortar particles connected to both cracked valleys. This was also confirmed by an SEM image where the morphology of large fibres was affected by a weaker fibre-matrix bond compared with the smaller fibres.

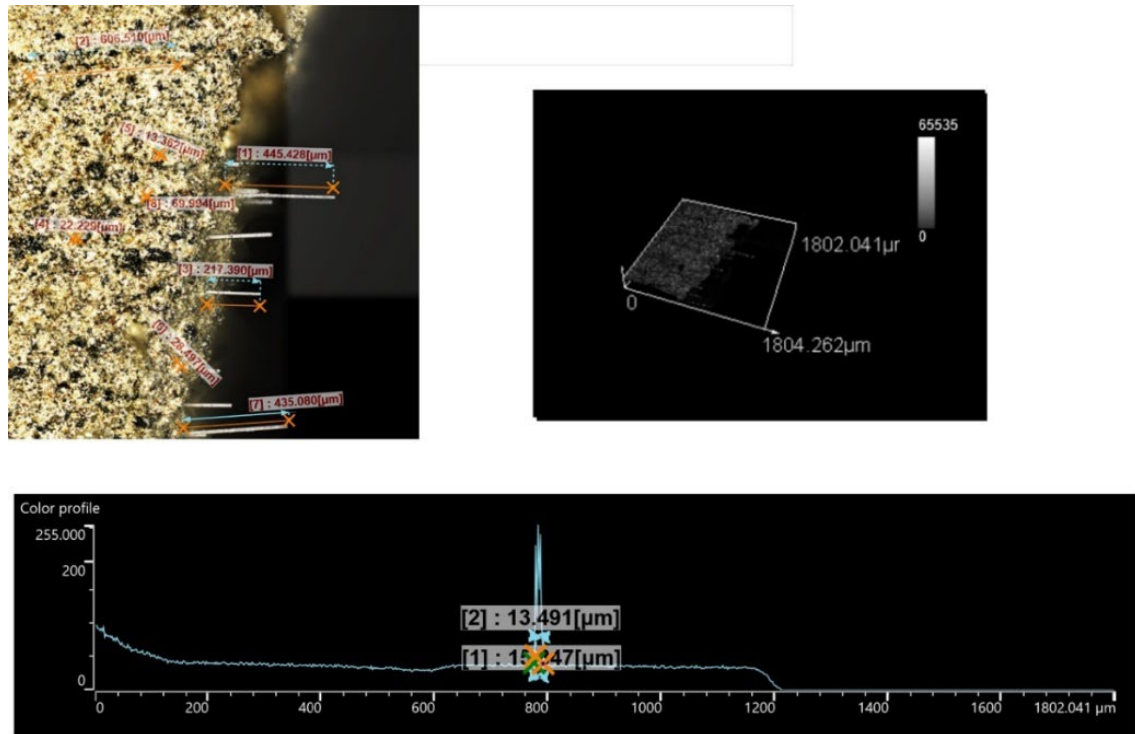


Figure 6. 51: Filament diameter and length of the fibre in the printed specimens.

However, the glass fibre strands did not have a direct influence on porosity and pore size distribution (Figure 6. 52). Furthermore, despite the surface fractures visible in Figure 6. 53, the inclusion of fibre allowed the prism to retain its shape and that it also contributed to the late fracture of the scaffold.

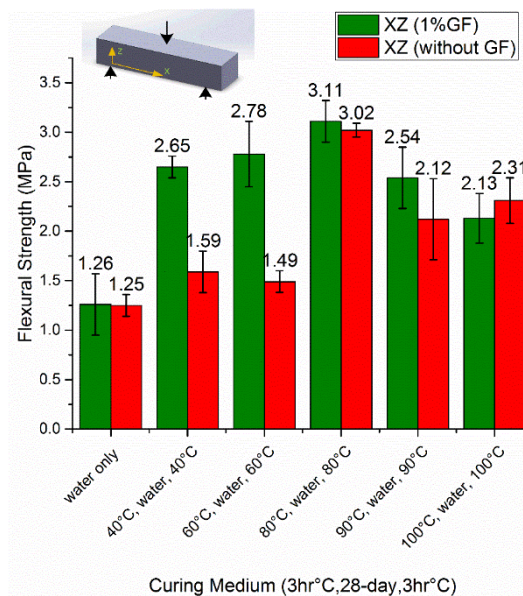


Figure 6. 52: Flexural strength of mortar sample (160×40×40)mm with and without glass fibre using curing media at different temperatures.

The investigation of mechanical properties using the three-point bending test found higher flexural strengths in fibre-reinforced samples, see *Figure 6. 53*. This represented a transfer of the mechanical load from the matrix into the fibre in addition to energy dissipation due to the frictional forces while fibres were stretched (Li & Maalej 1996) causing greater strains on the composite. It has also been found that the orientation of the fibre-reinforced strands in samples can have an effect on mechanical properties (Miguel et al. 2013). However, there was little difference between printing orientations when samples were fibre-reinforced. The fibre strands lined up mostly in the Y-direction so that the reinforcement in the Y-axis was primarily stronger than samples printed than in the X-direction, see *Figure 6. 43*. This is consistent with the study by (Christ et al. 2015) that used calcium hemihydrate (Note: in that study the X and Y axes were opposite to their orientation in the present work). While drying in the oven after printing greatly increased the mechanical properties, it may have affected the effectiveness of the fibre reinforcement in the sample, particularly at very high temperatures (over 80°C). This indicated that the elevated post-processing temperature and hardening had a greater impact on mechanical properties than the fibre strand reinforcement. Furthermore, *Figure 6. 53* shows that an elevated temperature of 100°C led to cracks appearing in the sample. Given that 100°C temperature is the boiling point of water, most of the water (binder liquid is more than 90% water) evaporated rapidly in the sample. Therefore, the cracks were visible on the surface of the sample *Figure 6. 53*.

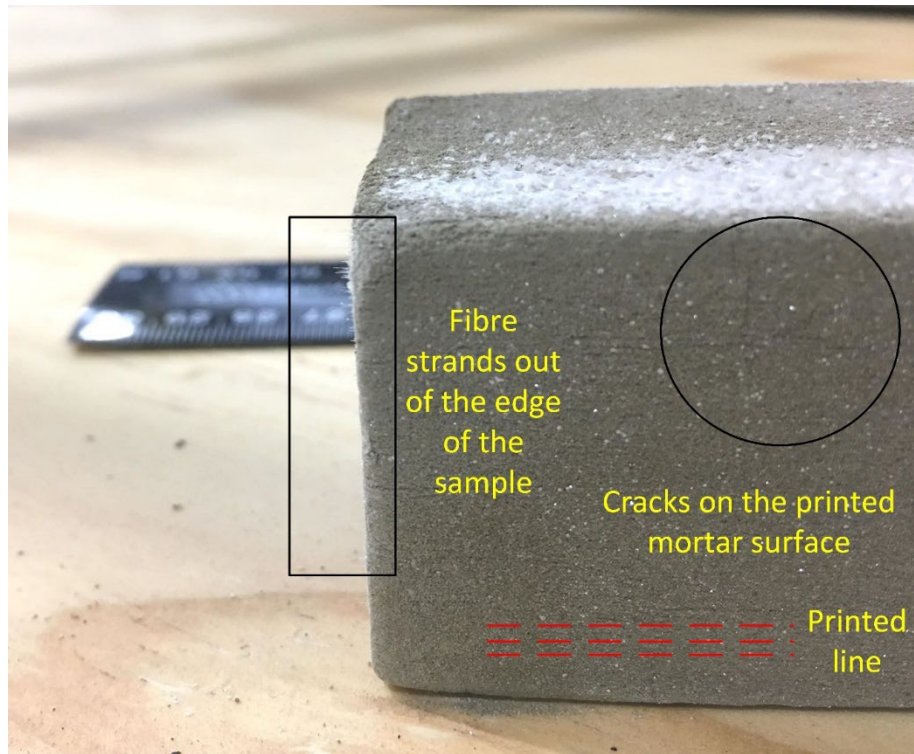


Figure 6. 53: Flexural strength of mortar sample (160×40×40)mm with glass fibre using curing media at different temperatures.

6.1.2 Extrusion Printing Materials

In extrusion-based mortar printing, the robotic arm is set up on bases to print horizontal and vertical lines. The main transition path taken by the robot, referred to as the ‘horizontal test’, is shown in *Figure 6. 54* and consists of a series of rows of approximately 300mm in length printed next to each other. The distance between the layers (in the Y-direction) is determined by the desired thickness of the layer which is reflected by the choice of nozzle. The ‘vertical’ test was simply the same footprint except, after completing the tenth line, the end-effector would return to the starting position, increment upwards, and repeat the same pattern.

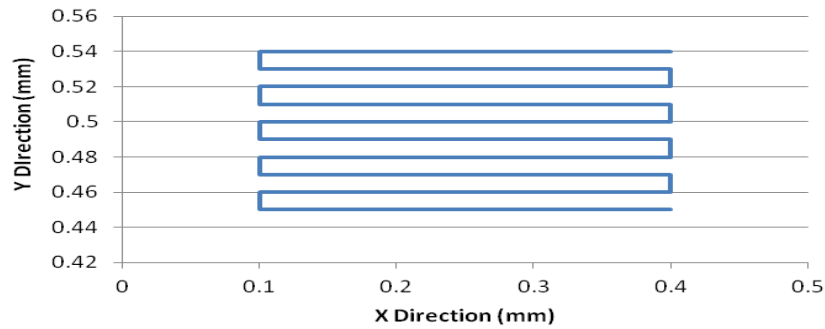


Figure 6. 54: 'Horizontal Test' cross-section path.

The different velocities of components that act in the system have significant impacts on the shape of the extruded mortar and concrete mixtures. The auger delivery method directly affects the flow rate of the mixture from the extruder. Reducing the effects of joint oscillations as the robot approaches singularities is essential to maintain a smooth print result. Tests were conducted to show the impact of the DLS method on joint velocities as a joint's measure of manipulability reduces.

Experimental trials were conducted to determine the effectiveness of mortar or concrete mixtures. Based on the consistency and rheology of the printed samples, several trials were chosen as 'optimum' trials for the squeeze flow tests and compressive strength tests. Ring moulds were prepared for the squeeze flow test.

Several mix designs were performed, similar to the mixtures presented in previous studies (Le, Austin, Lim, Buswell, Gibb, et al. 2012; Lim et al. 2011; Malaeb et al. 2015; Tay et al. 2016). These tests also depended on the capabilities of the extruder, see *Figure 6. 55*.

There were 12 different concrete mix design trials which were performed by the 6DOF industrial robot. Of these trials, only three were chosen for their performance in compressive strength and results yielded in the squeeze-flow test. These tests were the basis for the printing quality test, flow quality and buildability (i.e. each layer's capacity to hold subsequent layers without falling). These benchmarking keys for printing have

been stated by (Le, Austin, Lim, Buswell, Law, et al. 2012; Panda et al. 2018; Tay et al. 2016). Generally, the thickness of the printed line changed in a range of about (1-2) mm. According to *Table 6. 10*, the thickness for each printed line for the different nozzles produced different results.

It was also determined that the quality of the resolution of materials depended on the speed of the auger (flow rate) and velocity components associated with the various joints of the robot.

The squeeze-flow tests showed different results for single, double and triple layers of the selected mixtures, as shown in *Figure 6. 56*. In a test that used a single layer, the concrete mixture had better results until it reached the required displacement.




Trial Number	Image	Comment
Trial 5		Successful print
Trial 7		Slight flow
Trial 8		Good layers

Figure 6. 55: Several printed specimen shapes with comments

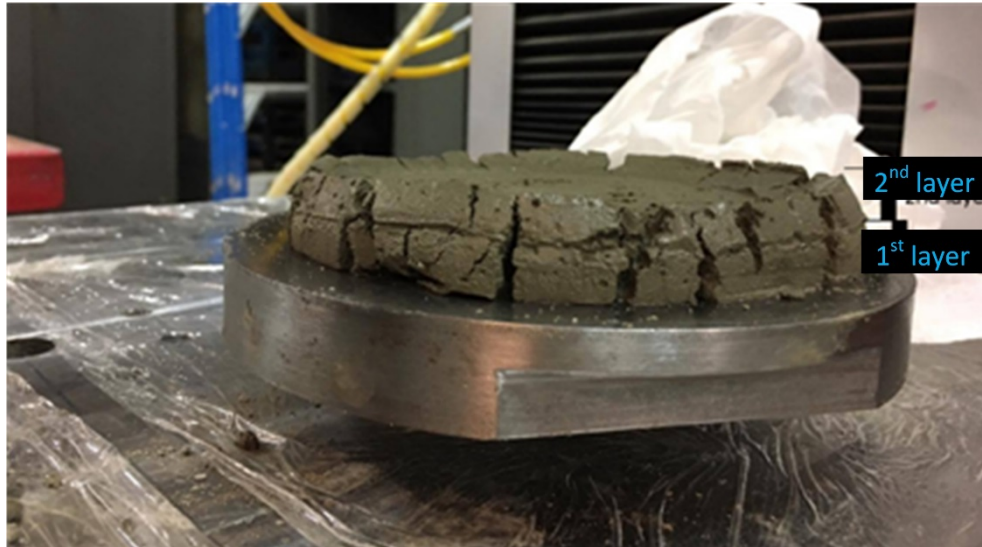


Figure 6. 56: Squeeze-flow for the double layers of trial 12

It was crucial that the mortar or concrete mix designs were compatible with the speed of the robot and the auger delivery methods. Researchers such as Hwang & Khoshnevis (2004) had mechanical speed limitations with the novel contour crafting system. The speed of material deposition was not well established in their research.

Mixtures with reduced workability were severely impacted when the velocity of the end effector was excessively fast. The robot ran the calculated path at a constant velocity before the extruder had time to move a proper volume of material. This resulted in layers with significant gaps between them. Alternatively, mixtures with increased workability were negatively impacted when the velocity of the end-effector was too slow. These instances resulted in the robot moving too large a volume of material before the robot could properly transition through the calculated path.

Regarding the auger delivery method, it was important to determine an appropriate velocity in which the end-effector would travel paired with a suitable supply voltage to the 24V motor which powered the extruder's auger to produce an acceptable flow. It was found that the auger could move substantial volumes of material. However, the flow rate tended to be inconsistent. Material tended to gather on the inside of the extruder tubing

and allowed the formation of air pockets in the flow. Despite this, it was determined that the optimal speed for the robot was between 39.36 and 42.12 mm/s when the auger voltage was set at approximately 15 to 19 volts. Another drawback was that the motor that powered the auger, struggled to rotate when put under increased loads. Loads from the mixes with higher densities and higher viscosities considerably reduced the auger's practicality.

As the robot's layer height increased, the more contorted were the required joint angles. The manipulability was significantly reduced at some points of the path and DLS was required to dampen the resulting oscillations. The immediate goal for the vertical print test was to achieve an ultimate print height of approximately 600mm (*Figure 6. 54* shows the cross-section). For the following graphs, the robot was set to print the vertical test at a height of 590mm from the printing plate with a layer thickness of 10mm. The process was discretised into approximately 130 robot poses in order to complete each layer.

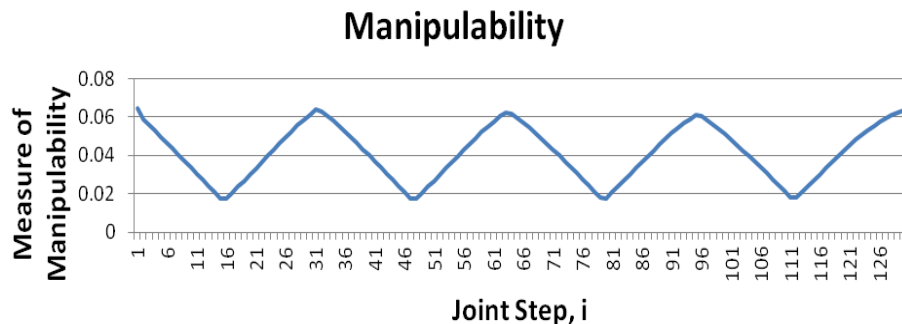


Figure 6. 57: Measure of Manipulability

Figure 6. 57 shows that the system utilised DLS on several occasions. The robot approached singularity between joint step intervals of 8–23, 40–56, 72–88 and 103–120 (with manipulability less than 0.4), and the system implemented DLS during these intervals to reduce the sudden change in rotational velocity.

Figure 6. 58 depict the change in rotational velocity for joint states from joint step 8 to joint step 23. Note that the other joint step intervals yielded similar results, hence, only one interval was examined.

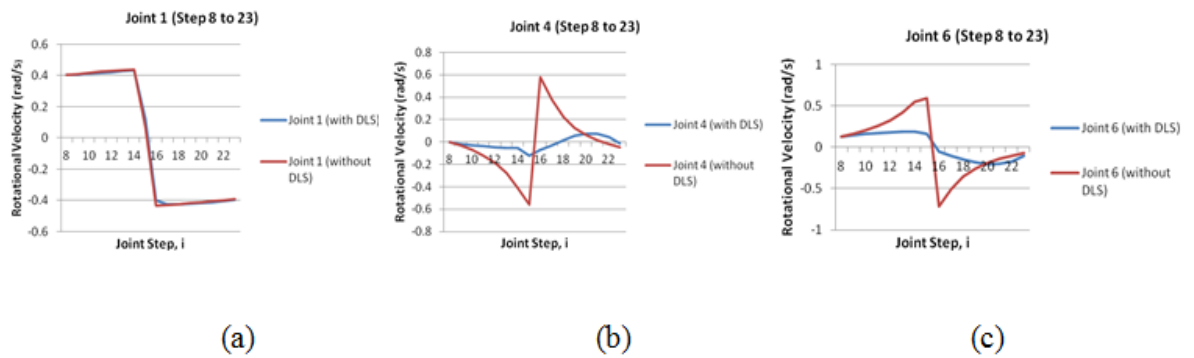


Figure 6. 58: Velocity comparison for joints: (a) 1, (b) 4, and (c) 6.

It can be seen that the smallest changes occurred in Joint 1. Joint 4 and Joint 6 show significant damping. This could be due to the fact that these joints had a much larger displacement requirement compared with the other joints. The most significant change in rotational velocity occurred between steps 16 and 17. With DLS the change in velocity was significantly smoother than without DLS.

The slump test produced three different results from the three different trail mixes. This difference in results was based on their w/c mix ratio and the cohesiveness of their particles. Consequently, all the trial results had a different slump ratio. The deformation of each slump was 8.5 mm, 8.8mm, and 12mm for trials 5, 8 and 12, respectively. It is noteworthy that trial 8 had a lower slump than trial 5, with the difference likely due to the amount of w/c and superplasticizer in this mortar mix. It is also interesting that the mixing time and the time taken to pour into the slump had a great influence on the resulting mix. Each trial was mixed for 5 minutes. Trial 5 was expected to achieve higher penetration than trial 8, but trial 5 was more coherent than trial 8, as explained in the squeeze flow test, see Figure 6. 59 and Figure 6. 60.



Figure 6. 59: Mini-cone slump test for trial 8.



Figure 6. 60: Spread-flow test: (a) for trial 5 which did not use fibre; (b) for the same trial by adding fibre with 1% polypropylene fibre.

Table 6. 10 shows the results of the relative slump for all main mixes used for the printed samples. The minimum flow and slump occurred in trial number 5 with 1% polypropylene fibre. This result was expected due to the consistency and cohesiveness of this mix and the fibre content. The use of polypropylene fibre increased the mechanical strength of the structural element (subsection 5.5) and it reduced flowability (Figure 6. 59) and shrinkage (Figure 5. 37). In addition, fibre increased the buildability of the mortar and stiffened the mass of the printed layer. For that reason, it is recommended that fibres be used in the printed specimens to increase stiffness and mitigate shrinkage in the printed part.

Table 6. 10 The relative slump value and height of the slump for selected trials.

Trial no.	Height of slump (mm)	Average diameter no. 1 (mm)	Average diameter no. 2 (mm)	Average relative slump value
Trial 5	8.5±0.54	190.63	184.65	2.52
Trial 5 (with 1% PP fibre)	6±0.16	148.27	155.25	1.30
Trial 8	8.8±0.61	199.52	201.84	3.02
Trial 12	12±0.58	201	201	3.04

The results of the squeeze-flow tests showed different values in the single, double and triple layers for each of the selected trial mixtures (5, 8, 12), as shown in *Figure 6. 60*. In the single layer mortar mix test, better results were obtained in the reaction force value until it reached the required displacement. For instance, at a displacement of 2.99mm, the required loads in trial 12 (concrete mix with small aggregate) were approximately 956.51 N. At the same displacement for trials 5 and 8 (cement mortar), the loads were approximately 277.82 N and 153.11 N, respectively. An examination of the results of the tests that utilised a double layer found significant differences when compared with the single layer results. Trial 5 (cement mortar) had a reaction force which reached approximately 622.54 N when the displacement was approximately 3.99 mm, whereas in trials 12 and 8 the loads were 536.05 N and 275.75 N, respectively. At the same displacement, the results for the triple layers exhibited a similar pattern.

These results show that the mortar was more coherent than the concrete mixtures in the fresh state, thus, it did not allow trapped air bubbles to remain in the mortar mixture. This is consistent with the study by Surendra, Yilmaz & Thomas (2003), who discovered that the mortar in the first 24 hours had a greater compressive strength compared with normal concrete. Hence, a much higher percentage of open pores will exist in the concrete mixtures compared with the cementitious mortar due to the presence of aggregates. The larger particle sizes lead to a higher porosity within the concrete mixtures.

The reaction force is dependent on the number of chains (layers) and the force between the particles. Trial 12, a single layer test, showed that the presence of the small aggregate in the mixture can resist more force over the given displacement, *Figure 6. 61*. Furthermore, *Figure 6. 61* shows that the mortar mix for more than one layer had better resistance than the concrete mix and that less penetration occurred between layers when the loads were applied.

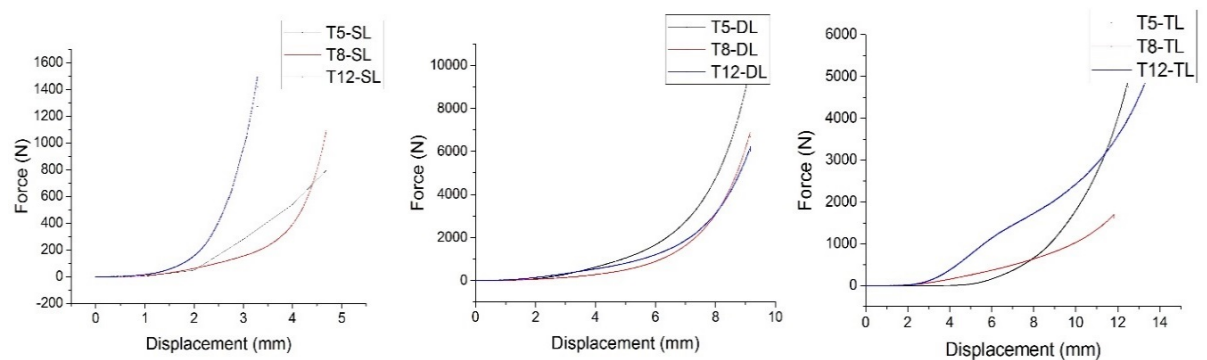


Figure 6. 61: Single layer (SL), double layer (DL), and triple layers (TL) for the trials (5,8,12) (cement 1: fine sand 1).

In *Table 6. 11*, the setting time results for the different trial mixes is shown. There were minimal differences in the initial setting times of these trials.

Table 6. 11 The setting time results for the three main trials.

Trial No	Initial setting time (min)	Final setting time (min)
T5	75	120
T8	85	225
T12	75	90

The setting time has a crucial effect on the bond between printed layers and penetration rate between each printed layer.

The buildability tests, which depend on the setting time, were applied to each trial by printing with an extrusion caulking gun.

Table 6. 12 relates to trial 5. This trial was based on the original mix design, which used a 1:1 cement to fine sand ratio with a w/c ratio of 0.33. This was able to be printed with the caulking gun and a circular nozzle of 14mm diameter. The settling observed was, to

some extent, expected with the relatively similar levels of sand and cement in the mix. Not much change was observed in the heights of the sample. Sample number 6 showed a failed extrusion that had collapsed considerably.

Table 6. 12 Caulking gun extrusion nozzle (Ø14mm).

Interval time (min)**	Buildability						Height (mm)					
	1	2	3	4	5	6	1	2	3	4	5	6
3	×	×	×	×	×	×	12	11.5	12	12	12.5	8*
7	×	×	×	×	×	-	12.5	12	12	12.1	12	-
10	✓	✓	✓	✓	✓	-	12	12.4	12.1	12.1	12.2	-

*Failed extrusion.

** Interval time between layers from mixing until the finish from 1 to 5 layers.

The speed of the mixer and the duration of mixing significantly affects the result of the cementitious mortar and flowability of the materials, Figure 6. 62.

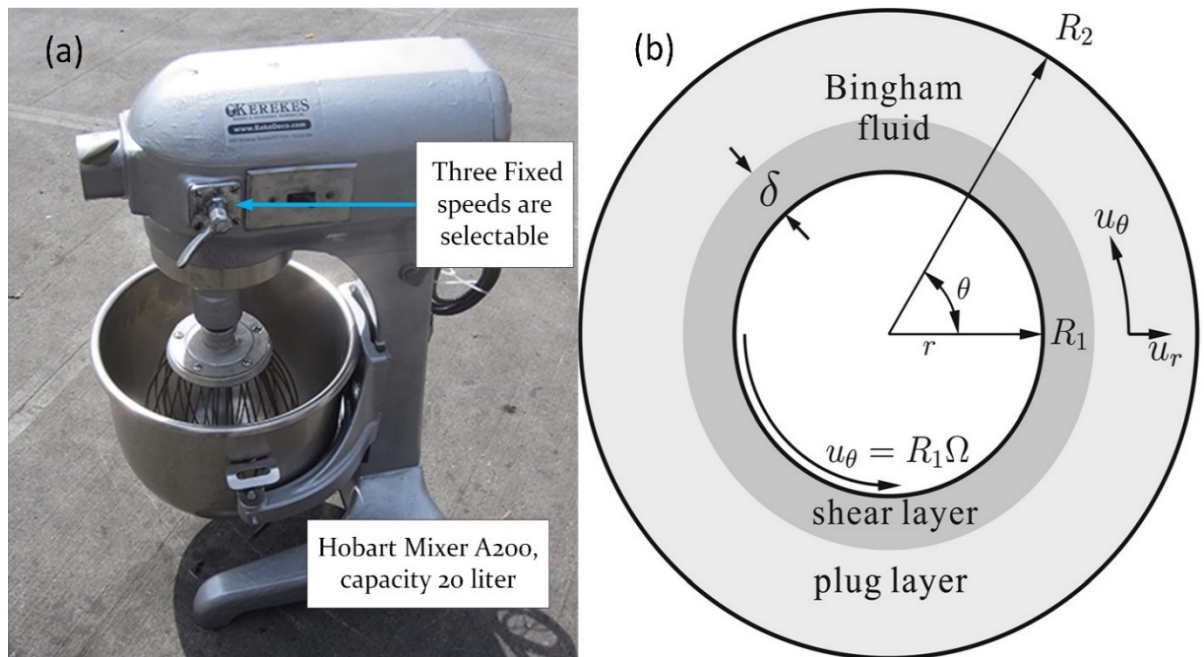


Figure 6. 62: (a) Hobart mixer A200; (b) The shear layer in the Hobart mixer (Wu & Liu 2015).

According to Wu & Liu (2015), the Bingham’s shear stress for fresh concrete is described by the following formula (6.11):

$$\tau = \tau_0 + \mu\gamma \tag{6.11}$$

Where, τ is the shear stress in (Pa), τ_0 is the yield stress in (Pa), μ is the plastic viscosity (Pa.s), and γ is the shear rate in (s^{-1}).

Roussel (2006) defined the apparent yield stress of the Δt concrete mix. The stress of the second layer is of the same order, $\tau_0 + \mu\gamma$, while the shear rate between the two layers is equal to the flow speed of the concrete divided by the depth of the second layer. To mix the two layers, this stress should be higher than the apparent yield stress of the first layer (Perrot, Rangaard & Pierre 2015). A_{thix} is known as the rate of the flocculation which is the shear stress divided by the torque (Pa/s), shown in Equation (6.12), (6.13).

$$A_{thix} = \frac{\tau_0}{T} \quad (6.12)$$

$$\tau_0(\Delta t) = \tau_0 + A_{thix} \Delta t \quad (6.13)$$

Where, $\tau_0(\Delta t)$ is the yield stress of the material at the variable time. A_{thix} is classified as having three levels: the flocculation rate which is non-thixotropic (<0.1 Pa/s); (0.1~0.5 Pa/s) thixotropic; and (>0.5 Pa/s) highly thixotropic. In the present work, A_{thix} was approximately 0.4 Pa/s, which suggests a thixotropic property for the mixed materials. When printing concrete, this suggests having higher thixotropic concrete, which means a lower rate of the viscosity of the concrete when faced with any shear rate. Therefore, when obtaining lower viscous materials, the flow rate increases through the pump. This occurs by having an agent, such as a superplasticizer or viscosity modifying admixtures or by moving the materials inside the hopper.

For each of the optimum trials that were printed successfully, a uniaxial compressive strength test was conducted. *Figure 6. 63* presents the results of the test conducted for the manual concrete mix, which included polypropylene fibres at different ratios.

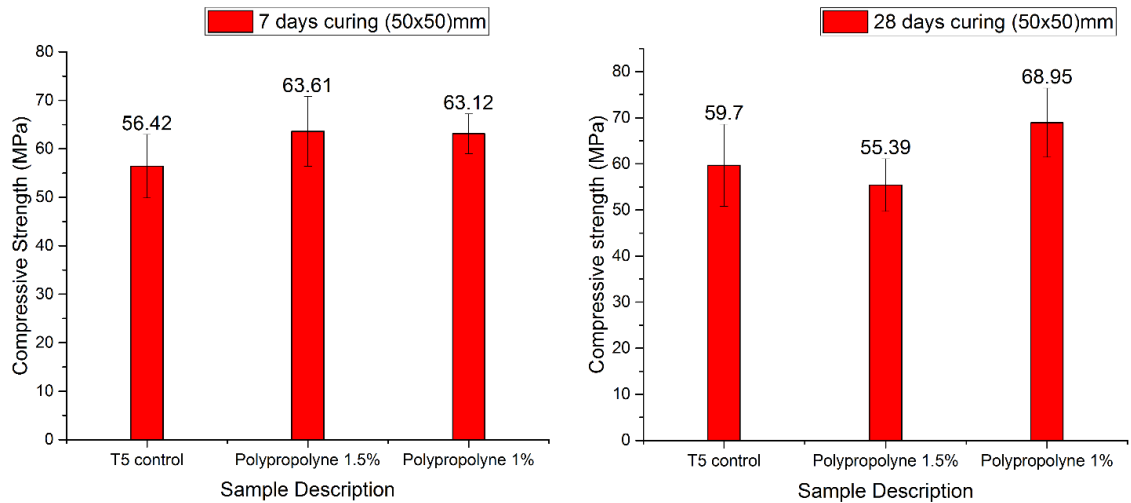


Figure 6. 63: Compressive for manual concrete mix after 7-day and 28-day curing (the values specify the actual strengths) with a cement fine sand ratio of 1:0.5

The printed short column was tested using the uniaxial loading test. The mix design and detail of the materials' properties are described in Table 5. 20.

The compression strength result for the 7 layers of the printed mortar is shown in Figure 6. 64. It can be observed that the highest compression result for printed mortar without curing and after 28 days was 13.45 kN as a maximum load. The printed specimens were left in the controlled temperature room at $20\pm 2^{\circ}\text{C}$ without any extra post-curing.

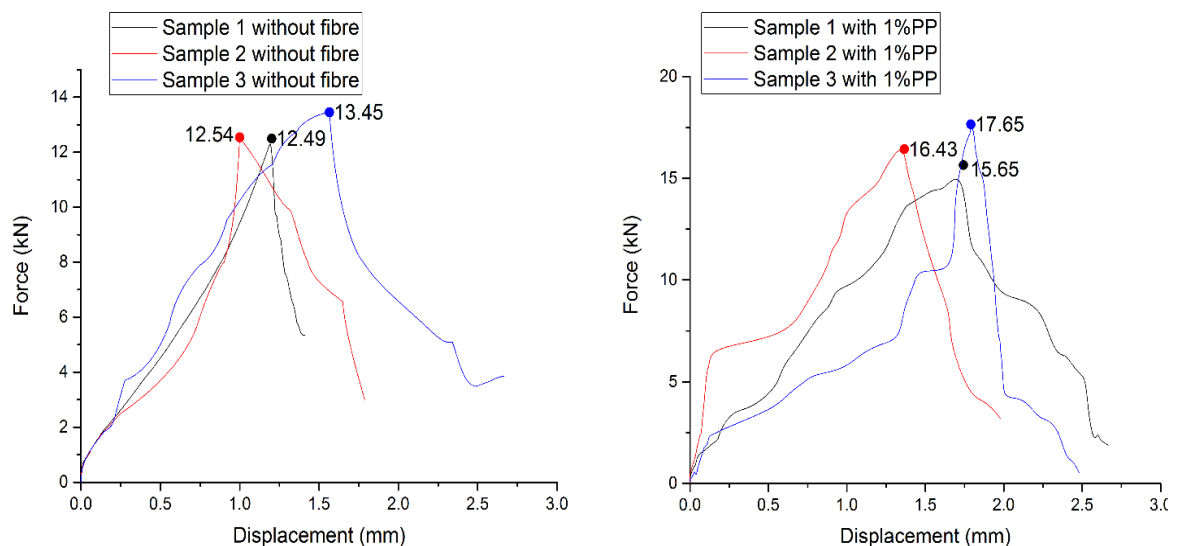


Figure 6. 64: Results after 28 days for the short column (7 layers) without any time lapse between printed layers and without post-curing with a cement fine sand ratio of 1:0.5.

Figure 6. 65 shows the printed sample after drying at the control temperature in the lab. They were no shrinkage cracks or hairline cracks on the printed specimens. After loading, cracks appeared on the edge of the printed column, as shown in Figure 6. 65 (b). The results for the printed column showed that the average rate of the printed column is $(12.83 \pm 0.54 \text{ kN})$. This is equal to a strength of 2.37 MPa, however, this needs to be improved by post-curing and the use of large particle sizes. It is clear that the low strength was due to the number of layers. The printed column was a mortar mix rather than a concrete mix which normally has less resistance than normal concrete after curing for 28 days.

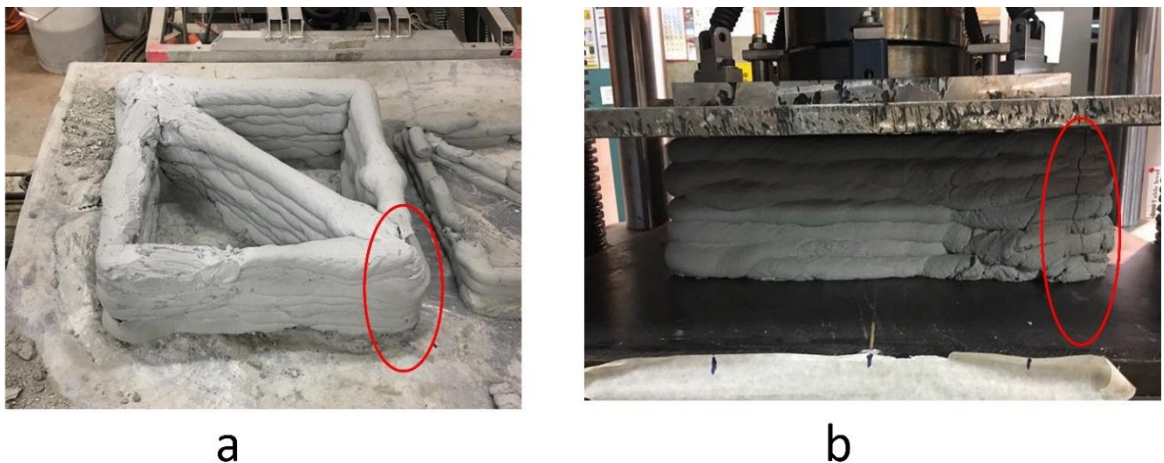


Figure 6. 65: (a) Printed specimen after drying at lab temperature; (b) Printed specimen under uniaxial load.

The short column under the uniaxial load cracked and ruptured at the edge of the sample. This was the weakest part of the column due to the irregular movement of the robot while printing.

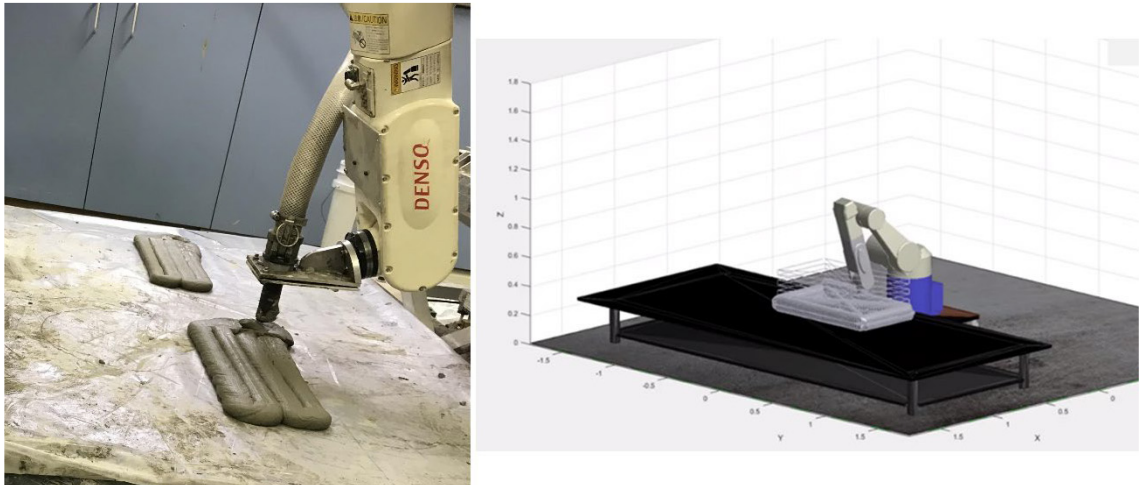


Figure 6. 66: 6-degree of freedom robot in the real-world and simulated MATLAB model.

Figure 6. 66 and Figure 6. 67 show the variously printed specimens in different layers with/without E6-glass fibre reinforcements.

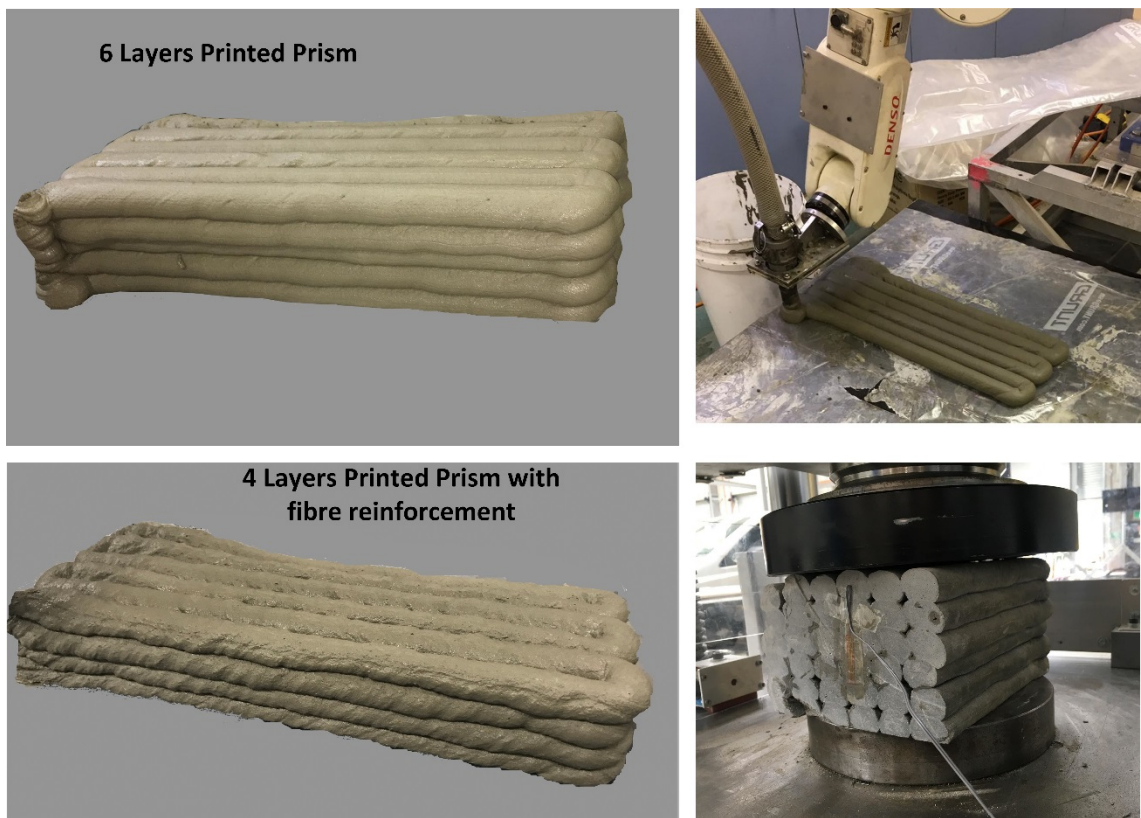


Figure 6. 67: Printed prism and cubes via a robotic arm for mortar specimen with/without glass fibre reinforcements.

The three-point bending test was applied to the optimum mix of mortar using a different type of fibre and different ratios. The flexural strength results for the different ratios are shown in *Figure 6. 68*.

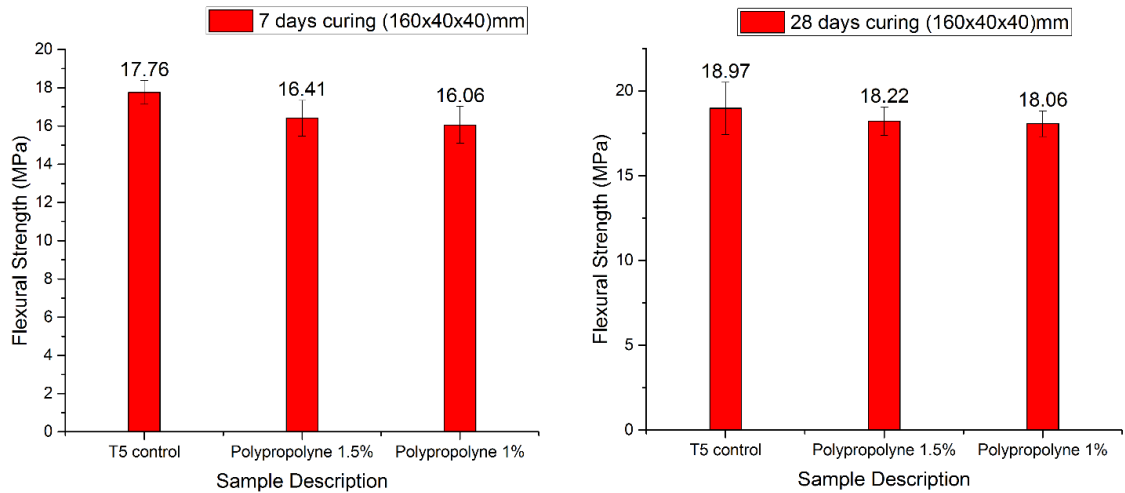


Figure 6. 68: Flexural strength of manual concrete mix after 7-day and 28-day curing (the values specify the actual strengths) with cement to the fine sand ratio of 1:0.5.

The three-point bending test and flexural strength for one, two, three and four layers of cementitious mortar with 1%PP fibre and without fibre are shown in *Figure 6. 69*. The maximum result of 5.78 MPa for 28 days curing was observed in the single layer with 1% PP fibre content in the sample. Another high result was achieved for three printed layers, which recorded 5.65 MPa. It is of interest that using PP fibre increased the flexural strength in all variable layers. In addition, it is noteworthy that, when increasing the number of layers, the flexural strength decreased due to inconsistency, a high ratio of moisture content and air trapped between layers.

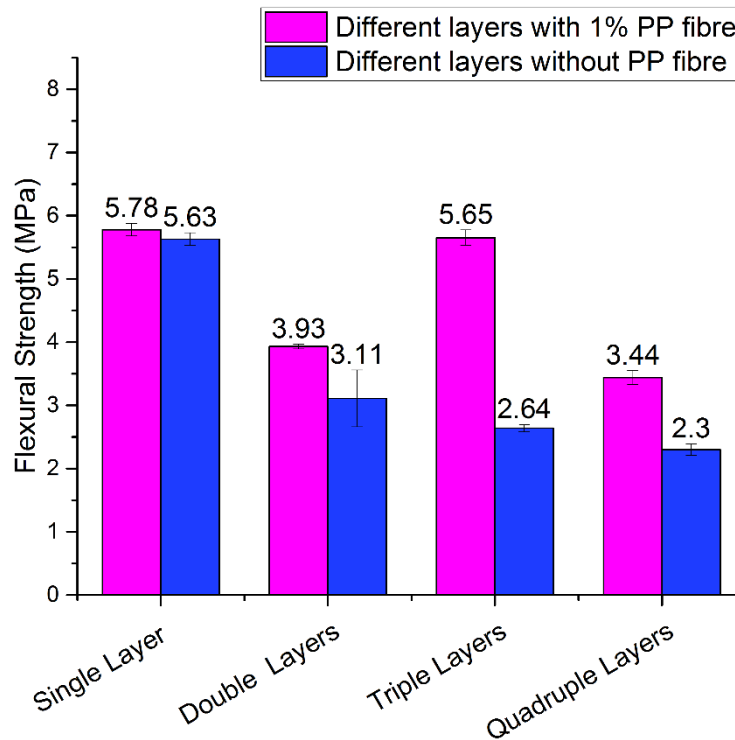


Figure 6. 69: Flexural strength for the (1,2,3,4) layers of mortar mix with 1% PP fibre and without fibre for a circular nozzle of 14mm after 28 days stored in controlled laboratories at the desired temperature (cement 1: fine sand 1).

Figure 6. 70 shows the effect of different nozzles on the flexural strength results. Note that, when investigating the highest flexural strength in circular and rectangular nozzles in the wet medium cure, the highest flexural strength was in the 3rd printed layer of the rectangular nozzles. In *Figure 6. 70* all layers of the rectangular nozzle achieved similar results, but the circular nozzle produced unstable results for each layer. Therefore, the load distribution of the circular nozzle reduced with its reduced surface area and width. This directly affected the mechanical strength results of the printed object, see *Figure 5. 33*. Consequently, the result suggests that a rectangular or square shape has a constant and better result than a circular nozzle print. This is consistent with the study of (Perrot, Rangeard & Courteille 2018). They observed voids in circular cross-section, however, the rectangular cross-section lacked cavities and voids. Conversely, it has been shown that wet medium curing is better than curing at air-temperature in vitro (Mindess, Young & Darwin 1981), *Figure 6. 70*. The use of fly ash in the mix is also highly recommended

to reduce the voids between particles and increase the durability of the mortar.

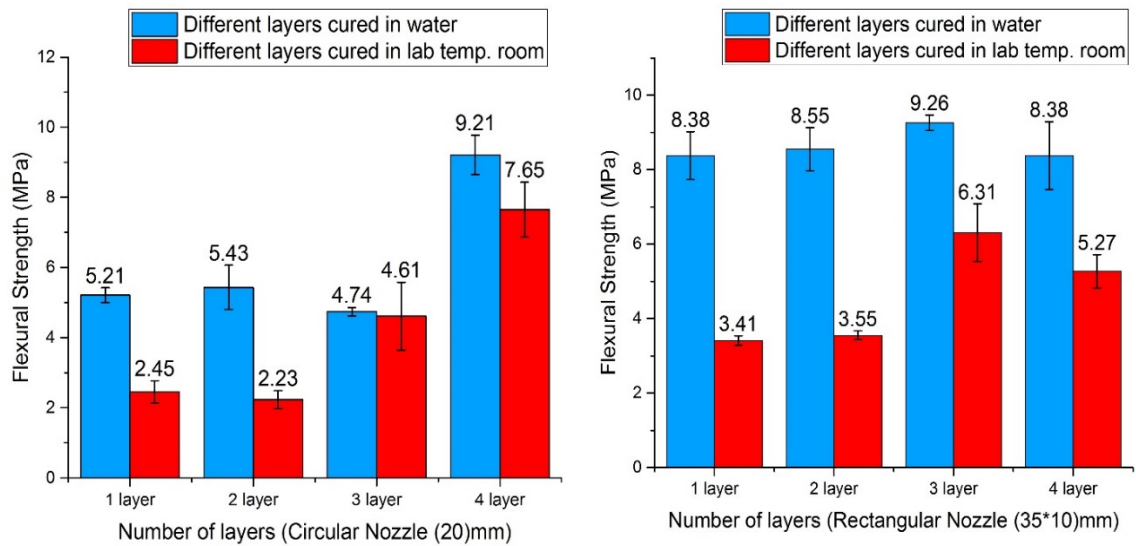


Figure 6. 70: Flexural strength for the (1,2,3,4) layers of mortar mix for a circular nozzle (20)mm and a rectangular nozzle (35×10)mm at air temperature and with water curing.

Glass fibre was used as another chopped strand reinforcement option after discovering that polypropylene presented many challenges while mixing and printing. The variety of glass fibre used is known as chopped strand E6-glass fibre (high-performance E6 enhanced glass fibre), Table 5. 8 summarises the physical properties of this glass fibre (JushiUSA). The 1% glass fibre used was equal to 1% of the total weight of cementitious powder.

The mix design of mortar is depicted in Table 5. 19, which presents the optimum mortar slurry that is capable of being transported through the pump and delivery system. Figure 6. 71 depicts the relationship between the velocity of the end-effector(mm/s), the amount of slurry discharged (g), and the printed line width (mm). The end-effector speeds used during the experiments were approximately, 11.99mm/s, 23.78mm/s, 34.99mm/s, 46.56 mm/s, 60.32mm/s, 70.97mm/s, 81.56mm/s, and 98.88mm/s.

To print the prismatic and cubic specimens, an end-effector speed of 34.99 mm/s was selected. Consequently, it was hypothesised that the optimum end-effector speed should

be 81.56 mm/s, as the line width corresponded to a nozzle diameter of 20.02mm, see *Figure 5. 40*. However, in *Figure 5. 40*, it is apparent that depositing material at this speed was detrimental to the structural integrity of the specimen as detrimental faults could be visually ascertained.

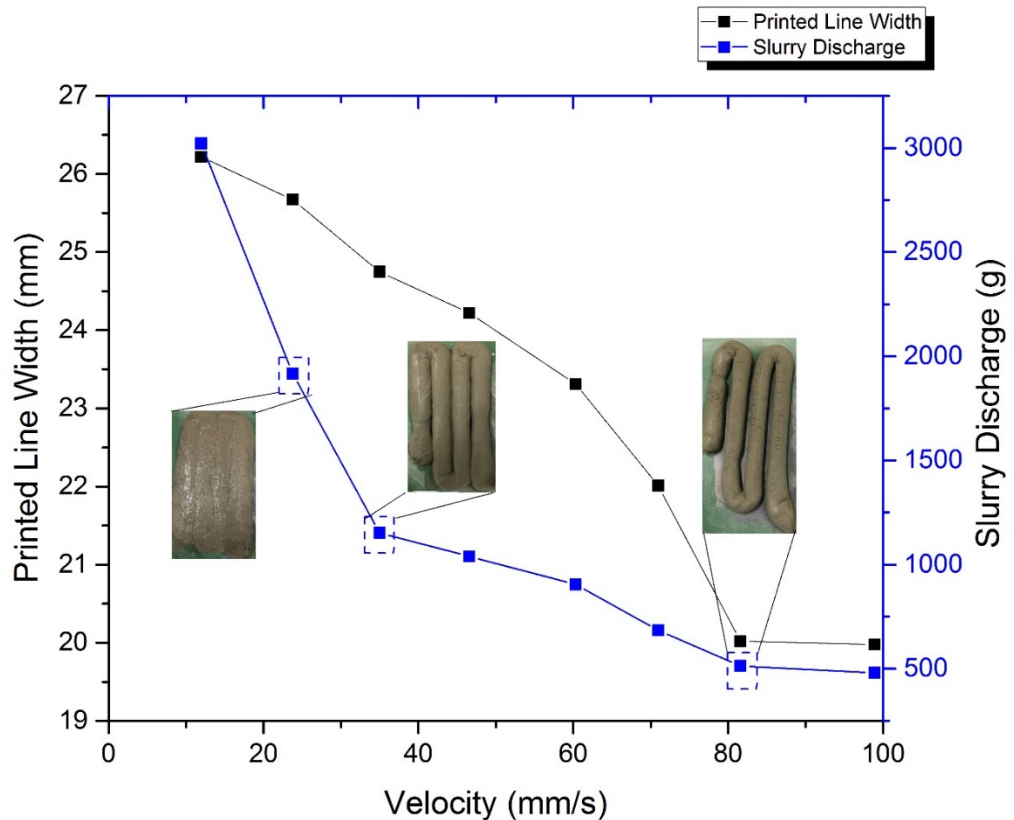


Figure 6. 71: Velocity (mm/s) versus printed line width (mm) and slurry discharge (g).

Figure 6. 72 shows fibre dispersion post-printing, with the dimensions of the fibre remaining uniform pre- and post-mortar mixing. This supports the observations made during the printing process and after it crashed under the uniaxial loading test. Therefore, it is evident that the fibre filament was not damaged during any process of experimentation, in particular, during the mixing process and whilst the material was being transferred through the pump and hose.

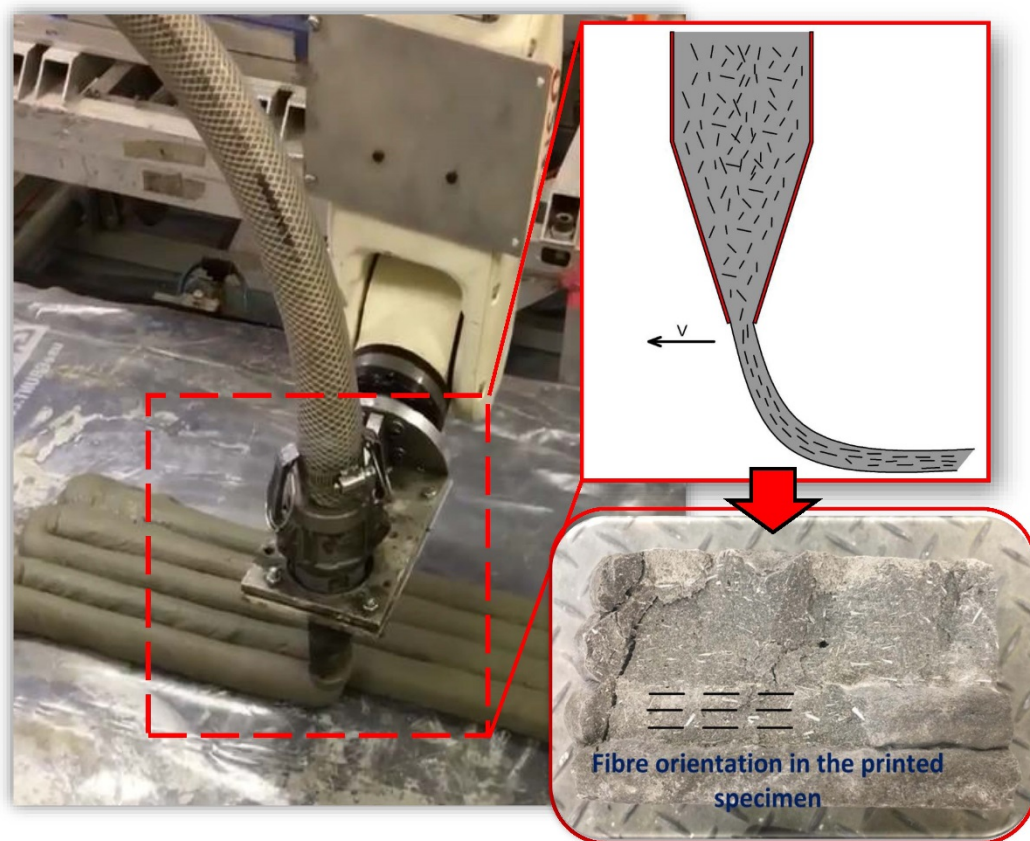


Figure 6. 72: Fibre orientation in the printed specimens after crashing under the uniaxial compressive strength.

Figure 6. 73 shows the fibre orientation and joint gap between layers with surface roughness taken by the 3D laser scanner. The image shows the orientation bedded in the horizontal layers.

Using the ImageJ software, a number of voids were observed. From *Figure 6. 74*, it was observed that voids were present on the surface of printed samples, with an average diameter of $350.24 \pm 101 \mu\text{m}$. These voids could be a result of chemical additives used, such as the superplasticizer and the effect of the pumping process. These voids are known as open pores. It should be noted except the voids where happen due to chemical reactions, the gaps between layers clearly shown in red colour in *Figure 6. 74*.

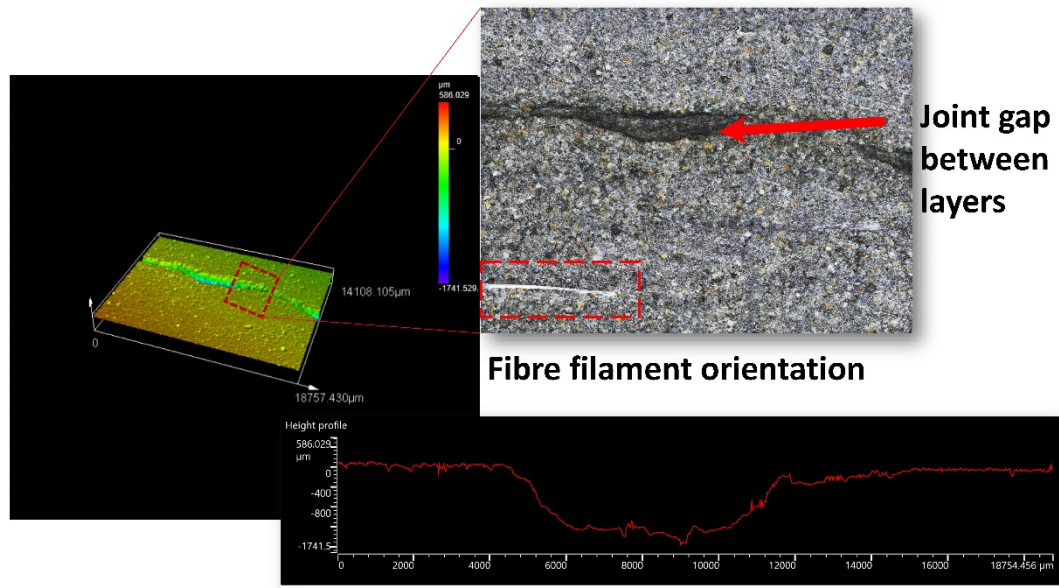


Figure 6. 73: Fibre orientation embedded in horizontal layers, and joint gap between layers with surface roughness taken by the 3D laser scanner.

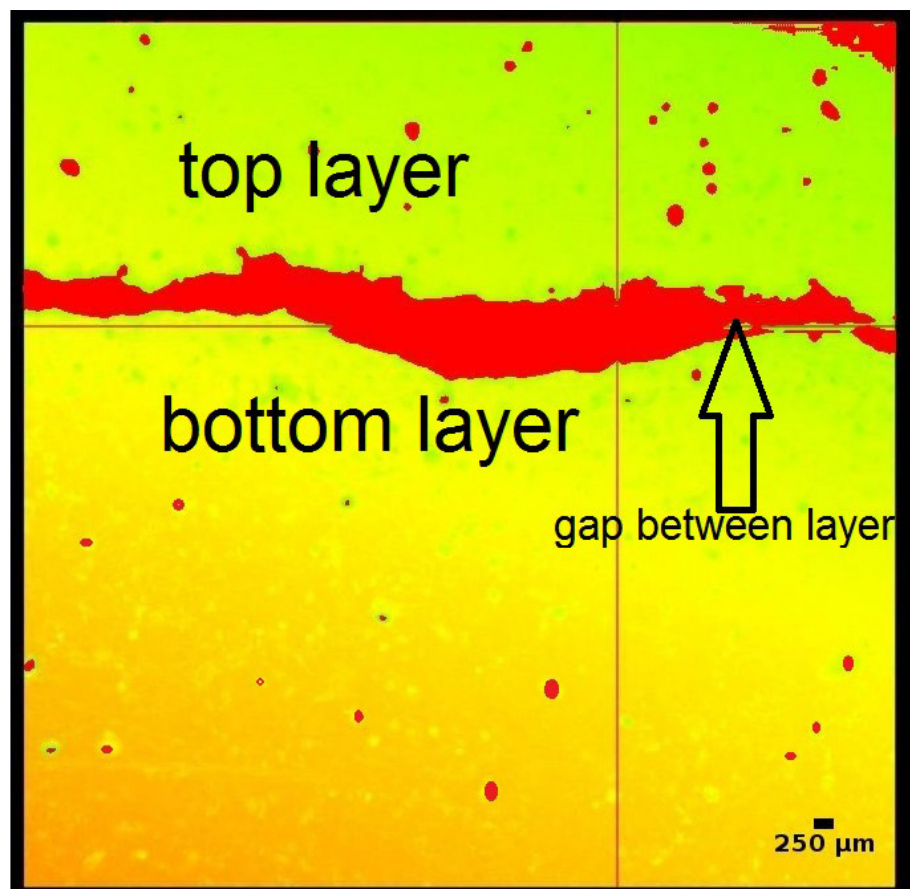


Figure 6. 74: Voids and gaps between layers are distinguished from the printed surface using the colour red.

Figure 6. 75 depicts a (15.5×11.1)mm area of the printed specimen. This sample was used

to determine the orientation of the fibre in the printed specimen. By selecting 6 strands found in *Figure 6. 75* it was determined that the fibre parallel to the printed line possesses an orientation angle within $-10.05^{\circ} \pm 7.65$.

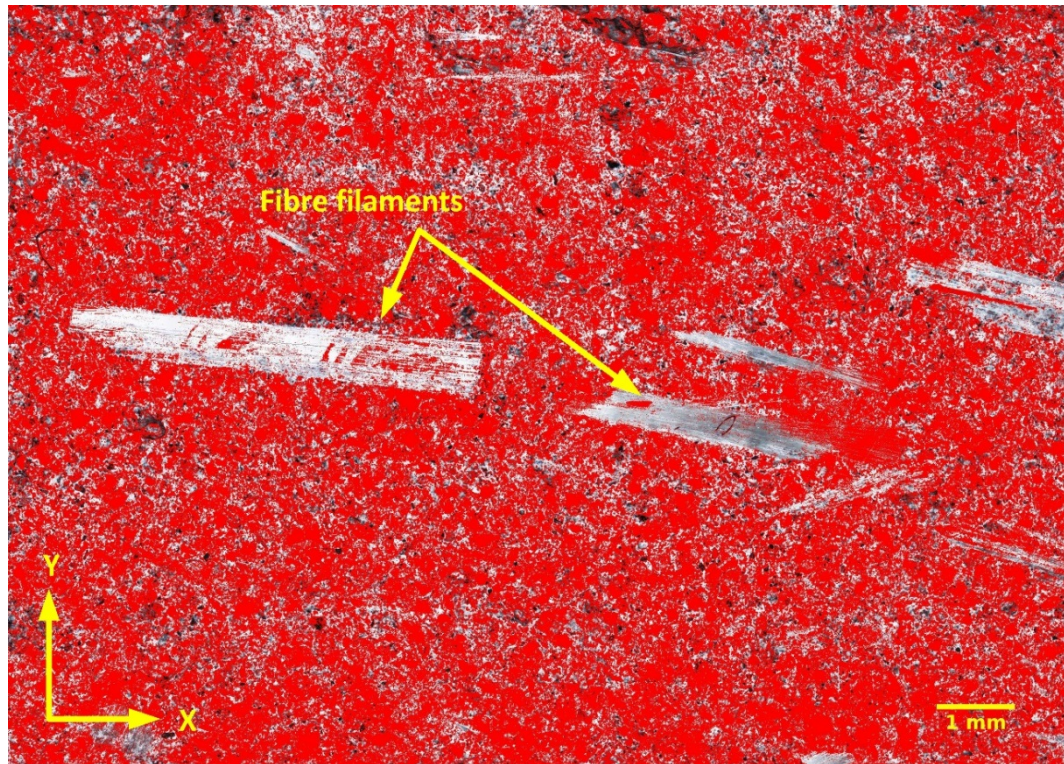


Figure 6. 75: Image of the surface of the printed sample after colour threshold to indicate the fibre strand on the surface of the printed sample.

The compressive stress is calculated according to the following equation (6.14):

$$\sigma = \frac{f}{l*b} \quad (6.14)$$

Where l is the length and b is the width of the specimens, and f is the maximum applied force on the specimens.

The flexural stress can be calculated using the following equation (6.15):

$$\sigma = \frac{3*f*l}{2*b*d^2} \quad (6.15)$$

Where d represents the thickness of the specimens.

All samples were cured in a tap water bath for 28 days before being tested for compressive and flexural strength properties.

A comparison of the cubic mortar samples is shown in *Figure 6. 76*, with the compressive strength values calculated according to Equation (6.14).

Figure 6. 76 highlights the varying degrees of performance based upon the number of layers in the structure. The standard deviation between the 6 specimens differs vastly due to the existence of fibre in the printed structures. It can be seen that the compressive strength of the specimen gradually decreased as the number of layers in the structure increased. This behaviour was expected due to the increased number of voids between layers and the larger dimensions of the specimens.

The total printing line width for 4 layers was 100 mm, while the deposited slurry for one printed line width after placement was approximately 24 mm. Thus, the increase in the number of layers vertically and horizontally was another factor that contributed to the loss of material strength.

The 1 layer printed specimens were 31.09 ± 3.43 MPa, 2 layers 28.25 ± 1.87 MPa, 4 layers 25.37 ± 3.47 MPa and 6 layers 25.33 ± 0.75 MPa. The result for the (50×50)mm sample was 51.92 ± 1.85 MPa, a very high result compared with the printed part. The result for the cubic mould was approximately 45.59% higher compared with the 2 layer printed cubes with 1% glass fibre, *Table 6. 13*.

Table 6. 13 Results of the compressive strength for the printed samples and conventional samples.

Sample description	Compressive strength (MPa) with 1% glass fibre	Compressive strength (MPa) without glass fibre
1 layer	31.09±3.43	14.91±1.91
2 layers	28.25±1.87	23.34±0.29
4 layers	25.37±3.47	13.83±0.26
6 layers	25.33±0.75	13.43±0.21
Conventional sample	51.92±1.85	50.82±0.62

The performance of the specimens containing the glass fibre demonstrated better mechanical strength. Specimens with 1% glass fibre demonstrated better performance than the peak strength of all of the other specimens and the mechanical strength results for all samples containing glass fibre were higher than the samples without. These improvements were identified in both printed specimens and conventional specimens.

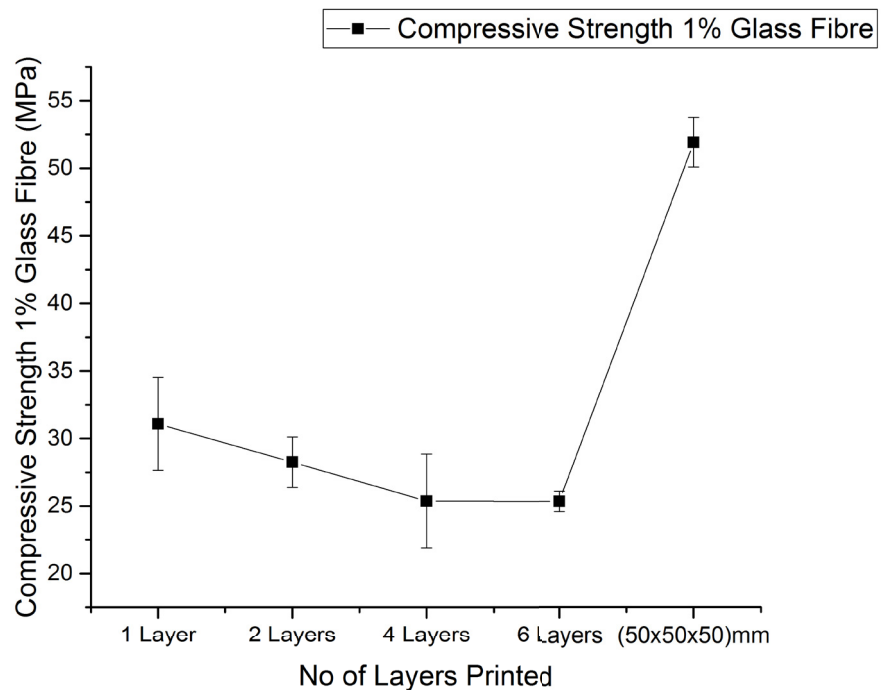


Figure 6. 76: Compressive strength results of cubic specimens containing 1% of glass fibre cured in a tap water bath for 28 days.

Figure 6. 77 shows the compressive strength test results of the printed specimens without glass fibre. The results are for all various layers and conventionally cast cubes. The figure shows that the printed structure possessed low mechanical strength compared with the conventional samples, which can be observed specifically in samples of 6 layers. The compressive strength tests for each of the layers can be seen in Table 6. 14, namely, 1 layer 14.91 ± 1.91 MPa, 2 layers 23.34 ± 0.29 MPa, 4 layers 13.83 ± 0.26 MPa, and 6 layers 13.43 ± 0.21 MPa. The result for the conventional mould was also high for mortar specimens 50.82 ± 0.62 MPa, however, it is still lower than the samples incorporating glass fibre. This demonstrates that the glass fibre effectively improves the mechanical strength of the printed specimens rather than improving the strain of the materials' property.

The effectiveness of glass fibre in the printed samples is shown by the twofold increase in strength compared with samples without glass fibre. Comparing Figure 6. 76 and Figure 6. 77, it can be observed that for 6 layers printed samples, the presence of 1% glass fibre increased the mechanical strength by 46.98%.

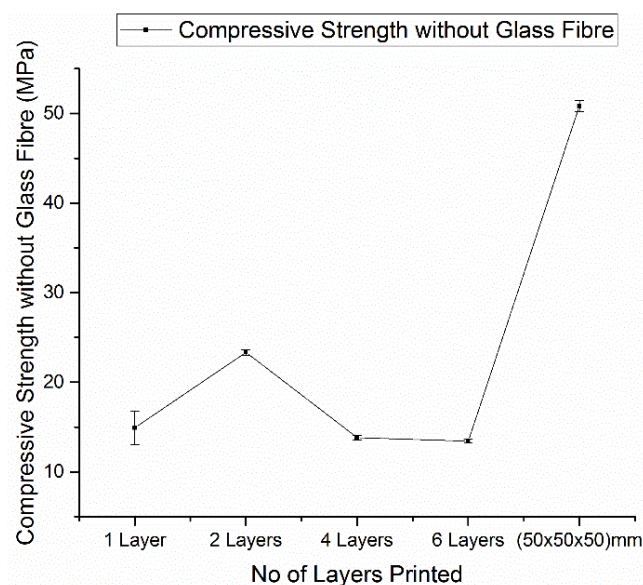


Figure 6. 77: Compressive strength for the (1, 2, 4, 6, conventional) layers of mortar mix without glass fibre.

Figure 6. 78 presents the outcomes of the flexural strength tests for specimens containing 1% glass fibre after curing for 28 days in tap water. The results show that the printed specimens with 2 layers had an approximate value of 8.69 ± 0.82 MPa, where the conventional mould had a result of 8.76 ± 0.92 MPa. This result 9.03 ± 1.50 MPa is an increase compared to the printed specimens with 1 layer. However, the calculated results for specimens with 4 and 6 layers dropped to 6.31 ± 0.60 MPa and 6.43 ± 0.52 MPa, respectively. Table 6. 14 presented the result of the flexural strength for the printed samples. It is hypothesised that this was caused by undesired voids in the specimens.

Table 6. 14 Results of the flexural strength for the printed samples and conventional samples.

Sample description	Flexural strength (MPa) with 1% glass fibre	Flexural strength (MPa) without glass fibre
1 layer	9.03 ± 1.50	5.38 ± 0.22
2 layers	8.69 ± 0.82	6.48 ± 0.05
4 layers	6.31 ± 0.60	4.36 ± 0.21
6 layers	6.43 ± 0.52	6.38 ± 0.54
Conventional sample	8.76 ± 0.92	8.53 ± 0.58

These outcomes support the work of Hambach & Volkmer (2017) with cement paste printed specimens with 1% volume carbon fibre. Their results highlighted a three-fold increase in flexural strength (approximately 30 MPa) in printed specimens possessing 1% carbon fibre. Hence, this study could have expected improvements in compressive strength. However, the results showed that, when considering the standard deviations, flexural strength in the second layer was always greater when glass fibre was used in the mortar mix, compared with the samples omitting the glass fibre.

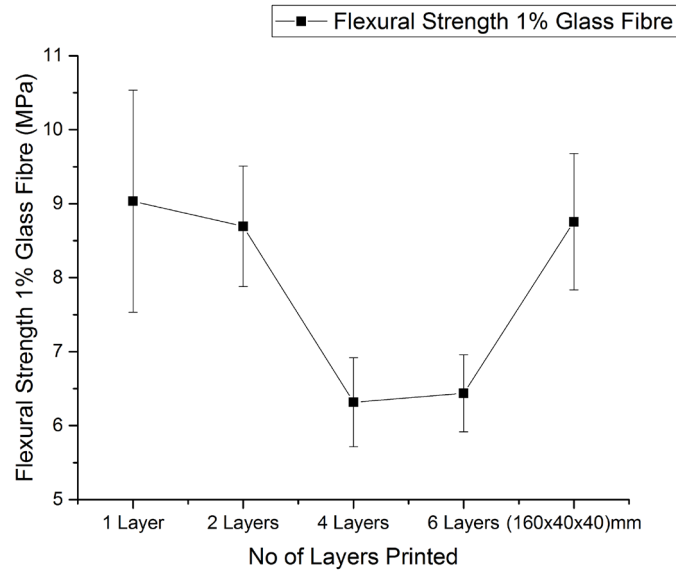


Figure 6. 78: Flexural strength for the (1, 2, 4, 6, conventional) layers of mortar mix with 1% glass fibre.

Figure 6. 79 depicts the flexural strength results of the printed specimens and conventional samples without glass fibre. The graph indicates a fluctuation in the result for the printed specimen with 2 layers, but it significantly falls at 4 layers. The result increases steeply at 6 layers 6.38 ± 0.54 MPa, but no more than the conventionally cast mould 8.53 ± 0.58 MPa.

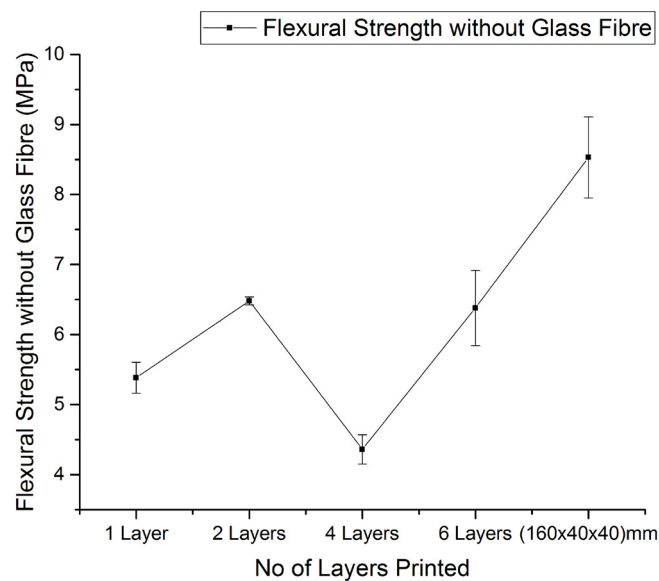


Figure 6. 79: Result of 28 days for flexural strength of the printed cube specimens without glass fibre.

6.2 Numerical Analysis Using ABAQUS

Additive Manufacturing (AM) can be used to create objects in complicated shapes without the help of formworks and these techniques mostly available for the small structures (Cesaretti et al. 2014; Lowke et al. 2018; Ngo et al. 2018; Upadhyay, Sivarupan & El Mansori 2017). These techniques are cost-effective and time-saving, it does not require machining (Kazemian et al. 2017; Reiter et al. 2018; Wangler et al. 2016). AM growth after many discoveries; thus, the advantageous of the AM emerged significantly. These techniques can be found in the various fields such as; medical, automotive, aerospace, food industry, construction and architects (Liu et al. 2017).

Generally, the 3DP procedures are as follows (Jurrens Kevin 1999):

- a) Using computer-aided design (CAD) software to draw a 3D model.
- b) The model is transformed into a Standard Triangulation Language (STL) format.
- c) STL file is divided into thin layers.
- d) Each layer, consisting of geometric information, is conveyed to the 3D printer in sequence.
- e) Each layer over another layer constructed according to the received data from the 3D printed part.

The powder-based three dimensional (3D) printing techniques is rapidly developed during the last decades in various fields. This is not only seen in the developing techniques but also could be seen in the size of the printers (Colla et al. 2013). In 2010, Dini is the Italian inventor, developed a large 3D printer called D-shape (Dini 2009), which created complicated geometries with sand and magnesium-based binder. The D-shape innovation

is open-up to create 3D printed structures with mortar and concrete by means of powder-based printers. This technique is very promising and has a reliable mechanical strength results. It has been used on the 3DSystem powder-based printer ProJet (360) to create various structures and geometries.

Finite Element numerical Analysis (FEA) was conducted to verify the mechanical characterisation of the 3DP specimens. The results of the experiments conducted on the (50×50×50)mm 3DP cubic specimens are presented in *Figure 5. 21*. The samples were prepared according to the ASTM:C109/C109M (2016), with strain gauges are attached to the surface of the samples to measure the axial strains. These data were then used to obtain the elastic modulus and Poisson's ratio of the materials. The values gathered from the experimental program are shown in *Table 6. 15* and *Table 6. 16*.

Table 6. 15 Compressive strength and Elastic modulus for 3DP cement mortar specimens.

Specimen label (50×50×50)mm	Compressive Strength (MPa)		Elastic Modulus (GPa)		Plane
	Value	Average	Value	Average	
S 1.1	23.04	23.21	9.50	9.57	XY
S 1.2	23.41		9.65		
S 1.3	23.20		9.57		
S 2.1	15.99	15.95	3.44	3.55	XZ
S 2.2	15.97		3.65		
S 2.3	15.91		3.55		
S 3.1	10.17	10.15	4.75	4.63	YZ
S 3.2	10.13		4.64		
S 3.3	10.15		4.51		

Table 6. 16 Poisson's ratio for 3DP cement mortar printed cube.

Specimen label (50×50×50)mm	Poisson's Ratio			
	XY	Average	XZ	Average
S 1.1	0.31	0.29	0.31	0.32
S 1.2	0.27		0.29	
S 1.3	0.29		0.35	
	YZ		YX	
S 2.1	0.24	0.26	0.31	0.31
S 2.2	0.27		0.31	
S 2.3	0.27		0.30	

	ZX		ZY	
S 3.1	0.19	0.15	0.14	0.16
S 3.2	0.14		0.14	
S 3.3	0.13		0.19	

The results for the properties of the cement mortar materials were entered into ABAQUS 6.10. Based on the equations (6.16 to 6.25), it is found that the properties of the cubes have an orthotropic characteristics, in all three directions (see *Table 6. 17*). These equations define the orthotropic materials for the ABAQUS software (refer to Appendix D).

$$D_{1111} = E_1(1 - \nu_{23}\nu_{32})Y \quad (6.16)$$

$$D_{2222} = E_2(1 - \nu_{12}\nu_{31})Y \quad (6.17)$$

$$D_{3333} = E_3(1 - \nu_{12}\nu_{21})Y \quad (6.18)$$

$$D_{1122} = E_1(\nu_{21} + \nu_{31}\nu_{23})Y = E_2(\nu_{12} + \nu_{32}\nu_{13})Y, \quad (6.19)$$

$$D_{1133} = E_1(\nu_{31} + \nu_{21}\nu_{32})Y = E_3(\nu_{13} + \nu_{12}\nu_{23})Y, \quad (6.20)$$

$$D_{2233} = E_2(\nu_{32} + \nu_{12}\nu_{31})Y = E_3(\nu_{23} + \nu_{21}\nu_{13})Y, \quad (6.21)$$

$$D_{1212} = G_{12}, \quad (6.22)$$

$$D_{1313} = G_{13}, \quad (6.23)$$

$$D_{2323} = G_{23}, \quad (6.24)$$

$$Y = \frac{1}{1 - \nu_{12}\nu_{21} - \nu_{23}\nu_{32} - \nu_{31}\nu_{13} - 2\nu_{21}\nu_{32}\nu_{13}} \quad (6.25)$$

Where, E is Young's modulus, and ν is Poisson's ratio. The shear modulus is known as G , which can be found according to the Equation, $G = E/2(1 + \nu)$. As an engineering constant, the D matrix defines the property of orthotropic materials. *Table 6. 18* lists the orthotropic properties of 3DP cementitious mortar.

Table 6. 17 Orthotropic properties of 3DP cubic cement mortar.

D_{1111}	D_{2222}	D_{3333}	D_{1122}	D_{1133}	D_{2233}	D_{1212}	D_{1313}	D_{2323}
11506.7	4284.7	5342.3	4190.18	2396.4	915.90	6108.1	2343	2916.9

6.3 Stress-Strain Diagram for inkjet 3DP Mortar

Before creating a model, it is necessary to know all the mechanical properties of the samples. The mechanical properties of samples will enable the physical characterisation and reaction of the materials to be determined when a load is applied under various environmental conditions.

Figure 6. 80 shows the strain gauge attached to the surface of the specimens to check the mechanical properties of the specimens in the axial direction. The displacement was very small at the launch of the loading on the 3DP mortar specimens. The cracks started when the specimens reached the peak load. The cracks formed an approximately vertical line close to the edge of the samples in both the (XZ) and (YZ) planes. The red dashed lines in *Figure 6. 80* indicate the crack lines on the surface of the specimens.

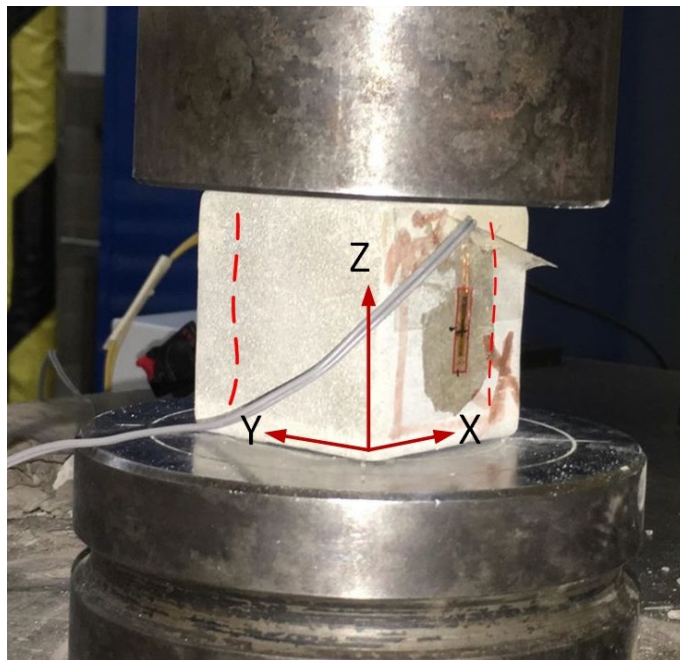


Figure 6. 80: Strain gauge and failure description on a (50×50×50)mm specimen.

To create a model in ABAQUS, a typical model with the mesh standard hexahedron shape properties were chosen with approximate global size (0.01). Due to the limited applicability of cement mortar in construction, a mortar masonry block with dimensions of (390×190×190)mm and meeting Australian standard (AS3700-2001 2001) was chosen(see *Figure 6. 81*). This model was simulated numerically using ABAQUS, with loads being applied in all three orthogonal planes (XY, XZ, YZ), as shown in *Figure 6. 82*.

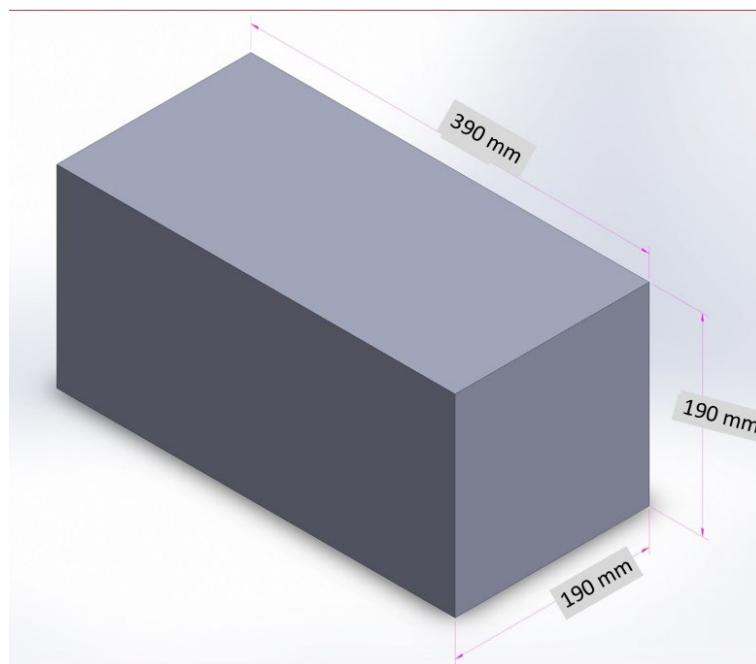


Figure 6. 81: Masonry block model with dimensions of (390×190×190)mm.

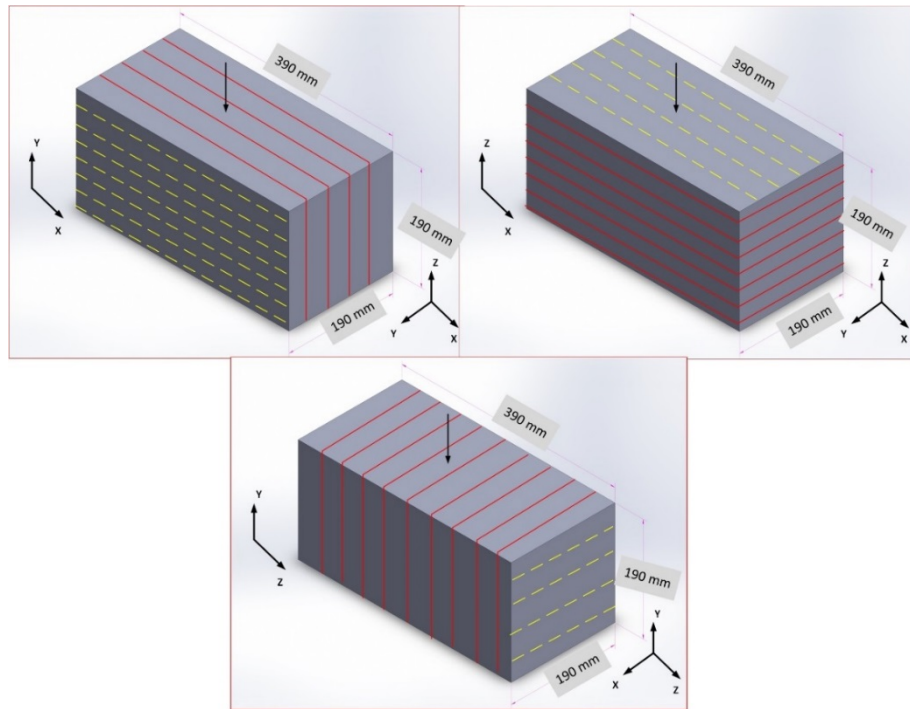


Figure 6. 82: Load applied on the three planes of the masonry block in ABAQUS.

The load was applied in the ABAQUS software as a uniform static-load for all the planes under the same load conditions. Progressive failure analysis was conducted on. The masonry block was simulated under a uniform dead load and under a vertical load distribution on the top surface of the block. The bottom of the block was restrained by fixed support, and we applied the load on the top surface of the block.

The compressive loading strength test was simulated for all three planes (XY, XZ, YZ) on the masonry block.

Figure 6. 83, Figure 6. 84, Figure 6. 85, Figure 6. 86, Figure 6. 87, and Figure 6. 88 show the failure locations, which are different for each plane for the displacement and stress of the masonry block. Figure 6. 89 shows that the maximum stress resistance of the structure in the (XY) plane was the highest, with an average stress of 24 MPa. In the (XZ) plane, the stress was 15 MPa. When the stress was applied in the (YZ) plane, the stress was the lowest, at 10 MPa. The results show that printing in a different plane has a

substantial influence on the overall stress-strain diagram of the structure. This is significant and indicates the importance of carefully selecting a suitable printing plane before fabricating the 3DP scaffold.

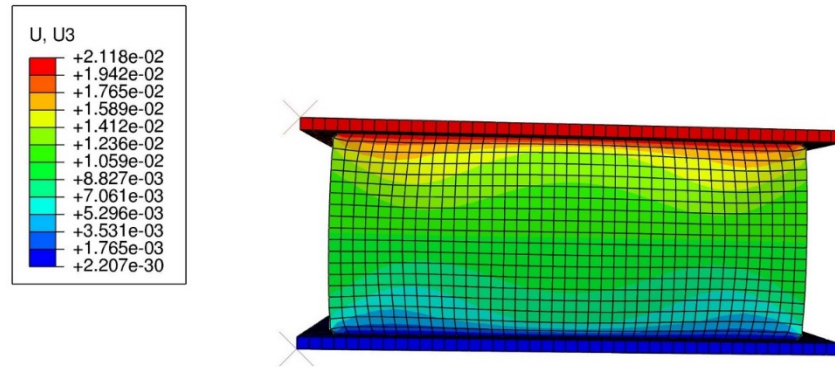


Figure 6. 83: XY plane displacement failure of the masonry block under a compression test.

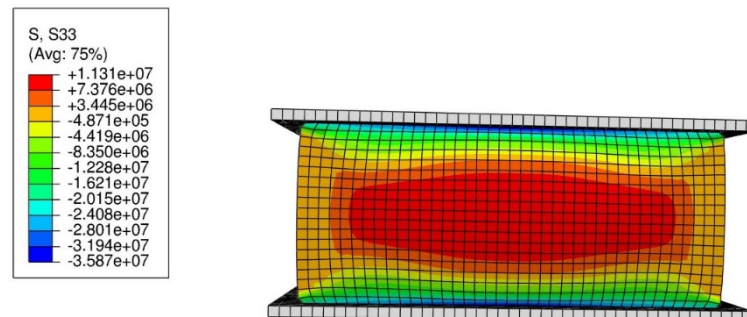


Figure 6. 84: XY plane stress failure of the masonry block under a compression test.

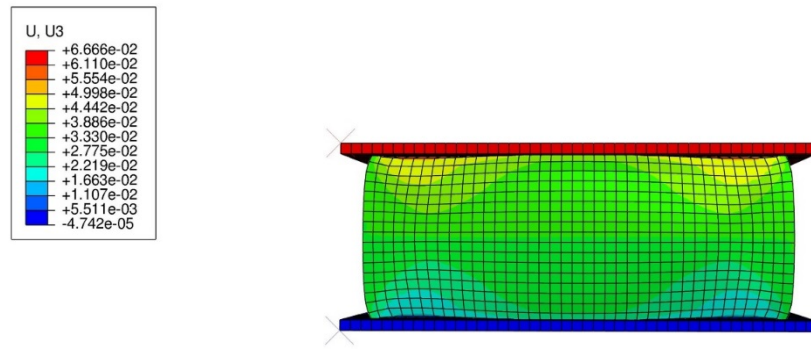


Figure 6. 85: XZ plane displacement failure of the masonry block under a compression load.

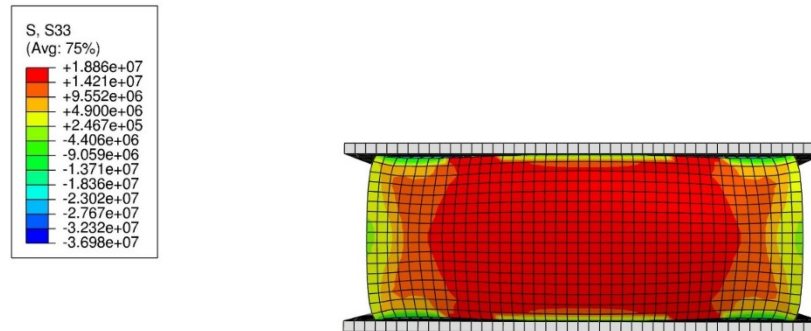


Figure 6. 86: XZ plane stress failure of the masonry block under a compression load.

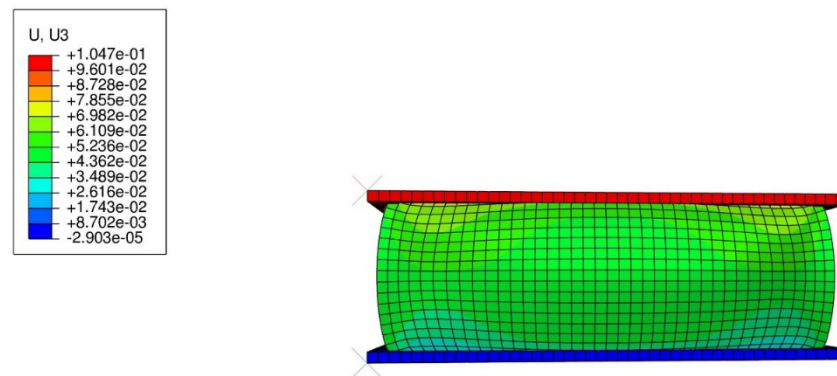


Figure 6. 87: YZ plane displacement failure of the masonry block under a compression load.

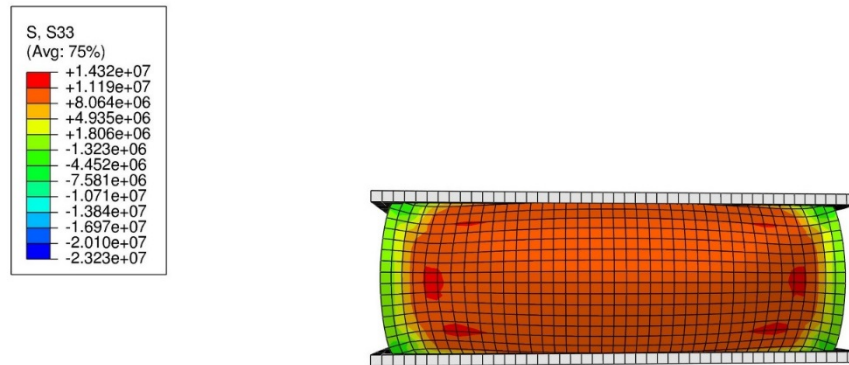


Figure 6. 88: YZ plane stress failure of the masonry block under a compression load.

The numerical (FEA) and experimental (Exp.) results of the compression test for the three planes are shown and compared in Figure 6. 89. The loading process was applied by means of a static load on the masonry block. The loads applied in each plane illustrate the differences in the stress-strain diagram (see Figure 6. 89).

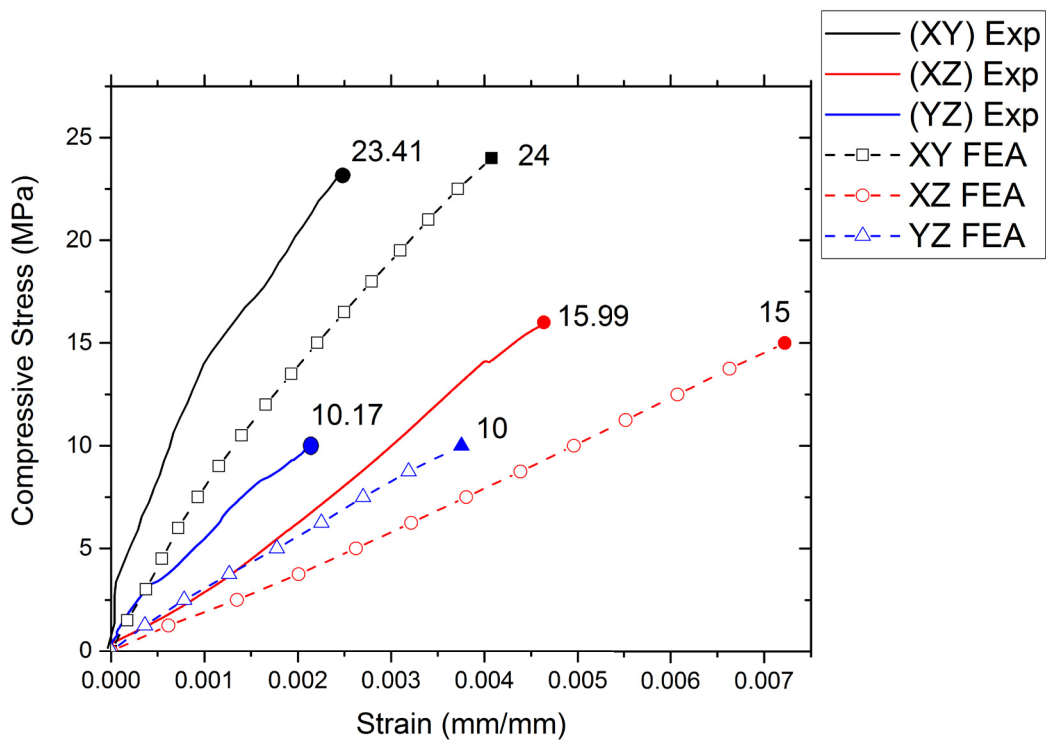


Figure 6. 89: Stress-strain diagram for the FEA and Exp. of the 3DP block under compression.

CHAPTER SEVEN

7. SUMMARY AND CONCLUSION

7.1 Summary

This research has made innovative contributions to additive manufacturing by enabling the fabrication of fibre-reinforced, mortar-based precise structural members by utilizing three-dimensional printing (3DP) technique, which is ideal for construction applications. The key innovations are twofold: (1) a powder-based 3DP technique; (2) an extrusion-based 3DP technique by employing mortar. These are both multipurpose processes for producing structural members using a sequential layer by layer printing approach.

This investigation used powder-based 3DP to print different geometries using a layer thickness of 0.102mm and a novel printing process. The innovative achievements are as follows: (a) formulating powder-based materials from recommended materials replaced to the cement mortar powders; (b) identifying the water/cement ratio (saturation level) in the powder-based 3DP and comparing it with conventional mix proportions; (c) producing a modified powder that is cost-effective (62 times cheaper) and twice as strong as the recommended materials; (d) determination of the strongest plane (XY) for the mechanical properties of the printed cement mortar samples in the presence and absence of E6-glass fibre reinforcement; (e) exploring of the size effect on printed specimens.

In addition, the investigation enhanced extrusion-based techniques for construction by printing cubic and prismatic specimens with various layer thickness (eg.20mm). The innovative achievements include: (a) optimization and design of the adaptor nozzle for extrusion-based mortar 3DP; (b) comparison of the rectangular and circular nozzles on the printed specimens by monitoring the results; (c) optimization of the print materials by inclusion of E6-glass fibre; (d) comparison of the printed specimens of different sizes, both with and without E6- glass fibre.

7.2 Conclusion

7.2.1 Inkjet 3D Printing

An approach has been developed to use a new material instead of Z-powder 3DP (Z-corp 150). Recently, 3DP has been used for a variety of purposes and, in this thesis, 3D printing is applied to civil engineering materials. This investigation is conducted using inkjet 3DP and replaced the 3DP powder to a powder has similar properties. The results indicate that, by increasing the saturation level, the compressive strength increases when the shell and core of samples have the same saturation level. In the maximum saturation level of 170%, the highest compressive strength was recorded (Section 5.1.1).

To conclude, 3DP cubics, prisms and dogbone specimens were printed using original materials (ZP 151) and cement mortar (CP) materials (Section 5.2.1). These specimens were printed at different orientation angles to investigate the effect on mechanical properties. The deflection for the tensile strength of the printed objects for original materials and cement mortar (custom-made) specimens was discussed in chapter 5 and 6. The results show that the maximum deflections emerged at 45° (XZ plane) due to the maximum inclined position of the specimens and also due to the maximum unbounded powder loaded on the printed specimens in the build chamber (Section 5.2.1).

This research also investigated the effect of the orientation angle on the printed structural members using CP (mortar) and ZP 151 (gypsum). The results show that this is an important factor that should be considered in future studies of 3DP for construction applications. The most suitable orientation and the strongest angle of the printed sample were discovered to be 0° for both flexural and compression strength. The maximum shear strength test of the printed CP specimens was recorded at 45° and, for the tensile test,

maximum strength was recorded at 0°. Finally, the effects of different curing media on the mechanical strength of the CP was studied and discussed.

Experiments were also conducted, and the results presented, on the achievement of higher compressive strength using cement mortar powder and curing in a furnace (Section 5.2.1.1). Compressive strength under different curing conditions and drying at high temperatures were also examined. Comparisons were made with other samples such as 5% Ca(OH)₂ dissolved in water and 100% water. Further experimental tests were conducted on flexural strength in different 3DP directions. It found that samples printed along the X-directional axis have the highest flexural strength (Section 5.2.1.2). In addition, the compressive strength of the cube increases by 14% when the dimensions of the cube change from (20×20×20)mm to (50×50×50)mm. This is contrary to the case for conventional mortar cubic specimens. The droplet penetration time on original powder and cement mortar powders were also investigated in this research. The outcome is that the heterogeneous powder quickly absorbs liquid into the powder due to the higher porosity among its particles.

It is generally agreed that porosity influences the compressive strength of cementitious members, where more pores result in less toughness (Section 5.2.1.5). Therefore, by increasing the *w/c* ratio, the strength of cement will reduce. The reverse is the case for 3DP, with highly *w/c* ratio achieving high mechanical strength. In addition, the results show that the powder bed porosity in cement mortar is 73.6% and in ZP 151 is 64.9%.

A lower level of apparent porosity was recorded at a high saturation level of printed samples. In addition, it has been discovered that a small amount of lithium carbonate had a positive impact on the porosity effect in the low saturation level of the printed samples.

It was found that the reduction in the porosity contributes to a significant improvement in the compressive strength of the specimens.

Furthermore, the dimensional accuracy of the printed scaffold in all three axes was measured and compared with the CAD model dimensions (Section 5.2.1.8). The wettability of the binder was also investigated, and cement mortar was found to have quicker wettability than original material (ZP 151) powder (Section 5.2.1.7).

In general, this investigation demonstrated some of the major limitations and weaknesses of inkjet 3DP and also examined the effect of the various parameters and how they can affect the quality of the sample. The compressive strength of the samples under different curing conditions and drying at high temperatures was also examined.

This research investigated the use of delay time between the printing of layers and how it affects the mechanical properties of the specimens. Groups of samples were constructed using a variety of printing delay times and curing conditions to identify and choose the most appropriate manufacturing parameters. The results show that layer printing delay has a major influence on the compressive strength of the printed objects. The printed cube with a 200ms delay between the printing of each layer was found to be most suitable for cementitious mortar (CP), with the highest compressive strength recorded as 18.77 MPa for 7-day curing. Therefore, it is highly recommended that this delay value is used when printing CP materials (Section 5.2.1.9).

Moreover, the effect of elevated temperature and glass fibre reinforcement on the printed mortar samples were investigated. Two types of cubics were tested for compressive strength and one type of prism was tested for flexural strength in the presence and absence of glass fibre reinforcement. The result was that the larger size has better mechanical

strength and performance. The maximum compressive strength and flexural strength were recorded at 80°C in the presence of 1% E6-glass fibre (Section 5.2.1.11).

7.2.2 Extrusion 3D Printing

In this thesis, the initial stages that involved in developing a model of 3D printing concrete line using a 6DOF Industrial Robot were also presented (Section 5.4). The used mix design properties and how these mixes were evaluated in several trials and tests are discussed too. It found that the impact of the optimum material mixes and use of DLS paired with RMRC to control joint velocities of the robot are crucial to establish a good printing process. The results show that mortar was more suitable and efficient for the printing and construction of layers due to the existence of fewer voids and less porosity between particles, while the concrete mixes with large particles result in more openings and internal porosity due to trapped air. Opening pores can be formed in the concrete mixes and therefore, there is significantly more internal spacing for air to enter.

It also described in detail how these mixes can be evaluated using numerous trials and tests. It was found that optimisation of the cementitious mixes has a significant impact on the structure created by the robot (Section 5.4). For instance, printed specimens need to be cured using advanced technologies for different media when printing mortar members. The main contributions of the thesis in extrusion-based technique are:

- Validation of the optimum mix proportions in conjunction with the different delivery mechanisms for printing cementitious slurry (Section 5.4.1.1).
- Presentation of the limitations and challenges inherent in this printing process.
- Comparison of different sized of the nozzle and rectangle- and circle-shaped printer nozzles, for a variety of layer thicknesses and heights.

- Conducting comparative slump, spread-flow and squeeze-flow tests to identify the optimum mix (Section 5.4.1.4, Section 5.4.1.5).

In overall, the 3DP process of concrete or mortar is one that still faces many challenges and requires further research. The mortar mixture containing OPC and fine sand was combined with glass fibre reinforcement to produce a robust structural member for construction applications. This study also identified the ideal mix design for the cement mortar in the presence and absence of glass fibre. It was also found that the addition of 1% glass fibre results in an increase in compressive and flexural strength by 46% compared with the specimens without the glass fibre. The mechanical behaviour of the printed samples using glass fibre, such as the strain and ductility of the materials, showed improvement when loads applied on the printed sample. This study also discovered and presented the relationship between the end-effector velocity of the robot versus the slurry discharge and printed line width. The results demonstrate a significant effect of the robot end-effector speed the shapeability and surface of the printed structures (Section 5.5.1).

Using robotic arms in 3DP with fibre reinforcement offers an alternative option to the conventional methods of structural construction. In fact, it is an effective means to create structures possessing complicated geometries. This research also went some way towards understanding ideal concrete or mortar mix designs that are suitable, sustainable and environmentally friendly for such applications.

7.3 Recommendations for Future Research

To develop a full picture of additive manufacturing in the construction industry, additional studies are required. These techniques could be further investigated in construction applications by adding aggregates and reinforcements. Furthermore, other

techniques used in additive manufacturing, such as robocasting and stereolithography, could be useful in the construction field.

The following matters should be investigated in more detail for mortar and concrete printing applications:

- 1- Developing concrete materials used in the extrusion-based process. The aim of this work would be to examine the technique of flowing coarse aggregate and adding fly ash to the mix. To achieve stronger mechanical strength, it is recommended to investigate the high-performance concrete (HPC) in 3D printing by powder-based and extrusion-based techniques.
- 2- Developing a 6 DOF robot process which is made more economical and feasible to implement at a large scale and which is practical for construction on site. Further detail is necessary to change the parameters (e.g. nozzle, position of the arm, rotational angle) of the robotic arm to make it adaptable for construction purposes.
- 3- Using a rotary lobe pump (such as a peristaltic pump or pneumatic pump) instead of a cavity pump to print members, given the constant flow rate in a rotary lobe pump. The design of progressive cavity pumps creates many cavities and voids in the slurry which would lead to air being discharged at the end of the pump.
- 4- Further development in the printing and testing processes requires quantitative values to correlate the effects of voids and porosity in the delivery system and the pumping process with the physical properties of the printed structure. Future studies will aim to discern the effect of the rotational angle of the robot's printhead on the mechanical properties of the printed specimens.

- 5- The height of the nozzle to the platform of the printed objects must be investigated in further detail with respect to the shear stress at the angle of the deposited mortar.
- 6- Future work should focus on analysing the various percentages of $\text{Ca}(\text{OH})_2$ in water and employ various temperatures or steam conditions for the powder-based 3DP technique. Finally, it is also necessary to evaluate the effect of larger particle sizes of fine sand in the powder. It is important to use distilled water instead of the Zb63 liquid from ZCorp/3DSYSTEMS until a better reaction is achieved between the particles.

In summary, these results of this research can contribute significantly in production of higher strength and higher mechanical properties in the printed structural components using both methods of additive manufacturing (powder-based and extrusion-based printing). Accordingly, the time aspect, mix design, different techniques, material properties and physical behaviour of the materials are also addressed in this thesis; which considerably influence final production of the printed components.

References

References:

3DConcretePrinting,

<https://www.tue.nl/universiteit/faculteiten/bouwkunde/onderzoek/onderzoeksprogrammas/structural-design/research/research-areas-and-chairs/concrete-research-areas/3d-concrete-printing>.

3dprintingfromscratch 2019, <<http://3dprintingfromscratch.com/common/types-of-3d-printers-or-3d-printing-technologies-overview/#dlp>>.

3DSystems 2012, 'ZB63 Safety Data Sheet', Series ZB63 Safety Data Sheet.

3DSystems 2013, 'ZP151 Powder Safety Data Sheet', Series ZP151 Powder Safety Data Sheet.

3dWASP, <https://www.3dwasp.com/>.

A200MIXER, *A200 hobart mixer speed specification*, HobartCorp.

Abd elaty, M.a.a. 2014, 'Compressive strength prediction of Portland cement concrete with age using a new model', *HBRC Journal*, vol. 10, no. 2, pp. 145-55.

ABNT-NBR15839 2010, *Argamassa de assentamento e revestimento de paredes e tetos – caracterização reológica pelo método Squeeze-flow*.

ACI308R-01 2001, *Standard Guide to Curing Concrete*.

ACI330R-01, A.c.i. 2001, *Guide for Design and Construction of Concrete Parking Lots*.

Ahmed, S.M. & Pechev, A.N. 2009, 'Performance analysis of FIK and DLS inverse kinematics using six degree of freedom manipulator', *IEEE*, pp. 1405-10.

References

- Al-Qutaifi, S., Nazari, A. & Bagheri, A. 2018, 'Mechanical properties of layered geopolymer structures applicable in concrete 3D-printing', *Construction and Building Materials*, vol. 176, pp. 690-9.
- Altan, E. & Erdoğan, S.T. 2012, 'Alkali activation of a slag at ambient and elevated temperatures', *Cement and Concrete Composites*, vol. 34, no. 2, pp. 131-9.
- Altuzarra, O., Salgado, O., Petuya, V. & Hernández, A. 2008, 'Computational kinematics for robotic manipulators: Jacobian problems', *Engineering Computations*, vol. 25, no. 1, pp. 4-27.
- Ambrosi, A. & Pumera, M. 2016, '3D-printing technologies for electrochemical applications', *Chemical Society Reviews*, vol. 45, no. 10, pp. 2740-55.
- Amin, M.N., Khan, K., Saleem, M.U., Khurram, N. & Niazi, M.U.K. 2017, 'Aging and curing temperature effects on compressive strength of mortar containing lime stone quarry dust and industrial granite sludge', *Materials*, vol. 10, no. 6, p. 642.
- Anell, L. 2015, 'Concrete 3d printer', Master Thesis thesis, Lund University, Sweden.
- Ann, K.Y. & Cho, C.-G. 2014, 'Corrosion resistance of calcium aluminate cement concrete exposed to a chloride environment', *Materials*, vol. 7, no. 2, pp. 887-98.
- Antohe, B.V. & Wallace, D.B. 2002, 'Acoustic phenomena in a demand mode piezoelectric ink jet printer', *Journal of Imaging Science and Technology*, vol. 46, no. 5, pp. 409-14.
- ARD09-8 2009, *ADINA Thermal Theory and Modeling Guide*.
- AS1012.8.3 2015, *Methods of making and curing concrete—Mortar and grout specimens*.

References

- AS1012.9:2014 2014, *Methods of testing concrete - Compressive strength tests - Concrete, mortar and grout specimens.*
- AS1774.2-2001(R2013) 2013, *Refractories and refractory materials - Physical test methods Determination of bulk density of granular materials*, AS, Australia.
- AS1774.5:2014 2014, *Refractories and refractory materials - Physical test methods, Method 5: Determination of bulk density, apparent porosity and true porosity (ISO 5017:2013, MOD) ISO 5017-2013*, Australia.
- AS1774.6-2001(R2013) 2013, *Refractories and refractory materials - Physical test methods Determination of true density*, AS, Australia.
- AS3700-2001 2001, *Masonry Structures.*
- Asadi-Eydivand, M., Solati-Hashjin, M., Farzad, A. & Abu Osman, N.A. 2016, 'Effect of technical parameters on porous structure and strength of 3D printed calcium sulfate prototypes', *Robotics and Computer-Integrated Manufacturing*, vol. 37, pp. 57-67.
- Ashraf, M., Gibson, I. & Rashed, M.G. 2018, 'Challenges and prospects of 3d printing in structural engineering', Perth, Australia.
- Asprone, D., Auricchio, F., Menna, C. & Mercuri, V. 2018, '3D printing of reinforced concrete elements: Technology and design approach', *Construction and Building Materials*, vol. 165, pp. 218-31.
- ASTM C29/29M, A. 2007, 'C29/C29M-07 Standard Test Method for Bulk Density ("Unit Weight") and Voids in Aggregate.', *ASTM International West Conshohocken, PA.*

References

- ASTM:C109/C109M 2016, *Compressive Strength of Hydraulic Cement Mortars (Using 2-in. or [50-mm] Cube Specimens)*.
- ASTM:D638 2014, *Standard Test Method for Tensile Properties of Plastics*.
- ASTMC39 2001, '39, Standard test method for compressive strength of cylindrical concrete specimens', *ASTM International*.
- ASTMC191-13 2013, *Standard Test Methods for Time of Setting of Hydraulic Cement by Vicat Needle*, ASTM.
- ASTMC293/C293M 2002, '293 Standard Test Method for Flexural Strength of Concrete (Using Simple Beam With Center-Point Loading)', *ASTM Standard*.
- ASTMC1437 2015, *Standard Test Method for Flow of Hydraulic Cement Mortar*.
- Atwood, C., Griffith, M., Schlienger, M., Harwell, L., Ensz, M., Keicher, D., Schlienger, M., Romero, J. & Smugeresky, J. 1998, 'Laser engineered net shaping (LENS): a tool for direct fabrication of metal parts', vol. 98, pp. 16-9.
- Bai, Y., Wall, C., Pham, H., Esker, A. & Williams, C.B. 2019, 'Characterizing Binder–Powder Interaction in Binder Jetting Additive Manufacturing Via Sessile Drop Goniometry', *Journal of Manufacturing Science and Engineering*, vol. 141, no. 1, p. 011005.
- Barnett, E. & Gosselin, C. 2015, 'Large-scale 3D printing with a cable-suspended robot', *Additive Manufacturing*, vol. 7, pp. 27-44.
- Beauchamp, Y., Stobbe, T.J., Ghosh, K. & Imbeau, D. 1991, 'Determination of a safe slow robot motion speed based on the effect of environmental factors', *Human factors*, vol. 33, no. 4, pp. 419-27.

References

- Bellego, C.L., Gérard, B. & Pijaudier-Cabot, G. 2000, 'Chemo-mechanical effects in mortar beams subjected to water hydrolysis', *Journal of Engineering Mechanics*, vol. 126, no. 3, pp. 266-72.
- Berman, B. 2012, '3-D printing: The new industrial revolution', *Business Horizons*, vol. 55, no. 2, pp. 155-62.
- BiolinScientific, *Influence of surface roughness on contact angle and wettability*.
- Böhmer, M.R., Schroeders, R., Steenbakkens, J.A.M., de Winter, S.H.P.M., Duineveld, P.A., Lub, J., Nijssen, W.P.M., Pikkemaat, J.A. & Stapert, H.R. 2006, 'Preparation of monodisperse polymer particles and capsules by ink-jet printing', *Colloids and Surfaces A: Physicochemical and Engineering Aspects*, vol. 289, no. 1, pp. 96-104.
- Boring, R.J. 2016, *Rotary lobe pumps versus progressive cavity pumps*
<https://www.flowcontrolnetwork.com/rotary-lobe-pumps-versus-progressive-cavity-pumps/>.
- Bos, F., Wolfs, R., Ahmed, Z. & Salet, T. 2016, 'Additive manufacturing of concrete in construction: potentials and challenges of 3D concrete printing', *Virtual and Physical Prototyping*, vol. 11, no. 3, pp. 209-25.
- Bos, F.P., Ahmed, Z.Y., Wolfs, R.J.M. & Salet, T.A.M. 2018, '3D Printing Concrete with Reinforcement', Cham.
- Brown, A. 2015, '3D Printing in Instructional Settings: Identifying a Curricular Hierarchy of Activities', *TechTrends*, vol. 59, no. 5, pp. 16-24.

References

- Buss, S.R. 2004, 'Introduction to inverse kinematics with jacobian transpose, pseudoinverse and damped least squares methods', *IEEE Journal of Robotics and Automation*, vol. 17, no. 1-19, p. 16.
- Buswell, R.A., Leal de Silva, W.R., Jones, S.Z. & Dirrenberger, J. 2018, '3D printing using concrete extrusion: A roadmap for research', *Cement and Concrete Research*, vol. 112, pp. 37-49.
- Buswell, R.A., Soar, R., Gibb, A.G. & Thorpe, A. 2007, 'Freeform construction: mega-scale rapid manufacturing for construction', *Automation in construction*, vol. 16, no. 2, pp. 224-31.
- Buswell, R.A., Soar, R., Gibb, A.G. & Thorpe, T. 2005, 'The potential of freeform construction processes'.
- Cañete Vela, I. 2014, '3D printer electronics design', Universitat Politècnica de Catalunya.
- Cao, R.H., Cao, P., Lin, H., Ma, G.W., Zhang, C.Y. & Jiang, C. 2018, 'Failure characteristics of jointed rock-like material containing multi-joints under a compressive-shear test: Experimental and numerical analyses', *Archives of Civil and Mechanical Engineering*, vol. 18, no. 3, pp. 784-98.
- Cao, S., Qiu, Y., Wei, X.-F. & Zhang, H.-H. 2015, 'Experimental and theoretical investigation on ultra-thin powder layering in three dimensional printing (3DP) by a novel double-smoothing mechanism', *Journal of Materials Processing Technology*, vol. 220, pp. 231-42.
- Cassie, A.B.D. & Baxter, S. 1944, 'Wettability of porous surfaces', *Transactions of the Faraday Society*, vol. 40, no. 0, pp. 546-51.

References

- Castilho, M., Gouveia, B., Pires, I., Rodrigues, J. & Pereira, M. 2015, 'The role of shell/core saturation level on the accuracy and mechanical characteristics of porous calcium phosphate models produced by 3Dprinting', *Rapid Prototyping Journal*, vol. 21, no. 1, pp. 43-55.
- Castilho, M., Pires, I., Gouveia, B. & Rodrigues, J. 2011, 'Structural evaluation of scaffolds prototypes produced by three-dimensional printing', *The International Journal of Advanced Manufacturing Technology*, vol. 56, no. 5-8, pp. 561-9.
- Cesarano, J. 2011, 'A Review of Robocasting Technology', *MRS Proceedings*, vol. 542, p. 133.
- Cesaretti, G., Dini, E., De Kestelier, X., Colla, V. & Pambaguian, L. 2014, 'Building components for an outpost on the Lunar soil by means of a novel 3D printing technology', *Acta Astronautica*, vol. 93, pp. 430-50.
- Chiaverini, S., Siciliano, B. & Egeland, O. 1994, 'Review of the damped least-squares inverse kinematics with experiments on an industrial robot manipulator', *IEEE Transactions on Control Systems Technology*, no. 2, pp. 123-34.
- Christ, S., Schnabel, M., Vorndran, E., Groll, J. & Gbureck, U. 2015, 'Fiber reinforcement during 3D printing', *Materials Letters*, vol. 139, pp. 165-8.
- Chua, C.K. & Leong, K.F. 2014, *3D Printing And Additive Manufacturing: Principles And Applications (With Companion Media Pack) Of Rapid Prototyping*, World Scientific Publishing Co Inc, Singapore, Singapore
- Chuang, M.Y. 2017, 'Inkjet Printing of Ag Nanoparticles using Dimatix Inkjet Printer, No 2'.

References

- Clifton, M., Paul, G., Kwok, N., Liu, D. & Wang, D.-L. 2008, 'Evaluating performance of multiple RRTs', *IEEE*, pp. 564-9.
- Cole, R.J. 1998, 'Energy and greenhouse gas emissions associated with the construction of alternative structural systems', *Building and Environment*, vol. 34, no. 3, pp. 335-48.
- CONPrint3D.In:TUDresd, 'https://tu-dresden.de/bu/bauingenieurwesen/ifb/das-institut/news/CONPrint3D?set_language=en.%20Accessed%2011%20Aug%202011'.
- Cox, S.C., Thornby, J.A., Gibbons, G.J., Williams, M.A. & Mallick, K.K. 2015, '3D printing of porous hydroxyapatite scaffolds intended for use in bone tissue engineering applications', *Materials Science and Engineering: C*, vol. 47, no. Supplement C, pp. 237-47.
- Crowley, S.V., Gazi, I., Kelly, A.L., Huppertz, T. & O'Mahony, J.A. 2014, 'Influence of protein concentration on the physical characteristics and flow properties of milk protein concentrate powders', *Journal of Food Engineering*, vol. 135, no. Supplement C, pp. 31-8.
- Cwalina, C.D., Harrison, K.J. & Wagner, N.J. 2016, 'Rheology of cubic particles suspended in a Newtonian fluid', *Soft Matter*, vol. 12, no. 20, pp. 4654-65.
- Cyr, M., Legrand, C. & Mouret, M. 2000, 'Study of the shear thickening effect of superplasticizers on the rheological behaviour of cement pastes containing or not mineral additives', *Cement and Concrete Research*, vol. 30, no. 9, pp. 1477-83.
- Dalgarno, K. & Stewart, T. 2001, 'Manufacture of production injection mould tooling incorporating conformal cooling channels via indirect selective laser sintering',

References

- Proceedings of the Institution of Mechanical Engineers, Part B: Journal of Engineering Manufacture*, vol. 215, no. 10, pp. 1323-32.
- de Vicente, J., Ruiz-López, J.A., Andablo-Reyes, E., Segovia-Gutiérrez, J.P. & Hidalgo-Alvarez, R. 2011, 'Squeeze flow magnetorheology', *Journal of Rheology*, vol. 55, no. 4, pp. 753-79.
- De Witte, D. 2015, 'Concrete in an AM process: freeform concrete processing', TU Delft, Netherlands, Delft, Netherlands.
- Delgado Camacho, D., Clayton, P., O'Brien, W.J., Seepersad, C., Juenger, M., Ferron, R. & Salamone, S. 2018, 'Applications of additive manufacturing in the construction industry – A forward-looking review', *Automation in Construction*, vol. 89, pp. 110-9.
- Dias, W.P.S. 2000, 'Reduction of concrete sorptivity with age through carbonation', *Cement and Concrete Research*, vol. 30, no. 8, pp. 1255-61.
- Dikshit, V., Nagalingam, A.P., Yap, Y.L., Sing, S.L., Yeong, W.Y. & Wei, J. 2018, 'Crack monitoring and failure investigation on inkjet printed sandwich structures under quasi-static indentation test', *Materials & Design*, vol. 137, pp. 140-51.
- Dini, E. 2009, 'D-shape', *Monolite UK Ltd.* <https://d-shape.com/>.
- Dizon, J.R.C., Espera, A.H., Chen, Q. & Advincula, R.C. 2018, 'Mechanical characterization of 3D-printed polymers', *Additive Manufacturing*, vol. 20, pp. 44-67.
- Doerr, S.H. 1998, 'On standardizing the 'Water Drop Penetration Time' and the 'Molarity of an Ethanol Droplet' techniques to classify soil hydrophobicity: A

References

- case study using medium textured soils', *Earth Surface Processes and Landforms*, vol. 23, no. 7, pp. 663-8.
- Edwards, L., Holt, C., Keyte, L. & Lloyd, R. 2015, 'Construction 3D Printing', paper presented to the *Concrete 2013*, Gold Coast, Australia
- El Cheikh, K., Rémond, S., Khalil, N. & Aouad, G. 2017, 'Numerical and experimental studies of aggregate blocking in mortar extrusion', *Construction and Building Materials*, vol. 145, pp. 452-63.
- Elhag, H., Glass, J., Gibb, A.G., Clarke, M., Budge, C. & Bailey, G. 2008, 'Implementing environmental improvements in a manufacturing context: a structured approach for the precast concrete industry', *International Journal of Environmental Technology and Management*, vol. 8, no. 4, pp. 369-84.
- Famy, C., Scrivener, K., Atkinson, A. & Brough, A. 2002, 'Effects of an early or a late heat treatment on the microstructure and composition of inner CSH products of Portland cement mortars', *Cement and Concrete Research*, vol. 32, no. 2, pp. 269-78.
- Farina, I., Fabbrocino, F., Colangelo, F., Feo, L. & Fraternali, F. 2016, 'Surface roughness effects on the reinforcement of cement mortars through 3D printed metallic fibers', *Composites Part B: Engineering*, vol. 99, pp. 305-11.
- Farzadi, A., Solati-Hashjin, M., Asadi-Eydivand, M. & Abu Osman, N.A. 2014, 'Effect of layer thickness and printing orientation on mechanical properties and dimensional accuracy of 3D printed porous samples for bone tissue engineering', *PLoS One*, vol. 9, no. 9, p. e108252.

References

- Farzadi, A., Waran, V., Solati-Hashjin, M., Rahman, Z.A.A., Asadi, M. & Osman, N.A.A. 2015, 'Effect of layer printing delay on mechanical properties and dimensional accuracy of 3D printed porous prototypes in bone tissue engineering', *Ceramics International*, vol. 41, no. 7, pp. 8320-30.
- Feng, L.Y. 2014, 'Study on the Status Quo and Problems of 3D Printed Buildings in China', *Global Journal of Human-Social Science Research*, vol. 14, no. 5.
- Feng, P., Meng, X., Chen, J.-F. & Ye, L. 2015, 'Mechanical properties of structures 3D printed with cementitious powders', *Construction and Building Materials*, vol. 93, pp. 486-97.
- Feng, P., Meng, X. & Zhang, H. 2015, 'Mechanical behavior of FRP sheets reinforced 3D elements printed with cementitious materials', *Composite Structures*, vol. 134, pp. 331-42.
- Feys, D., Verhoeven, R. & De Schutter, G. 2009, 'Why is fresh self-compacting concrete shear thickening?', *Cement and Concrete Research*, vol. 39, no. 6, pp. 510-23.
- Fitzpatrick, J.J., Barringer, S.A. & Iqbal, T. 2004, 'Flow property measurement of food powders and sensitivity of Jenike's hopper design methodology to the measured values', *Journal of Food Engineering*, vol. 61, no. 3, pp. 399-405.
- Fuhr, M.J., Schubert, M., Stührk, C., Schwarze, F.W. & Herrmann, H.J. 2013, 'Penetration capacity of the wood-decay fungus *Physisporinus vitreus*', *Complex Adaptive Systems Modeling*, vol. 1, no. 1, p. 6.

References

- Geldart, D., Abdullah, E.C., Hassanpour, A., Nwoke, L.C. & Wouters, I. 2006, 'Characterization of powder flowability using measurement of angle of repose', *China Particuology*, vol. 4, no. 3, pp. 104-7.
- Gharaie, S.H., Morsi, Y. & Masood, S.H. 2013, 'Tensile Properties of Processed 3D Printer ZP150 Powder Material', *Advanced Materials Research*, vol. 699, pp. 813-6.
- Ghosh, A. & Subbarao, C. 2006, 'Tensile strength bearing ratio and slake durability of class F fly ash stabilized with lime and gypsum', *Journal of Materials in Civil Engineering*, vol. 18, no. 1, pp. 18-27.
- Gibbons, G.J., Williams, R., Purnell, P. & Farahi, E. 2010, '3D printing of cement composites', *Advances in Applied Ceramics*, vol. 109, no. 5, pp. 287-90.
- Gosselin, C., Duballet, R., Roux, P., Gaudillière, N., Dirrenberger, J. & Morel, P. 2016, 'Large-scale 3D printing of ultra-high performance concrete – a new processing route for architects and builders', *Materials & Design*, vol. 100, pp. 102-9.
- Goto, S. & Roy, D.M. 1981, 'The effect of w/c ratio and curing temperature on the permeability of hardened cement paste', *Cement and Concrete Research*, vol. 11, no. 4, pp. 575-9.
- Goyanes, A., Chang, H., Sedough, D., Hatton, G.B., Wang, J., Buanz, A., Gaisford, S. & Basit, A.W. 2015, 'Fabrication of controlled-release budesonide tablets via desktop (FDM) 3D printing', *International journal of pharmaceutics*, vol. 496, no. 2, pp. 414-20.

References

- Gupta, A. 2010, 'Recent trends of fast dissolving tablet-an overview of formulation technology', *International Journal of Pharmaceutical & Biological Archive*, vol. 1, no. 1.
- Hager, I., Golonka, A. & Putanowicz, R. 2016, '3D Printing of Buildings and Building Components as the Future of Sustainable Construction?', *Procedia Engineering*, vol. 151, pp. 292-9.
- Hamad, A.J. 2017, 'Size and shape effect of specimen on the compressive strength of HPLWFC reinforced with glass fibres', *Journal of King Saud University - Engineering Sciences*, vol. 29, no. 4, pp. 373-80.
- Hambach, M. & Volkmer, D. 2017, 'Properties of 3D-printed fiber-reinforced Portland cement paste', *Cement and Concrete Composites*, vol. 79, pp. 62-70.
- Hapgood, K.P., Litster, J.D., Biggs, S.R. & Howes, T. 2002, 'Drop Penetration into Porous Powder Beds', *Journal of Colloid and Interface Science*, vol. 253, no. 2, pp. 353-66.
- Hapgood, K.P., Litster, J.D. & Smith, R. 2003, 'Nucleation regime map for liquid bound granules', *AIChE Journal*, vol. 49, no. 2, pp. 350-61.
- Haroglu, H. 2010, 'Investigating the structural frame decision making process', © Hasan Haroglu.
- Henke, K. & Treml, S. 2012, 'Wood based bulk material in 3D printing processes for applications in construction', *European Journal of Wood and Wood Products*, vol. 71, no. 1, pp. 139-41.

References

- Hewit, J. & Love, J. 1983, 'Resolved motion rate control of a materials-handling machine', *Transactions of the Institute of Measurement and Control*, vol. 5, no. 3, pp. 155-9.
- Hiremath, P.N. & Yaragal, S.C. 2017, 'Influence of mixing method, speed and duration on the fresh and hardened properties of Reactive Powder Concrete', *Construction and Building Materials*, vol. 141, pp. 271-88.
- Holman, R.K., Uhland, S.A., Cima, M.J. & Sachs, E. 2002, 'Surface Adsorption Effects in the Inkjet Printing of an Aqueous Polymer Solution on a Porous Oxide Ceramic Substrate', *Journal of Colloid and Interface Science*, vol. 247, no. 2, pp. 266-74.
- Huang, W., Zheng, Q., Sun, W., Xu, H. & Yang, X. 2007, 'Levofloxacin implants with predefined microstructure fabricated by three-dimensional printing technique', *International journal of pharmaceutics*, vol. 339, no. 1-2, pp. 33-8.
- HuaShangTengda, <http://www.hstdgm.com/>, <<http://www.hstdgm.com/>>.
- Hutmacher, D.W., Schantz, T., Zein, I., Ng, K.W., Teoh, S.H. & Tan, K.C. 2001, 'Mechanical properties and cell cultural response of polycaprolactone scaffolds designed and fabricated via fused deposition modeling', *Journal of Biomedical Materials Research: An Official Journal of The Society for Biomaterials, The Japanese Society for Biomaterials, and The Australian Society for Biomaterials and the Korean Society for Biomaterials*, vol. 55, no. 2, pp. 203-16.
- Hwang, D. & Khoshnevis, B. 2004, 'Concrete wall fabrication by contour crafting', paper presented to the *21st International Symposium on Automation and Robotics in Construction (ISARC 2004)*, Jeju, South Korea.

References

- Ian, G. & Dongping, S. 1997, 'Material properties and fabrication parameters in selective laser sintering process', *Rapid Prototyping Journal*, vol. 3, no. 4, pp. 129-36.
- Jeng, J.-Y., Peng, S.-C. & Chou, C.-J. 2000, 'Metal Rapid Prototype Fabrication Using Selective Laser Cladding Technology', *The International Journal of Advanced Manufacturing Technology*, vol. 16, no. 9, pp. 681-7.
- Jenike, A.W. 1964, 'Storage and flow of solids', *Bulletin No. 123, Utah State University*.
- Jeon, K.-H., Park, M.-B., Kang, M.-K. & Kim, J.-H. 2013, 'Development of an automated freeform construction system and its construction materials', paper presented to the *Proceedings of the 30th International Symposium on Automation and Robotics in Construction and Mining*.
- Jianchao, Z., Zhang, T., Faried, M. & Wengang, C. 2017, '3D printing cement based ink, and it's application within the construction industry', paper presented to the *MATEC Web of Conferences*, Malacca, Malaysia.
- JushiUSA, *Chopped Strands 552B for BMC*, <<http://jushiusa.com/>>.
- Kazemian, A., Yuan, X., Cochran, E. & Khoshnevis, B. 2017, 'Cementitious materials for construction-scale 3D printing: Laboratory testing of fresh printing mixture', *Construction and Building Materials*, vol. 145, pp. 639-47.
- Khoshnevis, B., Bukkapatnam, S., Kwon, H. & Saito, J. 2001, 'Experimental investigation of contour crafting using ceramics materials', *Rapid Prototyping Journal*, vol. 7, no. 1, pp. 32-42.

References

- Khoshnevis, B. & Dutton, R. 1998, 'Innovative rapid prototyping process makes large sized, smooth surfaced complex shapes in a wide variety of materials', *Materials Technology*, vol. 13, no. 2, pp. 53-6.
- Kim, K.-B., Kim, J.-H., Kim, W.-C., Kim, H.-Y. & Kim, J.-H. 2013, 'Evaluation of the marginal and internal gap of metal-ceramic crown fabricated with a selective laser sintering technology: two-and three-dimensional replica techniques', *The journal of advanced prosthodontics*, vol. 5, no. 2, pp. 179-86.
- Kirchberg, S., Abdin, Y. & Ziegmann, G. 2011, 'Influence of particle shape and size on the wetting behavior of soft magnetic micropowders', *Powder Technology*, vol. 207, no. 1, pp. 311-7.
- Klaus, S.R., Neubauer, J. & Goetz-Neunhoeffler, F. 2016, 'Influence of the specific surface area of alumina fillers on CAC hydration kinetics', *Advances in Cement Research*, vol. 28, no. 1, pp. 62-70.
- Ko, N.Y. 2015, 'Extended RMRC and its Application to the Motion of a Mobile Manipulator', *International Journal of Humanoid Robotics*, vol. 12, no. 02, p. 1550016.
- Kodur, V. 2014, 'Properties of concrete at elevated temperatures', *ISRN Civil engineering*, vol. 2014.
- Kolossov, S., Boillat, E., Glardon, R., Fischer, P. & Locher, M. 2004, '3D FE simulation for temperature evolution in the selective laser sintering process', *International Journal of Machine Tools and Manufacture*, vol. 44, no. 2, pp. 117-23.

References

- Kommu, A., Kanchi, R.R. & Uttarkar, N.K. 2014, 'Design and development of microcontroller based peristaltic pump for automatic potentiometric titration', pp. 157-61.
- Kruth, J.P., Mercelis, P., Van Vaerenbergh, J., Froyen, L. & Rombouts, M. 2005, 'Binding mechanisms in selective laser sintering and selective laser melting', *Rapid Prototyping Journal*, vol. 11, no. 1, pp. 26-36.
- Kullmann, C., Schirmer, N.C., Lee, M.-T., Ko, S.H., Hotz, N., Grigoropoulos, C.P. & Poulidakos, D. 2012, '3D micro-structures by piezoelectric inkjet printing of gold nanofluids', *Journal of Micromechanics and Microengineering*, vol. 22, no. 5, p. 055022.
- Kumar, S. 2003, 'Selective laser sintering: A qualitative and objective approach', *JOM*, vol. 55, no. 10, pp. 43-7.
- Kvan, T. & Kolarevic, B. 2002, 'Rapid prototyping and its application in architectural design', *Automation in Construction*, vol. 11, no. 3, pp. 277-8.
- Laghi, V., Palermo, M., Pragliola, M., Girelli, V.A., Velden, G.V.D. & Trombetti, T. 2018, 'Towards 3D-printed steel grid-shells: the main idea and first studies', paper presented to the *Proceedings of the IASS Symposium 2018 Creativity in Structural Design*, Boston, USA.
- Lander, L.M., Siewierski, L.M., Brittain, W.J. & Vogler, E.A. 1993, 'A systematic comparison of contact angle methods', *Langmuir*, vol. 9, no. 8, pp. 2237-9.
- Le, H.P. 1998, 'Progress and trends in ink-jet printing technology', *Journal of Imaging Science and Technology*, vol. 42, no. 1, pp. 49-62.

References

- Le, T.T., Austin, S.A., Lim, S., Buswell, R.A., Gibb, A.G.F. & Thorpe, T. 2012, 'Mix design and fresh properties for high-performance printing concrete', *Materials and Structures*, vol. 45, no. 8, pp. 1221-32.
- Le, T.T., Austin, S.A., Lim, S., Buswell, R.A., Law, R., Gibb, A.G. & Thorpe, T. 2012, 'Hardened properties of high-performance printing concrete', *Cement and Concrete Research*, vol. 42, no. 3, pp. 558-66.
- Leach, N., Carlson, A., Khoshnevis, B. & Thangavelu, M. 2012, 'Robotic construction by contour crafting: The case of lunar construction', *International Journal of Architectural Computing*, vol. 10, no. 3, pp. 423-38.
- Lee, C.S., Kim, S.G., Kim, H.J. & Ahn, S.H. 2007, 'Measurement of anisotropic compressive strength of rapid prototyping parts', *Journal of Materials Processing Technology*, vol. 187–188, pp. 627-30.
- Lee, J.-Y., An, J. & Chua, C.K. 2017, 'Fundamentals and applications of 3D printing for novel materials', *Applied Materials Today*, vol. 7, pp. 120-33.
- Lewis, J.A., Smay, J.E., Stuecker, J. & Cesarano, J. 2006, 'Direct Ink Writing of Three-Dimensional Ceramic Structures', *Journal of the American Ceramic Society*, vol. 89, no. 12, pp. 3599-609.
- Lewry, A.J. & Williamson, J. 1994, 'The setting of gypsum plaster', *Journal of Materials Science*, vol. 29, no. 23, pp. 6085-90.
- Li, T., Aspler, J., Kingsland, A., Cormier, L.M. & Zou, X. 2016, '3d printing—a review of technologies, markets, and opportunities for the forest industry', *J. Sci. Technol. For. Prod. Process*, vol. 5, no. 2, p. 30.

References

- Li, V.C. & Maalej, M. 1996, 'Toughening in cement based composites. Part II: Fiber reinforced cementitious composites', *Cement and Concrete Composites*, vol. 18, no. 4, pp. 239-49.
- Li, X., Zhou, R., Yao, W. & Fan, X. 2017, 'Flow characteristic of highly underexpanded jets from various nozzle geometries', *Applied Thermal Engineering*, vol. 125, no. Supplement C, pp. 240-53.
- Lim, S., Buswell, R.A., Le, T.T., Austin, S.A., Gibb, A.G. & Thorpe, T. 2012, 'Developments in construction-scale additive manufacturing processes', *Automation in construction*, vol. 21, pp. 262-8.
- Lim, S., Buswell, R.A., Le, T.T., Wackrow, R., Austin, S.A., Gibb, A.G.F. & Thorpe, T. 2011, 'Development of a viable concrete printing process'.
- Lim, S., Buswell, R.A., Valentine, P.J., Piker, D., Austin, S.A. & De Kestelier, X. 2016, 'Modelling curved-layered printing paths for fabricating large-scale construction components', *Additive Manufacturing*, vol. 12, Part B, pp. 216-30.
- Lin, X., Zhang, T., Huo, L., Li, G., Zhang, N. & Liao, J. 2015, 'Preparation and Application of 3D Printing Materials in Construction', paper presented to the *27th Biennial Conference of the Concrete Institute of Australia*, Melbourne, Australia
- Lipson, H. & Kurman, M. 2013, *Fabricated: The new world of 3D printing*, John Wiley & Sons, New York, USA
- Liu, Z., Zhang, M., Bhandari, B. & Wang, Y. 2017, '3D printing: Printing precision and application in food sector', *Trends in Food Science & Technology*, vol. 69, pp. 83-94.

References

- Lloret, E., Shahab, A.R., Linus, M., Flatt, R.J., Gramazio, F., Kohler, M. & Langenberg, S. 2015, 'Complex concrete structures: Merging existing casting techniques with digital fabrication', *Computer-Aided Design*, vol. 60, pp. 40-9.
- Lothenbach, B., Winnefeld, F., Alder, C., Wieland, E. & Lunk, P. 2007, 'Effect of temperature on the pore solution, microstructure and hydration products of Portland cement pastes', *Cement and Concrete Research*, vol. 37, no. 4, pp. 483-91.
- Low, Z.-X., Chua, Y.T., Ray, B.M., Mattia, D., Metcalfe, I.S. & Patterson, D.A. 2017, 'Perspective on 3D printing of separation membranes and comparison to related unconventional fabrication techniques', *Journal of Membrane Science*, vol. 523, pp. 596-613.
- Lowke, D., Dini, E., Perrot, A., Weger, D., Gehlen, C. & Dillenburger, B. 2018, 'Particle-bed 3D printing in concrete construction – Possibilities and challenges', *Cement and Concrete Research*.
- Lu, K., Hiser, M. & Wu, W. 2009, 'Effect of particle size on three dimensional printed mesh structures', *Powder Technology*, vol. 192, no. 2, pp. 178-83.
- Lu, K. & Reynolds, W.T. 2008, '3DP process for fine mesh structure printing', *Powder technology*, vol. 187, no. 1, pp. 11-8.
- Lv, X., Ye, F., Cheng, L., Fan, S. & Liu, Y. 2019, 'Binder jetting of ceramics: Powders, binders, printing parameters, equipment, and post-treatment', *Ceramics International*.

References

- Ma, G., Li, Z., Wang, L. & Bai, G. 2019, 'Micro-cable reinforced geopolymer composite for extrusion-based 3D printing', *Materials Letters*, vol. 235, pp. 144-7.
- Ma, G., Wang, L. & Ju, Y. 2017, 'State-of-the-art of 3D printing technology of cementitious material—An emerging technique for construction', *Science China Technological Sciences*.
- Ma, Y., Yin, X., Fan, X., Travitzky, N. & Greil, P. 2015, 'Fabrication of MAX-phase-based ceramics by three-dimensional printing', *Journal of Ceramic Science and Technology*, vol. 6, no. 2, pp. 87-94.
- Maier, A.-K., Dezmirean, L., Will, J. & Greil, P. 2011, 'Three-dimensional printing of flash-setting calcium aluminate cement', *Journal of materials science*, vol. 46, no. 9, pp. 2947-54.
- Majeed, S.A. 2011, 'Effect of specimen size on compressive, modulus of rupture and splitting strength of cement mortar', *Journal of applied sciences*, vol. 11, no. 3, pp. 584-8.
- Malaeb, Z., Hachem, H., Tourbah, A., Maalouf, T., El Zarwi, N. & Hamzeh, F. 2015, '3d Concrete Printing: Machine And Mix Design', *International Journal of Civil Engineering*, no. 6.
- Marchelli, G., Prabhakar, R., Storti, D. & Ganter, M. 2011, 'The guide to glass 3D printing: developments, methods, diagnostics and results', *Rapid Prototyping Journal*, vol. 17, no. 3, pp. 187-94.
- Marchment, T. & Sanjayan, J. 2018, 'Method of Enhancing Interlayer Bond Strength in 3D Concrete Printing', Springer, pp. 148-56.

References

- Marmur, A. 2009, 'Solid-Surface Characterization by Wetting', *Annual Review of Materials Research*, vol. 39, no. 1, pp. 473-89.
- Maskuriy, R., Selamat, A., Ali, K.N., Maresova, P. & Krejcar, O. 2019, 'Industry 4.0 for the Construction Industry—How Ready Is the Industry?', *Applied Sciences*, vol. 9, no. 14, p. 2819.
- Miguel, C., Marta, D., Uwe, G., Jürgen, G., Paulo, F., Inês, P., Barbara, G., Jorge, R. & Elke, V. 2013, 'Fabrication of computationally designed scaffolds by low temperature 3D printing', *Biofabrication*, vol. 5, no. 3, p. 035012.
- Mindess, S., Young, J.F. & Darwin, D. 1981, 'Concrete, prentice hall', *Englewood Cliffs, NJ*, vol. 481.
- Miyanaji, H., Zhang, S., Lassell, A., Zandinejad, A.A. & Yang, L. 2016, 'Optimal Process Parameters for 3D Printing of Porcelain Structures', *Procedia Manufacturing*, vol. 5, pp. 870-87.
- Morissette, S.L., Lewis, J.A., Cesarano, J., Dimos, D.B. & Baer, T. 2000, 'Solid freeform fabrication of aqueous alumina–poly (vinyl alcohol) gelcasting suspensions', *Journal of the American Ceramic Society*, vol. 83, no. 10, pp. 2409-16.
- Mueller, S., Im, S., Gurevich, S., Teibrich, A., Pfisterer, L., Guimbretière, F. & Baudisch, P. 2014, 'WirePrint: 3D printed previews for fast prototyping', paper presented to the *Proceedings of the 27th annual ACM symposium on User interface software and technology*, Honolulu, HI, USA.
- Mukesh, A., David, B., Joseph, B., Harris, M. & Joel, B. 1995, 'Direct selective laser sintering of metals', *Rapid Prototyping Journal*, vol. 1, no. 1, pp. 26-36.

References

- Nazari, A. 2011, 'The effects of curing medium on flexural strength and water permeability of concrete incorporating TiO₂ nanoparticles', *Materials and Structures*, vol. 44, no. 4, pp. 773-86.
- Nerella, V.N., Schroefl, C., Yazdi, M.A., Alghazali, A., Secrieru, E., Shyshko, S., Liebscher, M., Heravi, A.A., Dudziak, L. & Beigh, M.A.B. 2017, 'Micro-and macroscopic investigations on the interface between layers of 3d-printed cementitious elements', *Journal of Materials in Civil Engineering*, vol. 29, no. 7.
- Ngo, T.D., Kashani, A., Imbalzano, G., Nguyen, K.T.Q. & Hui, D. 2018, 'Additive manufacturing (3D printing): A review of materials, methods, applications and challenges', *Composites Part B: Engineering*, vol. 143, pp. 172-96.
- Nguyen, T., Shen, W. & Hapgood, K. 2009, 'Drop penetration time in heterogeneous powder beds', *Chemical Engineering Science*, vol. 64, no. 24, pp. 5210-21.
- Nowotarski, P. & Paslawski, J. 2017, 'Industry 4.0 concept introduction into construction SMEs', vol. 245, IOP Publishing, p. 052043.
- Panda, B., Ruan, S., Unluer, C. & Tan, M.J. 2019, 'Improving the 3D printability of high volume fly ash mixtures via the use of nano attapulgite clay', *Composites Part B: Engineering*, vol. 165, pp. 75-83.
- Panda, B., Tay, Y., Paul, S.C., Jen, T.M., Leong, K. & Gibson, I. 2018, 'Current Challenges And Future Perspectives Of 3d Concrete Printing'.
- Parr, C., Simonin, F., Touzo, B., Wohrmeyer, C., Valdelièvre, B. & Namba, A. 2005, 'The impact of calcium aluminate cement hydration upon the properties of refractory castables', *Journal of Technical Association of Refractories Japan*, vol. 25, no. 2, pp. 78-88.

References

- Parrott, L.J. 1994, 'Moisture conditioning and transport properties of concrete test specimens', *Materials and Structures*, vol. 27, no. 8, p. 460.
- Patel, H., Bland, C. & Pool, A. 1996, 'The microstructure of steam-cured precast concrete', *Advances in Cement Research*, vol. 8, no. 29, pp. 11-9.
- Paul, S.C., Tay, Y.W.D., Panda, B. & Tan, M.J. 2018, 'Fresh and hardened properties of 3D printable cementitious materials for building and construction', *Archives of Civil and Mechanical Engineering*, vol. 18, no. 1, pp. 311-9.
- Pegna, J. 1997, 'Exploratory investigation of solid freeform construction', *Automation in Construction*, vol. 5, no. 5, pp. 427-37.
- Perrot, A., Rangeard, D. & Courteille, E. 2018, '3D printing of earth-based materials: Processing aspects', *Construction and Building Materials*, vol. 172, pp. 670-6.
- Perrot, A., Rangeard, D. & Pierre, A. 2015, 'Structural built-up of cement-based materials used for 3D-printing extrusion techniques', *Materials and Structures*, pp. 1-8.
- Peter, M. & Jean-Pierre, K. 2006, 'Residual stresses in selective laser sintering and selective laser melting', *Rapid Prototyping Journal*, vol. 12, no. 5, pp. 254-65.
- Petzing, J.N., Coupland, J.M. & Leach, R.K. 2010, 'The measurement of rough surface topography using coherence scanning interferometry'.
- Pfister, A., Landers, R., Laib, A., Hubner, U., Schmelzeisen, R. & Mulhaupt, R. 2004, 'Biofunctional rapid prototyping for tissue-engineering applications: 3D bioplotting versus 3D printing', *Journal of Polymer Science Part a-Polymer Chemistry*, vol. 42, no. 3, pp. 624-38.

References

- Popovics, S. & Ujhelyi, J. 2008, 'Contribution to the concrete strength versus water-cement ratio relationship', *Journal of Materials in Civil Engineering*, vol. 20, no. 7, pp. 459-63.
- Prescott, J.K. & Barnum, R.A. 2000, 'On powder flowability', *Pharmaceutical technology*, vol. 24, no. 10, pp. 60-85.
- Rael, R. & San Fratello, V. 2011, 'Material Design and Analysis for 3D-Printed Fiber-Reinforced Cement Polymer Building Components', Series Material Design and Analysis for 3D-Printed Fiber-Reinforced Cement Polymer Building Components Rael San Fratello Studio, California, USA.
- Reiter, L., Wangler, T., Roussel, N. & Flatt, R.J. 2018, 'The role of early age structural build-up in digital fabrication with concrete', *Cement and Concrete Research*, vol. 112, pp. 86-95.
- Rengier, F., Mehndiratta, A., Tengg-Kobligk, H., Zechmann, C.M., Unterhinninghofen, R., Kauczor, H.-U. & Giesel, F.L. 2010, '3D printing based on imaging data: review of medical applications', *International Journal of Computer Assisted Radiology and Surgery*, vol. 5, no. 4, pp. 335-41.
- Rossi, E., Di Nicolantonio, M., Barcarolo, P. & Lagatta, J. 2019, 'Sustainable 3D Printing: Design Opportunities and Research Perspectives', Springer, pp. 3-15.
- Roussel, N. 2006, 'A thixotropy model for fresh fluid concretes: Theory, validation and applications', *Cement and Concrete Research*, vol. 36, no. 10, pp. 1797-806.
- Rudenko3DPrinter, <http://www.totalkustom.com/>.

References

- Rushing, T.S., Al-Chaar, G., Eick, B.A., Burroughs, J., Shannon, J., Barna, L. & Case, M. 2017, 'Investigation of concrete mixtures for additive construction', *Rapid Prototyping Journal*, vol. 23, no. 1, pp. 74-80.
- Sachs, E.M., Haggerty, J.S., Cima, M.J. & Williams, P.A. 1994, 'Three-dimensional printing techniques', Series Three-dimensional printing techniques Google Patents.
- Sagoe-Crentsil, K. & Weng, L. 2007, 'Dissolution processes, hydrolysis and condensation reactions during geopolymer synthesis: Part II. High Si/Al ratio systems', *Journal of Materials Science*, vol. 42, no. 9, pp. 3007-14.
- Sandor, P. 1986, 'Effect of Curing Method and Final Moisture Condition on Compressive Strength of Concrete', *Journal Proceedings*, vol. 83, no. 4.
- Sanjayan, G. & Stocks, L. 1993, 'Spalling of high-strength silica fume concrete in fire', *Materials Journal*, vol. 90, no. 2, pp. 170-3.
- Sarangapani, G., Venkatarama Reddy, B. & Jagadish, K. 2005, 'Brick-mortar bond and masonry compressive strength', *Journal of materials in civil engineering*, vol. 17, no. 2, pp. 229-37.
- Seitz, H., Rieder, W., Irsen, S., Leukers, B. & Tille, C. 2005, 'Three-dimensional printing of porous ceramic scaffolds for bone tissue engineering', *Journal of Biomedical Materials Research Part B: Applied Biomaterials*, vol. 74B, no. 2, pp. 782-8.
- Shakor, P. & Nejadi, S. 2017, '3D Printed Concrete Evaluations by Using Different Concrete Mix Designs', paper presented to the *Recent Trends in Engineering and Technology*, Bangkok, Thailand.

References

- Shakor, P., Nejadi, S. & Paul, G. 2019, 'A Study into the Effect of Different Nozzles Shapes and Fibre-Reinforcement in 3D Printed Mortar', *Materials*, vol. 12, no. 10, p. 1708.
- Shakor, P., Nejadi, S., Paul, G. & Malek, S. 2019, 'Review of Emerging Additive Manufacturing Technologies in 3D Printing of Cementitious Materials in the Construction Industry', *Frontiers in Built Environment*, vol. 4, no. 85.
- Shakor, P., Nejadi, S., Paul, G. & Sanjayan, J. 2018, 'A Novel Methodology of Powder-based Cementitious Materials in 3D Inkjet Printing for Construction Applications ', paper presented to the *Sixth International Conference on the Durability of Concrete Structures*, Leeds, UK.
- Shakor, P., Nejadi, S., Paul, G., Sanjayan, J. & Aslani, F. 2019, 'Heat Curing as a Means of Post-processing Influence on 3D Printed Mortar Specimens in Powder-based 3D Printing', vol. 93, no. 09, pp. 62-71.
- Shakor, P., Nejadi, S., Paul, G., Sanjayan, J. & Nazari, A. 2019, 'Mechanical Properties of Cement-Based Materials and Effect of Elevated Temperature on Three-Dimensional (3-D) Printed Mortar Specimens in Inkjet 3-D Printing', *Materials Journal*, vol. 116, no. 2, pp. 55-67.
- Shakor, P., Pimplikar, S. & Ghare, U. 2011, 'Techno-Commercial aspects of use of glass fibre in construction industry', paper presented to the *Advances and Trends in Engineering Materials and their Applications*, Montreal, Canada, 2011.
- Shakor, P., Renneberg, J., Nejadi, S. & Paul, G. 2017, 'Optimisation of Different Concrete Mix Designs for 3D Printing by Utilising 6DOF Industrial Robot',

References

- paper presented to the *ISARC. Proceedings of the International Symposium on Automation and Robotics in Construction*, Taipei, Taiwan.
- Shakor, P., Sanjayan, J., Nazari, A. & Nejadi, S. 2017, 'Modified 3D printed powder to cement-based material and mechanical properties of cement scaffold used in 3D printing', *Construction and Building Materials*, vol. 138, pp. 398-409.
- Shakor, P.N. & Pimplikar, S. 2011, 'Glass fibre reinforced concrete use in construction', *Int. J. Technol. Eng. Syst*, vol. 2, no. 2.
- Shanjani, Y., Hu, Y., Pilliar, R.M. & Toyserkani, E. 2011, 'Mechanical characteristics of solid-freeform-fabricated porous calcium polyphosphate structures with oriented stacked layers', *Acta biomaterialia*, vol. 7, no. 4, pp. 1788-96.
- Shofner, M., Lozano, K., Rodríguez-Macías, F. & Barrera, E. 2003, 'Nanofiber-reinforced polymers prepared by fused deposition modeling', *Journal of applied polymer science*, vol. 89, no. 11, pp. 3081-90.
- Siebold, A., Nardin, M., Schultz, J., Walliser, A. & Oppliger, M. 2000, 'Effect of dynamic contact angle on capillary rise phenomena', *Colloids and Surfaces A: Physicochemical and Engineering Aspects*, vol. 161, no. 1, pp. 81-7.
- Sleiman, H., Perrot, A. & Amziane, S. 2010, 'A new look at the measurement of cementitious paste setting by Vicat test', *Cement and Concrete Research*, vol. 40, no. 5, pp. 681-6.
- Soltan, D.G. & Li, V.C. 2018, 'A self-reinforced cementitious composite for building-scale 3D printing', *Cement and Concrete Composites*, vol. 90, pp. 1-13.

References

- Spath, S. & Seitz, H. 2013, 'Influence of grain size and grain-size distribution on workability of granules with 3D printing', *The International Journal of Advanced Manufacturing Technology*, vol. 70, no. 1-4, pp. 135-44.
- Sun, K., Wei, T.S., Ahn, B.Y., Seo, J.Y., Dillon, S.J. & Lewis, J.A. 2013, '3D Printing of Interdigitated Li-Ion Microbattery Architectures', *Advanced Materials*, vol. 25, no. 33, pp. 4539-43.
- Surendra, P.S., Yilmaz, A. & Thomas, V. 2003, 'Determination of Early Age Mortar and Concrete Strength by Ultrasonic Wave Reflections'.
- Sutjipto, S., Tish, D., Paul, G., Vidal-Calleja, T. & Schork, T. 2019, 'Towards Visual Feedback Loops for Robot-Controlled Additive Manufacturing', eds J. Willmann, P. Block, M. Hutter, K. Byrne & T. Schork, Springer International Publishing, pp. 85-97.
- Szucs, T.D. & Brabazon, D. 2009, 'Effect of saturation and post processing on 3D printed calcium phosphate scaffolds', vol. 396, *Trans Tech Publ*, pp. 663-6.
- Tam, V.W., Tam, C., Chan, J.K. & Ng, W.C. 2006, 'Cutting construction wastes by prefabrication', *International Journal of Construction Management*, vol. 6, no. 1, pp. 15-25.
- Tay, Y.W., Panda, B., Paul, S.C., Tan, M.J., Qian, S.Z., Leong, K.F. & Chua, C.K. 2016, 'Processing and properties of construction materials for 3D printing', vol. 861, *Trans Tech Publ*, pp. 177-81.
- Tay, Y.W.D., Panda, B., Paul, S.C., Noor Mohamed, N.A., Tan, M.J. & Leong, K.F. 2017, '3D printing trends in building and construction industry: a review', *Virtual and Physical Prototyping*, vol. 12, no. 3, pp. 261-76.

References

- Teizer, J., Blickle, A., King, T., Leitzbach, O. & Guenther, D. 2016, 'Large Scale 3D Printing of Complex Geometric Shapes in Construction', vol. 33, Vilnius Gediminas Technical University, Department of Construction Economics & Property, p. 1.
- Thomas, R.J. & Peethamparan, S. 2017, 'Effect of Specimen Size and Curing Condition on the Compressive Strength of Alkali-Activated Concrete', *Transportation Research Record*, vol. 2629, no. 1, pp. 9-14.
- Thrane, L.N., Pade, C. & Nielsen, C.V. 2009, 'Determination of rheology of self-consolidating concrete using the 4C-Rheometer and how to make use of the results', *Journal of ASTM International*, vol. 7, no. 1, pp. 1-10.
- Tschapek, M. 1984, 'Criteria for Determining the hydrophilicity-hydrophobicity of Soils', *Zeitschrift für Pflanzenernährung und Bodenkunde*, vol. 147, no. 2, pp. 137-49.
- Upadhyay, M., Sivarupan, T. & El Mansori, M. 2017, '3D printing for rapid sand casting—A review', *Journal of Manufacturing Processes*, vol. 29, pp. 211-20.
- Utela, B. 2008, *Development and application of new material systems for three dimensional printing (3DP)*, University of Washington.
- Utela, B., Storti, D., Anderson, R. & Ganter, M. 2008, 'A review of process development steps for new material systems in three dimensional printing (3DP)', *Journal of Manufacturing Processes*, vol. 10, no. 2, pp. 96-104.
- Vaezi, M. & Chua, C. 2011, 'Effects of layer thickness and binder saturation level parameters on 3D printing process', *The International Journal of Advanced Manufacturing Technology*, vol. 53, no. 1-4, pp. 275-84.

References

- Verma, R. & Kaushal, G. 2019, 'State of the Art of Powder Bed Fusion Additive Manufacturing: A Review', in L.J. Kumar, P.M. Pandey & D.I. Wimpenny (eds), *3D Printing and Additive Manufacturing Technologies*, Springer Singapore, Singapore, pp. 269-79.
- Vlasea, M., Pilliar, R. & Toyserkani, E. 2015, 'Control of structural and mechanical properties in bioceramic bone substitutes via additive manufacturing layer stacking orientation', *Additive Manufacturing*, vol. 6, pp. 30-8.
- Vlasea, M., Toyserkani, E. & Pilliar, R. 2015, 'Effect of Gray Scale Binder Levels on Additive Manufacturing of Porous Scaffolds with Heterogeneous Properties', *International Journal of Applied Ceramic Technology*, vol. 12, no. 1, pp. 62-70.
- Wang, Q.J. & Zhu, D. 2013, 'Hertz Theory: Contact of Spherical Surfaces', in Q.J. Wang & Y.-W. Chung (eds), *Encyclopedia of Tribology*, Springer US, Boston, MA, pp. 1654-62.
- Wangler, T., Lloret, E., Reiter, L., Hack, N., Gramazio, F., Kohler, M., Bernhard, M., Dillenburger, B., Buchli, J. & Roussel, N. 2016, 'Digital concrete: opportunities and challenges', *RILEM Technical Letters*, vol. 1, pp. 67-75.
- Weger, D., Lowke, D. & Gehlen, C. 2016, '3D printing of Concrete Structures with Calcium Silicate based Cements using the Selective Cinding Method—Effects of Concrete Technology on Penetration Depth of Cement Paste in: Ultra-High Performance Concrete and High Performance Construction Materials', paper presented to the *HiPerMat 2016*.
- Wenzel, R.N. 1936, 'Resistance of solid surfaces to wetting by water', *Industrial & Engineering Chemistry*, vol. 28, no. 8, pp. 988-94.

References

- Will, J., Detsch, R. & Boccaccini, A.R. 2013, 'Structural and biological characterization of scaffolds', *Characterization of Biomaterials*, Elsevier, pp. 299-310.
- Withell, A., Diegel, O., Grupp, I., Reay, S., de Beer, D. & Potgieter, J. 2011, 'Porous ceramic filters through 3D printing', paper presented to the *Innovative Developments in Virtual and Physical Prototyping: Proceedings of the 5th International Conference on Advanced Research in Virtual and Rapid Prototyping, Leiria, Portugal, 28 September-1 October, 2011*, Leiria, Portugal.
- Wohlers, T. 2004, *Rapid Prototyping, Tooling and Manufacturing: State of the Industry*, Wohlers Associates Inc, USA0-9754429-0-2.
- Wu, P., Wang, J. & Wang, X. 2016, 'A critical review of the use of 3-D printing in the construction industry', *Automation in Construction*, vol. 68, pp. 21-31.
- Wu, Y.-H. & Liu, K.-F. 2015, 'Formulas for Calibration of Rheological Parameters of Bingham Fluid in Couette Rheometer', *Journal of Fluids Engineering*, vol. 137, no. 4, pp. 041202--11.
- Yang, F. 1997, 'Tension and compression of electrorheological fluid', *Journal of colloid and interface science*, vol. 192, no. 1, pp. 162-5.
- Yildirim, I. 2001, 'Surface free energy characterization of powders', Virginia Tech.
- Yoshikawa, T. 1985, 'Manipulability of robotic mechanisms', *The international journal of Robotics Research*, vol. 4, no. 2, pp. 3-9.
- Zein, I., Hutmacher, D.W., Tan, K.C. & Teoh, S.H. 2002, 'Fused deposition modeling of novel scaffold architectures for tissue engineering applications', *Biomaterials*, vol. 23, no. 4, pp. 1169-85.

References

- Zhang, H., Zhao, H., Chen, J., Li, J., Yu, J. & Nie, J. 2013, 'Defect Study of MgO-CaO Material Doped with CeO₂', *Advances in Materials Science and Engineering*, vol. 2013, p. 5.
- Zhang, J., Wang, J., Dong, S., Yu, X. & Han, B. 2019, 'A review of the current progress and application of 3D printed concrete', *Composites*, vol. v. 125, p. 2019 v.125.
- Zhang, L., Bi, X. & Grace, J.R. 2015, 'Measurements of Electrostatic Charging of Powder Mixtures in a Free-fall Test Device', *Procedia Engineering*, vol. 102, pp. 295-304.
- Zhang, W., Lian, Q., Li, D., Wang, K., Hao, D., Bian, W., He, J. & Jin, Z. 2014, 'Cartilage repair and subchondral bone migration using 3D printing osteochondral composites: a one-year-period study in rabbit trochlea', *BioMed research international*, vol. 2014.
- Zhou, Z., Buchanan, F., Mitchell, C. & Dunne, N. 2014, 'Printability of calcium phosphate: calcium sulfate powders for the application of tissue engineered bone scaffolds using the 3D printing technique', *Mater Sci Eng C Mater Biol Appl*, vol. 38, pp. 1-10.
- Zhou, Z., Mitchell, C.A., Buchanan, F.J. & Dunne, N.J. 2013, 'Effects of Heat Treatment on the Mechanical and Degradation Properties of 3D-Printed Calcium-Sulphate-Based Scaffolds', *ISRN Biomaterials*, vol. 2013, pp. 1-10.
- Zijl, G., Suvash, C., Paul, S., Ming, J. & Tan 2016, 'Properties of 3D Printable Concrete', *2nd International Conference on Progress in Additive Manufacturing (Pro-AM 2016), At Nanyang, Singapore.*

References

Zortuk, M., Kılıc, K., Uzun, G., Ozturk, A. & Kesim, B. 2008, 'The effect of different fiber concentrations on the surface roughness of provisional crown and fixed partial denture resin', *European journal of dentistry*, vol. 2, no. 3, pp. 185-90.

ZprinterManual 2012, 'User Manual ZP 150, ZP 250', Series User Manual ZP 150, ZP 250.

Appendix A

ZPrinter[®] 150

ProJet[®] 360

Appendix A

Introduction

In this study, it has been used two types of 3DP which are manufactured by 3DSystems. The specifications for the ZPrinter® 150, *Table A. 1* and *Table A. 2*.

Table A. 1 Zprinter 150 build size dimensions

Model	Colour	Cleaning	Build Volume
ZPrinter® 150	Monochrome	Separate core recycling unit	7.3" x 9.3" x 5" (185 x 236 x 132 mm)

The ProJet® x60 Series has 4 main models with different capabilities. The model has been used in this is study, which is called ProJet® 360, *Table A.2*.

Table A. 2 ProJet 360 build size dimensions

Model	Colour	Cleaning	Build Volume
ProJet® 360	Monochrome	Built-in	8" x 10" x 8" (203 x 254 x 203 mm)

Specifications

Specifications are for both the ZPrinter 150 and ProJet 360. All the technical specifications and dimensions have been declared in *Table A. 3* and *Table A. 4*.

Appendix A

Table A. 3 General specification for the ZPrinter 150

Build Volume	8" x 10" x 8" (203 mm x 254 mm x 203 mm) 640 cubic inches build capacity
Build Speed	2-4 layers per minute
Layer Thickness	.0035" - .004" (.089 - .102 mm)
Resolution	300 x 450 dpi print resolution
Materials - High-Performance Composite	(ZP 151)VisiJet [®] PXL [™] Core [™] with (ZB 63) VisiJet [®] PXL [™] Binder
Print Head	HP11 clear
Liquid Waste System	Disposable absorbent waste tray - no liquid to spill

Table A. 4 General specification for the ProJet 360

Build Volume	7.3" x 9.3" x 5" (185 x 236 x 132 mm) 340 cubic inches build capacity
Build Speed	2-4 layers per minute
Layer Thickness	.004" (.102 mm)
Resolution	300 x 450 dpi print resolution Minimum feature size .016" (.41 mm)
Materials - High-Performance Composite	zp [®] 150 Powder with zb [®] 63 Binder
Print Head	HP11 (clear)
Liquid Waste System	Disposable absorbent waste tray - no liquid to spill

Important Terms

Binder - Solution that is dispensed through the HP11 print head and applied to the powder. The binder saturation value will vary depending on the part geometry. The ZPrint software uses a default core and shell saturation value that is suitable for the most part geometries.

Appendix A

Build Bed - The area in front of the Feeder where the part is printed. The platform of the Build Bed can be raised or lowered using the appropriate command on the printer LCD menu. Before each build, the printer fills the Build Bed with powder and then spreads a layer of powder to ensure the surface of the Build Bed is completely smooth.

Build Chamber - The interior of the printer that houses the Build Bed, Service Station, the Debris Separator, the Carriage, the Fast Axis assembly, the Vacuum Hose, and the Feeder.

Carriage - Assembly that houses the Print Head and its Pogo Pin Connectors.

Consumables - Powder-Binder-Infiltrant products that are available in a variety of systems for all of your modeling needs. All consumables have been developed for the fastest printing speeds and lowest materials costs.

Debris Separator - Located in the Build Chamber. Its function is to prevent chunks or particles from going back into the printer Feeder during any vacuuming operation.

Deck - Area surrounding the Build Bed.

Depowder - Process of removing excess powder from a newly printed part. First, there is the initial manual “gross” powder removal process, which removes the bulk of the powder after the part has dried in the Build Bed. After the initial powder removal, there is the fine-powder removal process - which cleans the part of all remaining powder. Fine powder removal is easily accomplished in the separate Powder Recycling Station, or in another printer equipped with a Fine Powder Removal chamber.

Feeder - Printer component that stores powder. Powder that is vacuumed up after a build, or powder that is manually emptied from the Build Bed, is recycled and returned to the Feeder for reuse.

Appendix A

Fast Axis - Printer component that houses the Carriage and the Fast Axis rails that the Carriage moves on. The Fast Axis moves on the Slow Axis rails which are housed beneath the Build Chamber Deck.

Infiltration - Process of applying various post-processing products (resins, wax, epoxy, etc.) to fully depowdered parts to give them specific properties such as strength and durability.

LCD - Liquid Crystal Display.

Platform - The metal plate in the Build Bed. The platform (or Build Platform) can be raised or lowered by selecting the appropriate command on the printer LCD menu. The Build Platform is also removable for ease of moving delicate parts to the Powder Recycling Station.

Pogo Pins - Gold contact pins for the print head contacts. Clean the Pogo Pins with an alcohol swab whenever a print head is removed, cleaned, or replaced.

Powder - Very fine particles that are not bound together. The powder is spread layer by layer and saturated with the binder to create a solid object.

Print Head - There is one HP11 Print Head for the ZPrinter 150. When a new HP11 print head is installed, the printer runs an automatic purge cycle to clean the print head of its ink and to prepare it for dispensing binder. Note: Only HP11 model C4810A Black cartridges can be used in the ZPrinter 150.

Print Head Contacts - The contact points on a print head cartridge that match up with the Pogo Pins.

Appendix A

Purge - Process of removing ink from the HP11 print head to prepare it for dispensing binder.

Service Station - Cleans the print head jets to remove powder residue during printing. It is extremely important to clean the Service Station after every build to remove residue buildup that gets left on the Service Station during a build. If the Service Station is not clean, your print head will not get properly cleaned and this will result in shortened print head life.

Waste Tray - Absorbs the binder waste and will require changing only when you are prompted to in ZPrint. Located at the bottom rear of the printer after removing the rear panel.

ZPrinter 150 and ProJet 360 Components

The main components of the ZPrinter and ProJet 360 systems are highlighted below. Most of the components are similar unless the new version updated with built-in cleaning system and upgrade the consumable materials, *Figure A. 1*.

Appendix A



Figure A. 1: Exterior part of the powder-base 3DP.

System Exterior Parts Description

Number	ZPrinter 150	ProJet 360
1	Build Chamber	Build Chamber
2	Control Panel	Post-Processing Unit
3	LCD Display	Arm Holes
4	Control Knob	Control Panel
5		LCD Display
6		Control Knob

Appendix B

Denso Industrial Robot

Appendix B

General Introduction to Operation Modes and Additional Functions

X-Y mode allows you to drive the robot arm in base coordinates (whose origin is defined at the centre of the robot basement). Pressing the X, Y, or Z key in X-Y mode moves the robot flange linearly along the X, Y, or Z axis, respectively, as shown below.

If work coordinates (whose origin is defined at a corner of the rectangular parallelepiped envelope of an object piece) is defined, then the robot flange moves linearly in the work coordinates.

If you use the RX, RY, or RZ key in X-Y mode, the robot arm rotates on each axis of the virtual work coordinates defined on the centre of the flange surface without changing the centre position of the flange surface, as shown in *Figure B. 1*.

To rotate the robot arm on the origin of work coordinates, refer to the "external TCP function".

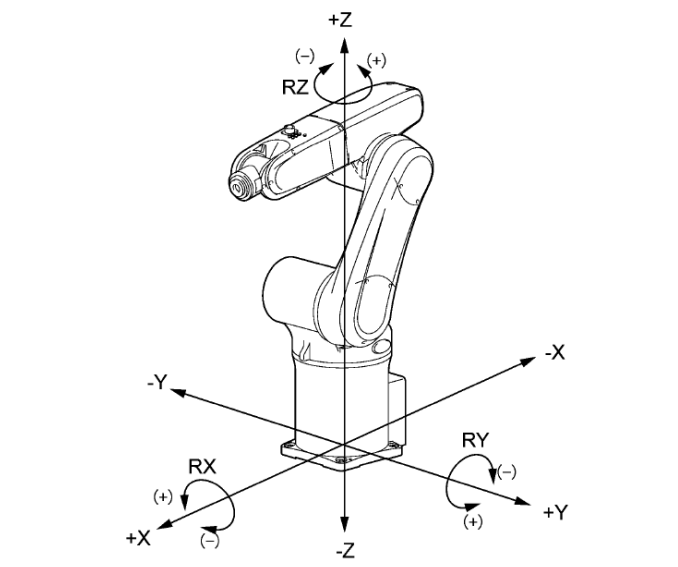


Figure B. 1: Movements in X-Y Mode

Appendix B

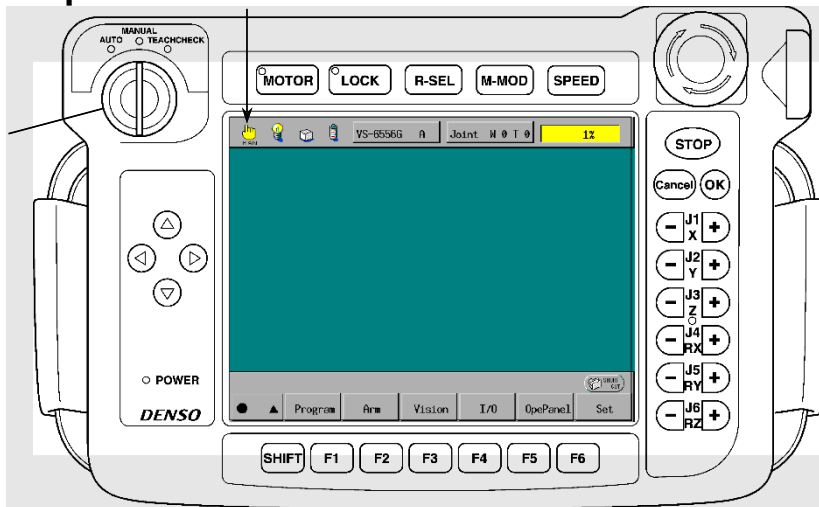
Operating procedure

CAUTION: At the start, set the reduced ratio of the programmed speed to 20% or less. If you run the robot manually at high speeds from the beginning, you may mistakenly strike the robot against the surrounding objects.

NOTE: In X-Y or Tool mode, if a pass runs through the vicinity of a singular point during manual operation, the robot will issue error code 6080s (Overspeed) and come to a halt. Avoid running a pass through the vicinity of a singular point.

From the teach pendant

Step 1 Set the mode selector switch to the MANUAL position.

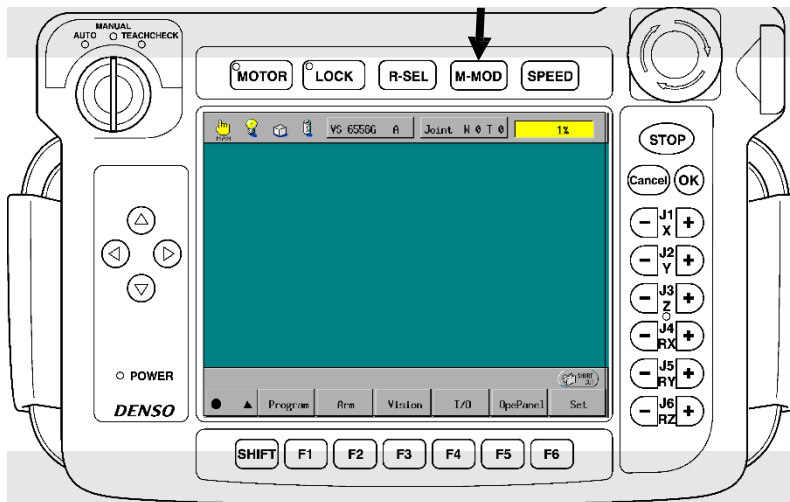


Step 2 Press the MOTOR key to turn the motor on.

Step 3 Press the M-MOD key.

Appendix B

Mode selector switch



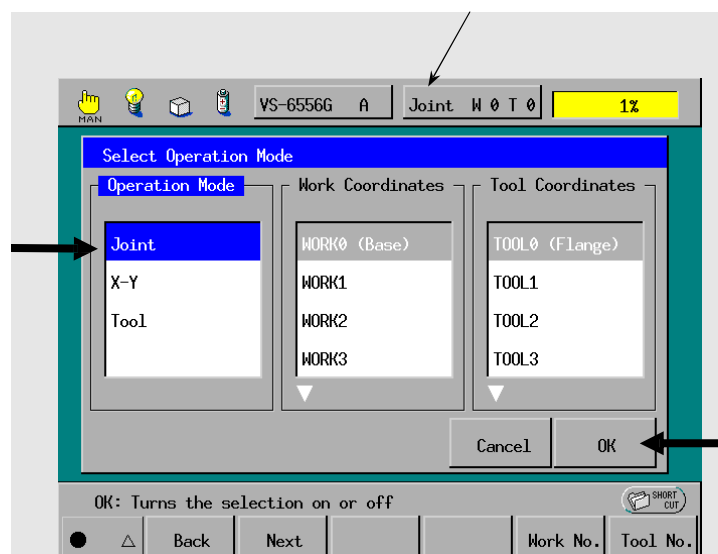
The Select Operation Mode window appears as shown in the next step.

Step 4

Select the desired operation mode by using the cursor keys or touching the screen directly, then press the OK key.

On the operation mode button in the status bar appears the selected operation mode.

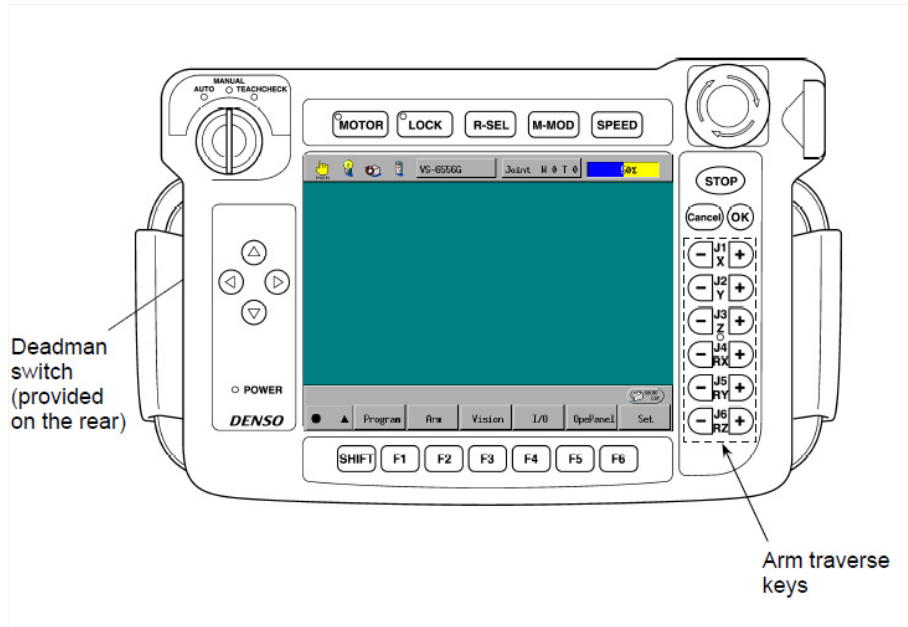
Operation mode displayed



Appendix B

Step 5

While holding down the deadman switch, press one of the arm traverse keys to drive the robot arm.



Coordinates

This section describes the coordinates required for correct handling of the robot.

[1] Base coordinates

[1.1] Base (world) coordinates and work coordinates

The base coordinates are so-called world coordinates which refer to 3-dimensional Cartesian coordinates whose origin is at the centre of the robot basement. It has components X_b , Y_b , and Z_b which are identical with X , Y , and Z in X-Y mode explained in Section 3.2.1, "Running the Robot Manually," [2] X-Y mode."

Work coordinates are 3-dimensional Cartesian coordinates defined for each operation space of workpiece. The origin can be defined anywhere and as much as needed. It lies at

Appendix B

a corner of the rectangular parallelepiped envelope of an object workpiece as shown in *Figure B. 2*. Work coordinates are expressed by the coordinate origin (X, Y, Z) corresponding to the base coordinates and the angles of rotation (R_x , R_y , R_z) around X, Y and Z axes of base coordinates. If work coordinates are not defined, base coordinates go into effect.

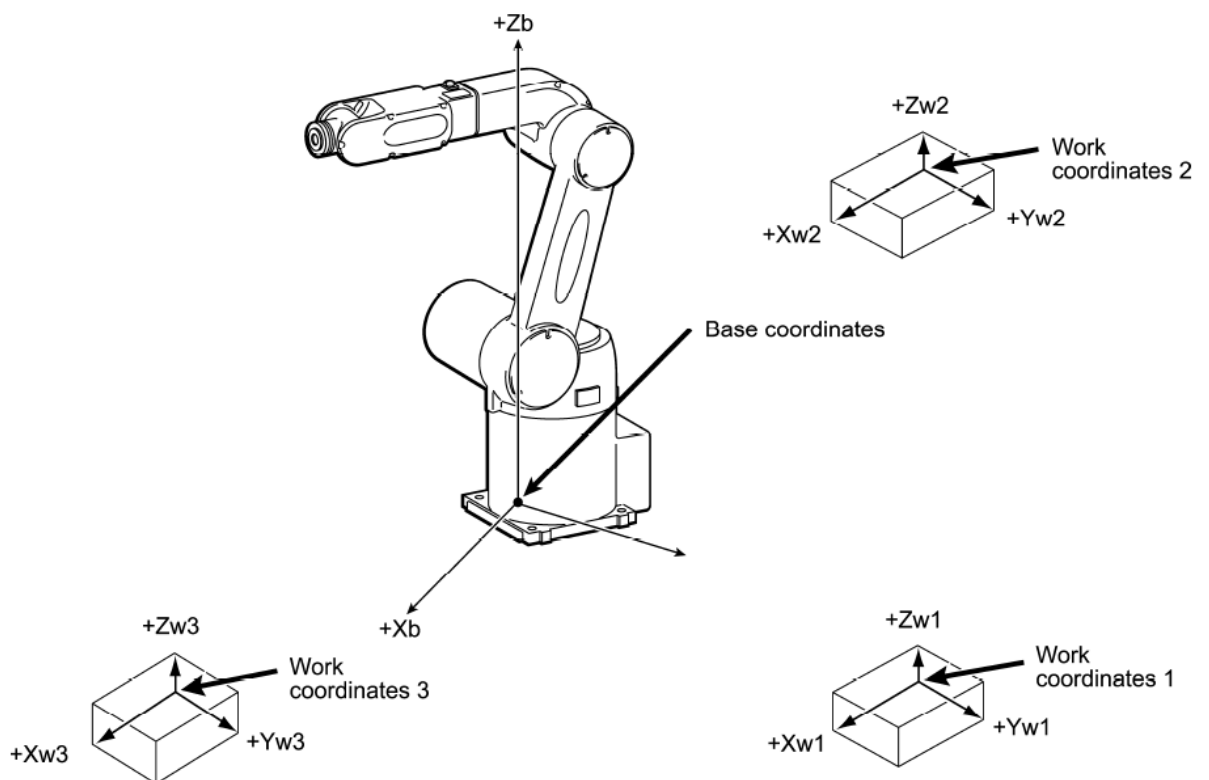


Figure B. 2: Base Coordinates and Work Coordinates

Position data

Position data refers to a set of data which includes seven components of base coordinates. Of these seven components, three are robot flange centre coordinates (the end-effector tip coordinates if an end-effector is defined) and four are current robot attitude components, as shown in *Figure B. 3*.

Appendix B

Position data allows you to represent the current position of the robot flange centre and object points.

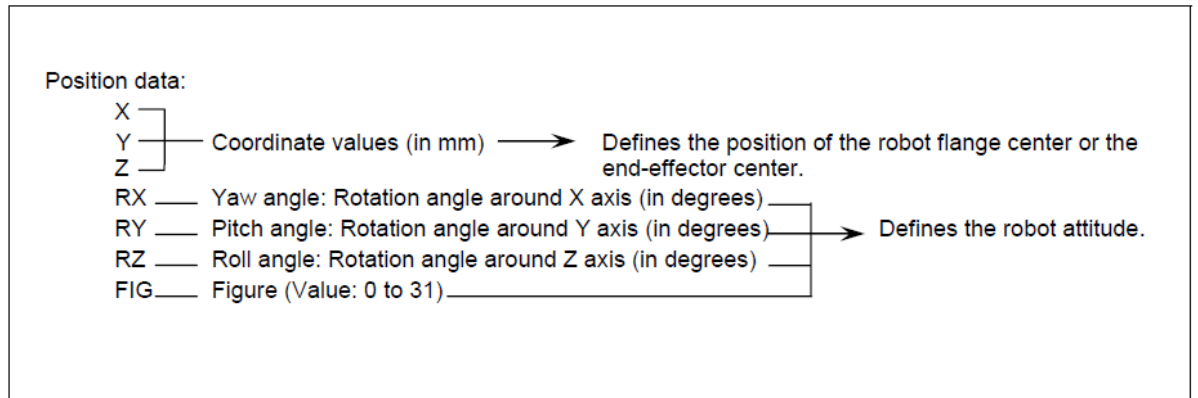


Figure B. 3: Components of Position Data

A set of X, Y, and Z coordinate values represents the position of the robot flange centre (or tip of the end-effector if defined) expressed in base coordinates (X_b , Y_b , and Z_b) in units of mm.

As shown in *Figure B. 3*, the yaw, pitch, and roll angles, which are expressed by RX, RY, and RZ, refer to rotation angles around the respective axes of the base coordinate system defined by the mechanical interface coordinate system whose origin is at the centre of the flange surface. These angles are expressed in units of degree.

With respect to the positive (+) direction on axes of the base coordinates, clockwise rotation is treated as positive (+).

You should always preserve the rotation order of RZ, RY, and RX. Changing it will cause the robot to take a different attitude in spite of the same rotation angle defined.

Appendix C

Experimental preparations and experimental tests for powder-based 3DP and extrusion-based 3DP

Appendix C

Appendix C

In this study, numerous tests were performed for powder-based 3DP; for example, the contact angle goniometry, 3D laser scanner, scanning electronic microscope, flowability test, porosity test, shear test, dimensional accuracy, delay printing time, compressive strength, flexural strength, tensile strength.

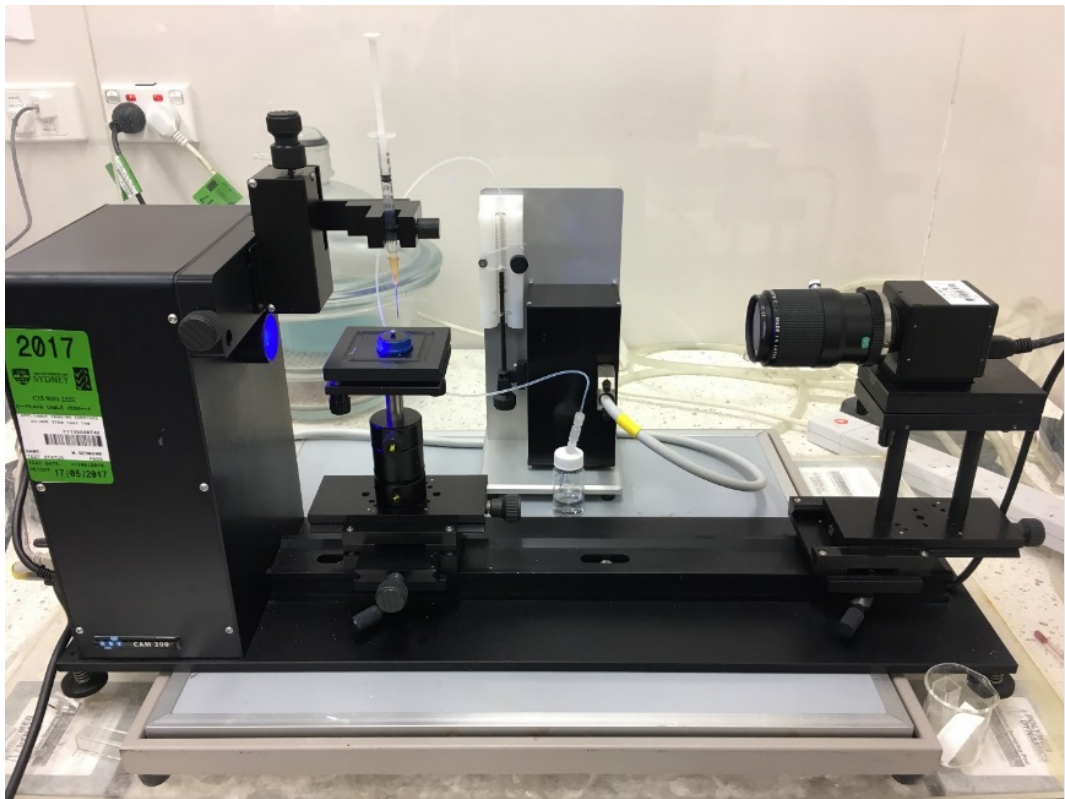


Figure C. 1: Contact angle goniometry test

Appendix C



Figure C. 2: 3D laser scanner

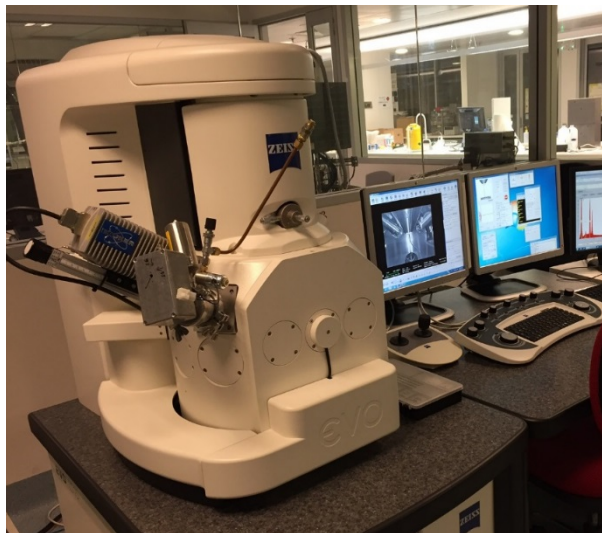


Figure C. 3: scanning electron microscope

Appendix C



Figure C. 4: Powder flow test apparatus



Figure C. 5: Apparent porosity test machine

Appendix C

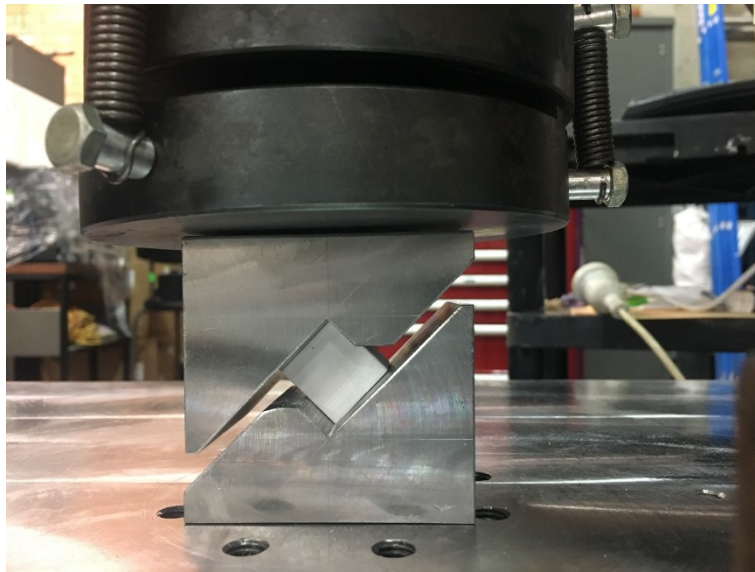


Figure C. 6: shear test

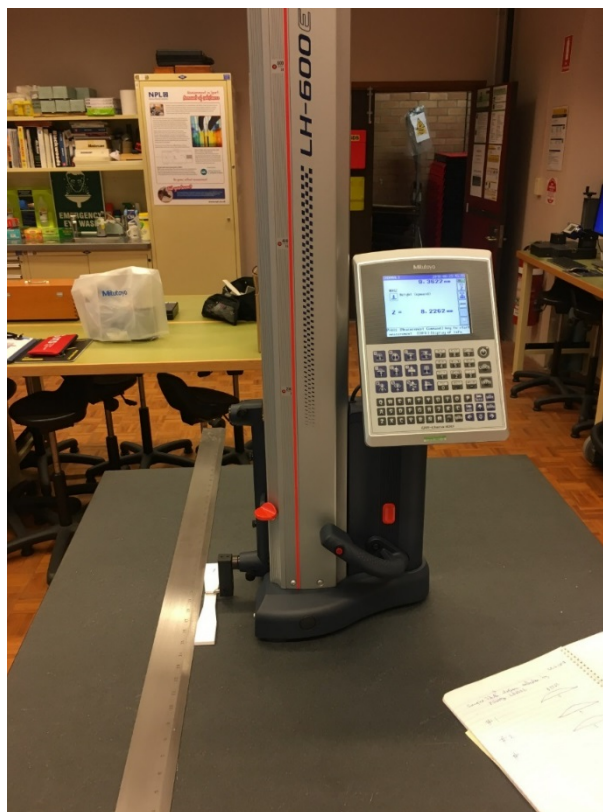


Figure C. 7: dimensional accuracy

Appendix C

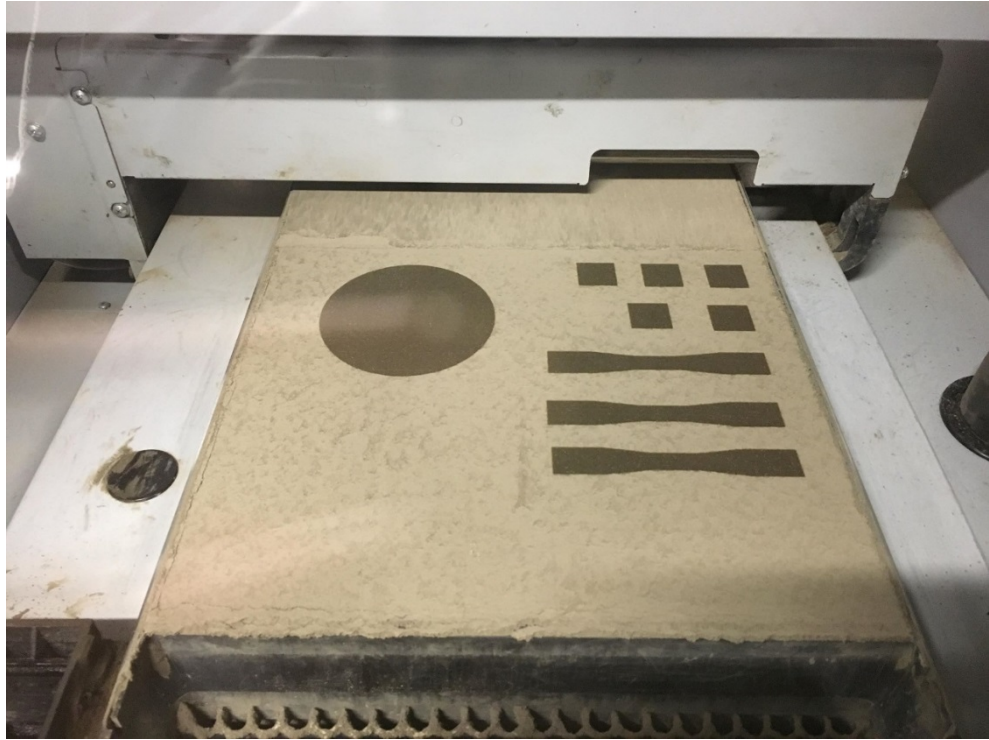


Figure C. 8: delay printing time

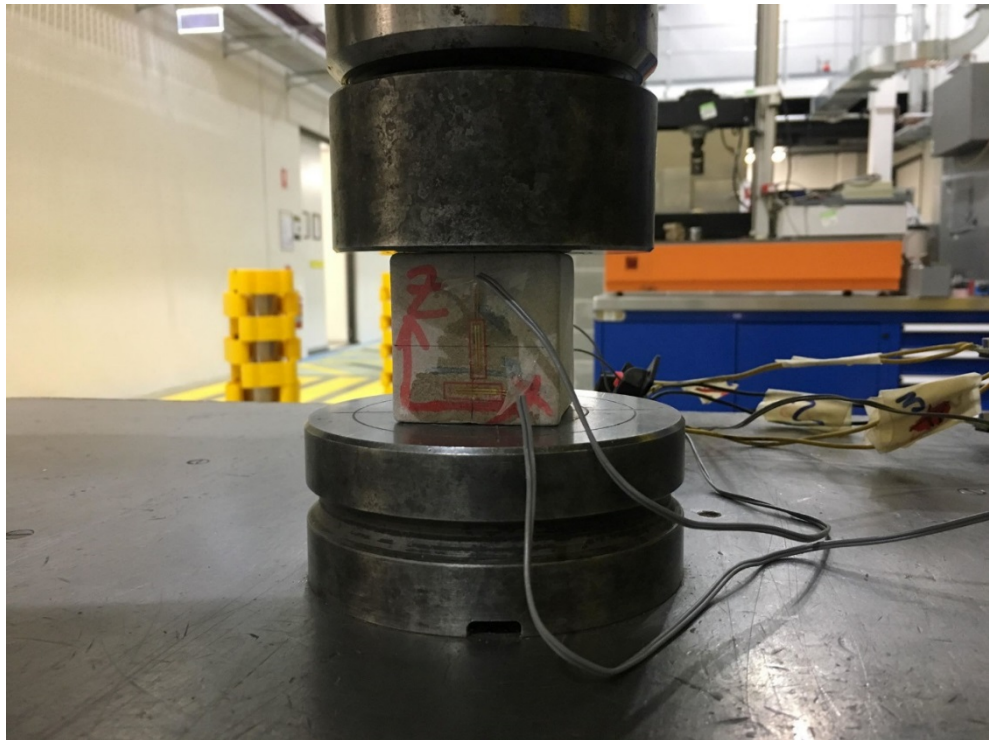


Figure C. 9: compressive strength

Appendix C

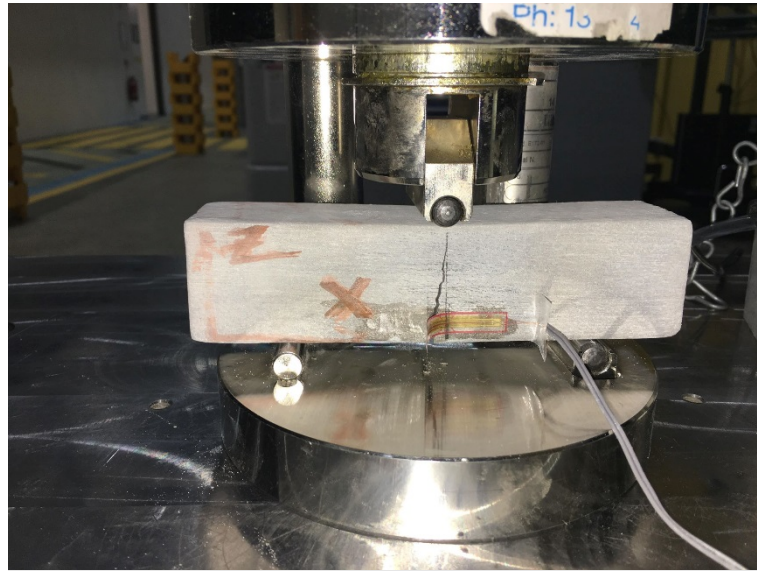


Figure C. 10: flexural strength

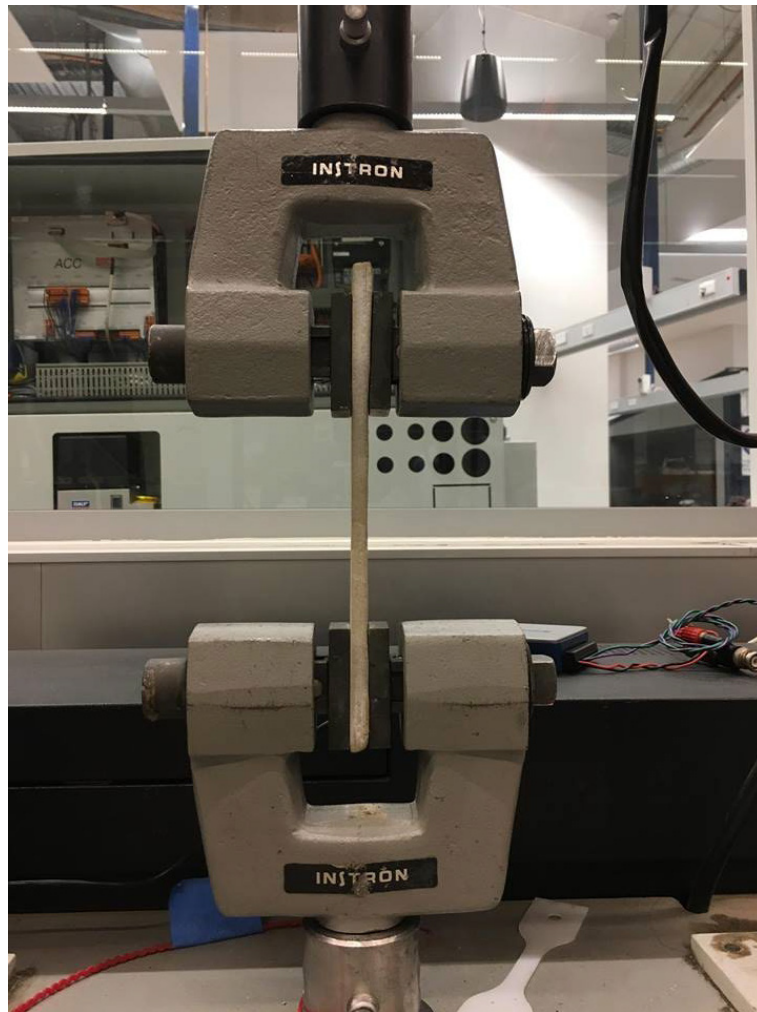


Figure C. 11: tensile strength

Appendix C

In similar, there were prepared tests for the extrusion-based technology; such as squeeze flow test, slump test, spread flow test, speed flow test, setting time test, compressive strength, flexural strength.

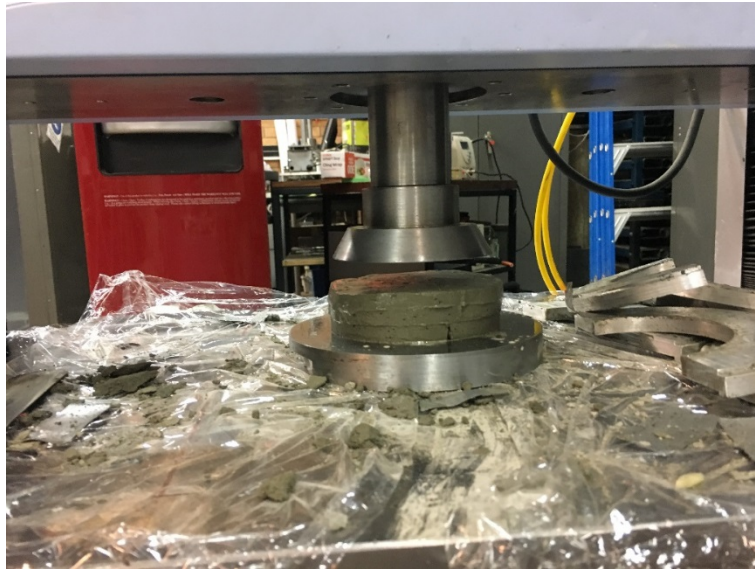


Figure C. 12: squeeze flow test



Figure C. 13: slump test

Appendix C



Figure C. 14: spread flow test

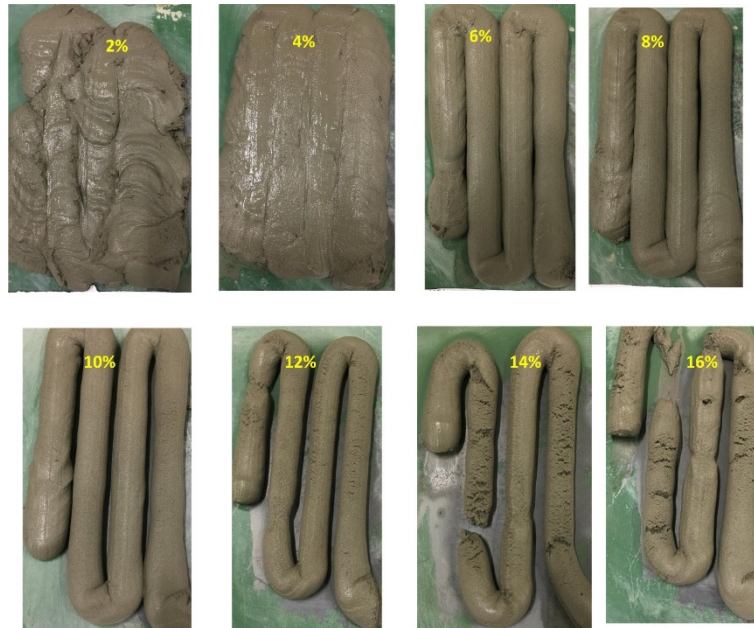


Figure C. 15: speed flow test

Appendix C



Figure C. 16: setting time test



Figure C. 17: compressive strength



Figure C. 18: flexural strength

Appendix D

ABAQUS documentation

Appendix D

Overview

A linear elastic material model:

- is valid for small elastic strains (normally less than 5%);
- can be isotropic, orthotropic, or fully anisotropic; and
- can have properties that depend on temperature and/or other field variables.

Defining linear elastic material behaviour

The total stress is defined from the total elastic strain as

$$\boldsymbol{\sigma} = \mathbf{D}^{el} \boldsymbol{\varepsilon}^{el},$$

where $\boldsymbol{\sigma}$ is the total stress (“true,” or Cauchy stress in finite-strain problems), \mathbf{D}^{el} is the fourth-order elasticity tensor, and $\boldsymbol{\varepsilon}^{el}$ is the total elastic strain (log strain in finite-strain problems). Do not use the linear elastic material definition when the elastic strains may become large; use a hyperelastic model instead. Even in finite-strain problems, the elastic strains should still be small (less than 5%).

Defining linear elastic response for viscoelastic materials

The elastic response of viscoelastic material (“Time domain viscoelasticity,” Section 17.7.1) can be specified by defining either the instantaneous response or the long-term response of the material. To define the instantaneous response, experiments to determine the elastic constants have to be performed within time spans much shorter than the characteristic relaxation time of the material.

Input File Usage: [*ELASTIC](#), MODULI=INSTANTANEOUS

Appendix D

ABAQUS/CAE Usage: Property module: material editor: **Mechanical**→**Elasticity**→**Elastic: Moduli time scale (for viscoelasticity): Instantaneous**

If, on the other hand, the long-term elastic response is used, data from experiments have to be collected after time spans much longer than the characteristic relaxation time of the viscoelastic material. Long-term elastic response is the default elastic material behaviour.

Input File Usage: [*ELASTIC](#), MODULI=LONG TERM

ABAQUS/CAE Usage: Property module: material editor: **Mechanical**→**Elasticity**→**Elastic: Moduli time scale (for viscoelasticity): Long-term**

Directional dependence of linear elasticity

Depending on the number of symmetry planes for the elastic properties, a material can be classified as either isotropic (an infinite number of symmetry planes passing through every point) or anisotropic (no symmetry planes). Some materials have a restricted number of symmetry planes passing through every point; for example, orthotropic materials have two orthogonal symmetry planes for the elastic properties. The number of independent components of the elasticity tensor \mathbf{D}^{el} depends on such symmetry properties. You define the level of anisotropy and method of defining the elastic properties, as described below. If the material is anisotropic, a local orientation (“Orientations,” Section 2.2.5) must be used to define the direction of anisotropy.

Stability of a linear elastic material

Linear elastic materials must satisfy the conditions of material or Drucker stability (see the discussion on material stability in “Hyperelastic behavior of rubberlike materials,” Section 17.5.1). Stability requires that the tensor \mathbf{D}^{el} be positive definite, which leads to

Appendix D

certain restrictions on the values of the elastic constants. The stress-strain relations for several different classes of material symmetries are given below. The appropriate restrictions on the elastic constants stemming from the stability criterion are also given.

Defining isotropic elasticity

The simplest form of linear elasticity is the isotropic case, and the stress-strain relationship is given by

$$\begin{Bmatrix} \varepsilon_{11} \\ \varepsilon_{22} \\ \varepsilon_{33} \\ \gamma_{12} \\ \gamma_{13} \\ \gamma_{23} \end{Bmatrix} = \begin{bmatrix} 1/E & -\nu/E & -\nu/E & 0 & 0 & 0 \\ -\nu/E & 1/E & -\nu/E & 0 & 0 & 0 \\ -\nu/E & -\nu/E & 1/E & 0 & 0 & 0 \\ 0 & 0 & 0 & 1/G & 0 & 0 \\ 0 & 0 & 0 & 0 & 1/G & 0 \\ 0 & 0 & 0 & 0 & 0 & 1/G \end{bmatrix} \begin{Bmatrix} \sigma_{11} \\ \sigma_{22} \\ \sigma_{33} \\ \sigma_{12} \\ \sigma_{13} \\ \sigma_{23} \end{Bmatrix}.$$

The elastic properties are completely defined by giving the Young's modulus, E , and the Poisson's ratio, ν . The shear modulus, G , can be expressed in terms of E and ν as $G = E/2(1 + \nu)$. These parameters can be given as functions of temperature and of other predefined fields, if necessary.

Input File Usage: [*ELASTIC](#), TYPE=ISOTROPIC

ABAQUS/CAE Usage: Property module: material editor: **Mechanical**→**Elasticity**→**Elastic: Type: Isotropic**

Stability

The stability criterion requires that $E > 0$, $G > 0$, and $-1 < \nu < 0.5$. Values of Poisson's ratio approaching 0.5 result in nearly incompressible behavior. With the exception of plane stress cases (including membranes and shells) or beams and trusses, such values generally require the use of “hybrid” elements in ABAQUS/Standard and generate high frequency noise and result in excessively small stable time increments in

Appendix D

ABAQUS/Explicit.

Defining orthotropic elasticity by specifying the engineering constants

Linear elasticity in an orthotropic material is most easily defined by giving the “engineering constants”: the three moduli E_1 , E_2 , E_3 ; Poisson's ratios ν_{12} , ν_{13} , ν_{23} ; and the shear moduli G_{12} , G_{13} , and G_{23} associated with the material's principal directions.

These moduli define elastic compliance according to

$$\begin{Bmatrix} \varepsilon_{11} \\ \varepsilon_{22} \\ \varepsilon_{33} \\ \gamma_{12} \\ \gamma_{13} \\ \gamma_{23} \end{Bmatrix} = \begin{bmatrix} 1/E_1 & -\nu_{21}/E_2 & -\nu_{31}/E_3 & 0 & 0 & 0 \\ -\nu_{12}/E_1 & 1/E_2 & -\nu_{32}/E_3 & 0 & 0 & 0 \\ -\nu_{13}/E_1 & -\nu_{23}/E_2 & 1/E_3 & 0 & 0 & 0 \\ 0 & 0 & 0 & 1/G_{12} & 0 & 0 \\ 0 & 0 & 0 & 0 & 1/G_{13} & 0 \\ 0 & 0 & 0 & 0 & 0 & 1/G_{23} \end{bmatrix} \begin{Bmatrix} \sigma_{11} \\ \sigma_{22} \\ \sigma_{33} \\ \sigma_{12} \\ \sigma_{13} \\ \sigma_{23} \end{Bmatrix}.$$

The quantity ν_{ij} has the physical interpretation of the Poisson's ratio that characterizes the transverse strain in the j -direction when the material is stressed in the i -direction. In general, ν_{ij} is not equal to ν_{ji} : they are related by $\nu_{ij}/E_i = \nu_{ji}/E_j$. The engineering constants can also be given as functions of temperature and other predefined fields, if necessary.

Input File Usage: `*ELASTIC, TYPE=ENGINEERING CONSTANTS`

ABAQUS/CAE Usage: Property module: material editor: **Mechanical** → **Elasticity** → **Elastic: Type: Engineering Constants**

Stability

Material stability requires

Appendix D

$$\begin{aligned}
 &E_1, E_2, E_3, G_{12}, G_{13}, G_{23} > 0, \\
 &|\nu_{12}| < (E_1/E_2)^{1/2}, \\
 &|\nu_{13}| < (E_1/E_3)^{1/2}, \\
 &|\nu_{23}| < (E_2/E_3)^{1/2}, \\
 &1 - \nu_{12}\nu_{21} - \nu_{23}\nu_{32} - \nu_{31}\nu_{13} - 2\nu_{21}\nu_{32}\nu_{13} > 0.
 \end{aligned}$$

When the left-hand side of the inequality approaches zero, the material exhibits incompressible behavior. Using the relations $\nu_{ij}/E_i = \nu_{ji}/E_j$, the second, third, and fourth restrictions in the above set can also be expressed as

$$\begin{aligned}
 &|\nu_{21}| < (E_2/E_1)^{1/2}, \\
 &|\nu_{31}| < (E_3/E_1)^{1/2}, \\
 &|\nu_{32}| < (E_3/E_2)^{1/2}.
 \end{aligned}$$

Defining transversely isotropic elasticity

A special subclass of orthotropy is transverse isotropy, which is characterized by a plane of isotropy at every point in the material. Assuming the 1–2 plane to be the plane of isotropy at every point, transverse isotropy requires that $E_1 = E_2 = E_p$, $\nu_{31} = \nu_{32} = \nu_{tp}$, $\nu_{13} = \nu_{23} = \nu_{pt}$, and $G_{13} = G_{23} = G_t$, where p and t stand for “in-plane” and “transverse,” respectively. Thus, while ν_{tp} has the physical interpretation of the Poisson's ratio that characterizes the strain in the plane of isotropy resulting from stress normal to it, ν_{pt} characterizes the transverse strain in the direction normal to the plane of isotropy resulting from stress in the plane of isotropy. In general, the quantities ν_{tp} and ν_{pt} are not equal and are related by $\nu_{tp}/E_t = \nu_{pt}/E_p$. The stress-strain laws reduce to

$$\begin{Bmatrix} \varepsilon_{11} \\ \varepsilon_{22} \\ \varepsilon_{33} \\ \gamma_{12} \\ \gamma_{13} \\ \gamma_{23} \end{Bmatrix} = \begin{bmatrix} 1/E_p & -\nu_p/E_p & -\nu_{tp}/E_t & 0 & 0 & 0 \\ -\nu_p/E_p & 1/E_p & -\nu_{tp}/E_t & 0 & 0 & 0 \\ -\nu_{pt}/E_p & -\nu_{pt}/E_p & 1/E_t & 0 & 0 & 0 \\ 0 & 0 & 0 & 1/G_p & 0 & 0 \\ 0 & 0 & 0 & 0 & 1/G_t & 0 \\ 0 & 0 & 0 & 0 & 0 & 1/G_t \end{bmatrix} \begin{Bmatrix} \sigma_{11} \\ \sigma_{22} \\ \sigma_{33} \\ \sigma_{12} \\ \sigma_{13} \\ \sigma_{23} \end{Bmatrix},$$

Appendix D

where $G_p = E_p / 2(1 + \nu_p)$ and the total number of independent constants is only five.

Input File Usage: `*ELASTIC, TYPE=ENGINEERING CONSTANTS`

ABAQUS/CAE Usage: Property module: material editor: **Mechanical** → **Elasticity** → **Elastic: Type: Engineering Constants**

Stability

In the transversely isotropic case the stability relations for orthotropic elasticity simplify to

$$\begin{aligned} E_p, E_t, G_p, G_t &> 0, \\ |\nu_p| &< 1, \\ |\nu_{pt}| &< (E_p/E_t)^{1/2}, \\ |\nu_{tp}| &< (E_t/E_p)^{1/2}, \\ 1 - \nu_p^2 - 2\nu_{tp}\nu_{pt} - 2\nu_p\nu_{tp}\nu_{pt} &> 0. \end{aligned}$$

Defining orthotropic elasticity in plane stress

Under plane stress conditions, such as in a shell element, only the values of $E_1, E_2, \nu_{12}, G_{12}, G_{13},$ and G_{23} are required to define an orthotropic material. (In all of the plane stress elements in ABAQUS the (1, 2) surface is the surface of plane stress, so that the plane stress condition is $\sigma_{33} = 0$.) The shear moduli G_{13} and G_{23} are included because they may be required for modeling transverse shear deformation in a shell. The Poisson's ratio ν_{21} is implicitly given as $\nu_{21} = (E_2/E_1)\nu_{12}$. In this case the stress-strain relations for the in-plane components of the stress and strain are of the form

$$\begin{Bmatrix} \varepsilon_1 \\ \varepsilon_2 \\ \gamma_{12} \end{Bmatrix} = \begin{bmatrix} 1/E_1 & -\nu_{12}/E_1 & 0 \\ -\nu_{12}/E_1 & 1/E_2 & 0 \\ 0 & 0 & 1/G_{12} \end{bmatrix} \begin{Bmatrix} \sigma_{11} \\ \sigma_{22} \\ \tau_{12} \end{Bmatrix}.$$

Input File Usage: `*ELASTIC, TYPE=LAMINA`

ABAQUS/CAE Usage: Property module: material editor: **Mechanical** → **Elasticity** → **Elastic: Type: Lamina**

Appendix D

Stability

Material stability for plane stress requires

$$E_1, E_2, G_{12}, G_{13}, G_{23} > 0,$$

$$|\nu_{12}| < (E_1/E_2)^{1/2}.$$

Defining orthotropic elasticity by specifying the terms in the elastic stiffness matrix

Linear elasticity in an orthotropic material can also be defined by giving the nine independent elastic stiffness parameters, as functions of temperature and other predefined fields, if necessary. In this case the stress-strain relations are of the form

$$\begin{Bmatrix} \sigma_{11} \\ \sigma_{22} \\ \sigma_{33} \\ \sigma_{12} \\ \sigma_{13} \\ \sigma_{23} \end{Bmatrix} = \begin{bmatrix} D_{1111} & D_{1122} & D_{1133} & 0 & 0 & 0 \\ & D_{2222} & D_{2233} & 0 & 0 & 0 \\ & & D_{3333} & 0 & 0 & 0 \\ & & & D_{1212} & 0 & 0 \\ & \text{sym} & & & D_{1313} & 0 \\ & & & & & D_{2323} \end{bmatrix} \begin{Bmatrix} \varepsilon_{11} \\ \varepsilon_{22} \\ \varepsilon_{33} \\ \gamma_{12} \\ \gamma_{13} \\ \gamma_{23} \end{Bmatrix} = [D^{el}] \begin{Bmatrix} \varepsilon_{11} \\ \varepsilon_{22} \\ \varepsilon_{33} \\ \gamma_{12} \\ \gamma_{13} \\ \gamma_{23} \end{Bmatrix}$$

For an orthotropic material the engineering constants define the \mathbf{D} matrix as

$$D_{1111} = E_1(1 - \nu_{23}\nu_{32})\Upsilon,$$

$$D_{2222} = E_2(1 - \nu_{13}\nu_{31})\Upsilon,$$

$$D_{3333} = E_3(1 - \nu_{12}\nu_{21})\Upsilon,$$

$$D_{1122} = E_1(\nu_{21} + \nu_{31}\nu_{23})\Upsilon = E_2(\nu_{12} + \nu_{32}\nu_{13})\Upsilon,$$

$$D_{1133} = E_1(\nu_{31} + \nu_{21}\nu_{32})\Upsilon = E_3(\nu_{13} + \nu_{12}\nu_{23})\Upsilon,$$

$$D_{2233} = E_2(\nu_{32} + \nu_{12}\nu_{31})\Upsilon = E_3(\nu_{23} + \nu_{21}\nu_{13})\Upsilon,$$

$$D_{1212} = G_{12},$$

$$D_{1313} = G_{13},$$

$$D_{2323} = G_{23},$$

where

$$\Upsilon = \frac{1}{1 - \nu_{12}\nu_{21} - \nu_{23}\nu_{32} - \nu_{31}\nu_{13} - 2\nu_{21}\nu_{32}\nu_{13}}.$$

When the material stiffness parameters (the D_{ijkl}) are given directly, ABAQUS imposes

Appendix D

the constraint $\sigma_{33} = 0$ for the plane stress case to reduce the material's stiffness matrix as required.

Input File Usage: `*ELASTIC, TYPE=ORTHOTROPIC`

ABAQUS/CAE Usage: Property module: material editor: **Mechanical** → **Elasticity** → **Elastic: Type: Orthotropic**

Stability

The restrictions on the elastic constants due to material stability are

$$\begin{aligned} D_{1111}, D_{2222}, D_{3333}, D_{1212}, D_{1313}, D_{2323} &> 0, \\ |D_{1122}| &< (D_{1111} D_{2222})^{1/2}, \\ |D_{1133}| &< (D_{1111} D_{3333})^{1/2}, \\ |D_{2233}| &< (D_{2222} D_{3333})^{1/2}, \\ \det(D^{el}) &> 0. \end{aligned}$$

The last relation leads to

$$D_{1111} D_{2222} D_{3333} + 2D_{1122} D_{1133} D_{2233} - D_{2222} D_{1133}^2 - D_{1111} D_{2233}^2 - D_{3333} D_{1122}^2 > 0.$$

These restrictions in terms of the elastic stiffness parameters are equivalent to the restrictions in terms of the “engineering constants.” Incompressible behavior results when the left-hand side of the inequality approaches zero.

Defining fully anisotropic elasticity

For fully anisotropic elasticity 21 independent elastic stiffness parameters are needed.

The stress-strain relations are as follows:

$$\begin{Bmatrix} \sigma_{11} \\ \sigma_{22} \\ \sigma_{33} \\ \sigma_{12} \\ \sigma_{13} \\ \sigma_{23} \end{Bmatrix} = \begin{bmatrix} D_{1111} & D_{1122} & D_{1133} & D_{1112} & D_{1113} & D_{1123} \\ & D_{2222} & D_{2233} & D_{2212} & D_{2213} & D_{2223} \\ & & D_{3333} & D_{3312} & D_{3313} & D_{3323} \\ & & & D_{1212} & D_{1213} & D_{1223} \\ & sym & & D_{1313} & D_{1323} & \\ & & & & D_{2323} & \end{bmatrix} \begin{Bmatrix} \epsilon_{11} \\ \epsilon_{22} \\ \epsilon_{33} \\ \gamma_{12} \\ \gamma_{13} \\ \gamma_{23} \end{Bmatrix} = [D^{el}] \begin{Bmatrix} \epsilon_{11} \\ \epsilon_{22} \\ \epsilon_{33} \\ \gamma_{12} \\ \gamma_{13} \\ \gamma_{23} \end{Bmatrix}$$

Appendix D

When the material stiffness parameters (the D_{ijkl}) are given directly, ABAQUS imposes the constraint $\sigma_{33} = 0$ for the plane stress case to reduce the material's stiffness matrix as required.

Input File Usage: `*ELASTIC, TYPE=ANISOTROPIC`

ABAQUS/CAE Usage: Property module: material editor: **Mechanical** → **Elasticity** → **Elastic: Type: Anisotropic**

Stability

The restrictions imposed upon the elastic constants by stability requirements are too complex to express in terms of simple equations. However, the requirement that \mathbf{D}^{el} is positive definite requires that all of the eigenvalues of the elasticity matrix $[D^{el}]$ be positive.

Defining orthotropic elasticity for warping elements

For two-dimensional meshed models of solid cross-section Timoshenko beam elements modelled with warping elements (see “Meshed beam cross-sections,” Section 10.4.1), ABAQUS offers a linear elastic material definition that can have two different shear moduli in the user-specified material directions. In the user-specified directions the stress-strain relations are as follows:

$$\begin{Bmatrix} \sigma \\ \tau_1 \\ \tau_2 \end{Bmatrix} = \begin{bmatrix} E & & \\ & G_1 & \\ & & G_2 \end{bmatrix} \begin{Bmatrix} \varepsilon \\ \gamma_1 \\ \gamma_2 \end{Bmatrix}.$$

A local orientation is used to define the angle α between the global directions and the user-specified material directions. In the cross-section directions the stress-strain relations are as follows:

Appendix D

$$\begin{Bmatrix} \sigma \\ \tau_1 \\ \tau_2 \end{Bmatrix} = \begin{bmatrix} E & 0 & 0 \\ G_1(\cos \alpha)^2 + G_2(\sin \alpha)^2 & (G_1 - G_2) \cos \alpha \sin \alpha & \\ \text{sym} & G_1(\sin \alpha)^2 + G_2(\cos \alpha)^2 & \end{bmatrix} \begin{Bmatrix} \varepsilon \\ \gamma_1 \\ \gamma_2 \end{Bmatrix},$$

where σ represents the beam's axial stress and τ_1 and τ_2 represent two shear stresses.

Input File Usage: [*ELASTIC](#), TYPE=TRACTION

ABAQUS/CAE Usage: Property module: material editor: **Mechanical**→**Elasticity**→**Elastic: Type: Traction**

Stability

The stability criterion requires that $E > 0$, $G_1 > 0$, and $G_2 > 0$.